

ABSTRACT

Rapid Deuterium Labeling and Localization for Structural Elucidation of Carbohydrates

H. Jamie Kim, Ph.D.

Mentor: Elyssia Steinwinter Gallagher, Ph.D.

Carbohydrates are crucial components of life, serving a variety of cellular functions with broad implications. Characterization of carbohydrate structures is a significant step for understanding cell biology. While mass spectrometry (MS) is a powerful tool that provides both qualitative and quantitative information on a number of analytes, ranging in size and functionality, structural characterizations of carbohydrates via MS generally focuses on sequencing rather than analyzing conformations.

Hydrogen/deuterium exchange (HDX) is a well-established technique that is traditionally used to study protein conformations and dynamics. However, application of HDX for carbohydrate analysis has been limited due to the rapid HDX rates of carbohydrate hydroxyls, which range in the microsecond timescale. The goal of this work was to develop HDX methods to characterize carbohydrate conformations and provide additional dimension for MS analysis of carbohydrates.

HDX was performed in electrospray (ESI) droplets, thus achieving rapid labeling of biologically relevant structures in solution-phase. Residual solvents in ESI sources were found to cause additional deuterium labeling or loss beyond the HDX reactions in

bulk-solution (Chapter Two). The HDX in ESI was affected by changes in the equilibrium of solvent vapors inside the source as samples are infused in real-time during analysis. This in-ESI HDX effect affected not only carbohydrates but also rapidly-exchanging functional groups of peptides, indicating broader implications for protein HDX analysis. Chapter Three presents utilization of theta-ESI emitters to achieve variable HDX timepoints of carbohydrates by varying initial ESI droplet sizes from varying ESI tip diameters.

Deuterium labels on carbohydrates were localized by collision induced dissociation (CID). Chapter Four investigates scrambling by vibrational activation during CID, concluding that sodium-adduction to carbohydrates reduces scrambling and maintains meaningful HDX information. In Chapter Five, HDX-CID-MS is applied to carbohydrate isomers to assign deuterium labels. Computational methods are employed to examine fragmentation pathways of each carbohydrate based on their conformations and the relative exchange rates of different functional groups. Deuterium localization on carbohydrates, with their limited number of functional groups and narrow range of exchange rates, displays a positive outlook for HDX analysis of carbohydrates that can detect transient inter- and intramolecular interactions of carbohydrates.

Rapid Deuterium Labeling and Localization for Structural Elucidation of Carbohydrates

by

Hyunjoo Jamie Kim, B.S.

A Dissertation

Approved by the Department of Chemistry and Biochemistry

Patrick J. Farmer, Ph.D., Chairperson

Submitted to the Graduate Faculty of
Baylor University in Partial Fulfillment of the
Requirements for the Degree
of
Doctor of Philosophy

Approved by the Dissertation Committee

Elyssia S. Gallagher, Ph.D., Chairperson

Touradj Solouki, Ph.D.

C. Kevin Chambliss, Ph.D.

Kevin L. Shuford, Ph.D.

Erich J. Baker, Ph.D.

Accepted by the Graduate School

May 2021

J. Larry Lyon, Ph.D., Dean

Copyright © 2021 by H. Jamie Kim

All rights reserved

TABLE OF CONTENTS

LIST OF FIGURES	ix
LIST OF TABLES	xiv
LIST OF ABBREVIATIONS.....	xvii
ACKNOWLEDGMENTS	xviii
DEDICATION	xx
CHAPTER ONE	1
Introduction.....	1
1.1 Glycosylation	1
1.1.1 Structures and Nomenclature.....	1
1.1.2 Glycoprotein Heterogeneity.....	6
1.1.3 Glycoprotein Interactions.....	7
1.1.4 Analytical Techniques to Study Glycans.....	8
1.2 Mass Spectrometry.....	12
1.2.1 Electrospray Ionization	12
1.2.2 Tandem Techniques Coupled to Mass Spectrometry	17
1.3 Hydrogen/Deuterium Exchange.....	25
1.3.1 Basics of HDX.....	25
1.3.2 HDX Rates	30
1.3.3 HDX of Carbohydrates	33
1.4 Dissertation Outline	34
CHAPTER TWO	35
Mass Spectral Detection of Forward- and Reverse-Hydrogen/Deuterium Exchange Resulting from Residual Solvent Vapors in Electrospray Sources	35
2.1 Abstract	35
2.2 Introduction.....	36
2.3 Experimental	40
2.3.1 Materials	40
2.3.2 Sample Preparation	40
2.3.3 HDX During Direct Infusion of Carbohydrates.....	40
2.3.4 HDX Following Pre-Equilibration of the Source	41
2.3.5 HDX with Defined Solution Labeling Times	42
2.3.6 Calculations.....	43
2.4 Results and Discussion	45

2.4.1 Faster Sample Infusion Rates Increase the Deuterium Labeling Rate of Hydroxyls.....	45
2.4.2 Residual Solvent Vapors in the ESI Source Result in HDX of Hydroxyls .	47
2.4.3 Solvent Vapors Differentially Affect Functional Groups with Different Exchange Rates.....	53
2.4.4 Solvent Vapors Affect Exchange of Glu-fib Peptides	56
2.5 Conclusions.....	58
2.6 Acknowledgements.....	60
CHAPTER THREE	61
Achieving Multiple Hydrogen/Deuterium Exchange Timepoints of Carbohydrate Hydroxyls Using Theta-Electrospray Emitters.....	61
3.1 Abstract	61
3.2 Introduction.....	62
3.3 Methods.....	64
3.3.1 Materials	64
3.3.2 Sample preparation	65
3.3.3 Open-Source Setup with Pulled Theta ESI Emitters	65
3.3.4 HDX Experiments.....	66
3.3.5 Calculations and Data Presentation	66
3.3.6 Protein Folding Experiments	67
3.4 Results and Discussion	68
3.4.1 Orientation of the Theta Tip Results in Changes to the Ion Transmission from Each Channel	68
3.4.2 Minimal HDX is Observed for Carbohydrates When Varying the Applied Voltage or the Distance Between the Theta Tip and the MS Cone	69
3.4.3 HDX Labeling Times and the Resulting Magnitude of HDX Can be Increased by Increasing Initial ESI Droplet Sizes	72
3.5 Conclusions.....	78
3.6 Acknowledgements.....	79
CHAPTER FOUR.....	80
Deuterium Localization with Minimal Scrambling on Carbohydrate-Metal Complexes via Collision Induced Dissociation.....	80
4.1 Abstract	80
4.2 Introduction.....	81
4.3 Methods.....	83
4.3.1 Materials	83
4.3.2 Collision Induced Dissociation	84

4.3.3 Calculations and Data Presentation	85
4.3.4 Energy Calculations for HDX of Carbohydrate Hydroxyls.....	86
4.3.5 Molecular Dynamics and Electronic Structure Calculations of Sodium-Adducted Melezitose	86
4.4. Results and Discussion	87
4.4.1 Glycosidic Bond Cleavage Mechanisms Can be Used to Localize Deuterium Labels on Sodium-Adducted Melezitose Fragments	87
4.4.2 HDX-CID MS of Calcium-Adducted Melezitose Reveals Minimal Differentiation Between Fragments.....	95
4.4.3 Sodium-Adduction Reduces Scrambling During CID.....	101
4.5 Conclusion	106
4.6 Acknowledgments.....	107
CHAPTER FIVE	108
Analysis of Conformational Differences in Carbohydrate Isomers via Hydrogen/Deuterium Exchange Coupled to Tandem Mass Spectrometry.....	108
5.1 Abstract	108
5.2 Introduction.....	109
5.3 Methods.....	111
5.3.1 Materials	111
5.3.2 Collision Induced Dissociation of Deuterated Carbohydrate-Sodium Complexes	112
5.3.3 Data Analysis and Presentation	113
5.3.4 Computational Methods for Structural Analysis of Carbohydrate-Sodium Complexes	114
5.4 Results and Discussion	116
5.4.1 Exchange Rates of Primary and Secondary Hydroxyls on HDX of Melezitose.....	116
5.4.2 Hydrogen Bonds and Cooperativity Effects on HDX of Raffinose with Asymmetric Terminal Sugars	122
5.4.3 HDX of Maltotriose with Fast-Exchanging Anomeric Hydroxyls on the Reducing End.....	128
5.5 Conclusion	133
5.6 Acknowledgments.....	134
CHAPTER SIX.....	135
Summary and Future Directions	135
6.1 Summary.....	135
6.2 Future Directions	138
APPENDIX A.....	141

Supplementary Information for Chapter Two: Mass Spectral Detection of Forward- and Reverse-Hydrogen/Deuterium Exchange Resulting from Residual Solvent Vapors in Electrospray Sources.....	141
APPENDIX B.....	153
Supplementary Information for Chapter Three: Achieving Multiple Hydrogen/Deuterium Exchange Timepoints of Carbohydrate Hydroxyls Using Theta-Electrospray Emitters.....	153
APPENDIX C.....	157
Supplementary Information for Chapter Four: Deuterium Localization with Minimal Scrambling on Carbohydrate-Metal Complexes via Collision Induced Dissociation.....	157
APPENDIX D.....	183
Supplementary Information for Chapter Five.....	183
APPENDIX E.....	213
Investigating Carbohydrate-Metal Complex Fragmentation Pathways via Collision Induced Dissociation and Transition State Calculations.....	213
E.1 Introduction.....	213
E.2 Materials and Methods.....	215
E.2.1 Sample Preparation.....	215
E.2.2 Collision Induced Dissociation.....	215
E.2.3 Transition State Calculations.....	217
E.3 Results and Discussion.....	219
E.4 Conclusions and Future Directions.....	244

LIST OF FIGURES

Figure 1.1. Chemical structures of common monosaccharides in mammalian glycans	2
Figure 1.2. Acyclic and cyclic carbohydrate structures in Fischer, Haworth, and chair conformations	3
Figure 1.3. Mechanism of mutarotation between α - and β -anomers of glucose.....	4
Figure 1.4. Chemical structures of melezitose and maltotriose	6
Figure 1.5. Schematic of electrospray ionization process in positive ion mode.....	13
Figure 1.6. Proposed mechanisms of ESI.....	15
Figure 1.7. Roepstorff and Fohlman nomenclature for peptide fragmentation	22
Figure 1.8. Domon and Costello nomenclature for carbohydrate fragmentation	24
Figure 1.9. Workflow of bottom-up, continuous-labeling HDX experiments of proteins	26
Figure 1.10. HDX rates of protein functional groups	31
Figure 1.11. Solution-phase HDX mechanisms for protein backbone amides	32
Figure 1.12. Gas-phase HDX mechanisms for protein backbone amides	32
Figure 2.1. Representative deuterium-exchange spectra for sodiated-melezitose detected by ESI-MS	46
Figure 2.2. Representative HDX spectrum for sodiated-melezitose infused at different rates	46
Figure 2.3. Residual solvent vapors caused in-ESI HDX of sodiated-melezitose.....	48
Figure 2.4. Residual solvent vapors were observed to cause HDX of sodiated-melezitose in an Ion Max Source of an LTQ Orbitrap Discovery MS	51
Figure 2.5. Deuterium exchange for sodiated-melezitose and sodiated-NAG ₃ after a defined in-solution HDX time	54

Figure 2.6. Residual solvent vapor HDX causes labeling of rapidly exchanging functional groups of glu-fib, a peptide.....	57
Figure 3.1. Representative mass spectra of Leu- and Met-enkephalin when varying the orientation of the theta tip with respect to the MS cone	69
Figure 3.2. HDX of sodiated melezitose sprayed from theta tips with 0.5 μm channels...	71
Figure 3.3. Representative mass spectra of deuterated, sodiated melezitose sprayed from theta tips with varying sizes.....	76
Figure 4.1. (A) Fragmentation spectrum of sodium-adducted melezitose, (B) structures of fragments, and (C) deuteration plot of fragments from sodium-adducted melezitose in 50% D_2O	88
Figure 4.2. (A) Fragmentation spectrum of calcium-adducted melezitose, (B) structures of fragments, and (C) deuteration plot of fragments from calcium-adducted melezitose in 50% D_2O	96
Figure 4.3. Deuteration plots of common fragments from sodium- and calcium-adducted melezitose in 50% D_2O	101
Figure 4.4. Deuteration plot of C_1/Y_1 and B_2/Z_2 fragments generated from deprotonated melezitose in 50% D_2O	104
Figure 5.1. (A) Deuteration plot of B_2/Z_2 and C_1/Y_1 fragments generated from sodium-adducted melezitose and (B) representative structure of melezitose-sodium complex optimized by DFT	118
Figure 5.2. (A) Deuteration plot of B_2/Z_2 and C_2/Y_2 fragments generated from sodium-adducted melezitose and (B) representative structure of melezitose-sodium complex optimized by DFT	120
Figure 5.3. (A) Deuteration plot of B_2/Z_2 and C_1/Y_1 fragments generated from sodium-adducted raffinose and (B) representative structure of raffinose-sodium complex optimized by DFT	123
Figure 5.4. (A) Deuteration plot of B_2/Z_2 and C_2/Y_2 fragments generated from sodium-adducted raffinose and (B) representative structure of raffinose-sodium complex optimized by DFT	126
Figure 5.5. (A) Deuteration plot of B_2/Z_2 and C_1/Y_1 fragments generated from sodium-adducted maltotriose and (B) representative structure of maltotriose-sodium complex optimized by DFT	129

Figure 5.6. Representative structures of maltotriose-sodium complexes with extensive hydrogen bonding networks on the non-reducing end.....	130
Figure 5.7. (A) Deuteration plot of B ₂ /Z ₂ and C ₂ /Y ₂ fragments generated from sodium-adducted maltotriose and (B) representative structure of maltotriose-sodium complex optimized by DFT	131
Figure A.1. Structures of melezitose and tri- <i>N</i> -acetylglucosamine (NAG ₃)	141
Figure A.2. HDX spectra of sodiated-melezitose in mixtures of D ₂ O and H ₂ O following pre-equilibration of the source	142
Figure A.3. Proton uptake of deuterated melezitose-sodium adducts following pre-equilibration of the source with H ₂ O, methanol (MeOH), or acetonitrile (ACN).	143
Figure A.4. Correlation plot illustrating no observable relationship between source temperature and time for deuterium uptake to decrease by 95 %.	146
Figure A.5. Correlation plots of source gas flow rates and residual solvent vapor HDX. ...	150
Figure A.6. Mechanism of mutarotation between α- and β-tri- <i>N</i> -acetylglucosamine (NAG ₃)	151
Figure B.1. Schematic drawing of a theta capillary cross-section	153
Figure B.2. (A) Diagram and (B) pictures of the open-source setup used for theta-tip HDX experiments.....	154
Figure B.3. Representative mass spectra of apomyoglobin and cytochrome c in protein folding experiments via theta tips	155
Figure C.1. Representative mass spectra of (A) [Melezitose+Na] ⁺ at 50% deuteration and [M+Na+5D] ⁺ (<i>m/z</i> 532) isolated with LM Res parameters of (B) 4.9 and (C) 15.0	157
Figure C.2. Deuteration plots of B ₂ /Z ₂ and C ₂ /Y ₂ fragments generated from sodium-adducted melezitose in (A) 25% and (B) 75% D ₂ O.....	158
Figure C.3. Undeuterated and fully deuterated fragment spectra of sodium-adducted melezitose	159
Figure C.4. Representative molecular structure of [Melezitose + Na] ⁺ complex.....	160
Figure C.5. Representative mass spectra of C ₁ /Z ₁ fragments of melezitose adducted to (A) sodium or (B) calcium and singly-charged by deprotonation in 98% D ₂ O.....	169

Figure C.6. Deuteration plots of three common fragments from (A) sodium- and (B) calcium-adducted melezitose in 50% MeOD.	177
Figure C.7. Deuteration plots of sodium-adducted melezitose at collision voltage of (A) 24 V, (B) 28 V, (C) 32 V, and (D) 36 V.	182
Figure D.1. Structures of (A) melezitose, (B) raffinose, and (C) maltotriose.....	183
Figure D.2. Proposed fragmentation pathways of sodium-adducted melezitose via CID. ...	184
Figure D.3. Representative fragmentation spectra of C ₁ /Y ₁ fragment generated from sodium-adducted raffinose in (A) water and (B) 98% D ₂ O.	194
Figure D.4. Proposed fragmentation pathways of sodium-adducted raffinose via CID.....	198
Figure D.5. Proposed fragmentation pathways of sodium-adducted maltotriose via CID. ...	207
Figure E.1. Chemical structures of (A) melezitose, (B) raffinose, and (C) maltotriose with their glycosidic bond cleavage fragments.....	217
Figure E.2. (A) Representative fragmentation spectrum of sodium-adducted melezitose at collision voltage of 32 V. (B) Intensities of sodium-adducted melezitose fragments at collision voltage ranging 4 – 36 V.	221
Figure E.3. Melezitose fragmentation nomenclature.....	223
Figure E.4. Representative structure of the sodium-adducted melezitose precursor optimized by DFT calculations.	225
Figure E.5. Transition state structures for (A) C ₁ /Z ₂ and (B) Y ₁ /B ₂ fragments.....	226
Figure E.6. Representative conformations of melezitose-sodium complexes in which hydroxyl contributions to glycosidic oxygens lead to different fragmentation pathways favoring production of (A) B ₁ /Y ₂ and B ₂ /Y ₁ or (B) only B ₁ /Y ₂	228
Figure E.7. Optimized structures of (A) B ₂ /Y ₁ and (B) C ₁ /Z ₂ fragment pairs adducted to sodium after glycosidic bond dissociation of melezitose.	230
Figure E.8. (A) Representative fragmentation spectrum of sodium-adducted raffinose at collision voltage of 32 V. (B) Intensities of sodium-adducted raffinose fragments at collision voltages ranging from 4 – 32 V.	231
Figure E.9. Representative structures of sodium-adducted raffinose.	232
Figure E.10. Optimized structures of (A) B ₂ /Y ₁ , (B) C ₂ /Z ₁ , and (C) B ₁ /Y ₂ fragment pairs adducted to sodium after glycosidic bond dissociation of raffinose.	234

Figure E.11. (A) Representative fragmentation spectrum of sodium-adducted maltotriose at collision voltage of 32 V. (B) Intensities of sodium-adducted maltotriose fragments at collision voltages ranging from 4 – 44 V.	235
Figure E.12. Intensities of lithium-adducted (A) melezitose, (B) raffinose, and (C) maltotriose fragments at varying collision voltages.	237
Figure E.13. Intensities of calcium-adducted (A) melezitose, (B) raffinose, and (C) maltotriose fragments at varying collision voltages.	238
Figure E.14. Intensities of deprotonated (A) melezitose, (B) raffinose, and (C) maltotriose fragments at varying collision voltages.	239
Figure E.15. Representative structures of sodium-adducted (A) melezitose, (B) raffinose, and (C) maltotriose, and deprotonated (D) melezitose, (E) raffinose, and (F) maltotriose.....	241
Figure E.16. Representative fragmentation spectrum of deprotonated maltotriose in negative-ion mode at collision voltage of 4 V.	241
Figure E.17. Representative fragmentation spectrum of permethylated melezitose adducted to sodium and the proposed structures of the fragments resulting from glycosidic bond cleavages.....	243

LIST OF TABLES

Table 2.1. Exact mass-to-charge ratios (m/z) of undeuterated and fully deuterated carbohydrates	44
Table 3.1. Opening sizes of theta tips and estimated initial droplet sizes	72
Table 3.2. Opening sizes of theta tips with measured droplet lifetimes and the average number of deuterium exchanges	74
Table A.1. Effect of source temperature on the time required for the initial deuterium uptake to decrease by 95 %.....	145
Table A.2. Effect of desolvation temperature on residual solvent vapor HDX	147
Table A.3. Effect of gas flow on residual solvent vapor HDX	149
Table C.1. Test for statistical significance of differences in deuteration levels between B ₂ /Z ₂ and C ₂ /Y ₂ fragments from sodium-adducted melezitose in 25% D ₂ O	163
Table C.2. Test for statistical significance of differences in deuteration levels between B ₂ /Z ₂ and C ₁ /Y ₁ fragments from sodium-adducted melezitose in 25% D ₂ O	164
Table C.3. Test for statistical significance of differences in deuteration levels between B ₂ /Z ₂ and C ₂ /Y ₂ fragments from sodium-adducted melezitose in 50% D ₂ O	165
Table C.4. Test for statistical significance of differences in deuteration levels between B ₂ /Z ₂ and C ₁ /Y ₁ fragments from sodium-adducted melezitose in 50% D ₂ O	166
Table C.5. Test for statistical significance of differences in deuteration levels between B ₂ /Z ₂ and C ₂ /Y ₂ fragments from sodium-adducted melezitose in 75% D ₂ O	167
Table C.6. Test for statistical significance of differences in deuteration levels between B ₂ /Z ₂ and C ₁ /Y ₁ fragments from sodium-adducted melezitose in 75% D ₂ O	168
Table C.7. Test for statistical significance of differences in deuteration levels between B ₂ /Z ₂ and C ₂ /Y ₂ fragments from calcium-adducted melezitose in 25% D ₂ O	171
Table C.8. Test for statistical significance of differences in deuteration levels between B ₂ /Z ₂ and C ₂ /Y ₂ fragments from calcium-adducted melezitose in 50% D ₂ O	172

Table C.9. Test for statistical significance of differences in deuteration levels between B ₂ /Z ₂ and C ₂ /Y ₂ fragments from calcium-adducted melezitose in 75% D ₂ O	173
Table C.10. Test for statistical significance of differences in deuteration levels between ^{0,4/1,3/2,4} X _{Glc} B ₂ /A _{Glc} Z ₂ and ^{0,4/1,3/2,4} X _{Glc} C ₂ /A _{Glc} Y ₂ fragments from calcium-adducted melezitose in 25% D ₂ O	174
Table C.11. Test for statistical significance of differences in deuteration levels between ^{0,4/1,3/2,4} X _{Glc} B ₂ /A _{Glc} Z ₂ and ^{0,4/1,3/2,4} X _{Glc} C ₂ /A _{Glc} Y ₂ fragments from calcium-adducted melezitose in 50% D ₂ O	175
Table C.12. Test for statistical significance of differences in deuteration levels between ^{0,4/1,3/2,4} X _{Glc} B ₂ /A _{Glc} Z ₂ and ^{0,4/1,3/2,4} X _{Glc} C ₂ /A _{Glc} Y ₂ fragments from calcium-adducted melezitose in 75% D ₂ O	176
Table D.1. Test for statistical significance of differences in deuteration levels between B ₂ /Z ₂ and C ₁ /Y ₁ fragments of sodium-adducted melezitose in 25% D ₂ O	186
Table D.2. Test for statistical significance of differences in deuteration levels between B ₂ /Z ₂ and C ₁ /Y ₁ fragments of sodium-adducted melezitose in 50% D ₂ O	187
Table D.3. Test for statistical significance of differences in deuteration levels between B ₂ /Z ₂ and C ₁ /Y ₁ fragments of sodium-adducted melezitose in 75% D ₂ O	188
Table D.4. Distances between hydroxyl hydrogens and glycosidic oxygens of sodium-adducted melezitose that can initiate fragmentation pathways for production of Z ₂ and B ₂ fragments	189
Table D.5. Test for statistical significance of differences in deuteration levels between B ₂ /Z ₂ and C ₂ /Y ₂ fragments of sodium-adducted melezitose in 25% D ₂ O	190
Table D.6. Test for statistical significance of differences in deuteration levels between B ₂ /Z ₂ and C ₂ /Y ₂ fragments of sodium-adducted melezitose in 50% D ₂ O	191
Table D.7. Test for statistical significance of differences in deuteration levels between B ₂ /Z ₂ and C ₂ /Y ₂ fragments of sodium-adducted melezitose in 75% D ₂ O	192
Table D.8. Distances between hydroxyl hydrogens and glycosidic oxygens of sodium-adducted melezitose that can initiate fragmentation pathways for production of B ₁ and Z ₁ fragments.	193
Table D.9. Test for statistical significance of differences in deuteration levels between B ₂ /Z ₂ and C ₁ /Y ₁ fragments of sodium-adducted raffinose in 25% D ₂ O	195
Table D.10. Test for statistical significance of differences in deuteration levels between B ₂ /Z ₂ and C ₁ /Y ₁ fragments of sodium-adducted raffinose in 50% D ₂ O	196

Table D.11. Test for statistical significance of differences in deuteration levels between B ₂ /Z ₂ and C ₁ /Y ₁ fragments of sodium-adducted raffinose in 75% D ₂ O	197
Table D.12. List of distances between hydroxyl hydrogens and glycosidic oxygens of sodium-adducted raffinose that can initiate fragmentation for production of Z ₂ /C ₁ and B ₂ /Y ₁ fragments	199
Table D.13. Test for statistical significance of differences in deuteration levels between B ₂ /Z ₂ and C ₂ /Y ₂ fragments of sodium-adducted raffinose in 25% D ₂ O	200
Table D.14. Test for statistical significance of differences in deuteration levels between B ₂ /Z ₂ and C ₂ /Y ₂ fragments of sodium-adducted raffinose in 50% D ₂ O	201
Table D.15. Test for statistical significance of differences in deuteration levels between B ₂ /Z ₂ and C ₂ /Y ₂ fragments of sodium-adducted raffinose in 75% D ₂ O	202
Table D.16. List of distances between hydroxyl hydrogens and glycosidic oxygens of sodium-adducted raffinose that can initiate fragmentation for production of Y ₂ and C ₂ fragments	203
Table D.17. Test for statistical significance of differences in deuteration levels between B ₂ /Z ₂ and C ₁ /Y ₁ fragments of sodium-adducted maltotriose in 25% D ₂ O	204
Table D.18. Test for statistical significance of differences in deuteration levels between B ₂ /Z ₂ and C ₁ /Y ₁ fragments of sodium-adducted maltotriose in 50% D ₂ O	205
Table D.19. Test for statistical significance of differences in deuteration levels between B ₂ /Z ₂ and C ₁ /Y ₁ fragments of sodium-adducted maltotriose in 75% D ₂ O	206
Table D.20. List of distances between hydroxyl hydrogens and glycosidic oxygens of sodium-adducted maltotriose that can initiate fragmentation pathways for production of Z ₂ and B ₂ fragments	208
Table D.21. Test for statistical significance of differences in deuteration levels between B ₂ /Z ₂ and C ₂ /Y ₂ fragments of sodium-adducted maltotriose in 25% D ₂ O	209
Table D.22. Test for statistical significance of differences in deuteration levels between B ₂ /Z ₂ and C ₂ /Y ₂ fragments of sodium-adducted maltotriose in 50% D ₂ O	210
Table D.23. Test for statistical significance of differences in deuteration levels between B ₂ /Z ₂ and C ₂ /Y ₂ fragments of sodium-adducted maltotriose in 75% D ₂ O	211
Table D.24. List of distances between hydroxyl hydrogens and glycosidic oxygens of sodium-adducted maltotriose that can initiate fragmentation pathways for production of Y ₂ and C ₂ fragments	212
Table E.1. Glycosidic bond cleavage energetics of sodium-adducted melezitose	223s

LIST OF ABBREVIATIONS

<i>Abbreviation</i>	<i>Description</i>
AMBER	Assisted Model Building with Energy Refinement
CCS	Collisional Cross Section
CID	Collision Induced Dissociation
CEM	Chain Ejection Model
CHARMM	Chemistry at Harvard Macromolecular Mechanics
CRM	Charged Residue Model
CSD	Charge State Distribution
DFT	Density Functional Theory
DTIM	Drift-Tube Ion Mobility
ESI	Electrospray Ionization
ETD	Electron Transfer Dissociation
Fru	Fructose
GAG	Glycosaminoglycan
Gal	Galactose
GalNAc	<i>N</i> -Acetylgalactosamine
GBP	Glycan-Binding Protein
Glc	Glucose
GlcA	Glucuronic Acid
GlcNAc	<i>N</i> -AcetylGlucosamine
HDX	Hydrogen/Deuterium Exchange
HILIC	Hydrophilic Interaction Chromatography
HSEA	Hard-Sphere <i>exo</i> -Anomeric Force Field
HPAEC	High-pH Anion-Exchange Chromatography
HPLC	High-Performance Liquid Chromatography
IEM	Ion Evaporation Model
IM	Ion Mobility
LC	Liquid Chromatography
MALDI	Matrix-Assisted Laser Desorption Ionization
Man	Mannose
MD	Molecular Dynamics
MS	Mass Spectrometry
NeuA	<i>N</i> -acetylneuraminic Acid
NMR	Nuclear Magnetic Resonance
PGC	Porous Graphitized Carbon
PTM	Post-Translational Modification
SLIM	Structures for Lossless Ion Manipulations
S/N	Signal-to-Noise
TOF	Time-of-Flight
TWIMS	Traveling-Wave Ion Mobility Spectrometry
UPLC	Ultra-High-Performance Liquid Chromatography

ACKNOWLEDGMENTS

First, I would like to sincerely thank my advisor, Dr. Elyssia S. Gallagher, for her guidance and support throughout my time at Baylor. Her passion and dedication for research and learning have been true inspirations in my academic, professional, and even personal life, that I could not have asked for from a different mentor. She has provided an environment in which I was encouraged to be creative and collaborative, and opportunities that facilitated personal growth in critical and analytical thinking, communication, and mentorship. It was a great privilege to work with her and shape my identity as a scientist.

I also thank my committee members, Dr. Touradj Solouki, Dr. C. Kevin Chambliss, Dr. Kevin L Shuford, and Dr. Erich Baker, for their guidance. I am extremely grateful for their time and eagerness to provide invaluable discussions, which have had great influence on establishing the direction and perspectives of my research.

I would like to acknowledge and thank my colleagues and collaborators, Dr. Emvia Calixte, Dr. Tara Liyanage, Amanda Pearson, Meg McCutcheon, Emily Ziperman, Marina Mulenios, Darren Gass, Bruno Brenes, Ana Victoria Quintero, Alexis Edwards, Jacob Hatvany, and Bryan Hettick. It has been a great experience and motivation working with each of them and sharing each other's perspectives.

I would also like to thank Dr. Alejandro Ramirez and Dr. Chinthaka Seneviratne of the Baylor Mass Spectrometry Center, and Dr. Bernd Zechmann of the Baylor Center

for Microscopy and Imaging for their continuous and prompt support with instrument training and maintenance, without which I could not have completed my work.

I am genuinely and perpetually thankful for my family and friends for their encouragement, inspirations, many prayers, and love, who have kept me moving through both good and bad days. Finally, I thank God Almighty for His countless blessings.

DEDICATION

To my parents, Hak Soo and Sunhye

CHAPTER ONE

Introduction

1.1 Glycosylation

Glycosylation is the attachment of glycans, or carbohydrate moieties, to biomolecules, typically as post-translational modifications (PTM) of proteins or by covalent linkage to lipids. Glycosylation is found in all domains of life as well as in viruses.¹⁻⁷ It is estimated that at least 50% of the human proteome is glycosylated⁸ and 1-2% of the human genome codes for proteins involved in glycosylation.⁹ It has also been found that proteins with carbohydrate-recognition domains (CRDs) are present throughout evolution¹⁰, suggesting significant biological roles of glycans and their recognition from the early stages of life. Interest in glycans has increased over the years due to their involvement in various cellular activities, including cell-cell communication and host-pathogen interactions, and their roles as biomarkers for different disease types and stages, such as cancer. Therefore, investigating glycan structures and their impact on cellular behavior is crucial for understanding many aspects of cell biology.

1.1.1 Structures and Nomenclature

Glycans are a diverse and complex class of biomolecules composed of monosaccharide building blocks, which have the chemical formula $C_x(H_2O)_n$. Three-letter abbreviations are used for monosaccharides (*e.g.* Gal for galactose, Glc for glucose, and Man for mannose). Derivatives of monosaccharides are also commonly found in glycans. A common derivative is the amide derivative of monosaccharides, called *N*-

acetylhexosamine (e.g. *N*-acetylglucosamine (GlcNAc) and *N*-acetylgalactosamine (GalNAc) for amide derivatives of glucose and galactose, respectively). Acid derivatives of simple monosaccharides include glucuronic acid (GlcA), which has a carboxylic acid added to glucose, or sialic acids, which are a class of nine-carbon monosaccharides that have both carboxylic acid and amide functional groups, with *N*-acetylneuraminic acid (NeuAc) being the most common form of sialic acid for humans (Figure 1.1).

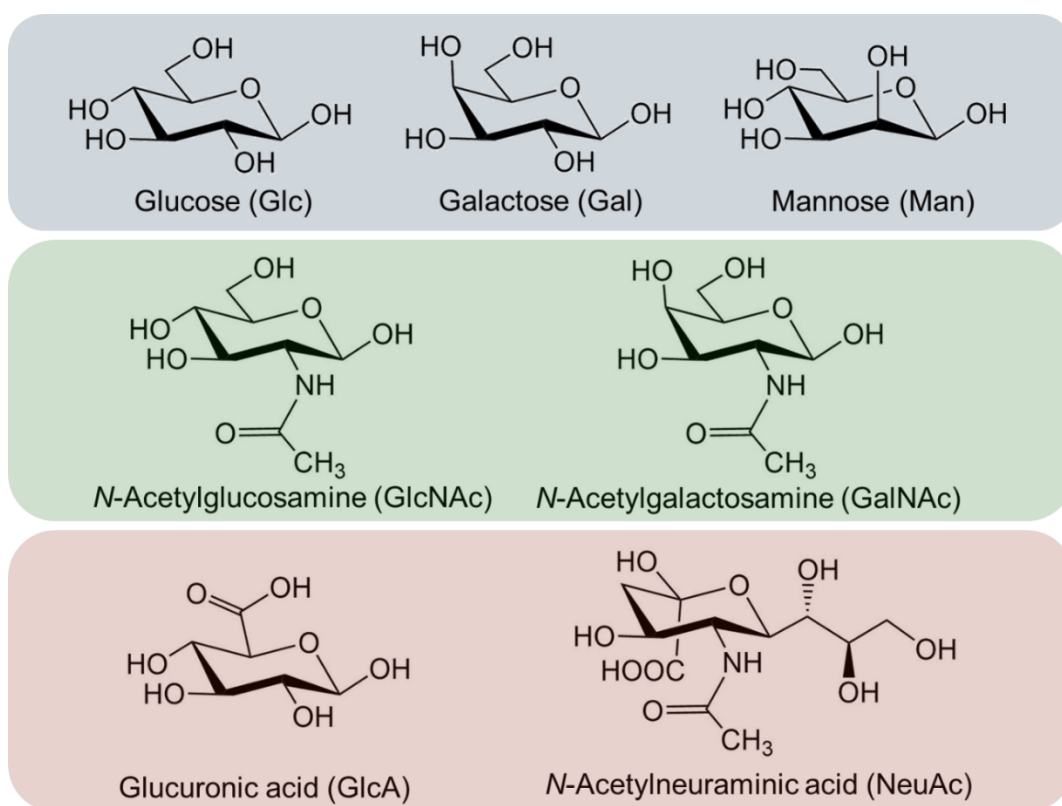


Figure 1.1. Chemical structures of common monosaccharides used in mammalian glycan synthesis and their abbreviated names.¹¹ Simple monosaccharides (top, blue), amide derivatives (green, middle) and acid derivatives (red, bottom) are shown. Adapted from reference.¹¹

In solution, monosaccharides exist in equilibrium as a mixture of acyclic and cyclic forms, either five- or six-membered rings. Aldohexoses, or aldehyde-containing hexoses, can form both six- and five-membered rings via a C-1—O—C-5 ring closure

and a C-1—O—C-4 ring closure, respectively. Ketohehexoses, or ketone-containing hexoses, only forms five-membered rings via a C-2—O—C-5 ring closure. A five-membered ring is called a furanose and a six-membered ring is called a pyranose. Acyclic forms are typically drawn as Fischer projections and cyclic forms are drawn in Haworth projections or as chair conformations (Figure 1.2).

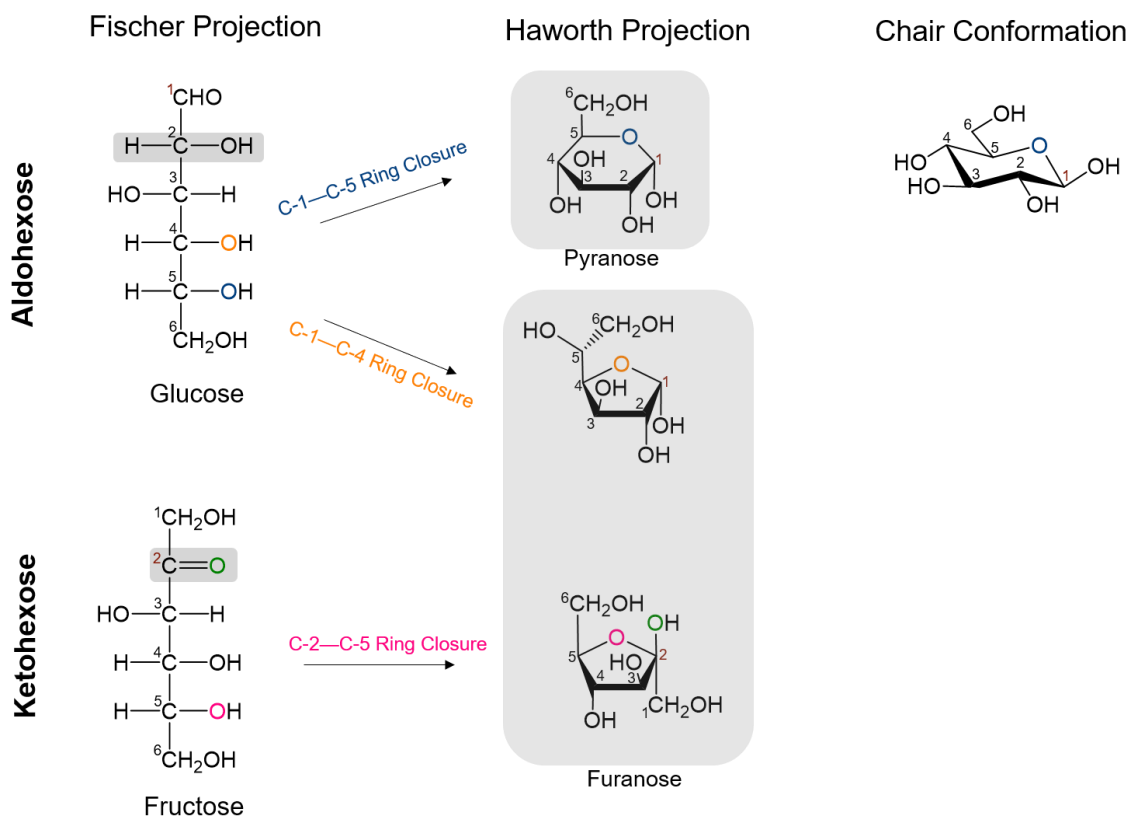


Figure 1.2. Presentation of acyclic and cyclic carbohydrate structures as Fischer, Haworth, or chair conformations. The oxygens adjacent to the location of the ring closure are color-coded.

1.1.1.1 Anomerism of carbohydrates. While each carbon of a monosaccharide is a chiral center, the cyclization of carbohydrates introduces a unique asymmetric center called the anomeric carbon. The hydroxyl on the anomeric carbon can take two different orientations via mutarotation, which is the interconversion of the two stereoisomers

during ring opening and closing events. When the hydroxyl at the anomeric carbon (C-1) is in the *trans* configuration with the reference carbon that is furthest away (C-5), the carbohydrate is defined as the α -anomer. When C-1 and C-5 are in the *cis* configuration, the carbohydrate is defined as the β -anomer (Figure 1.3). Varying proportions of α - and β - anomers are formed in equilibrium for different sugars. For instance, the ratio between α - and β - anomers of glucopyranose in aqueous solution is 36:64¹², but α -anomer is more stable in the gas phase due to anomeric effect^{13, 14}, or the preference of an electronegative group on the anomeric position to take an axial position. The gas-phase stability of β - anomers is predominantly determined by the interactions between adjacent and nonadjacent hydroxyl groups, while solvent interaction with the free electron pair of the anomeric oxygen is greater in solution.¹⁵

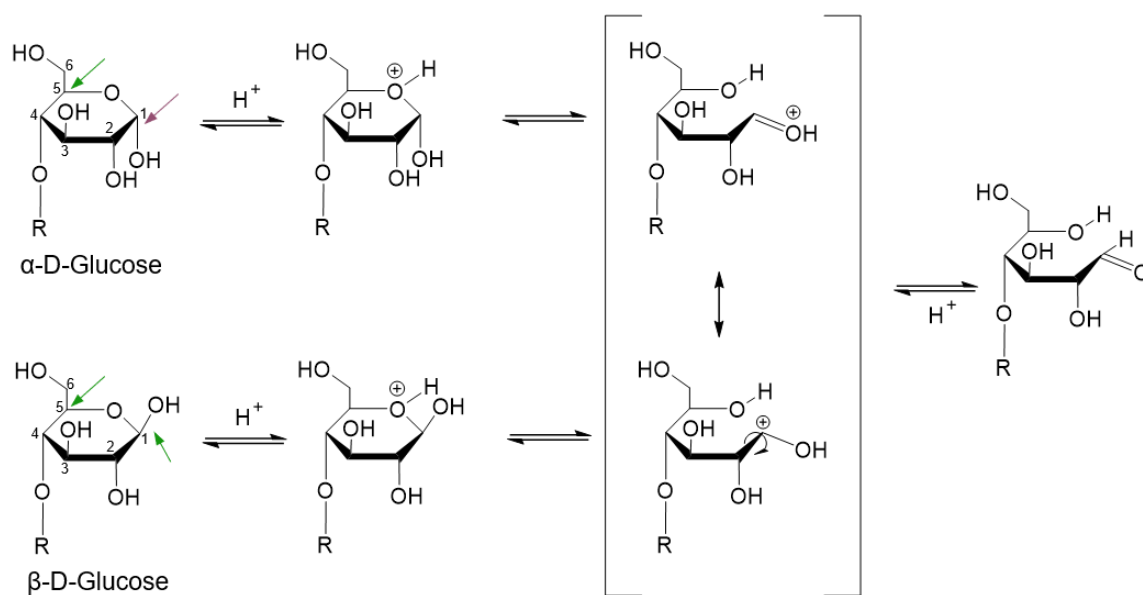


Figure 1.3. Mechanism of mutarotation between α - and β -anomers of glucose at the reducing end. R groups can be replaced with carbohydrate chains. Reducing sugars exist at equilibrium in solution as mixtures of the two anomers and the open-chain structure. α - and β -anomericty is assigned based on the relative position of the anomeric carbon (C-1) to C-5, indicated by arrows. Adapted and modified from reference.¹⁶

When the hydroxyl on the anomeric carbon is free and not covalently bonded, the anomericity of the carbohydrate may change via mutarotation and the carbohydrate is called a reducing sugar. However, when the hydroxyl on the anomeric carbon is covalently bonded with another carbohydrate to form a polysaccharide, that carbohydrate ring cannot open anymore and the anomericity of that ring becomes permanent. When none of the terminal sugars of a polysaccharide have the anomeric carbon available for mutarotation, the polysaccharide is called a non-reducing sugar. A non-reducing sugar exists in solution as a single anomer, whereas a reducing sugar may exist in an equilibrium as a mixture of the two anomers, regardless of the size of the polysaccharide.

1.1.1.2 Glycosidic linkages. Monosaccharide subunits form polysaccharides via glycosidic bonds between the anomeric carbon of one monosaccharide and a hydroxyl of another through condensation reactions. A simple monosaccharide has five hydroxyls available for glycosidic bond linkage, including the hydroxyl at the anomeric carbon. Glycosidic bonds can form at any of the hydroxyls, and one monosaccharide can form more than two glycosidic bonds and serve as a branch point, adding to the complexity of glycans. Carbohydrate nomenclature includes the anomeric configuration and linkage information (Figure 1.4).

Melezitose, a trisaccharide that is used as a model system throughout the research presented in the following chapters, is also referred to as α -D-Glc-[1 \rightarrow 3]- β -D-Fru-[2 \rightarrow 1]- α -D-Glc. The second glucose linked to fructose by [2 \rightarrow 1] linkage has a permanent α configuration, because the hydroxyl on the anomeric carbon C-1 is covalently bound in a glycosidic linkage, making melezitose a non-reducing sugar. On the other hand, maltotriose, another trisaccharide, has the structure α -D-Glc-[1 \rightarrow 4]- α -D-

Glc-[1→4]-D-Glc. The third glucose unit does not have an anomeric configuration assigned because the anomeric carbon on the third glucose is free and undergoes mutarotation in solution to generate both α - and β -anomers in equilibrium, making maltotriose a reducing sugar.

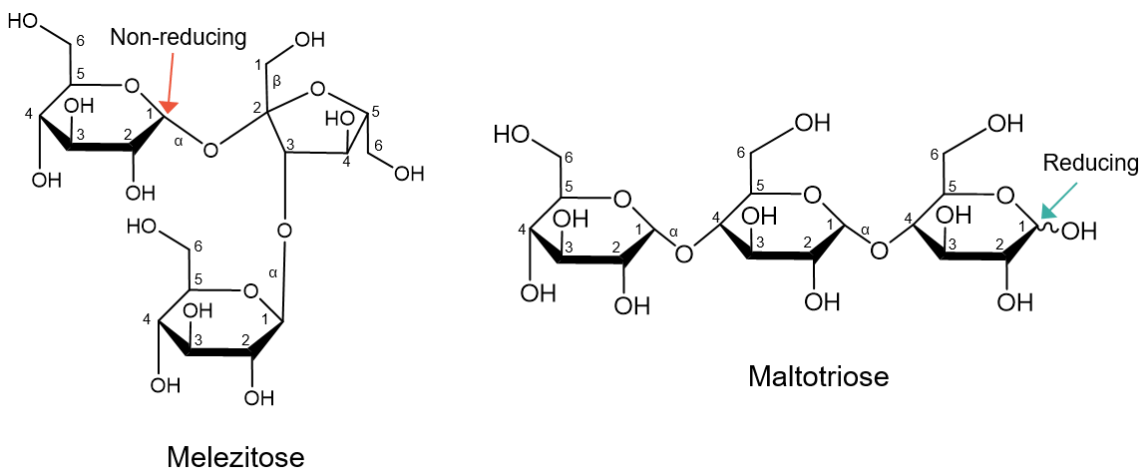


Figure 1.4. Chemical structures of trisaccharides: melezitose and maltotriose. Melezitose (left) is a non-reducing sugar and maltotriose (right) is a reducing sugar. The anomeric carbon on the terminal saccharide is indicated with an arrow for both sugars. The wavy line symbol, indicated with blue arrow, represents a mixture of α - and β -anomeric configurations.

1.1.2 Glycoprotein Heterogeneity

Glycans are a diverse and complex class of biomolecules. Glycans on proteins are largely classified as *N*-linked glycans and *O*-linked glycans, based on the amino acids to which the glycans are attached. *N*-linked glycans are bound to an asparagine residue of the sequence Asn-X-Ser/Thr, in which “X” is any amino acid except proline. Eukaryotic *N*-linked glycans share a common core: Man₃GlcNAc₂. *O*-linked glycans are attached to Ser or Thr residues by GalNAc with eight potential core structures that can be extended to form linear or branched glycans.

Glycosylation is a non-template driven process. Unlike DNA, RNA, and proteins, which are duplicated or synthesized from the genetic code of the cell, glycosylation is driven by both internal and external factors, ranging from expression of genes encoding for glycosidases and glycosyltransferases that synthesize glycans¹⁷ to the extracellular environment.¹⁸ Such characteristics of glycan synthesis lead to heterogeneous glycoforms, which are isoforms of glycoproteins. Glycoforms can be generated from macro- or microheterogeneity. Macroheterogeneity results from variations in the sites of glycan attachment in a protein. Microheterogeneity refers to diversity in the glycan structures at a given glycosylation site.

1.1.3 Glycoprotein Interactions

Glycoform diversity plays a significant biological role, as altered glycan structures often lead to changes in glycan-protein or glycoprotein-protein interactions. For instance, glycan structures are intimately related to immune responses. Many pathogen-associated molecular patterns (PAMPs) are glycoconjugates and their host immune receptors are lectins.¹⁹ Lectins within the immune system can also recognize self-associated molecular patterns (SAMPs) that lower immune response against non-pathogens or self. The ability of glycans to activate or suppress immune responses also relates closely to the idea of autoimmunity, which is the hyperactivation of immune responses against self. Altered glycans are observed in many autoimmune diseases including rheumatoid arthritis²⁰, Crohn's disease²¹, and multiple sclerosis.²² Glycoproteins also serve significant roles in host-pathogen interactions. Glycoproteins can act as barriers against pathogen invasion by physically preventing pathogens, such as mucins do^{23,24} or facilitating the growth of probiotics that can serve as chemical barriers

against pathogens.²⁵ The pathogen cell surface glycoproteins, on the other hand, can initiate infection by adhering to host cell.²⁶ Pathogens can also glycosylate host proteins and increase virulence²⁷ by modifying host cell signaling pathways.²⁸

1.1.4 Analytical Techniques to Study Glycans

1.1.4.1 Nuclear magnetic resonance (NMR) spectroscopy. NMR is a powerful tool for structural analysis of carbohydrates. While ¹H NMR of carbohydrates reveals that most resonances are clustered around 3.4 to 4.0 ppm²⁹⁻³¹, anomeric protons (4.4 – 5.5 ppm) as well as acetyl (2.0 – 2.1 ppm) and methyl groups (~ 1.2 ppm) can be resolved.³² ¹H NMR provides good estimates for the number of monosaccharide subunits and the number of residues in each anomeric configuration. Even within the narrow range of chemical shifts observed for carbohydrate protons, the chemical shifts, splitting patterns, and line widths of resonances, named structural reporter group signals, have been shown to be highly specific to the carbohydrate structures, allowing for primary structural assignment of carbohydrates.³³ However, the limited dispersion of ¹H chemical shifts still presents challenges in assignment and interpretation of NMR spectra, especially for larger polysaccharides. ¹³C resonances are more dispersed, but ¹³C NMR spectroscopy is less sensitive than ¹H NMR because only 1% of naturally occurring isotopes of carbon is ¹³C. Methods for the synthesis of isotopically labeled carbohydrates^{34, 35} have been published to improve ¹³C NMR analysis of carbohydrates.

One advantage of structural analysis by NMR spectroscopy is that the solution-phase structures can be directly determined, because biologically relevant activities of carbohydrates occur in solution. For instance, NMR spectroscopy has been used to examine the mutarotation of carbohydrates and the equilibrium of the anomers³⁶⁻³⁹,

monitor carbohydrate-protein interactions⁴⁰⁻⁴², and observe reactive intermediates or transition states of glycosylation reactions.⁴³⁻⁴⁷ NMR is also a non-destructive technique, meaning that the samples can be recovered for further analysis. However, NMR is less sensitive than other analytical techniques such as mass spectrometry and needs larger and more concentrated samples for analysis, and such requirements may be impractical and difficult for analysis of biological samples in highly complex mixtures.

1.1.4.2 Mass spectrometry (MS). MS is a popular tool for studying glycans and carbohydrates because of its high sensitivity, which enables the use of smaller sample volumes and its versatility, which allows multi-dimensional analysis by coupling to other analytical techniques. Although the isomeric carbohydrate subunits cannot be directly identified from the mass-to-charge ratio detected in MS, separation techniques in the liquid and gas phase may be used in tandem with MS to provide more detailed insight into carbohydrate structures from their interactions with the stationary phase or collisional cross sections. One advantage of MS over NMR is its ability to analyze biomolecules with high molecular weight, such as multiprotein complexes, and complex mixtures. MS can also perform both targeted and non-targeted analysis.⁴⁸ Targeted analysis in MS, for instance by isolating a known analyte, can increase selectivity and sensitivity for the analyte of interest. Non-targeted analysis, on the other hand, can be used for analysis of both known and unknown analytes in the sample in cases where the goal is to identify unknowns. However, it has been shown that MS analysis depends on ionization conditions and the instrumentation. For instance, mobile phases used for liquid chromatography (LC) separation prior to ionization have shown to affect analyte sensitivity.^{49, 50} Also, the varying ionization efficiencies of different analytes may

introduce bias against detection of less polar molecules that are harder to ionize.⁵¹ Ionization of neutral carbohydrates is poor due to lack of acidic and basic sites, but derivatization methods, such as permethylation⁵²⁻⁵⁴ and peracetylation⁵⁵, can improve ionization efficiency by stabilizing glycan structures. More details on the principles and applications of mass spectrometry will be discussed in section 1.2.

1.1.4.3 Computation. While experimental data from analytical techniques, such as NMR and MS, offer valuable structural information on carbohydrates and glycans, the acquired data are averaged over time and are correlated with a single conformer rather than the distribution of multiple structures within a population in solution resulting from the flexible nature of carbohydrates.^{56, 57} Theoretical studies can provide additional information, such as carbohydrate conformations, carbohydrate-protein interactions, and carbohydrate fragmentation energetics, to assist in interpretation of experimental data often in conjunction with NMR, IM-MS, and MS/MS.

The flexibility of carbohydrates and thus limited empirical methods to test the force fields, or the mathematical descriptions to estimate the forces between atoms or molecules, have demanded a long history of trial-and-error in finding suitable computational methods for carbohydrate modeling.⁵⁸ Early success for approximating carbohydrate structures was achieved with hard-sphere *exo*-anomeric (HSEA) force field^{59, 60} which assumed rigid conformation of individual monosaccharide subunits, that also generated conformations supported by NMR data.^{60, 61} However, HSEA omits solvent effects on conformations and electrostatic interactions. Other approaches to carbohydrate modeling used macro-molecular force fields such as Assisted Model Building with Energy Refinement (AMBER)⁶²⁻⁶⁴ and Chemistry at Harvard

Macromolecular Mechanics (CHARMM)^{65, 66} that use the sum of energies from bond stretching, bending, and rotation as well as non-bonded interactions. These force fields have been employed in molecular dynamics (MD) simulations of carbohydrates with explicit solvation that reproduced conformations obtained from NMR.⁶⁷ Whereas AMBER and CHARMM force fields utilize partial atomic charges to model the distribution of charge density in a molecule, other macro-molecular force fields such as MM2⁶⁸ and MM3⁶⁹ use bond dipole moments. Although MM2 and MM3 displayed potential to correct inaccuracies from previous approaches from other macro-molecular force fields, they were inconsistent with any water model and were predominantly utilized for gas-phase calculations.⁵⁸

In recent years, computational methods based on electronic structure theory, rather than the traditional empirical methods, have been developed for carbohydrate structure analysis. Particularly, Density Functional Theory (DFT)⁷⁰⁻⁷³ has been widely used for its high success rate for approximating properties of complex molecular systems at moderate computational cost.⁷⁴ DFT calculations require computation of the total electron density, rather than the atomic or molecular wave function, to estimate the electron-electron interactions.⁷⁵ Unlike empirical methods, DFT does not require rigid bond connectivity for parameterization, making it applicable to a variety of carbohydrate systems including protonated, metal-adducted, and deprotonated sugars that may involve bond breaking and formation to monitor reactions. DFT has also shown to achieve accurate calculations for many mono- and disaccharide structures and interactions.⁷⁶⁻⁷⁸ It has been proposed that DFT can complement experimental data such as collisional cross

sections obtained from ion mobility mass spectrometry and infrared spectroscopic fingerprints of carbohydrates.⁷⁹

1.2 Mass Spectrometry

Mass spectrometry is an analytical technique that measures the mass-to-charge ratio (m/z) of gas-phase ions. MS has become an invaluable tool in numerous applications in field of life sciences, including: proteomics, lipidomics, glycomics, and metabolomics. MS can be used for identification and quantification of known and unknown molecules, detection of biomolecule structures, modifications, and interactions, and investigation of gas-phase ion-ion or ion-neutral chemistry. Such wide utilization of MS is has been enabled by diverse developments in MS components, including separation techniques prior to MS, ionization methods, and fragmentation methods to obtain different local information.

1.2.1 Electrospray Ionization

ESI, along with matrix-assisted laser desorption ionization (MALDI)⁸⁰, revolutionized the field of mass spectrometry by introducing non-volatile macromolecules into the gas phase. Both ESI and MALDI are soft ionization techniques, meaning molecules experience minimal fragmentation during ionization.

1.2.1.1 Principles of ESI. The observation of the electrospray jet was first reported by Malcolm Dole⁸¹ and developed into the electrospray ionization (ESI) technique by Yamashita and Fenn.⁸² ESI is initiated by applying high voltage to a solution containing analytes as it flows through a conductive ESI probe. While charge can be added to the solution by acidification, the high voltage also initiates redox

reactions of the solvent molecules, such as water and methanol, creating excess charge. The charged solvent at the opening of the probe forms a cone, called a Taylor cone, where the effect of the strong electric field on the charged particles competes with the surface tension of the solvent.^{83, 84} When sufficient voltage is applied, the cone breaks into a jet to produce a mist of highly charged droplets. The solvent molecules in the droplets evaporate and the charge density of the droplets increases until the surface tension can no longer balance the electrostatic repulsion of like charges, called the Rayleigh limit.⁸⁵ The Rayleigh limit is given by equation 1.1, where R is the radius of the droplet, ϵ_0 is the vacuum permittivity, and γ is the surface tension.

$$z_R = \frac{8\pi}{e} \sqrt{\epsilon_0 \gamma R^3} \quad \text{Equation 1.1}$$

The droplets undergo Coulombic fission to generate smaller progeny droplets, which repeatedly experience solvent evaporation and fission until gas-phase ions are produced (Figure 1.5). ESI can generate multiply-charged species, providing an advantage for large molecules (*e.g.* proteins) whose high mass range had been outside the mass ranges of common mass analyzers.⁸⁶

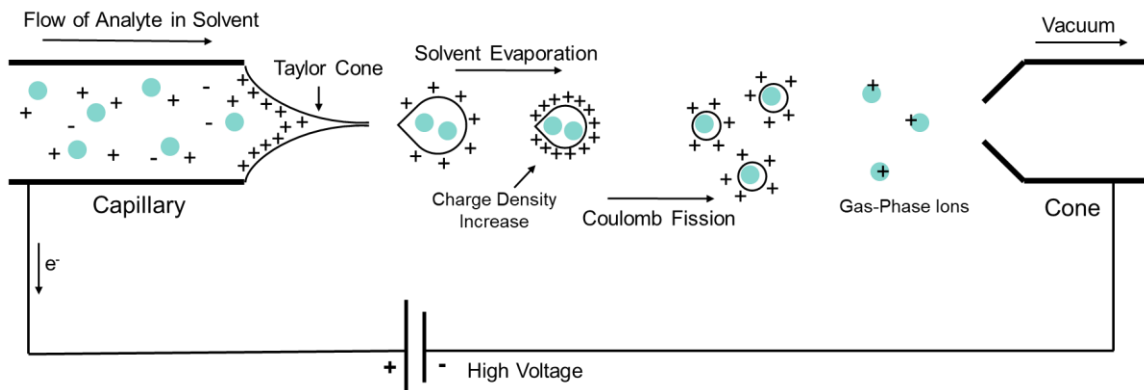


Figure 1.5. Schematic of electrospray ionization process in positive ion mode.

ESI can be operated in either positive- or negative-ion mode, depending on the voltage that is applied to the system. In positive-ion mode, the analytes are charged by protonation of basic sites or adduction of cations such as Na⁺ ions. In negative-ion mode, charging generally occurs via deprotonation of acidic sites or anion adduction. While salt clusters pose problems in protein MS due to signal suppression, metal adduction enables analysis of molecules with little to no acidic or basic sites that can be charged, such as carbohydrates, by enabling detection in MS. Both native and derivatized (*e.g.* permethylated) carbohydrates are often prepared as a mixture with salt to induce metal-adduction to increase signal.

1.2.1.2 Mechanisms of ESI. Three mechanisms of ESI have been proposed depending on the type of molecule that will be ionized (Figure 1.6): the ion evaporation model (IEM), charged residue model (CRM), and chain ejection model (CEM).⁸⁷ Low molecular weight species are thought to be ionized via IEM, where the small solvated ions are ejected from the surface of the droplet.⁸⁸ The mechanism of IEM is similar to that of Rayleigh fission events where smaller charged droplets are generated from larger droplets whose charge is close to the Rayleigh limit.⁸⁹ However, Rayleigh fission typically generates multiple progeny droplets, whereas IEM occurs via series of single ion ejection events.⁸⁹ CRM is proposed for large globular species, such as folded proteins. In CRM, the solvent shell evaporates and the charge that is left in the droplet is transferred to the analyte.^{81, 90, 91} Ejection of positively-charged small ions, as proposed by IEM, can reduce the charge of droplets during CRM so that the charge density of the droplets stay close to the Rayleigh limit while solvent evaporates.^{87, 92} Finally, CEM is the predicted ESI mechanism for molecules of disordered structures, such as unfolded

proteins⁹³ and nonpolar polymer chains.⁹⁴ Whereas the hydrophobic, nonpolar regions of proteins are not solvent accessible in folded proteins⁹⁵, the hydrophobic chains in unfolded proteins are now solvent accessible and migrate to the surface of the charged droplet. After one side of the chain gets ejected from the droplet picking up charges, like-charges are repelled from the surface of droplets, causing the remaining chain to be released into the gas phase.

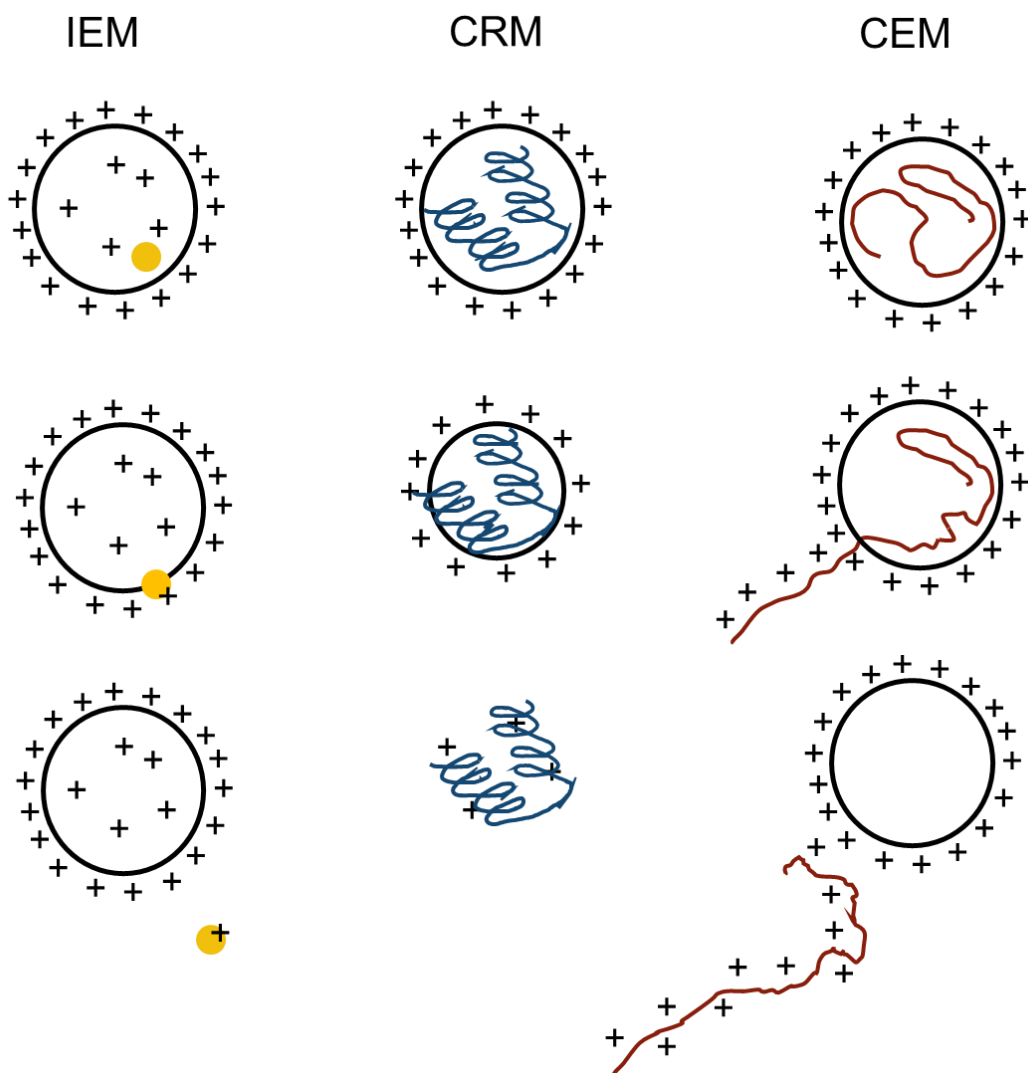


Figure 1.6. Proposed mechanisms of ESI for various molecules. Ion evaporation model (IEM) is the proposed mechanism for ionization of small, charged molecules, charged residue model (CRM) for folded, globular proteins, and chain ejection model (CEM) for unfolded, disordered proteins and nonpolar polymer chains. Adapted from reference.⁸⁷

The ESI mechanism of carbohydrates has been investigated computationally.⁹⁶ The most abundant functional group in native carbohydrates is hydroxyls, which form hydrogen bonds with hydrophilic solvent.⁹⁷⁻¹⁰⁰ Consistent with folded proteins with their hydrophilic surface interacting with solvent, underivatized carbohydrates reside in the core of ESI droplets, following CRM for ionization. On the other hand, permethylated carbohydrates, whose hydroxyls have been replaced with nonpolar, methyl functional groups, are ejected from the surface of the droplet into the gas phase, following IEM. Defining the ESI mechanism of carbohydrates is a significant step toward understanding the MS analysis of carbohydrates because it provides additional insight into carbohydrate-solvent and carbohydrate-metal interactions that dictate carbohydrate structures and behaviors.

1.2.1.3 Solution- vs gas-phase structures. One distinguishing advantage of ESI over other ionization methods is its ability to transfer analytes directly from the solution phase to the gas phase with minimal requirements for sample preparation, unlike for MALDI. However, there has been a prolonged debate about whether the solution-phase structures of molecules are preserved in the gas phase after desolvation and ionization.¹⁰¹ For proteins, the charge state distribution (CSD) is commonly used as an indicator of protein folding and unfolding, with high charge states correlating with unfolded structures as a result of acid¹⁰², heat¹⁰³, or solvent¹⁰⁴ denaturation. There is also evidence that non-covalent protein complexes and protein-ligand interactions are maintained in the gas phase^{105, 106}, suggesting that the structural integrity of proteins are maintained as gas-phase ions to some extent. On the other hand, there are also opposing observations that there are proteins which undergo structural changes after being released into the gas

phase.¹⁰⁷ It has been suggested that these gas-phase structural alterations are time-dependent¹⁰⁸, highlighting that careful and thorough optimization of ionization conditions is necessary to understand the structural transition from solution to gas phase.

On the other hand, carbohydrates undergo significant structural changes in the gas phase. While the carbohydrate rings are rigid, the glycosidic linkages of oligosaccharides are flexible. When carbohydrates are in aqueous solvent, the intramolecular interactions within the carbohydrate and the intermolecular interactions between the carbohydrate and water molecules compete for hydrogen bonding.¹⁰⁹ When carbohydrates are in the gas phase, strong inter-ring hydrogen bonding and metal coordination are observed¹¹⁰, suggesting more rigid structures compared to those observed in solution.

1.2.2 Tandem Techniques Coupled to Mass Spectrometry

One advantage of MS is its versatility to be coupled to various other techniques for multi-dimensional analysis. Particularly, liquid- and gas-phase separations and gas-phase fragmentation techniques are described in the following sections.

1.2.2.1 Liquid-chromatography. Liquid chromatography (LC) is a solution-phase separation technique that utilizes interactions between analytes and various stationary and mobile phase pairs to separate mixtures based on characteristics such as hydrophobicity, size, and charge. For proteins and peptides, typically a reversed-phase LC is used with a gradient of acidified aqueous solvent and acetonitrile. Depending on the particle size of the column and the maximum pressure that each system can handle, LC can be categorized as high-performance liquid chromatography (HPLC) or ultra-performance liquid chromatography (UPLC). Because separation occurs in the condensed phase with

high pressure, ionization techniques under atmospheric conditions, such as ESI, are compatible with online LC separations.

LC-MS of glycans are also commonly used for isomer separations.¹¹¹ A common LC technique used for separation of glycans is hydrophilic interaction chromatography (HILIC)¹¹², in which analytes interact with a hydrophilic stationary phase and are eluted by aqueous solvent. Carbohydrates are retained in HILIC columns by a combination of hydrogen bonding, ionic interactions, and dipole-dipole interactions.¹¹³ Glycans are generally eluted in order of increasing size.¹¹⁴ Reversed-phase LC can also be performed for derivatized (*e.g.* permethylated) glycans. Unlike normal phase LC, reversed-phase LC, such as C18 columns, utilizes hydrophobic stationary phases and polar mobile phase. Permethylated glycans not only enhances their interaction with hydrophobic stationary phases in reversed-phase LC, but it also increases ionization efficiency, and thus, sensitivity in ESI-MS.^{115, 116} However, reversed-phase separations of glycans often suffer from low resolution of isomeric glycan structures that have minimal differences in hydrophobicity.¹¹¹ On the other hand, porous graphitized carbon (PGC), which is a reversed-phase column, provides higher sensitivity for structural and linkage differences because the planar column material enhances solute-adsorbent interactions.¹¹⁷ PGC-LC can be used for both native and derivatized glycans. Finally, the hydroxyls of glycans can be deprotonated in strong base¹¹⁸, enabling glycan separation via high-pH anion-exchange chromatography (HPAEC). The five hydroxyls in monosaccharides have varying ionization efficiencies¹¹⁹, and the interactions between glycans and the anion exchange stationary phase change based on which hydroxyl is ionized. HPAEC can separate glycans based on their formal charges, sizes, composition, and linkages^{120, 121},

providing a unique alternative to traditionally used HILIC, reversed-phase LC, and PGC-LC.

1.2.2.2 Ion mobility. Ion mobility (IM) is a gas-phase separation technique that separates ions based on their collisional cross sections (CCS), measured by their mobility through a buffer gas. For proteins, larger CCS values often mean unfolded and elongated structures, whereas smaller CCS values are associated with folded, compact structures. Because IM provides information on shape and conformation of the analyte, which cannot be obtained from m/z alone, IM and MS can be coupled together to acquire complementary data. The simplest form of IM is drift-tube ion mobility (DTIM), in which gas-phase ions are introduced into a drift tube filled with a drift gas. Upon application of an electric field, ions move through the drift tube while interacting with the neutral drift-gas molecules. The ion mobility of analytes can vary depending on conformations, separating the ions in the gas phase. More compact analytes, which interact less with the drift gas, have higher ion mobility and arrive at the detector earlier than analytes with more elongated conformations, which interact more with the drift gas. The time that it takes for the ions to move through the drift tube, or t_D , can be used to calculate the CCS.

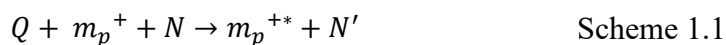
Traveling-wave ion mobility spectrometry (TWIMS), on the other hand, uses a stacked ring ion guide to which a non-uniform electric field is applied at different regions of the drift tube, creating a wave that pushes the ions through the IM cell as the electric field moves.¹²² A TWIMS device can operate at lower drift voltage compared to DTIM. Because TWIMS does not use a uniform electric field, like DTIM, the CCS cannot be

directly calculated from t_D , but rather, calibration of the instrument with standards of known CCS is required.

IM-MS provides a powerful tool for analysis of carbohydrates and glycans because many carbohydrates are isomeric species and MS alone cannot differentiate different carbohydrates. IM has been used to separate sodium-adducted di- and trisaccharides of various composition and linkages.¹²³ It has also been observed that reducing sugars were detected as more than one peak, suggesting the capability of IM-MS to resolve different anomeric configurations¹²⁴, including open-ring forms.¹²⁵ The CCS of carbohydrates can be altered by using different metal adducts^{126, 127} and derivatizations¹²⁸ to improve resolution. An extensive database for CCS calibration of TWIMS using sodium-adducted¹²⁹ and negatively-charged *N*-linked glycans¹³⁰ has been built for obtaining drift times of glycans from a TWIMS device. While separation of complex mixtures of isomers may still be a challenge^{131, 132}, IM-MS of carbohydrates and glycans can use an additional separation technique prior to IM, such as reversed-phase LC¹²⁹ and HILIC.¹³³ Carbohydrates can also be fragmented pre- or post-IM to confirm linkage isomers.^{134, 135} Recent developments in ion mobility, such as Structures for Lossless Ion Manipulations (SLIM)¹³⁶ and cyclic ion mobility¹³⁷, have also offered high-resolution separations of carbohydrates without derivatization.¹²⁵

1.2.2.3 Tandem mass spectrometry. Tandem mass spectrometry (MS/MS) is a technique with two or more stages of mass analysis¹³⁸ achieved by adding mass selection and fragmentation before m/z detection. It is also called MS^n where n is the total number of cycles, including both ion selection and fragmentation. Depending on the type of instrument used for MS/MS, the type of fragmentation that can be utilized varies.

Collision induced dissociation (CID)¹³⁹⁻¹⁴² is the most common type of fragmentation where selected ions (m_p^+) are accelerated through neutral gas molecules (N) by applying an electrical potential. CID is understood as a two-step process where the kinetic energy of the ions is converted into internal vibrational energy, which results in breakage of covalent bonds to produce fragments¹³⁸:



where Q is the change in kinetic energy of the system, m_p^+ and N are the precursor ion and neutral gas before collision, m_p^{+*} and N' are the precursor ion and neutral gas after collision, and m_a^+ and m_b are fragments of m_p^+ . The maximum conversion of kinetic to internal energy, Q_{\max} , is given by the equation:

$$Q_{\max} = \left(\frac{N}{m_p + N} \right) \left(\frac{1}{2} m_p v_i^2 \right) \quad \text{Equation 1.5}$$

where $\frac{1}{2} m_p v_i^2$ is simply the collision energy. CID is an ergodic fragmentation method, meaning that the vibrational excitation is redistributed over the activated ion^{143, 144} and the bond cleavage occurs at the weakest bonds. The Roepstorff and Fohlman nomenclature¹⁴⁵ is used to describe the fragments generated from proteins and peptides (Figure 1.7). Cleavage of the bond between the alpha carbon (C_α) and carbonyl carbon generates a_n/x_m fragments, where the charge is retained on the N-terminus for a_n and the C-terminus for x_m fragments, and n and m correspond to the number of amino acid residues counting from each respective terminus. b_n/y_m fragment pairs result from amide bond cleavage between the backbone amide and carbonyl carbon, and c_n/z_m fragments are generated from cleavage of the bond between the backbone amide and C_α . CID predominantly produces b/y fragments.¹⁴⁶

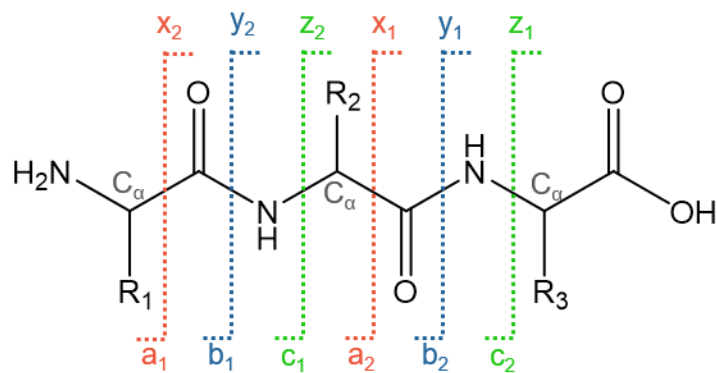
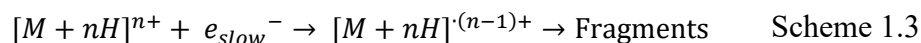


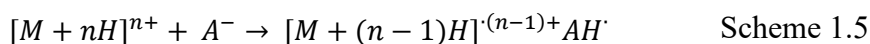
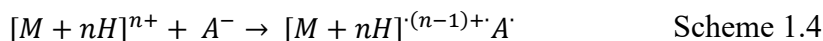
Figure 1.7. Roepstorff and Fohlman nomenclature for peptide fragmentation.

Other types of fragmentation techniques can be utilized to acquire different peptide fragments that give additional information. Electron capture dissociation (ECD) is a non-ergodic fragmentation technique¹⁴⁷⁻¹⁴⁹ where low-energy electrons are introduced to gas-phase ions in a trap to induce ion-electron reactions to produce fragmentation.



ECD yields predominantly *c/z* type fragments. While the same nomenclature by Roepstorff and Fohlman is followed for fragments from ECD regarding bond cleavage position, ECD fragments have an additional set of notations devoted to describing the electron and proton transfer reactions that occur during fragmentation. For instance, homolytic N—C_α cleavage gives *c'* and *z'* radical fragments, but hydrogen transfer to *c'* is observed, generating *c'* fragments, whereas hydrogen loss from *z'* fragments gives rise to *z* fragments.¹⁵⁰ ECD predominantly generates *c'/z'* fragments and *b/y'* fragments. While ECD is a valuable technique to complement data obtained from CID, ECD has been shown to be efficient only in a specific type of mass spectrometer, called a Fourier-transform ion cyclotron resonance (FT-ICR) mass spectrometer, that uses static magnetic

and electric fields for trapping ions in other types of mass spectrometers, rather than radiofrequencies (RF) that are typically used. This specific setup for ECD allows for introduction of low-energy electrons¹⁵¹ and long electron-ion interaction times¹⁵² that cannot be achieved in other types of analyzers. An alternative to ECD, that can be used in other types of mass spectrometers, is electron transfer dissociation (ETD).¹⁵³ ETD utilizes radical anions as ETD reagents to transfer electrons to gas-phase ions and generates predominantly c/z type fragments. Unlike ECD, two competing reactions are observed in ETD, either electron-transfer or proton-transfer.¹⁵⁴



Also, some peptides have been found to undergo electron transfer but not dissociate¹⁵³, but it is unclear whether a stable charge-reduced radical precursor is formed, or strong noncovalent interactions between fragments hold the complex together.¹⁵⁴ Nonetheless, multiple pathways for ETD mechanisms are viable.

CID and ECD/ETD produce different types of fragments in MS/MS analysis of glycans and carbohydrates as well. The Domon and Costello nomenclature is used to assign carbohydrate fragments (Figure 1.8).¹⁵⁵ Whereas peptide fragments are named by the type of bond that dissociates, carbohydrates have two C—O bonds across the glycosidic oxygen that can be cleaved. Fragments from glycosidic bond cleavages are named B_n/Y_m and C_n/Z_m fragments, where B- and Z-type fragments lose the glycosidic oxygen upon fragmentation and C- and Y-type fragments retain the glycosidic oxygen. A- and X-type fragments are produced from cross-ring cleavages, where multiple bonds across the carbohydrate ring dissociate. Depending on the position of the cross-ring

cleavage, fragments are named ${}^{ij}A_n/{}^{ij}X_m$ where i and j note the cleavage site and n and m refer to the number of residues from the terminal sugar. Fragments are termed A, B and C when the non-reducing end carries the charge and X, Y and Z when the reducing end retains the charge. CID predominantly generates glycosidic bond cleavages, whereas ECD and ETD result in more cross-ring cleavages. Fragmenting carbohydrates adducted to different metals has also produced varying cross-ring cleavage products from CID.¹⁵⁶

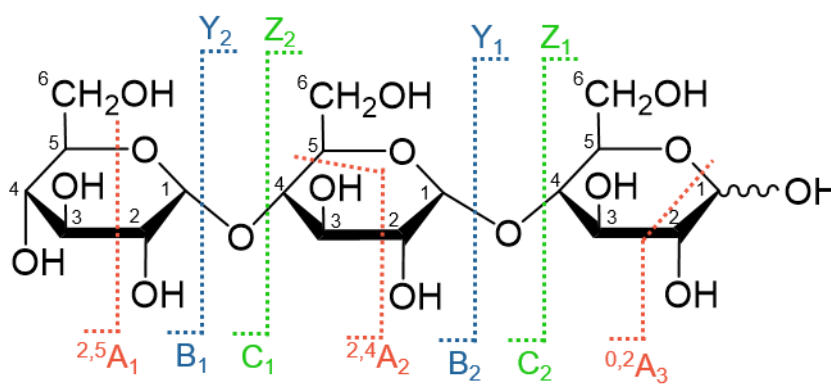


Figure 1.8. Domon and Costello nomenclature for carbohydrate fragmentation.

Another method for structural analysis of carbohydrates that gained popularity in recent years is infrared (IR) spectroscopy. IR spectroscopy combined with mass spectrometry has offered diagnostic fingerprints for various types of gas-phase mono- and oligosaccharide isomers containing hexoses^{157, 158}, *N*-acetylhexosamines^{159, 160}, and hexuronic acids.¹⁶¹⁻¹⁶³ The IR activation of gas-phase ions can induce fragmentation by a series of photo-absorption events, and the fragmentation technique is called infrared multiple photon dissociation (IRMPD).¹⁶⁴ IRMPD has been used to study glycosidic bond stabilities¹⁶⁵⁻¹⁶⁷ and carbohydrate fragment structures¹⁶⁸ as well as to observe anomeric configurations of carbohydrates.¹⁶⁹⁻¹⁷¹ The ability of IRMPD to identify specific

functional groups based on their absorption of resonant photons has made it a powerful tool for characterization of PTMs including glycans. Similar to ECD, IRMPD is best performed in ion traps or FT-ICR instruments for their ability to store ions for long times.

1.3 Hydrogen/Deuterium Exchange

1.3.1 Basics of HDX

Hydrogen/deuterium exchange (HDX) is a long-established chemical reaction that exchanges labile (*i.e.* exchangeable) hydrogens (^1H) with deuterium (^2H or D). Labile hydrogens refer to hydrogens on polar functional groups, such as amides or alcohols. HDX is often coupled to MS because the ^2H isotope can be detected as an increase in mass using MS. On the other hand, ^1H NMR can be used to detect the loss of signal as deuterium is incorporated into the analyte. HDX is a reversible reaction and deuterium can exchange back to hydrogen, called back-exchange.

1.3.1.1 Traditional bottom-up HDX of proteins. HDX is a time-dependent reaction where changes in exchange rates based on structure and interactions can be tracked via monitoring deuterium uptake at various time points. Traditionally, HDX of proteins is initiated by diluting proteins in a D_2O -containing buffer. HDX is quenched by diluting aliquots of deuterated proteins in an acidified quench buffer at $0\text{ }^\circ\text{C}$. The proteins are digested by acidic proteases, typically pepsin, and the resulting peptides are separated in reversed-phase columns and analyzed by MS. Then, the change in mass for each peptide is used to calculate deuterium uptake at various timepoints. This continuous-labeling protocol is optimized for deuterium labeling at backbone amide hydrogens, which simplifies data analysis by keeping the number of deuterium to one label per

amino acid. For longer HDX times, such as 100 minutes or longer, “pulse-” or short-labeling is recommended for control to ensure stability of the protein sample.¹⁷² Whereas the labeling time is varied in continuous labeling HDX, pulse-labeling varies the perturbation time while keeping the labeling time consistent between samples. Pulse-labeling can be conducted by incubating the sample for the same length of time as the longest labeling time, under the same HDX condition, but without deuterating reagent. Then, the control protein can be pulse-labeled for a short time, for instance for 30 seconds. The pulse-labeled control can be compared to sample that was labeled for equivalent length of time during the continuous-labeling HDX, without the incubation. Conducting pulse-labeled control experiment can detect structural changes that the protein sample might undergo during the course of HDX experiment.

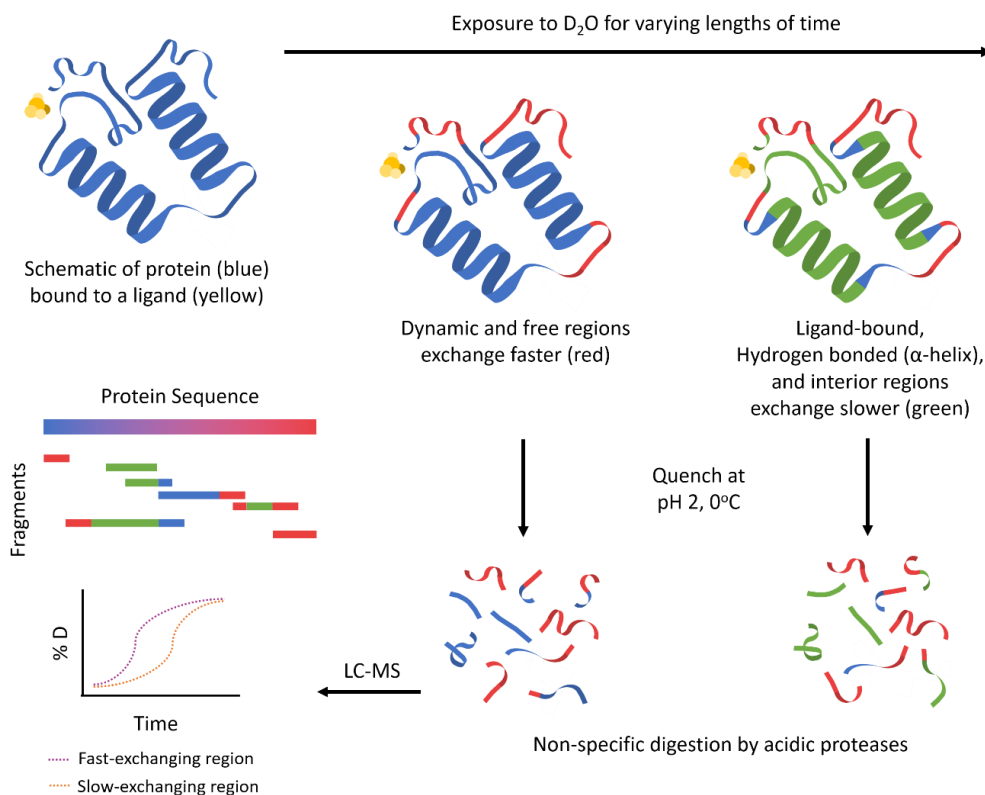


Figure 1.9. Workflow of bottom-up, continuous-labeling HDX experiments of proteins.

Amide hydrogen HDX of native proteins is proposed to occur in the following scheme¹⁷³⁻¹⁷⁵:



Where k_{op} is the rate of opening to a state accessible by the deuterating reagent, k_{cl} is the rate of closing to a state inaccessible by the deuterating reagent, such as hydrogen bonding, and k_{ch} is the intrinsic chemical exchange rate of backbone amides. The observed HDX rate is given by

$$k_{ex} = \frac{k_{op} \cdot k_{ch}}{k_{cl}} = K_{op} \cdot k_{ch} \quad \text{Equation 1.6}$$

When proteins are folded in their native state, $k_{cl} > k_{ch}$ and the observed HDX rate is a function of K_{op} which is the equilibrium constant of protein opening to an exchangeable state. K_{op} can also be written in terms of the Gibbs free energy (ΔG_{op}) as

$$\Delta G_{op} = -RT \ln(K_{op}) \quad \text{Equation 1.7}$$

Where R is the gas constant and T is temperature in Kelvin. Therefore, the unfolded state of proteins, with $K_{op} > 1$, is associated with a faster exchange rate. Thus the deuterium labels on protein amide hydrogens can be indicative of the thermodynamic stability of the labeled region.¹⁷³ Protein unfolding can occur at the local, sublocal, or global level, and the observed exchange equilibrium is the sum of all unfolding events at all levels.¹⁷⁶

$$K_{ex} = K_{local} + K_{sublocal} + K_{global} \quad \text{Equation 1.8}$$

The observed exchange of peptides at various positions and labeling times can give information about the protein structure and conformation. HDX can be utilized to monitor changes in conformation by comparing two states. HDX has been performed on protein-ligand pairs to observe allosteric effects of ligand binding on protein conformation and dynamics as well as binding sites.¹⁷⁷ Different glycoforms have been analyzed by HDX to detect changes in protein conformation and dynamics as a result of altered glycan structures.¹⁷⁸ And HDX has also been performed on phosphorylated proteins to examine protein-protein interactions to compare active and inactive proteins.¹⁷⁹

1.3.1.2 Non-traditional HDX. Since HDX-MS of proteins was first published in 1991¹⁸⁰, the method has been continually developed and adapted for different purposes and analytes. For proteins, top-down¹⁸¹ approaches to HDX-MS have been introduced to reduce back-exchange, which can cause the loss of deuterium labels, during long separation times following reaction quenching. Top-down HDX¹⁸² bypasses the proteolytic digestion and introduces intact proteins into the gas phase, where the protein is fragmented to reveal local information. Top-down approach can also improve spatial resolution by creating more fragments at more random cleavage sites, compared to the standard proteolytic cleavage sites targeted by proteases.¹⁷⁵ Moreover, top-down HDX can be selective of different conformers, for which information is lost during proteolysis in the bottom-up approach. For instance, even a single charge state of deuterated proteins could reveal the presence of two conformers, showing a bimodal distribution, and the top-down approach allows for separate analyses of the two conformers by selecting different precursors in the distribution to fragment.^{182, 183} Whereas CID was used for early

attempts at top-down HDX, CID is no longer the preferred method of fragmentation for deuterated samples because “scrambling” occurs during collisional activation.

Scrambling is the random movement of hydrogen and deuterium labels across the analyte that overwrites solution-phase labeling information.¹⁸⁴ The scrambling process is consistent with the mobile proton model that has been proposed for CID.^{175, 185} On the other hand, fast fragmentation techniques such as ECD and ETD have been found to reduce scrambling.¹⁸⁶⁻¹⁸⁹ Middle-down approaches have been developed as well¹⁹⁰, which combine solution-phase labeling and protease digestion from the bottom-up method with gas-phase fragmentation by ECD or ETD. Middle-down approaches have been shown to improve spatial resolution of deuterium labels on proteins by fragmenting longer peptides to obtain more site-specific information.¹⁹⁰

Typical HDX reactions are carried out on a range of seconds to weeks, and the traditional protocol may not be suitable for analysis of protein conformations or other biomolecules, such as nucleotides^{191, 192}, that require shorter labeling times. Various rapid HDX methods have been developed to examine short-lived intermediates. A continuous mixing device¹⁹³ composed of syringes containing analytes and buffers connected by mixing tees has been used to investigate protein folding intermediates¹⁹⁴ and disordered proteins¹⁹⁵. Electrospray setups where deuterating reagents are introduced into a mixing tee connected to a nanoelectrospray needle have been developed to shorten the quench time further with smaller solvent volumes.^{196, 197} Microfluidic devices and chip-based methods also offer rapid exchange times.¹⁹⁸⁻²⁰⁰ In-ESI HDX can be performed by introducing deuterating reagent into the ESI source as a droplet on a metal plate to be evaporated²⁰¹, through the gas inlet system²⁰²⁻²⁰⁴, or by dual spray using either the

lockspray system^{205, 206} or theta ESI emitters.^{207, 208} Finally, gas-phase HDX has also been performed by introducing gas-phase deuterating reagents into various parts of the mass spectrometer.²⁰⁹⁻²¹² The reaction times achieved by these methods are in the subsecond range.

1.3.2 HDX Rates

Solution-phase HDX reactions are catalyzed by acid, base and water, so that the rate of exchange, k_{ch} , can be written as

$$k_{ch} = k_{acid}[H_3O^+] + k_{base}[OH^-] + k_{water}[H_2O] \quad \text{Equation 1.9}$$

The rate of exchange is proportional to the acid and base concentrations, leading to a V-shaped curve for the exchange rate profile as a function of pH (Figure 1.10).²¹³ At the pH where the rate of exchange is the slowest, called pH_{min} , the contributions of the acid-, base- and water-catalyzed mechanisms are similar.²¹⁴⁻²¹⁶ At $pH > pH_{min}$ represented as part of the upward curve, HDX mostly proceeds by the base-catalyzed mechanism. At $pH < pH_{min}$, the acid-catalyzed mechanism predominates. HDX rates also increase with increasing temperature, as supported by Equations 1.6 and 1.7. HDX rates for different protein functional groups at varying pH and temperature, and their effect on neighboring functional groups, have been extensively described by Bai *et al.*²¹⁷ The quench conditions for HDX reactions of proteins at pH 2.5 and 0 °C is at pH_{min} of backbone amides so that the back-exchange at amides is minimized while deuterium labels on other functional groups are exchanged back to hydrogen. Such quench conditions can simplify HDX data analysis by omitting side chain functional groups that have varying numbers of labile hydrogens as well as exchange rates.

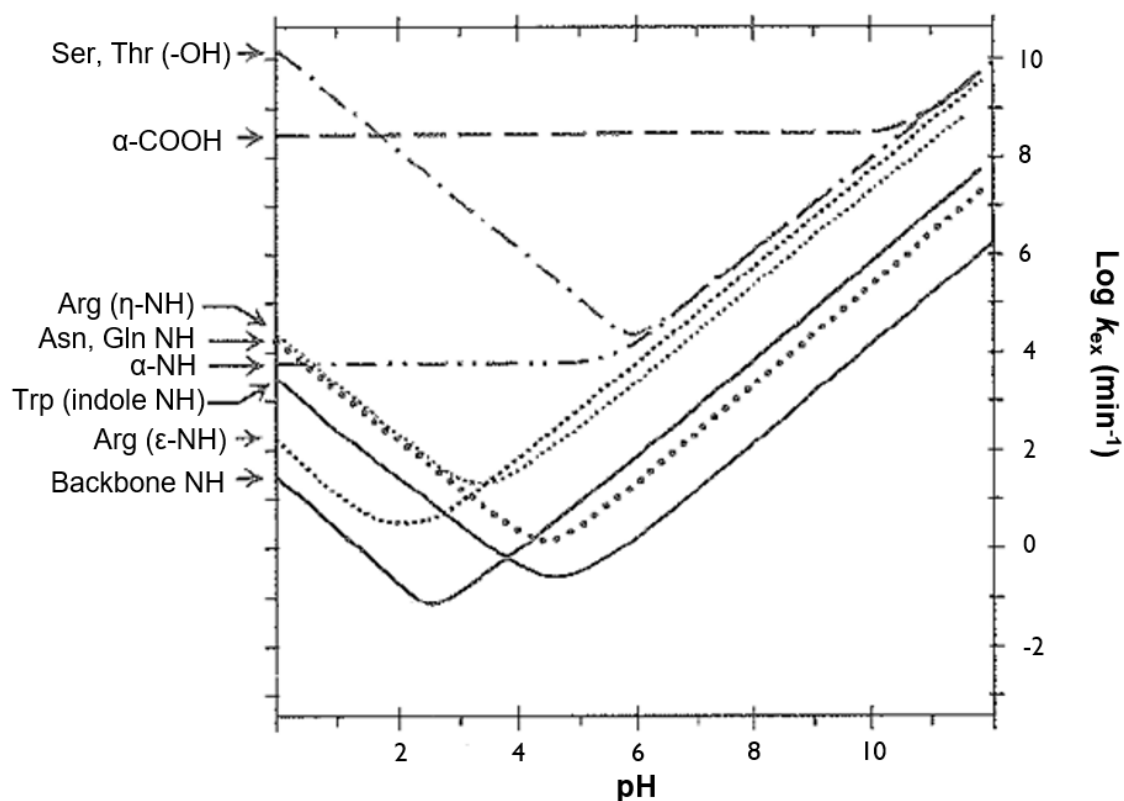


Figure 1.10. HDX rates of protein functional groups. Reprinted with permission from reference.²¹⁶

One mechanism for base-catalyzed and two mechanisms for acid-catalyzed reactions of backbone amide HDX in aqueous solution have been proposed (Figure 1.11).²¹⁸ In the base-catalyzed mechanism, the amide proton is abstracted by a OH^- or OD^- ion and re-protonated by D_2O . In the acid-catalyzed mechanism, the amide nitrogen is protonated by D_3O^+ and the proton is abstracted by D_2O . However, the amide oxygen is more basic than the amide hydrogen. Therefore, an alternative pathway for the acid-catalyzed mechanism is proposed in which the amide oxygen is protonated first, in turn acidifying the amide group. Then the amide hydrogen is abstracted by D_2O , enabling deuteration by D_3O^+ .²¹⁸

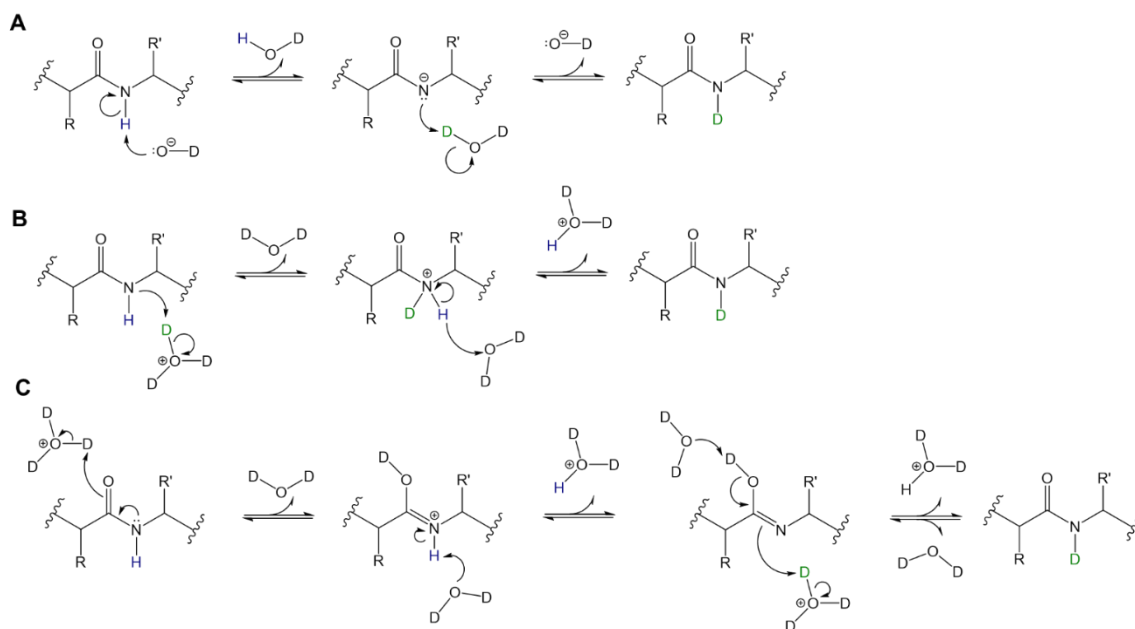


Figure 1.11. Solution-phase HDX mechanism for protein backbone amide. Adapted from reference.²¹⁹

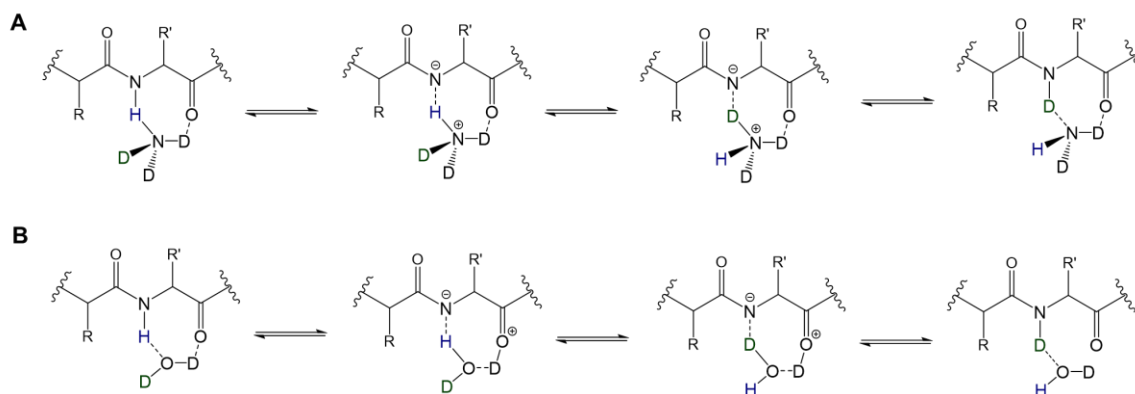


Figure 1.12. Gas-phase HDX mechanism for protein backbone amide. Adapted from reference.²¹⁹

For gas-phase HDX, two major mechanisms have been proposed, depending on the gas-phase basicity of the deuterating reagent (Figure 1.12).²²⁰ The “onium” mechanism²²⁰ is postulated for more basic deuterating reagents, such as ND_3 , where the endothermic proton transfer to ND_3 is energetically feasible by solvation of the resultant ND_4^+ ion. The “relay” mechanism is proposed for less basic deuterating reagents, such as

D₂O or MeOD in which two functional groups of the analyte are interacting with the deuterating reagent for simultaneous transfer of two protons.^{221, 222}

1.3.3 HDX of Carbohydrates

The most abundant functional groups on carbohydrates and glycans are hydroxyls. The exchange rate of hydroxyls calculated for serine and threonine amino acids are several orders of magnitudes faster than traditional backbone amide hydrogens. Under traditional solution-phase HDX conditions, the deuterium labels are only retained at acetamido hydrogens on HexNAc residues of glycans.²²³ Therefore, HDX of carbohydrates has developed around rapid HDX methods where fast reaction time is achieved. Particularly, HDX of carbohydrate hydroxyls, or rapidly-exchanging functional groups, has been achieved during ionization and in the gas-phase. HDX of carbohydrates during MALDI was initiated by preparing the matrix with acidified D₂O and deuterated acetonitrile. Methods to label carbohydrate hydroxyls during ESI have also been developed by placing D₂O droplets inside the ESI source^{100, 201, 224, 225}, introducing D₂O with the curtain gas²⁰³, or spraying D₂O coaxially to the sample via multi-barrel ESI tips.²⁰⁷ It should be noted that the analytes in these in-ESI HDX experiments were detected as metal-adducted species or glycopeptides, and that it was found that very limited HDX reactions occur on carbohydrate-metal adducts as gas-phase ions¹⁰⁰, indicating that HDX occurs during ESI when the analytes are solvated in droplets. Instead, gas-phase HDX was performed on protonated carbohydrate-protein complexes²²⁶ and collision-activated oxonium ions of carbohydrates.^{212, 227} Both in-ESI and gas-phase HDX of carbohydrates revealed differences in deuteration patterns between isomers^{212, 225} and various conformers of carbohydrates^{100, 224}, displaying potentials for expanding HDX

of carbohydrates to structural analysis of glycans and other biomolecules containing rapidly-exchanging functional groups.

1.4 Dissertation Outline

The biological significance and the complex nature of carbohydrates demand a thorough understanding of carbohydrate structures and novel methods to obtain such understanding. While HDX is a well-established method that has provided profound information on conformation and dynamics of proteins, it has yet to be optimized for structural analysis of carbohydrates. For the remainder of this dissertation, developments to HDX methods for structural elucidation of carbohydrates will be presented. We have investigated the effect of residual solvent vapors in ESI sources on HDX reactions of labile hydrogens on carbohydrates and peptides, specifically on hydroxyl and amide functional groups (Chapter Two). We have achieved HDX labeling times in the microsecond-range during ESI via theta-ESI emitters to obtain multiple sampling points (Chapter Three). We have investigated scrambling from collisional activation on metal-adducted carbohydrates and localized deuterium labels via a combination of computations and published fragmentation mechanisms (Chapter Four). We also extended the fragmentation analysis to isomeric carbohydrates to explain observed differences in deuterium labels (Chapter Five). Finally, we explored the energetics of fragmentation pathways for various carbohydrate isomers and multiple metals to investigate the relationship between inter- and intramolecular interactions and resulting fragmentation by correlating experimental and computational data (Appendix E).

CHAPTER TWO

Mass Spectral Detection of Forward- and Reverse-Hydrogen/Deuterium Exchange Resulting from Residual Solvent Vapors in Electrospray Sources

Reprinted with permission from Kim, H. J., Liyanage, O. T., Mulenos, M. R., Gallagher, E. S. *J. Am. Soc. Mass Spectrom.*, **2018**, 29, 2030-2040. Copyright (2021) American Chemical Society.

2.1 Abstract

Characterizing glycans is analytically challenging since glycans are heterogeneous, branched polymers with different three-dimensional conformations. Hydrogen/deuterium exchange-mass spectrometry (HDX-MS) has been used to analyze native conformations and dynamics of biomolecules by measuring the mass increase of analytes as labile protons are replaced with deuterium following exposure to deuterated solvents. The rate of exchange is dependent on the chemical functional group, the presence of hydrogen bonds, pH, temperature, charge, and solvent accessibility. HDX-MS of carbohydrates is challenging due to the rapid exchange rate of hydroxyls. Here, we describe an observed HDX reaction associated with residual solvent vapors saturating electrospray sources. When undeuterated melezitose was infused after infusing D₂O, samples with up to 73 % deuterium exchange were detected. This residual solvent HDX was observed for both carbohydrates and peptides in multiple instruments, and dependent on sample infusion rate, infusion time, and deuterium content of the solvent. This residual solvent HDX was observed over several minutes of sample analysis and persisted long enough to alter the measured deuterium labeling and possibly change the interpretation of

the results. This work illustrates that residual solvent HDX competes with in-solution HDX for rapidly exchanging functional groups. Thus, we propose conditions to minimize this effect, specifically for top-down, in-electrospray ionization, and quench-flow HDX experiments.

2.2 Introduction

With estimates that over 50 % of the human proteome is glycosylated²²⁸, there is increased interest in characterizing the biological structures of glycans. Glycosylation is a post-translational modification where branched carbohydrates are attached to proteins. Glycans are synthesized by a non-template-driven process in which the final structure is dependent on the enzymes that are present at the time of protein translation, producing heterogeneous structures with different monosaccharide composition, branching, and glycosidic bond stereochemistry. The complexity and diversity of glycans have multiple biological implications, including solubilizing and stabilizing folded proteins, and maintaining cellular communication and interactions, for instance to trigger immune responses²²⁹. Furthermore, glycans have shown promise as biomarkers for diseases, including cancer^{230, 231} and a number of autoimmune diseases^{232, 233}. For each of these systems, the three-dimensional structure of the glycan is crucial for glycoprotein function.

Hydrogen/deuterium exchange-mass spectrometry (HDX-MS) is a powerful technique for elucidating molecular structures, dynamics, and interactions. In HDX-MS, the mass increase of an analyte is measured as labile protons are replaced with deuterium (D) upon exposure to deuterated solvents. The rate of exchange is dependent on the chemical functional group, the presence of hydrogen bonds, pH, temperature, charge, and

solvent accessibility^{234, 235}. In traditional, bottom-up HDX procedures, proteins are diluted into D₂O-containing buffers for varying lengths of time. Following exchange, samples are quenched in acidic buffer (pH 2.5) to minimize back exchange, or loss of deuterium labels, at backbone amides. Pepsin, or other acidic proteases, are used to rapidly digest proteins and the resulting peptides are analyzed by liquid chromatography (LC) – MS. While quenching inhibits further deuterium labeling, back exchange occurs for rapidly exchanging side chains and some backbone amides²³⁶ due to water in the quench buffer and solvents for proteolysis and LC²³⁴. Solution-phase HDX-MS of carbohydrates is challenging due to the rapid exchange rate of hydroxyls. Previous work by Guttman, *et al.*²²³ and Huang, *et al.*¹⁷⁸ showed that amide-containing acetamido groups present in *N*-linked glycans retain deuterium in quench conditions and during sample work-up in bottom-up HDX-MS experiments. However, more rapidly exchanging functional groups, including hydroxyls, do not retain deuterium in quench conditions.

Other approaches to HDX can minimize back exchange, which may benefit HDX analysis of rapidly exchanging functional groups. Both bottom-up and top-down HDX-MS methods characterize analytes in their native, solvated conformations by exposing analytes to D₂O-containing buffers. However, top-down HDX eliminates in-solution sample work-up by ionizing immediately after quenching and using gas-phase fragmentation, rather than proteolytic digestion, to generate sub-local information¹⁸⁹. Back exchange is significantly reduced for backbone-amides through top-down HDX compared to bottom-up methods due to the shortened exposure time to protonated solvent, specifically quench buffer^{189, 237}. Yet, there are several disadvantages to top-down proteomics, including extensive sample preparation to make biological samples

suitable for MS analysis, lower sensitivity in MS compared to peptide analyses due to competing ionization of sample matrix components²³⁸, and decreased signal-to-noise ratios associated with increasing molecular weight, often resulting in lower sequence coverage compared to that obtained for digested peptides²³⁹. Moreover, even the short exposure to acidic quench buffer in top-down HDX methods was found to alter protein conformations from the native structure that was present during protein labeling^{240, 241}, and thus, any forward or back exchange that occurred after quenching would sample the altered conformation.

Alternative HDX methods can be utilized to label rapidly exchanging functional groups with further reductions in back exchange. For gas-phase HDX, deuterating agents, such as ND₃ or D₂O, are introduced as gaseous vapors and interact with gas-phase analyte ions²⁴². In-electrospray ionization (ESI) HDX methods involve exposing analytes to an atmosphere of gaseous D₂O in the source during droplet evaporation and analyte ionization. Kostyukevich *et al.* described a method in which a droplet of D₂O was placed inside the instrument source, which vaporized in the heated environment, causing the analyte to come in contact with D₂O vapors during ionization²⁰¹. Other in-ESI HDX methods introduce D₂O with the curtain gas^{202, 203}, nebulizer gas²⁰², through a dual sprayer²⁴³, or through a GC-ESI interface^{244, 245}. Both gas-phase HDX and in-source HDX with matrix assisted laser desorption ionization (MALDI) or ESI have been used to label carbohydrate hydroxyls^{212, 224, 246, 247}. These methods do not require quenching, thus minimizing back exchange. However, native conformations of carbohydrates may not be conserved as gas-phase ions during gas-phase HDX and at the end of the electrospray process. Strong inter-ring hydrogen bonding has been observed for carbohydrates in the

gas-phase, whereas carbohydrates in solution exhibited more flexible conformations¹¹⁰. Therefore, analyses to characterize biologically active carbohydrates should examine solvated structures to maintain native conformations.

While new, in-ESI HDX methods can be utilized for analyzing carbohydrate hydroxyls by sampling short labeling times and preserving some solution-phase conformations. However, we present here a caveat to consider: the vapor composition and equilibrium in the ionization source is constantly modified by the residual and currently incoming solvent introduced by the sample inlet. Here, we show that the residual solvent vapors that accumulate inside the source affect deuterium labeling of rapidly exchanging functional groups, including hydroxyls. Although back exchange from the atmospheric environment has been reported before^{248, 249}, effects of residual solvents on deuterium labeling or back exchange of rapidly exchanging functional groups have not been studied. Our findings are distinguished from those methods that utilize solvent vapors for labeling, such as in-ESI HDX, because residual solvent vapors introduced from the current or previous runs, including blanks, are not controlled, can vary with time, and are often neglected between runs.

Further development of HDX methods for analysis of solvated, biologically active conformations of carbohydrates requires an understanding of the forward- and back exchange that occurs between in-solution labeling and detection. Moreover, we show that residual solvent vapors affect deuterium exchange in multiple instruments for rapidly exchanging functional groups on other biomolecules, including peptides. This indicates that this effect extends beyond carbohydrates and may need to be taken into consideration as HDX continues to be developed and used for top-down and in-ESI methods.

2.3 Experimental

2.3.1 Materials

Melezitose, tri-*N*-acetylglucosamine (NAG₃), and sodium chloride (NaCl) were purchased from Sigma Aldrich (St. Louis, MO). Deuterated solvents with purity > 99 % (e.g. D₂O and CH₃OD, referred to as MeOD hereafter) were purchased from Cambridge Isotope Laboratories, Inc. (Tewksbury, MA). [Glu1]-Fibrinopeptide B (EGVNDNEEGFFSAR, glu-fib) was purchased from Waters Corporation (Milford, MA). All other materials were purchased from Fisher Scientific International, Inc. (Pittsburgh, PA). All chemicals were used without further purification. Nanopure water was acquired from a Purelab Flex 3 purification system (Elga, Veolia Environment S. A., Paris, France).

2.3.2 Sample Preparation

Carbohydrates were prepared with NaCl at a 1:10 molar ratio in H₂O or D₂O to aid ionization by sodium adduction. This molar ratio, which gave the best signal for our experiments, was maintained for all experiments. Glu-fib was prepared in a 50:50 volumetric mixture of H₂O and acetonitrile with 0.2 % formic acid.

2.3.3 HDX During Direct Infusion of Carbohydrates

Melezitose and NaCl were diluted into 99.9 % D₂O (v/v) and immediately infused at 5 μL/min, 10 μL/min, or 20 μL/min into a Waters Synapt G2-S High Definition MS (HDMS) with LockSpray Exact Mass Ionization Source (Waters Corporation, Millford, MA). Deuterium exchange was measured as melezitose was exposed to D₂O solvent for increasing lengths of time. Capillary voltage, source

temperature, desolvation temperature, and desolvation gas flow rate were 2.5 kV, 100 °C, 350 °C, and 500 L/h, respectively. The syringe, capillary, and ESI needle were washed with nanopure water for at least 5 minutes between runs to prevent salt precipitation.

2.3.4 HDX Following Pre-Equilibration of the Source

Melezitose and NaCl were diluted in H₂O or D₂O and directly infused. In separate experiments, glu-fib was directly infused. Experiments were performed on the Waters Synapt G2-S HDMS with the conditions described above or an LTQ Orbitrap Discovery MS equipped with an Ion Max Source (Thermo-Fisher, Waltham, MA). For the Orbitrap instrument, the source voltage and capillary temperature were 4.5 kV and 250 °C to yield optimum ionization.

Each experiment was composed of three parts: pre-equilibration of the source, sample infusion, and source evacuation. The source was pre-equilibrated with solvent vapor by infusing solvent (D₂O, MeOD, H₂O, MeOH, or acetonitrile) for five minutes at 20 µL/min. Then, the sample was infused at 10 µL/min for two minutes (Synapt G2-S) or five minutes (Orbitrap Discovery). Unless stated otherwise, the sample was prepared in a solvent different from that used for pre-equilibration to test whether the observed HDX came from residual vapors. For instance, when the source was pre-equilibrated with a deuterating agent, undeuterated sample was infused; when the source was pre-equilibrated with protonated solvent, deuterated sample was characterized. Deuterated samples were prepared by incubating carbohydrates with NaCl in 99.9 % D₂O for more than 48 hr at room temperature. This deuteration time effectively labeled all labile hydrogens, *e.g.* hydroxyls and amides, resulting in 11 D for the carbohydrates, and this state (11D) will be referred to as ‘fully deuterated’ in the rest of the text. Separate

syringes and capillaries were used for samples in H₂O and samples in D₂O to minimize carryover of solvents and potential exchange reactions before ionization, introducing approximately 30 s between pre-equilibration and sample infusion. Each run was followed by 20 minutes of source evacuation with no solvent or sample infusion to re-equilibrate the source to atmospheric conditions and remove solvent vapors. All gas parameters were maintained at constant flow rates during pre-equilibration, sample infusion, and source evacuation, unless specified otherwise.

For each trial, deuterium exchange was plotted as a function of time. The time points on all plots represent the elapsed time starting from initial signal detection, with $t = 0$ s as the first signal intensity above 500 ion counts with $S/N > 3$ for sodiated-carbohydrates.

2.3.5 HDX with Defined Solution Labeling Times

A mixing apparatus, modified from that described by Keppel, *et al.*¹⁹⁵ was used to ensure that in-solution labeling times were strictly defined. Two syringes, attached to fused silica capillaries (150 μm i.d., Polymicro Technologies, Phoenix, AZ), were joined to a mixing tee with a single outlet that connected to the ESI source. A 500 μL syringe was filled with carbohydrates and NaCl in H₂O with 0.1 % formic acid and a 2.5 mL syringe was filled with D₂O with 0.1 % formic acid. Both syringes were pumped using a single syringe pump (Fusion 400, Chemyx, Inc. Stafford, TX), resulting in solution mixing for a specified length of time downstream of the mixing tee. The concentrations of carbohydrates and NaCl after dilution into D₂O were 5 μM and 50 μM , respectively. Labeling time (t_{label}) was defined by Equation 2.1.

$$t_{label} = \frac{V_d}{F_1 + F_2} \cdot l \quad \text{Equation 2.1}$$

F_1 and F_2 are the flow rates of each syringe, V_d is the volume of the delay line between the mixing tee and ESI source, and l is the length of the delay line. The flow rate through the labeling capillary was 18 $\mu\text{L}/\text{min}$. The delay line included a capillary (150 μm i.d. and 7 cm length) and the ESI needle (127 μm i.d. and 23.57 cm length), resulting in a mixing time of 14.1 s.

Carbohydrates and NaCl mixtures were infused from the mixing apparatus for 5 minutes and the ESI needle was washed with H_2O containing 0.1 % formic acid for 5 minutes. The source was not pre-equilibrated with solvent between runs, but was evacuated for 45 minutes after each run, as described above for pre-equilibration experiments. To prevent salt precipitation, the mixing tee was sonicated for 30 minutes in nanopure water during source evacuation.

2.3.6 Calculations

The theoretical, average masses of undeuterated (D_0) and fully deuterated (D_{11}) sodiated-carbohydrates (Figure A.1) were calculated using isotopic distributions generated by Exact Mass Calculator (IonSpec Corporation, now Varian, Inc., Palo Alto, CA) at a resolution of 20,000 (Equation 2.2), where m/z is the mass-to-charge ratio and I is the intensity of each peak. Exact masses are presented in Table 2.1.

Table 2.1 Exact mass-to-charge ratios (m/z) of undeuterated (0D) and fully deuterated (11D) [Melezitose-Na]⁺ or [NAG₃+Na]⁺ with isotopic distributions.

Peaks ^a	Melezitose			NAG ₃		
	m/z		Relative Abundance	m/z		Relative Abundance
	D ₀	D ₁₁		D ₀	D ₁₁	
M ₁	527.1588	538.2278	100.00	650.2385	661.3075	100.00
M ₂	528.1622	539.2312	20.44	651.2417	662.3107	28.00
M ₃	529.1640	540.2330	5.23	652.2438	663.3128	7.04
M ₄	530.1669	541.2359	0.79	653.2464	664.3154	1.24
M ₅				654.2487	665.3177	0.19
Average ^b	527.4227	538.4901		650.5807	661.6497	

$$(m/z) = \frac{\sum(m/z) \cdot I}{\sum I} \quad \text{Equation 2.2}$$

The average mass of experimentally observed sodiated-carbohydrates were calculated using each peak in collected mass spectra. Deuterium exchange (#D) and percent deuteration (%D) were calculated using Equations 2.3 and 2.4, respectively.

$$\#D = (m/z)_{\text{experimental}} - (m/z)_{\text{theoretical,D0}} \quad \text{Equation 2.3}$$

$$\%D = \frac{(m/z)_{\text{experimental}} - (m/z)_{\text{theoretical,D0}}}{(m/z)_{\text{theoretical,D11}} - (m/z)_{\text{theoretical,D0}}} \times 100 \quad \text{Equation 2.4}$$

LockMass was not used, as the lockspray standard was deuterated in the source during analysis (Figure 2.6).

Each experiment was repeated with a minimum of three replicates. Data figures plot average values with error bars representing standard deviations unless specified otherwise. Where necessary, statistical analyses utilized Student's *t*-test at the 95 % confidence interval.

2.4 Results and Discussion

2.4.1 Faster Sample Infusion Rates Increase the Deuterium Labeling Rate of Hydroxyls

Melezitose and NaCl were diluted into D₂O, loaded into a syringe, and immediately infused into the ESI source at 5 $\mu\text{L}/\text{min}$ to monitor in-solution exchange of hydroxyls. For this experiment, the labeling time increased as melezitose was incubated in the syringe with D₂O, thus longer labeling times were achieved at later infusion times. Whereas the exchange rate of hydroxyls was expected to be on the microsecond time scale^{250, 251}, deuterium labeling was observed over five minutes (Fig. 2.1). Back exchange from moisture in the atmosphere likely contributed to low deuterium labeling at the earliest time points, but the five-minute time frame that was required to observe exchange suggested that back exchange inside the source was greater than expected.

To improve the consistency of the spray and signal intensity at earlier time points (< 75 s), the flow rate was increased to 10 $\mu\text{L}/\text{min}$ or 20 $\mu\text{L}/\text{min}$. Higher levels of deuterium labeling were measured with faster infusion rates at earlier time points (Fig. 2.2). For instance, when infused at 10 $\mu\text{L}/\text{min}$, melezitose was only $24 \pm 7\%$ deuterated (2.7 ± 0.8 D) after one minute of labeling, but when infused at 20 $\mu\text{L}/\text{min}$, melezitose reached $76 \pm 10\%$ deuteration (8 ± 1 D) even though the solution labeling time remained one minute (Fig. 2.2a). After two minutes of in-solution labeling, melezitose infused at 10 $\mu\text{L}/\text{min}$ or 20 $\mu\text{L}/\text{min}$ was $84 \pm 2\%$ (9.3 ± 0.2 D) or $88 \pm 2\%$ (9.8 ± 0.3 D) deuterated, respectively, whereas melezitose infused at 5 $\mu\text{L}/\text{min}$ was $55 \pm 12\%$ (6 ± 1 D) deuterated (Fig. 2.2b). This observation is different from previously reported in-ESI HDX experiments in which the amount of deuterium labeling was described as independent of sample infusion rate²⁰¹.

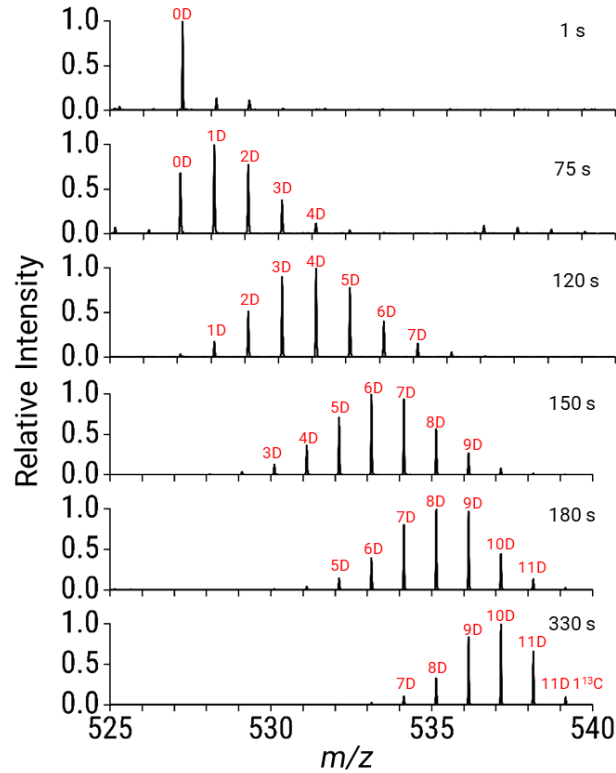


Figure 2.1. Representative deuterium-exchange spectra for sodiated-melezitose detected by ESI-MS. Melezitose and NaCl were diluted into D₂O (final solution 99% D₂O (v/v)) and spectra were collected at increasing solution incubation times.

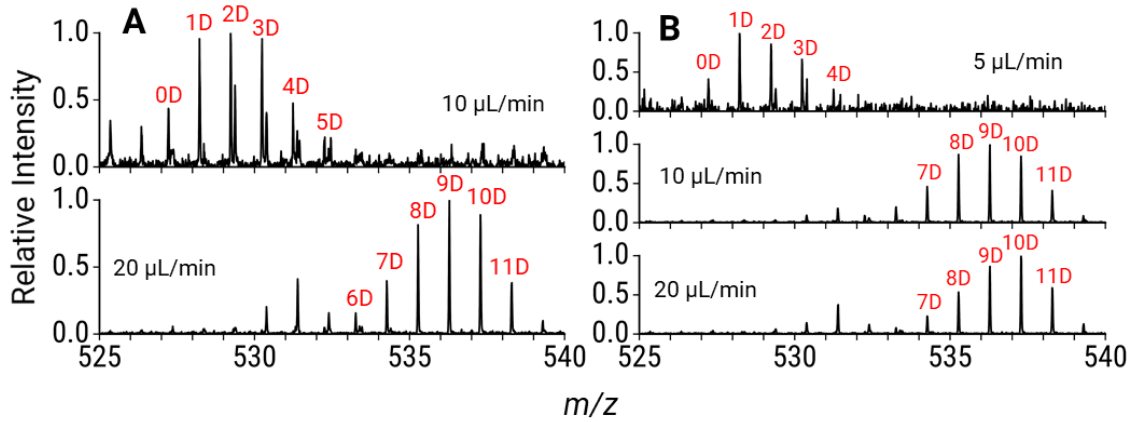


Figure 2.2. Representative HDX spectra for sodiated-melezitose infused at different rates. With a constant in-solution labeling time, (a) 1 min or (b) 2 min, deuterium labeling increased with faster sample infusion rates, indicating that an additional HDX labeling reaction was occurring besides the in-solution reaction.

Even though melezitose spent the same length of time interacting with the deuterating agent in solution, different deuterium exchange was measured when melezitose was infused at different flow rates, suggesting that an additional source of HDX was occurring as the carbohydrates were infused. Furthermore, when the source was pre-equilibrated with mixtures of D₂O and H₂O that matched the solvent composition of the sample, no difference in deuterium exchange was observed at varying flow rates or for different infusion times (Fig. A.2). We hypothesized that D₂O vapors introduced along with the analyte were accumulating in the ESI source at a time scale long enough to promote in-ESI HDX of hydroxyls. For instance, when D₂O was infused at a faster flow rate, more D₂O vapors accumulated in the source, resulting in more HDX in the same length of time. Alternatively, before D₂O vapors accumulated to an appreciable extent, atmospheric water vapor likely caused back exchange of the sample. Several assumptions were made in generating this hypothesis. First, we assumed that there was no additional exchange in the instrument under vacuum. Second, we assumed that the electrospray droplets desolvate in the source on the order of microseconds^{252, 253}, which correlates to the expected rate of hydroxyl exchange.

2.4.2 Residual Solvent Vapors in the ESI Source Result in HDX of Hydroxyls

To determine if residual vapors in the source were causing in-ESI HDX, the source was pre-equilibrated with D₂O, then protonated melezitose and NaCl in H₂O were directly infused. Although the carbohydrates were undeuterated, melezitose was detected at the earliest time point with an average of 8.0 ± 0.2 D, corresponding to 73 ± 2 % deuteration (Fig. 2.3a). The percent deuterium exchange decreased over time (Fig. 2.3a and 2.3c). Because fully protonated melezitose was infused into the instrument, the

deuterium exchange was attributed to HDX from residual solvent in the source. From the observation that deuterium labels were lost over time, it could be inferred that either the residual D₂O was evacuated at later time points or H-for-H exchange became greater than HDX at later time points due to increasing H₂O vapor as protonated solvent was infused.

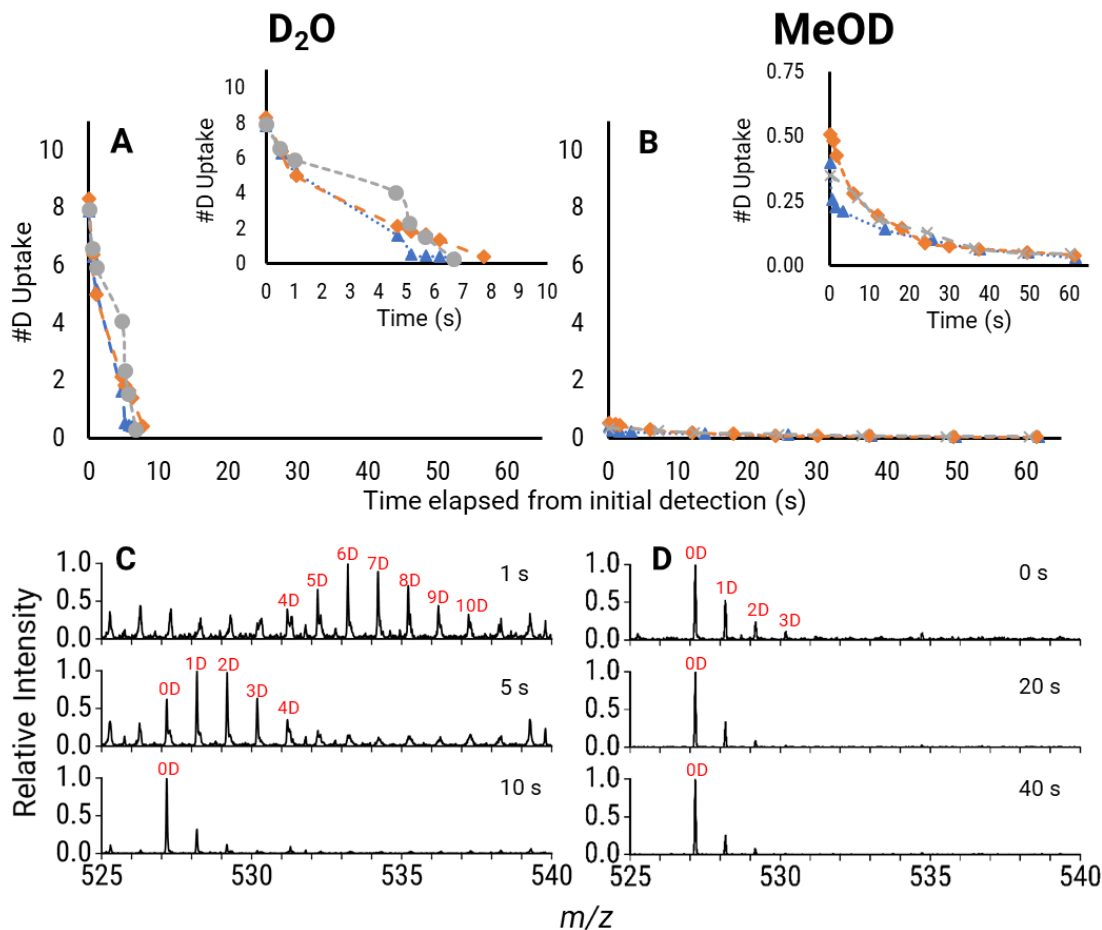


Figure 2.3. Residual solvent vapors caused in-ESI HDX of sodiated-melezitose. Deuterium exchange by melezitose is plotted for each replicate after pre-equilibration of the source with (a) D₂O or (b) MeOD. Different colors represent replicate experiments. Insets show expanded views of the time or deuterium exchange axes. (c) and (d) illustrate representative mass spectra of sodiated-melezitose at three time points after pre-equilibration with D₂O or MeOD, respectively. Unlabeled peaks in the mass spectra are chemical noise and not used for deuterium exchange calculations.

Pre-equilibration with MeOD followed by infusion of undeuterated melezitose and NaCl also showed an initial deuterium exchange (Fig. 2.3b). However, the initial deuterium exchange was considerably lower than that measured when pre-equilibrating with D₂O for the same length of time, with 0.4 ± 0.1 D (3 ± 1 %). Though the average deuterium exchange was low, it was significantly higher than the average deuterium exchange measured after infusing the sample for 60 s (0.03 ± 0.01 D or 0.3 ± 0.1 %), indicating that residual MeOD vapors also caused HDX. When the source was pre-equilibrated with acetonitrile, which contains no labile hydrogens, and fully deuterated melezitose with NaCl was infused, residual acetonitrile resulted in no detected back exchange (Fig. A.3). When the source was pre-equilibrated with H₂O or MeOH, fully deuterated melezitose showed back exchange at initial time points, with H₂O resulting in greater initial loss of deuterium than MeOH (Fig. A.3), consistent with the data presented in Fig. 3. Finally, when the source was pre-equilibrated with D₂O first, followed by an equal volume of acetonitrile, deuterium labeling from residual D₂O reduced to approximately 22 %, but was not completely removed (unpublished data). Based on the density of D₂O and MeOD, there are twice as many D₂O molecules as MeOD molecules in an equivalent volume of solvent. Also, D₂O has two deuteriums available for exchange whereas MeOD has only one. Therefore, pre-equilibration with D₂O results in four times as many deuterium present for labeling compared to MeOD pre-equilibration. However, initial deuterium exchange observed from residual D₂O is still disproportionately larger than labeling from residual MeOD.

Several additional explanations are plausible for the difference in exchange between D₂O and MeOD. (1) Although higher levels of deuteration may have been

achieved by melezitose from MeOD vapors, melezitose with higher deuterium labeling may not have been detected at these initial time points due to weak instrument signal. Thus, the first detected carbohydrates may have been exposed to a mixture of MeOD and H₂O vapors, resulting in less overall deuterium exchange. This point is supported by the observation that differences in spray stability within each run yielded different levels of initial deuterium labeling for each replicate. Additionally, data collected on a different instrument showed that higher levels of deuterium exchange could be observed from residual MeOD vapors (Fig. 2.4). Or (2) MeOD was evacuated from the source faster than D₂O, resulting in a lower accumulation of MeOD vapors and less exchange. The difference in evacuation rates could be due to differences in the solvent volatilities and/or condensation coefficients on the surfaces of the ESI source²⁵⁴. The source temperature was varied to examine the effect of volatility and condensation coefficient on residual solvent vapor HDX, but no observable correlation or statistical differences were found (Table A.1, Table A.2, and Fig. A.4). Though increasing the temperature was expected to decrease HDX by increasing evacuation of the volatile solvents from the source, it would also increase the rate of the exchange reaction according to the Arrhenius equation. By approximating the activation energy as between 2 and 10 kcal/mol for proton exchange between ethanol and water²⁵⁵, an increase in temperature from 120 °C to 350 °C would result in a rate increase between 3 and 113 times faster. If the activation energy was approximated to be similar to that reported for exchange of backbone amide hydrogens^{256, 257}, the rate difference would increase by three to four orders of magnitude for these two temperatures. While an increase in the reaction rate would increase deuterium labeling, the back exchange rate would also increase at the higher temperature; thus,

multiple forward and back exchanges could occur in the source prior to detection. In summary, all factors described above could contribute to the reduced deuterium exchange that was observed following MeOD pre-equilibration.

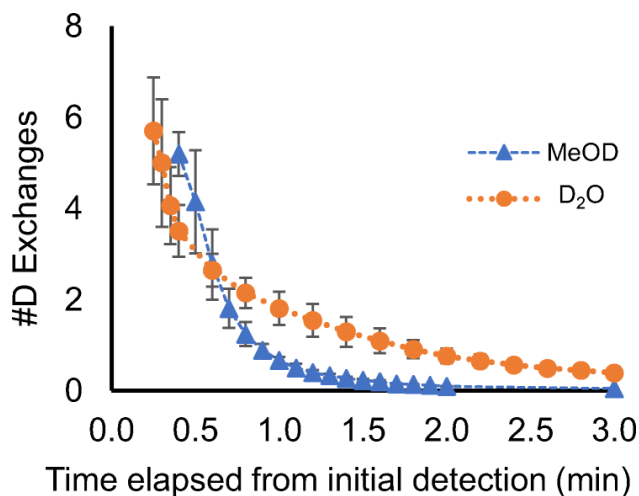


Figure 2.4. Residual solvent vapors were observed to cause HDX of sodiated-melezitose in an Ion Max Source of an LTQ Orbitrap Discovery MS. Deuterium exchange by sodiated-melezitose is plotted after pre-equilibration of the source with D₂O or MeOD.

Guttman *et al.* identified a source of HDX specific to instruments with StepWave ion guides²⁵⁸, including the Waters Synapt G2-S that was used to collect this data.

StepWave ion guides consist of two stages where a DC offset potential is used to push ions from the lower stage to the higher stage leading into the mass spectrometer, while neutral, bulk species are retained in the lower stage²⁵⁹. It was hypothesized by Guttman *et al.* that residual bulk solvent may linger in the lower stage of the StepWave and exchange with analytes²⁵⁸. To verify that the labeling in our specific experiments occurred in the source and not the ion optics, we replicated our experiments in a Thermo LTQ Orbitrap Discovery with an Ion Max Source, which is equipped with a linear stacked ring ion-guide. When undeuterated melezitose in H₂O was infused into the Ion

Max source following pre-equilibration with D₂O or MeOD, deuterated melezitose was detected (Fig. 2.4). For instance, when the source was pre-equilibrated with D₂O, melezitose with an average of 6 ± 1 D (52 ± 11 %) was initially detected and the deuteration level decreased to 0.4 ± 0.1 D (4 ± 1 %) at three minutes into the sample infusion. When the source was pre-equilibrated with MeOD, melezitose with 5.2 ± 0.5 D (47 ± 4 %) was initially detected and was back exchanged to 0.12 ± 0.00 D ($1.08 \pm 0.01\%$ D) after two minutes of sample infusion. Because deuterated melezitose was observed following pre-equilibration of the source with deuterating agent, in an instrument with a different ion guide compared to that with a StepWave, it was concluded that the labeling was occurring in the source rather than the ion guide. Moreover, from earlier findings that sodium-adducted carbohydrates and other molecules display limited HDX in the gas-phase^{212, 260-263}, vaporized sodiated-melezitose adducts in ion guides are less likely to be labeled, unlike peptides and proteins. Thus, the data supports our hypothesis that exchange occurred in the source while the carbohydrates were partially solvated rather than as gas-phase ions in the ion guide optics.

An interesting observation is that while the level of deuteration decreased to < 0.5 D within 10 s in the Synapt G2-S, in the Orbitrap Discovery, melezitose maintained higher levels of deuteration for over 2 minutes, suggesting that the rate of source evacuation was higher for the Synapt G2-S, possibly due to the faster build-up of pressure in the LockSpray Exact Mass Ionization Source. We hypothesized that changing the gas flow rates in the gas-tight ionization chamber of the LockSpray Exact Mass Ionization Source, would alter the rate of evacuation of solvent vapors and the deuterium exchange of the sample; however, no apparent correlations were found with different gas

flow rates (cone gas, desolvation gas, and nebulizer gas) and the residual solvent HDX (Table A.3 and Fig. A.5). However, large variations between replicates suggested that ionization efficiency and spray stability could have affected the measurement of deuterium exchange as the gas flow rates were modified.

2.4.3 Solvent Vapors Differentially Affect Functional Groups with Different Exchange Rates

The deuterium exchange of melezitose and NAG₃ was compared to examine the effect of residual solvent vapor HDX on exchange of different functional groups (Fig. A.1). The proton exchange rates of carbohydrate hydroxyls and acetamido hydrogens were assumed to be similar to those measured for serine hydroxyls and protein backbone amides, respectively. Thus, the difference in exchange rates was maximized at pH 2.5, where the exchange rate of hydroxyls was approximated to be eight orders of magnitude greater than that of backbone amides²¹³. A mixing apparatus was used to define the in-solution labeling time to ensure that both melezitose and NAG₃ were exposed to D₂O(l) solvent for the same length of time.

Even with the defined labeling time in solution, changes in deuterium labeling were observed for melezitose during the course of the experiment, confirming that HDX was occurring in the source. The average deuterium exchange for melezitose at the earliest time point was 10.78 ± 0.05 D (97.4 ± 0.5 %) which decreased to 10.2 ± 0.4 D (92 ± 3 %) after one minute. The average deuterium exchange for NAG₃ was 8.8 ± 0.1 D (78 ± 1 %) initially, and 8.59 ± 0.05 D (77.0 ± 0.5 %) near the end of the five-minute infusion. The decrease in deuterium exchange for melezitose was significant, implying that back exchange was occurring, likely from atmospheric water vapor in the source.

Yet, the deuterium exchange for NAG₃ was consistent throughout the five-minute duration. This consistent level of deuterium labeling for NAG₃ illustrates, for the first time, that solvent vapors saturate the source during ESI. Despite the decrease in deuterium exchange, melezitose achieved a higher level of deuteration compared to NAG₃ (Fig. 2.5 and Fig. A.6). This was expected due to the greater number of hydroxyls in melezitose.

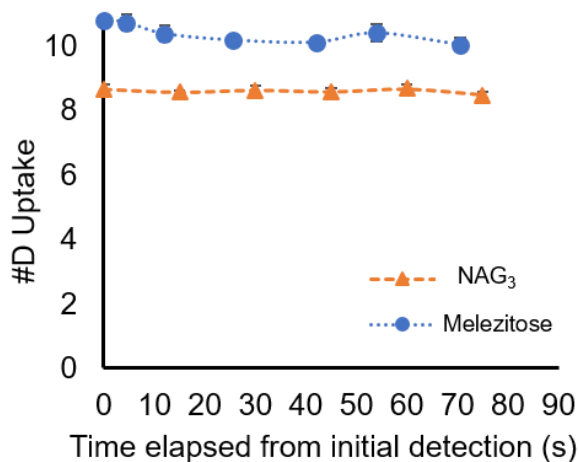


Figure 2.5. Deuterium exchange for sodiated-melezitose and sodiated-NAG₃ after a defined in-solution HDX time.

The numerical values for deuterium exchange are quite interesting, considering that the D₂O:H₂O ratio was 5:1, or 83.33 % D₂O by volume. When the source was pre-equilibrated with solvent mixtures matching the sample composition, the percent deuterium exchange was consistent with the percent deuterium of the solvent (Fig. A.2). On the other hand, the deuteration level for neither melezitose nor NAG₃ matched the percentage of D₂O in solution (Fig. 2.5), which would correspond to 9.17 D. The solvent pre-equilibration experiments (Fig. A.2) were performed without adjusting the solution pH; therefore, the exchange reaction was at neutral conditions. Because the exchange rate

of hydroxyls is minimized around pH 6, at higher pH, *e.g.* neutral conditions, the exchange reaction is primarily catalyzed by OH⁻ or OD⁻²³⁴. Whereas the experiments comparing deuterium exchange for melezitose and NAG₃ were performed at pH 2.5 and acid catalyzed. In changing the pH from neutral to 2.5, the exchange rate of hydroxyls would increase by approximately two orders of magnitude, while the exchange rate of amides would decrease by approximately five orders of magnitude²¹³. For hydroxyls at pH 2.5, it would be expected that the forward labeling and back exchange rates would increase to an equal extent. Thus, though the exchange rate was faster at pH 2.5, it would equally affect the forward and back exchange reactions in solution and the source. Compared to the solvent pre-equilibration experiments (Fig. A.2), the only difference in exchange conditions was the reaction pH, which appeared to result in an equilibrium favoring the deuterium-labeled species for melezitose at pH 2.5.

NAG₃ is a reducing sugar with eight hydroxyls when the reducing end forms a six-membered ring, as drawn in Fig. A.1, whereas melezitose is a non-reducing sugar. Because all 11 hydroxyls of melezitose were found to be deuterated to some extent in the current setup with the mixing apparatus, the differences in exchange rate between primary and secondary hydroxyls is assumed to be negligible. Therefore, based on the deuterium labeling equilibrium of melezitose, seven hydroxyls of NAG₃ that are not involved in mutarotation would be expected to be labeled. The mutarotation rate between α and β anomers of *N*-acetyl glucosamine was reported as $0.7 \pm 0.09 \times 10^{-3} \text{ s}^{-1}$ at pH 8.99 with a trend of decreasing rate with lower pH²⁶⁴. Thus, with a solution labeling time of 14.1 s, interconversion between the chain and ring forms is expected, but more likely to be catalyzed by D⁺ compared to H⁺ due to the volumetric percentages of D₂O and H₂O in

the solvent. Thus, interconversion would preferentially add deuterium either to the C5 oxygen as the ring opened into the chain form or at the α or β hydroxyl at C1 as the ring forms from the aldehyde, increasing the total deuterium content of the molecule at an eighth hydroxyl (Fig. A.6). The observed deuterium exchange was greater than the number of hydroxyls on NAG₃. At pH 2.5, the intrinsic chemical HDX rate for backbone amides is slowed compared to neutral pH²³⁴, but is still dependent on factors such as solvent accessibility and hydrogen bonding. Assuming the exchange rate of acetamido hydrogens is similar to that of backbone amides, it is possible that some of the amide hydrogens exchanged, given the minimal structuring and hydrogen bonding associated with the carbohydrate¹⁷³.

2.4.4 Solvent Vapors Affect Exchange of Glu-fib Peptides

The effect of solvent vapor HDX on peptides was examined using glu-fib, a common peptide standard in instruments with time-of-flight mass analyzers. The LockSpray Exact Mass Ionization Source is a dual-electrospray source and glu-fib was introduced through the lockspray inlet. When undeuterated glu-fib peptides were infused through the lockspray needle after pre-equilibration of the source with D₂O, glu-fib was found to be deuterated (4 ± 1 D) and the deuteration level decreased over time (0.6 ± 0.2 D) (Fig. 2.6a). The deuteration of glu-fib from residual solvent vapors illustrates several important points. First, because glu-fib and D₂O were infused through two separate spray needles, the lockspray and sample spray, respectively, there was no dead volume, indicating that deuteration was a result of solvent vapor rather than residual solvent in a shared electrospray needle. Second, solvent vapor was found to exchange with peptide protons, suggesting that the residual solvent vapor HDX could affect peptide and protein

analyses. Third, because glu-fib was deuterated by the residual solvent vapors, lockmass could not be used. For our experiments, the original undeuterated peptide mass could not be detected. Even if the undeuterated (0D) peak was detected, the presence of deuterated peaks would likely shift the m/z distribution and could cause incorrect lockmass assignment. A standard with no labile hydrogens would be required to use the lockmass function in the presence of deuterating vapors in the source.

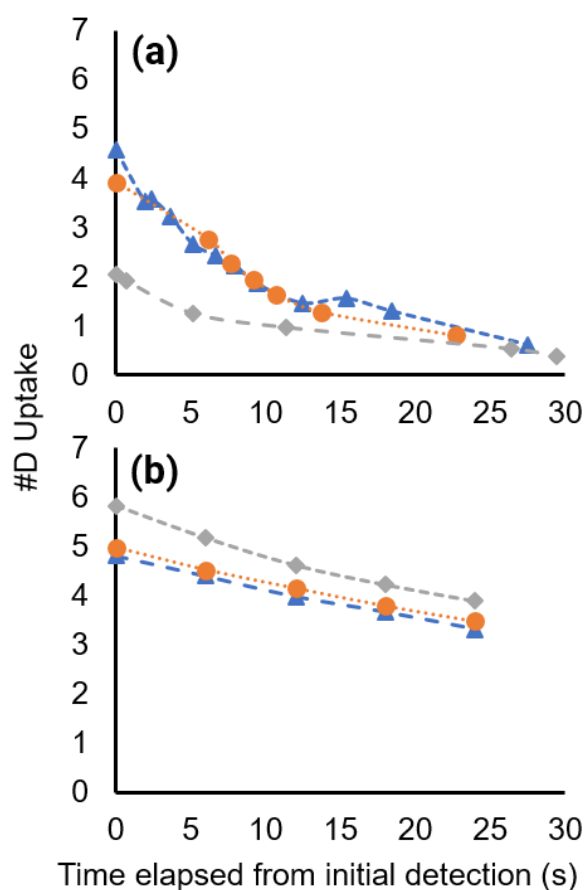


Figure 2.6. Residual solvent vapor HDX causes labeling of rapidly exchanging functional groups of glu-fib, a peptide. Deuterium exchange is plotted over time for glu-fib after pre-equilibration of the source with D_2O in (a) Waters Synapt G2-S HDMS with LockSpray Exact Mass Ionization Source or (b) Thermo LTQ Orbitrap Discovery MS with an Ion Max source. Different colors represent replicate experiments.

Glu-fib was also characterized on the Thermo LTQ Orbitrap Discovery MS following source pre-equilibration with D₂O. A trend similar to the data from the Synapt G2-S was observed (Fig. 2.6b). Glu-fib was initially detected with an average of 5.2 ± 0.5 D, and the deuteration level decreased to 0.84 ± 0.03 D by the end of the five-minute infusion time. The rate of decrease in deuteration was slower in the LTQ Orbitrap Discovery compared to that observed in the Synapt G2-S. After 30 s of data collection, the deuterium exchange in the Orbitrap Discovery decreased by 1.6 ± 0.3 D or 32 ± 1.5 %, compared to a decrease of 3 ± 1 D or 83 ± 4 % for the Synapt G2-S. Because the observed glu-fib peptides are not sodiated, unlike the carbohydrates, the earlier observation from Guttman *et al.* describing the labeling effects from StepWaves²⁵⁸ may have had an additive effect after residual solvent vapor HDX for experiments performed on the Synapt G2-S. The difference in deuterium exchange by glu-fib from two different instruments may be accounted for by the difference in the ion guide setup. However, since the effects of different ion guide optics parameters have been thoroughly studied by Guttman *et al.*; no further optimizations to minimize deuterium exchange of glu-fib in the ion guides were performed.

2.5 Conclusions

Residual solvent vapors accumulate in electrospray sources and exchange with rapidly exchanging functional groups of carbohydrates and peptides. This effect is distinguished from previously reported back exchange from atmospheric moisture or in-ESI HDX techniques, in that the HDX reported here results from saturation of the source with solvent vapors during an ongoing experiment. Residual solvent vapor HDX was observed on two different instruments. The magnitude of this effect was dependent on the

sample infusion rate and time as well as the deuterium content (v/v) of the solvent. Furthermore, as the vapor composition in the source changed with time, the observed deuterium exchange was altered. Since residual solvent vapor HDX occurs after in-solution labeling, non-native conformations could be sampled. Thus, the structure of the analyte should be considered during ionization and desolvation. Additionally, the residual solvent vapor HDX is significant because it shows that many biomolecules, including carbohydrates and amino acid side chains of peptides and proteins, are affected by this phenomenon. Thus, any biomolecules with rapidly exchanging functional groups could be deuterium labeled or back exchanged in electrospray sources, but many current methods for data analysis assume peptide labeling occurs at backbone amides. Thus, these results suggest that simple assumptions about deuterium-labeled sites in proteins should be carefully considered.

Through our experiments, we observed a number of ways to reduce the effects of residual solvent vapor HDX. Traditional bottom-up HDX methods that introduce peptides in protonated solvents into the source are unlikely to be affected by residual solvent vapor HDX. However, protocols that involve high percentages of labeling solvent and rapid quench times, combined with $\mu\text{L}/\text{min}$ flow rates will be more susceptible to residual solvent vapor HDX. As additional top-down, in-ESI, or quench-flow HDX methods are developed, this residual solvent vapor exchange will need to be controlled and/or measured when the deuterating reagent is introduced into the source as a volumetric fraction of the solvent. For many in-ESI HDX experiments, the residual solvent vapors will need to be removed between runs. This can be achieved in the following ways. For all the data presented here, “evacuation,” or 20-min purging with

source gas and no solvent introduction was included to ensure removal of residual solvent vapors. Opening the source for the Orbitrap Discovery also effectively reset the source to atmospheric conditions. Furthermore, purging the source after equilibrating to atmosphere with aprotic solvent (*e.g.* acetonitrile) minimized back exchange associated with environmental water vapor. However, purging with aprotic solvent alone (without evacuating) was not sufficient to remove all residual solvent vapors in the source. Similarly, purging the source with dry air would also reduce back exchange from atmospheric moisture²⁴⁸. For many top-down and quench-flow HDX experiments, it may be more important to maintain the same deuterium content in the source as in solution. This could be done by first pre-equilibrating the source with a solvent consisting of the same percentage of deuterating and aqueous (quench) reagents as the samples that will be analyzed. Because many variables including instrument parameters, analyte, solvent, and source shape could affect the extent and pattern of residual solvent vapor HDX, we recommend that the undesired effects be tested prior to running a full HDX experiment to ensure minimal residual solvent vapor HDX.

2.6 Acknowledgements

This work was supported by the Welch Foundation, Grant AA-1899. The authors acknowledge the Baylor University Mass Spectrometry Center. The authors thank Amber Taylor for initial assessment of the mixing apparatus efficiency.

HJK and ESG developed the experimental design. HJK, OTL, and MRM conducted experiments and analyzed data. HJK and ESG wrote the draft and all authors approved the final manuscript.

CHAPTER THREE

Achieving Multiple Hydrogen/Deuterium Exchange Timepoints of Carbohydrate Hydroxyls Using Theta-Electrospray Emitters

Republished from Ref. 302 (Kim, H. J., Gallagher, E. S. Achieving multiple hydrogen/deuterium exchange timepoints of carbohydrate hydroxyls using theta-electrospray emitters. *Analyst*, **2020**, 145, 3056-3063) with permission from The Royal Society of Chemistry.

3.1 Abstract

Hydrogen/deuterium exchange coupled to mass spectrometry (HDX-MS) is a well-established technique for structural analysis of proteins. In HDX experiments it is common to label for multiple, different lengths of time to characterize protein structures and dynamics. However, applications of HDX to carbohydrates have been limited due to the rapid exchange rates of hydroxyls, which have also prevented the development and application of methods that sample HDX at multiple timepoints. Theta capillaries pulled to electrospray tips have been used to achieve microsecond reaction times. Here, we report the utilization of theta-ESI emitters to achieve multiple timepoints for deuteration of carbohydrates. We increased the labeling time for HDX by increasing the initial ESI droplet sizes using theta-ESI emitters with increasing tip opening sizes. The reaction times achieved by varying the tip sizes ranged from sub-microsecond to $\sim 20 \mu\text{s}$, with the average number of deuterium exchanges varying from $0.5 \pm 0.2 \text{ D}$ to $5 \pm 3 \text{ D}$ for sodium-adducted melezitose, which contains 11 labile hydrogens. Our findings are significant because this is the first report of carbohydrates analyzed by solution-phase HDX to achieve multiple H/D exchange timepoints.

3.2 Introduction

Glycosylation is a post-translational modification that affects protein folding and function.²⁶⁵ Glycans play significant roles in cellular communication and interactions, including in immune responses.²⁶⁶ Therefore, investigating the conformations of carbohydrates is crucial for analyzing glycoprotein activities as well as biological processes where glycans are directly involved. However, analysis of glycosylation is challenging due to isomeric monosaccharide subunits, branching, linkage, and anomericity, all of which lead to a highly heterogeneous glycome, or the total population of carbohydrates in cells.

Hydrogen/deuterium exchange (HDX) – mass spectrometry (MS) is a powerful technique that can be used to study structure, dynamics, and conformations of molecules. While mostly focused on protein analysis, HDX has also been used to characterize other biomolecules, such as oligonucleotides,²⁶⁷ aromatic compounds,²⁶⁸ and oligosaccharides.^{16, 100, 212, 223, 224, 246, 247, 269} For oligosaccharides, HDX has been utilized to label analytes in the solution-phase,²²³ in the gas-phase,²¹² and during ionization by electrospray (ESI)^{100, 224, 247, 269} or matrix-assisted laser desorption ionization (MALDI).²⁴⁶ The main challenge of performing HDX for carbohydrate analysis is the rapid exchange rate of hydroxyls. Using the traditional, bottom-up HDX method with a quench step, carbohydrates lose labels at hydroxyl groups from extensive back-exchange.^{178, 223} Additionally, HDX analyses of proteins involve comparing the rate of deuterium exchange for two or more different states following HDX for different lengths of time. These experiments enable HDX to sample dynamics and structural differences that may not be observed by measuring HDX for a single labeling time.²⁷⁰ However, the rapid

exchange rate of hydroxyls makes it difficult to achieve labeling for multiple time points. Previous studies, applying HDX to carbohydrates, have shown spectra following deuteration at specific conditions and a single labeling time. Yet, without these intermediate stages of deuteration, variations in carbohydrate structure and dynamics may not be observed during HDX.

To enable the future analysis of carbohydrate structures and dynamics, we aimed to develop a method to expand the exchange time window by rapidly labeling carbohydrates for different lengths of time. The ideal characteristics for such a method would be (1) simplicity in varying the labeling time and (2) a time scale that results in meaningful differences in the number of deuterium exchange events. If a setup can be adjusted only on a timescale that is too large to generate enough data points, compared to the exchange rate of the targeted functional groups, useful information could be lost between the two labeling states. Mixing apparatus have been developed to achieve short reaction times^{195, 200, 271, 272} but the microliter-per-minute flow rates typically used by such mixing apparatus lead to the accumulation of solvent vapors in the ionization source that can exchange with the rapidly exchanging functional groups.¹⁶ Further, this modifies the reaction time since HDX occurs both in solution and during ESI, rather than the time predicted by mixing in the apparatus. Alternatively, gas-phase HDX is a viable method for labeling many small molecules; yet, carbohydrate-metal complexes do not undergo HDX in the gas-phase.¹⁰⁰ Thus, an alternative to these methods is to perform solution-phase labeling in droplets during ESI.

Theta ESI emitters segregate two reactants until they are sprayed by ESI.²⁰⁷ The reaction times achieved by theta tips are on the micro- to millisecond timescale.^{252, 273}

Theta tips have been used to examine complex formation,^{207, 252} protein folding and unfolding,^{274, 275} redox reactions,²⁵² supercharging reactions,²⁷⁵ and identification of sites where ionization occurs in the course of ESI.²⁷⁶ Theta tips have also been used for HDX of peptides^{207, 208} and have been shown to label rapidly exchanging functional groups. Jansson *et al.*²⁰⁸ found that moving a theta tip away from the MS cone changed the time for the analyte to interact with D₂O before entering the mass spectrometer, which resulted in observable changes in analyte deuteration. Because theta ESI emitters provide rapid reaction times in the sub-second scale, theta tips enable sampling of HDX of rapidly exchanging functional groups at multiple time points. Here, we examine the use of theta tips for modifying the HDX labeling time of carbohydrates. We present results that vary the distance between the spray tip and the cone, the capillary voltage, and the tip size as parameters to modify the exchange time on a scale suitable for HDX of carbohydrate hydroxyls.

3.3 Methods

3.3.1 Materials

Melezitose, Leu- and Met-enkephalin, apomyoglobin, and cytochrome c were purchased from Sigma Aldrich (St. Louis, MO). Sodium acetate, ammonium acetate, and formic acid were purchased from VWR (Randor, PA). Deuterium oxide and trimethyl deuterated (D₉) choline were purchased from Cambridge Isotopes (Tewksbury, MA). Choline and GELoader pipet tips were purchased from Fisher Scientific International, Inc. (Pittsburgh, PA). All chemicals were used without further purification. Nanopure water was acquired from a Purelab Flex 3 purification system (Elga, Veolia Environment S. A., Paris, France).

3.3.2 *Sample preparation*

Melezitose and sodium acetate were dissolved in nanopure water at a 1:1 molar ratio (5 μM). The ionic strength of the deuterating reagent was matched to that of the sample by making 5 μM sodium acetate in D_2O . Choline (1 μM) or choline- D_9 (1 μM) was added to the melezitose and sodium acetate mixture or the sodium acetate in D_2O , respectively, to measure the relative signals from each channel of the theta tip during HDX experiments. Apomyoglobin and cytochrome c were prepared in nanopure water with 0.1% formic acid (pH 3.07).

3.3.3 *Open-Source Setup with Pulled Theta ESI Emitters*

Theta capillaries (Sutter Instrument, Novato, CA) were pulled to electrospray tips using a P-1000 micropipette puller (Sutter Instrument). To increase reproducibility of the sizes of pulled tips, the jaw temperature was cooled to room temperature between pulling each tip. The opening size of each tip was measured on a tabletop scanning electron microscope (SEM, TM3030Plus, Hitachi, Tokyo, Japan) by determining the longest length between the middle of the septum to the end of each channel (see Supporting Information, Figure B.1).

All experiments were performed on a Waters Synapt G2-S High Definition MS (Waters Corporation, Milford, MA). Pulled theta-ESI tips were mounted on a theta tip holder (Warner Instruments, Hamden, CT) which was secured on a custom-built setup on a XYZ stage (Thorlabs, Newton, NJ). Platinum wires (ADInstruments, Sydney, Australia) were inserted into each channel of the theta tip and voltage was supplied from the instrument source via alligator clips (see Supporting Information, Figure B.2). All

experiments were performed with an open source by overriding the source lock. No desolvation, nebulizer, or cone gas was used.

3.3.4 HDX Experiments

Melezitose in aqueous buffer and buffer in D₂O were loaded into each channel of the theta tip and sprayed at varying distances from the MS cone. Spray was generated by voltage alone, without backing pressure. Backing pressure is nitrogen gas applied to the back of the theta-tip channels, resulting in laminar flow. Voltage was increased in increments of 100 V to find the minimum voltage for generating spray. Once stable spray was generated, data was collected from the same tip at different voltages and/or distances from the cone. Thus, a single tip was used to collect data using multiple experimental parameters. After each set of experiments, tips were discarded. Experiments were run in quadruplet for small tips (< 1 μm each channel height) or replicates of n > 6 for large tips (> 5 μm each channel height).

3.3.5 Calculations and Data Presentation

The number of H/D exchange events (#D) were calculated by first obtaining the weighted, experimentally determined average m/z of undeuterated and deuterated [M + Na]⁺ (Equation 3.1) and then taking the difference of the two m/z values (Equation 3.2), where m/z is the mass-to-charge ratio and I is the intensity of each isotopic peak.

$$(m/z) = \frac{\sum(m/z) \cdot I}{\sum I} \quad \text{Equation 3.1}$$

$$\#D = (m/z)_{deuterated} - (m/z)_{undeuterated} \quad \text{Equation 3.2}$$

Data are presented as the average #D \pm standard deviation. Student's *t*-test or Welch's *t*-test at the 95 % confidence interval was used for statistical analyses. The choice of *t*-test was dependent on the results of an F test. When appropriate, deuteration was also presented as % D for melezitose, which contains 11 labile hydrogens (Equation 3.3).

$$\%D = \frac{(m/z)_{\text{experimental}} - (m/z)_{\text{theoretical,D0}}}{(m/z)_{\text{theoretical,D11}} - (m/z)_{\text{theoretical,D0}}} \times 100 \quad \text{Equation 3.3}$$

3.3.6 Protein Folding Experiments

To estimate the time of mixing in the droplets, protein folding experiments were performed, as described by Mortensen *et al.*^{252, 273, 274} Briefly, denatured proteins in acidified conditions were sprayed along with ammonium acetate from theta tips. The resulting mass spectra showed protein at a wide range of charge states, representing both folded and unfolded states. Using protein folding constants and the relative intensity of the folded and unfolded states, droplet lifetimes were calculated.

Denatured protein was prepared in 0.1% formic acid. To induce folding via mixing in theta-ESI, 100 mM ammonium acetate was prepared as folding buffer. Denatured proteins were sprayed (1) by themselves from the acidic solution, (2) with ammonium acetate in the other channel, or (3) in a premixed solution, containing the acidic solution and folding buffer at a 1:1 (v/v) ratio. The premixed solution represents an equilibrium condition in which the proteins have folded to the maximum extent possible in theta spray. The charge state distributions were used to calculate the folding state and reaction time using Equation 3.4, where τ is the protein folding time constant and A_e , A_0 , and A_f are the relative abundances of folded protein populations in the premixed

equilibrium condition, acidic condition, and experiment via theta-mixing, respectively. τ of apomyoglobin and cytochrome c are $7 \mu\text{s}$ ²⁷⁷ and $57 \mu\text{s}$,²⁷⁸ respectively.²⁷³

$$t = \tau \ln \left(\frac{A_e - A_0}{A_e - A_t} \right) \quad \text{Equation 3.4}$$

3.4 Results and Discussion

3.4.1 Orientation of the Theta Tip Results in Changes to the Ion Transmission from Each Channel

The theta capillary was positioned perpendicular to the direction of the MS cone, similar to the conventional Z-spray of Synapt instruments (Figure 3.1A, Figure B.2). An important difference between the theta-tip setup and the Z-spray is that theta tips generate two Taylor cones²⁰⁸ along paths parallel to each other. Thus, the distance from each Taylor cone to the MS cone varies depending on the orientation of the theta tip and may affect ion transmission from each barrel. To ensure maximum ion transmission from both channels of the theta tip, Leu- and Met-enkephalin were separately loaded in the two channels of theta tips and sprayed at varying tip orientations in respect to the cone by rotating the tip. As a control, a premixed sample with both Leu- and Met-enkephalin was loaded and sprayed from both channels to determine the relative signal intensity of the two peptides (Figure 3.1B). When the tip was in the “parallel” orientation, with the septum that divides the two channels parallel to the ground so that one channel was directly above the other, the relative signal intensity of the two peptides was close to the ratio observed for the premixed control (Figure 3.1C). On the other hand, when the tip was in the “perpendicular” orientation, with the septum perpendicular to the ground and the two channels were side by side, the signal intensity was stronger for the peptide

loaded into the channel that was closer to the MS cone (Figure 3.1D, 3.1E). Therefore, all further experiments were performed with the tip in the “parallel” orientation to minimize variables in the signal resulting from the relative position of the two channels.

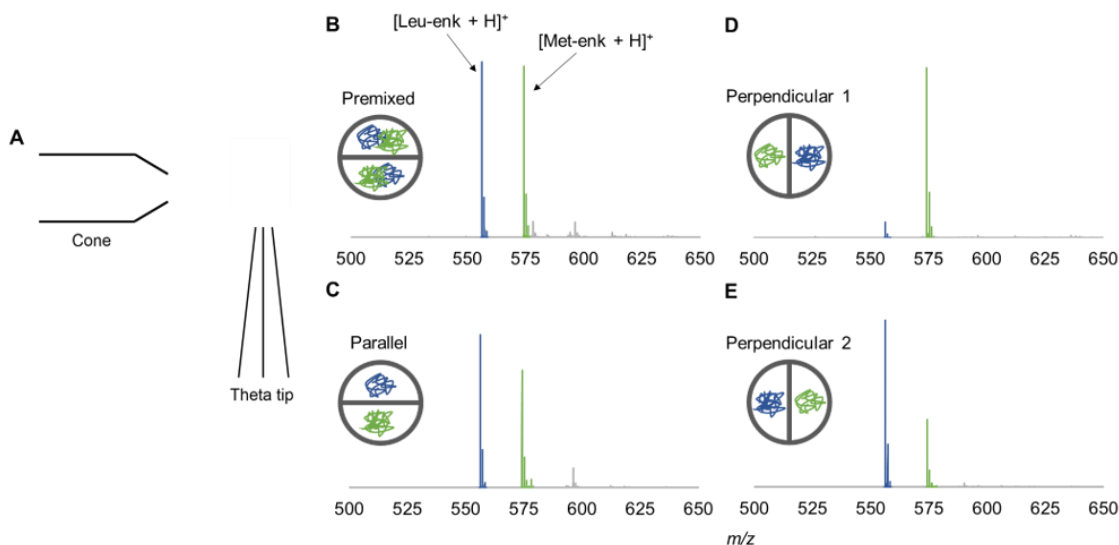


Figure 3.1. Representative mass spectra of Leu- and Met-enkephalin when varying the orientation of the theta tip with respect to the MS cone. The cone and the theta tip are positioned perpendicular to each other (A). The signal intensity of $[\text{Leu-enk} + \text{H}]^+$ peaks, colored blue, and $[\text{Met-enk} + \text{H}]^+$ peaks, colored green, is compared. A control sample, containing a mixture of both peptides, was sprayed to measure the relative intensity of the two peptides (B). Each peptide was then sprayed from a separate channel with the septum of the theta tip positioned either parallel to the ground (C) or perpendicular to the ground (D, E). In the parallel position, the distance between each of the two channels of the theta tip and the cone are approximately equal, but in the perpendicular positions, one of the channels is closer to the cone.

3.4.2 Minimal HDX is Observed for Carbohydrates When Varying the Applied Voltage or the Distance Between the Theta Tip and the MS Cone

Jansson *et al.* reported that the deuteration time in theta-tip-HDX experiments could be varied by changing the distance between the tip and the cone.²⁰⁸ An increase in the distance resulted in a longer droplet reaction time that increased the deuteration level of both phenethylamine and angiotensin I. Since angiotensin I has rapidly exchanging

functional groups that were deuterated to varying extents in these experiments; we hypothesized that changing the distance from the theta tip to the cone would alter the deuteration level of carbohydrate hydroxyls. The two channels of theta tips were loaded with either melezitose and sodium acetate in water or sodium acetate in D₂O and sprayed by applying voltage at 3, 4, or 5 mm from the cone. The average tip size for our experiments was 510 ± 40 nm ($n = 4$), which is similar to the theta tip sizes used in literature. Contrary to Jansson *et al.*'s findings, increasing the distance between the tip and the cone from 3 mm to 5 mm did not increase the #D exchanges (Figure 3.2A).

The HDX reaction time for carbohydrates is dependent on the time the analyte remains solvated in ESI droplets.¹⁰⁰ Because higher applied voltages result in higher electric fields between the theta tip and MS cone, the charged ESI droplets are expected to travel faster across the electric field at a higher voltage compared to at a lower voltage, which could decrease the time for interacting with D₂O. Thus, we measured the magnitude of HDX at varying capillary voltages. However, there was no correlation between the applied voltage and the number of H/D exchanges at the conditions tested (Figure 3.2B).

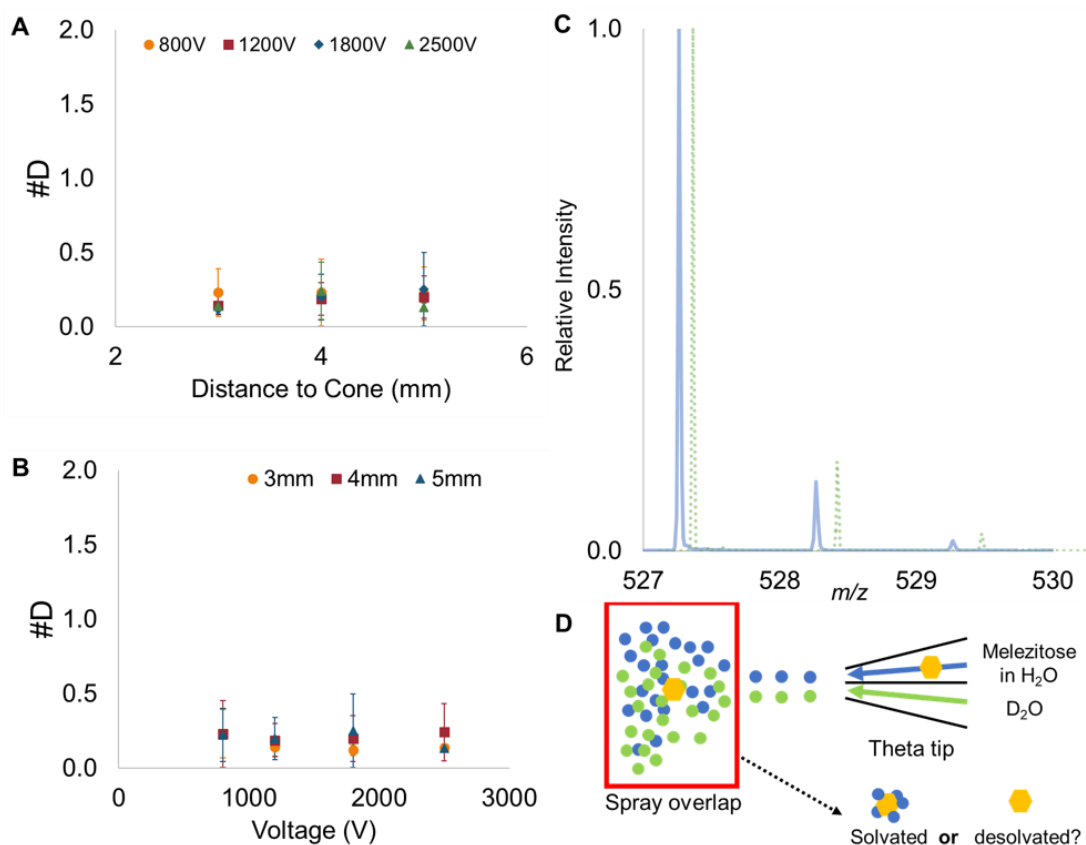


Figure 3.2. HDX of sodiated melezitose sprayed from theta tips with 0.5 μm channels. The average number of D exchanges ($n = 4$) versus (A) distance from MS cone or (B) applied spray voltage is plotted with error bars illustrating standard deviation. (C) Overlapped, representative mass spectra of undeuterated melezitose (blue, solid line) and deuterated melezitose (green, dashed line) via theta-tip HDX sprayed at 1800 V and 3 mm away from the cone. The two mass spectra have been offset to show relative intensities more clearly. The relative intensities of 0 D (m/z 527.2) and 1 D (m/z 528.2) in the two spectra are similar, illustrating the small magnitude of HDX. (D) Scheme of electro spray plumes generated by the two Taylor cones from theta tips. Because carbohydrate-metal complexes do not exchange in the gas-phase, the adducts must be solvated in the spray overlap region for HDX to occur.

The magnitude of HDX for our analytes was minimal (Figure 3.2C). Yet, Jansson *et al.* observed a distribution of 0 D to 5 D for angiotensin I after an HDX reaction time of 319 μs .²⁰⁸ Angiotensin I contains 17 labile hydrogens, including four rapidly exchanging functional groups. Furthermore, the peak associated with 2 D had the highest intensity and the level of deuteration was estimated at $\sim 50\%$ for angiotensin I.

Alternatively, we measured 2.2 % deuteration for melezitose, which is significantly lower. Liyanage and coworkers reported that HDX does not occur for sodium-adducted carbohydrates in the gas-phase.¹⁰⁰ Because the two plumes generated from the separate Taylor cones of a theta tip need to overlap for HDX to occur, we hypothesized that our metal-adducted analytes were desolvated by the time the spray plumes overlapped and thus exchange did not occur (Figure 3.2D). Therefore, we aimed to increase the droplet lifetime by increasing the initial ESI droplet sizes to increase the timeframe for HDX.

3.4.3 HDX Labeling Times and the Resulting Magnitude of HDX Can be Increased by Increasing Initial ESI Droplet Sizes

To force our analytes to be more solvated in the region where the spray plumes overlap, theta tips were pulled with new parameters to create larger openings, which generate bigger initial droplets and thus take longer to desolvate. Estimating the initial droplet sizes to be between 1/10 and 1/17 of the outer diameter of the ESI tip,^{252, 279} we selected theta tips with opening sizes that were expected to generate different droplet size distributions for HDX experiments (Table 3.1). Because there was more variation in the pulled tip sizes with bigger openings (> 10 μm), all tips were measured by SEM, and tips with similar sizes were selected for replicate experiments.

Table 3.1. Opening sizes of theta tips and estimated initial droplet sizes.^a

Measured opening Size (μm)	Initial Droplet Size Calculated as 1/17 Tip Size²⁷⁹ (μm)	Initial Droplet Size Calculated as 1/10 Tip Size²⁵² (μm)
0.51 \pm 0.04 (n = 4)	0.0299 \pm 0.002	0.051 \pm 0.004
4.6 \pm 0.4 (n = 5)	0.27 \pm 0.02	0.45 \pm 0.04
21 \pm 10 (n = 6)	1.2 \pm 0.6	2 \pm 1

^aData is represented as the average \pm standard deviation.

Previously, ESI droplet sizes have been measured.^{208, 280-282} However, to verify that the different tip sizes resulted in different droplet desolvation times, and thus different HDX labeling times, we experimentally measured droplet lifetimes by monitoring protein folding for proteins with known folding time constants.²⁷³ When sprayed from theta tips, denatured proteins are induced to fold by mixing with the folding buffer, which is observed in Figure B.3 based on the protein charge states. It was previously reported that protein folding reactions do not occur in the gas phase,²⁸³⁻²⁸⁷ therefore the protein folding reactions are limited by the droplet lifetimes. This observation is in agreement with the proposed ionization mechanism for folded proteins, the charged residue model (CRM),^{81, 91, 288} where the folded proteins remain solvated until the ESI droplets evaporate to dryness. Metal-adducted carbohydrates have also been reported to ionize by CRM⁹⁶ and to undergo limited HDX in the gas-phase.¹⁰⁰ Thus, measured droplet lifetimes represent the reaction times for both protein folding and the HDX exchange time for carbohydrates.

Apomyoglobin was used to calculate a droplet lifetime of $6 \pm 4 \mu\text{s}$ from the $4.6 \pm 0.4 \mu\text{m}$ channels ($n = 6$) and cytochrome c was used to calculate a droplet lifetime of $20 \pm 10 \mu\text{s}$ from the $20. \pm 9 \mu\text{m}$ channels ($n = 6$) (Table 3.2, Figure B.3). Mortensen *et al.* showed that the two proteins yield consistent results in calculating droplet lifetimes,²⁷³ so cytochrome c, which has a larger folding time constant, was used for theta tips with larger opening sizes. The lifetime of droplets from tips with $\sim 0.5 \mu\text{m}$ channels was not measured. However, previous reports from Mortensen *et al.* estimated the droplet lifetime to be $5 \mu\text{s}$ from theta tips with $1.5 \mu\text{m}$ channels and 5 psi backing pressure, with the minimum lifetime in the sub-microsecond range.²⁷³ Because our experiments were

performed with smaller tip sizes and no backing pressure, we expected our droplet lifetime from $\sim 0.5 \mu\text{m}$ tips to be faster than the fastest reaction time achieved by Mortensen *et al.* which was $1 \mu\text{s}$.²⁷³ Thus, we concluded that the droplet lifetimes from the three tip sizes were different (p of 0.04 when comparing the large- and intermediate-sized tips).

Table 3.2. Opening sizes of theta tips with measured droplet lifetimes and the average number of deuterium exchanges (#D).^a

Tip Opening Size for Protein Folding Experiments (μm)	Droplet Lifetime (μs)	Tip Opening Size for HDX Experiments (μm)	Average HDX (#D)
0.51 ± 0.04 (n = 4)	< 1 ^b	0.51 ± 0.04 (n = 4)	0.5 ± 0.2
4.6 ± 0.4 (n = 5)	6 ± 4	4.5 ± 0.4 (n = 7)	1.4 ± 0.7
20 ± 10 (n = 6)	18 ± 11	$20. \pm 9$ (n = 7)	5 ± 3

^aData is represented as the average \pm standard deviation.

^bSee Moretensen *et al.*,^{252, 273, 274}

The droplet lifetimes we obtained, between 6 and 20 μs , were orders of magnitude shorter than the reaction times achieved by Jansson *et al.* (319 μs).²⁰⁸ We hypothesize that the difference in droplet lifetimes is due to lower flow rates in our experiments, where only voltage was used to generate spray. It has been reported that increased backing pressure increases the flow rate, which generates larger initial ESI droplets^{280-282, 289, 290} with longer droplet lifetimes.²⁷³ Backing pressure would have been a useful parameter to vary our droplet lifetimes; however, the flow rate increased dramatically when backing pressure as low as 5 psi was applied to the intermediate and large tips. With the increased flow rate, the time available for data collection was greatly reduced to the extent that it was difficult to record data before the small sample volumes within each

tip were gone. Thus, tips with sizes from the two larger size distributions were used for HDX experiments without applying backing pressure.

The number of D exchanges increased significantly when the tip size was increased (Figure 3.3, Table 3.2). When sprayed from $0.51 \pm 0.04 \mu\text{m}$ tips, 0.5 ± 0.2 D was observed. The number of D exchanges increased to 1.4 ± 0.7 D when sprayed from $4.5 \pm 0.3 \mu\text{m}$ tips and 5 ± 3 D when sprayed from $20. \pm 9 \mu\text{m}$ tips. All three #D exchanges were statistically different from one another at the 95 % confidence interval (p of 0.01 when comparing the #D exchanges between the small and intermediate tips and p of 0.03 when comparing #D exchanges between the intermediate and large tips). The minimum voltage required to generate Taylor cones from small-, intermediate-, and large-tip sizes was 420 ± 50 V, 1160 ± 40 V, and 1700 ± 300 V, respectively. It is noteworthy that the extent of deuteration was significantly increased when sprayed from tips with sizes much greater than those that are conventionally used (typically 1 to 5 μm channels), and the change in the level of deuteration was also more distinctive when the tip sizes were varied compared to previously reported parameters, including the distance between the tip and the cone.

The standard deviation for #D exchanges increased with increasing tip size. We anticipate that ESI droplets sprayed from a single tip exhibit a distribution of sizes. However, when pulling the intermediate and large tips, we observed a greater range of opening sizes, $4.0 \mu\text{m} - 5.2 \mu\text{m}$ and $11 \mu\text{m} - 37 \mu\text{m}$, compared to $0.44 \mu\text{m} - 0.57 \mu\text{m}$ for the small tips. Thus, the variation in #D may also be due to the increased variation in tip-opening size associated with pulling the intermediate and large tips.

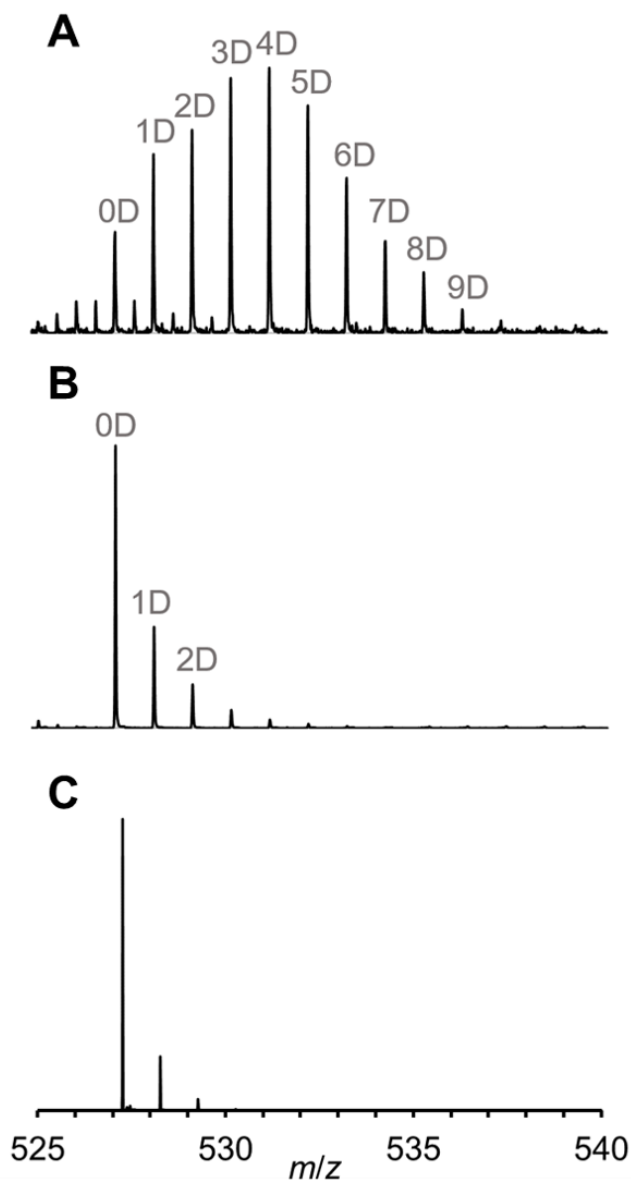


Figure 3.3. Representative mass spectra of deuterated, sodiated melezitose sprayed from theta tips with different sizes: (A) 28.22 μm , (B) 5.31 μm , and (C) 0.50 μm . Melezitose contains 11 labile hydrogens and the spectra show deuteration of (A) 3.44 D (31.06 % D), (B) 0.51 D (4.60 % D), and (C) 0.03 D (0.27 % D).

For a single theta tip, the opening sizes of each channel also varied. The average difference in the opening size of the two channels were $0.012 \pm 0.002 \mu\text{m}$, $0.2 \pm 0.1 \mu\text{m}$, and $0.7 \pm 0.7 \mu\text{m}$ for small, intermediate, and large tips, respectively. Therefore, the

initial droplet sizes generated from each channel of the same tip may have differed. Reactions resulting from collisions of droplets with different initial sizes could result in different mixing ratios of H₂O and D₂O. For instance, HDX via large tips resulted in distributions of melezitose with deuteration levels higher than 50%, including one population with 9.6 D, corresponding to 87% deuteration. Thus, deuteration levels higher than 50% may be attributed to uneven mixing in the droplets because of variation in the initial droplet sizes.

The voltages used for the large tips may also have contributed to variations in deuteration levels. The minimum voltage required to generate spray (*i.e.* E_{onset}) was used for each tip, and E_{onset} is dependent on tip size.^{291, 292} Because our experiments utilized electroosmotic flow, the velocity of the solutions through the channels of the theta tips depend on the applied electric field.²⁹³ The higher electric fields generated from higher applied voltages, which are necessary to generate spray from bigger tips, are expected to result in faster flow rates. It has been reported that higher flow rates lead to larger droplets.^{273, 280-282, 289, 290} Because the minimum voltage to generate spray was determined for both channels based on the observation of melezitose signal, the E_{onset} for channels containing D₂O may be different. It has been reported that changes in voltage can also affect the spray mode and shape,²⁹⁴ affecting the overlap region of the two spray plumes generated from the two channels of the theta tip when high voltage is used. Deuteration levels higher than 50% may have resulted from multiple collisions between droplets containing melezitose and droplets of D₂O, that could vary with the different electrospray mode and spray plume shapes for each tip. While the relative flow rate of the two channels were monitored using choline and deuterated choline, the signals were

inconclusive in monitoring differences in flow rates from the two channels due to the presence of one labile proton on each molecule. However, even with these factors, we measured statistically different deuteration levels for metal-adducted melezitose when HDX was performed from theta tips with different opening sizes.

3.5 Conclusions

Increasing the diameter of theta tips effectively increases the deuteration level of melezitose. To our knowledge, this is the first report describing multiple HDX reaction times for carbohydrate hydroxyls. This finding is significant because of the unique characteristics of metal-adducted carbohydrates, which do not undergo deuterium exchange in the gas phase, but which contain rapidly exchanging hydroxyls. Thus, the analytes must be solvated to observe deuterium labeling. Our main strategy to altering the deuteration time was to change the initial ESI droplet size, which resulted in different desolvation times, at the end of which, the HDX reaction was quenched because the carbohydrate-metal complexes were released into the gas-phase. The reaction times achieved with HDX using theta tips ranged from less than 1 μ s to an average of 20 (\pm 10) μ s, resulting in a maximum of \sim 87 % deuteration for melezitose.

HDX of metal-adducted carbohydrates, using theta tips, is advantageous for achieving multiple exchange timepoints for rapidly exchanging functional groups because the exchange time is defined by the droplet lifetimes. The relationship between theta-tip size and droplet lifetime is measurable. Moreover, the deuteration time was altered on a timescale that resulted in significant changes to the deuteration level that were distinctive from one another. The achievement of multiple deuteration stages is a crucial step towards structural and dynamic analysis of carbohydrates because the

intermediate deuteration can distinguish functional groups that undergo exchange at different rates. Therefore, we conclude that changing the size of the initial ESI droplet is an effective approach to achieving multiple exchange timepoints for HDX of metal-adducted carbohydrates via theta tips, given the special consideration that our analytes only undergo HDX when solvated. We expect that by expanding our strategies to perform HDX for carbohydrates, we will enable analyses of the biological structures of carbohydrates and glycans.

3.6 Acknowledgements

This work was supported by the Welch Foundation, Grant AA-1899. The authors acknowledge the Baylor University Mass Spectrometry Center and Baylor University Center for Microscopy and Imaging. The authors thank Mr. Joseph Gallagher for building the theta tip holder setup.

CHAPTER FOUR

Deuterium Localization with Minimal Scrambling on Carbohydrate-Metal Complexes via Collision Induced Dissociation

This chapter is prepared for publication in *Analytical Chemistry* as: Kim, H. J., McCutcheon, M. E., Calixte, E. I., Gallagher, E. S. Deuterium Localization with Minimal Scrambling on Carbohydrate-Metal Complexes via Collision Induced Dissociation

4.1 Abstract

Carbohydrate structures and conformations are a crucial part of cell biology that dictate many aspects of glycoprotein function. However, carbohydrates are complex biomolecules made up of isomeric monosaccharide subunits, and mass spectrometry (MS) analysis of carbohydrate structures is often limited to sequencing. Hydrogen/deuterium exchange (HDX) coupled to MS is a powerful technique for investigating the structures and dynamics of proteins. While HDX-MS has been previously applied to the analysis of carbohydrates, only global information has been obtained, with no local deuterium assignment. In this paper, we present a novel method to localize deuterium labels on deuterated carbohydrates. Collision induced dissociation (CID) of sodium-adducted melezitose revealed that isomeric B/Z- and C/Y-type fragments were detected at different deuteration levels with limited scrambling. By investigating the conformations of carbohydrate-metal complexes from DFT optimized structures, the fragmentation pathways of sodium-adducted melezitose were predicted to track deuterium labels. The hydrogen/deuterium labels were assigned based on the

difference in exchange rates of primary and secondary hydroxyls. To our knowledge, our report is the first localization of deuterium labels on carbohydrates.

4.2 Introduction

Carbohydrates are a class of biomolecules that are involved in a variety of cellular activities, including protein folding and function²⁶⁵, cell-cell communication, and immune responses against foreign agents.²⁹⁵ Therefore, understanding the structures of carbohydrates and their impact on cell biology is a crucial part of interpreting cellular behaviors. Carbohydrates are composed of isomeric monosaccharide subunits that generate a multitude of possibilities for polysaccharide structures with varying linkage sites and stereochemistry. Such structural diversity and heterogeneity have posed challenges in glycan analysis. Techniques have been developed to separate and differentiate isomers^{124, 296-298} and anomers^{171, 299} as well as linkage patterns.^{298, 300, 301} While identifying glycan sequences has been a primary focus, the three-dimensional conformations of glycans are also significant for glycan-protein interactions.

Hydrogen/deuterium exchange coupled to mass spectrometry (HDX-MS) is a well-established technique utilized for analysis of protein conformations and dynamics. HDX reactions are initiated in solution, during ESI, or in the gas phase to label labile (*e.g.* exchangeable) hydrogens, such as hydroxyls or amides, by introducing deuterating reagents to the analytes. The deuteration time can be varied to observe changes in deuteration at a given site to examine the dynamics of the analyte. The differences in deuteration between multiple sites of an analyte at a given deuteration time can also provide insight into the structure of the analyte. However, applications of HDX-MS to carbohydrates is challenging due to the rapid exchange rates of hydroxyls. Recent

publications of HDX-MS of carbohydrates have focused on differentiating carbohydrate isomers by performing in-ESI^{224, 225} or gas-phase HDX.^{212, 227} HDX time window of hydroxyls has been expanded to sample multiple deuteration timepoints by changing the initial ESI droplet sizes via theta-emitters³⁰² or by varying solvent conductivity.²²⁵ While these methods are promising for HDX analysis of carbohydrates, only global deuteration levels were analyzed. Assignment of deuterium labels to local regions of carbohydrates would enable analysis of carbohydrate conformations and interactions with metals or proteins that are significant in cellular behaviors.

Local information is often obtained via fragmentation in MS. Collision induced dissociation (CID) is one of the most common fragmentation techniques, including for peptides and carbohydrates. While CID is readily available on many commercial and custom-built instruments, the vibrational activation from multiple collisions during the CID process is associated with a phenomenon called “scrambling,”³⁰³⁻³⁰⁵ or the random redistribution of hydrogens across the analyte. This is problematic in HDX experiments because it may affect the interpretation of HDX measurement by assigning labels at the wrong locations.^{186, 306} Electron-based fragmentation techniques, such as electron capture dissociation (ECD) and electron transfer dissociation (ETD), are known to cause less scrambling as the bond dissociation occurs on a faster timescale compared to CID.³⁰⁷ However, use of ECD is limited to Fourier-transform ion cyclotron resonance (FT-ICR) instruments because of the ability to effectively trap both gas-phase ions and electrons. ETD is compatible with other types of MS, but still less accessible than CID. A method that utilizes CID would be advantageous because it can be easily performed in any tandem MS instrument as opposed to ETD or ECD. CID of sodium-adducted peptides has

been shown to reduce scrambling.³⁰⁸ Therefore, we present a CID-based method to localize deuterium labels on carbohydrates with metal adducts as charge carriers. To our knowledge, our findings are the first report to investigate scrambling of deuterated carbohydrates. We observe differences in deuteration levels between fragments generated from carbohydrate-metal complexes. Such differences are minimized in deprotonated carbohydrates which are known to experience hydrogen migration³⁰⁹, indicating that limited scrambling was observed for sodiated carbohydrates. We were able to identify the sources of labile hydrogens contributing to the differences in deuteration levels between fragments by combining previously published carbohydrate fragmentation mechanisms³¹⁰ and electronic structure calculations. Thus, our findings illustrate the potential of HDX-MS/MS to detect local conformational changes of carbohydrates.

4.3 Methods

4.3.1 Materials

Melezitose was purchased from Sigma Aldrich (St. Louis, MO). Acetate salts were from VWR International (Randor, PA). Deuterium oxide (D₂O, 99.96% purity) and deuterated methanol (CH₃OD, or MeOD, 99% purity) were from Cambridge Isotope Laboratories INC. (Tewksbury, MA). Mixtures of carbohydrate and sodium or calcium acetate were prepared at a 1:1 molar ratio in 25%, 50%, or 75% water with D₂O or methanol (MeOH) with deuterated methanol (MeOD). Deprotonated carbohydrates were analyzed by ionizing the carbohydrate sample with sodium acetate in negative-ion mode. Sample conductivity was measured using an Orion 013005MD DuraProbe 4-Electrode

conductivity cell probe coupled to an Orion Star A215 conductivity meter (Thermo Scientific, Waltham, MA).

4.3.2 Collision Induced Dissociation

All experiments were performed on a Waters Synapt G2-S High Definition Mass Spectrometer equipped with a LockSpray Exact Mass Ionization Source (Waters Corporation, Milford, MA). Data collection began after ~5 minutes of sample infusion to equilibrate the ESI source with matching solvent composition and reduce variability from residual solvent and atmospheric moisture, following a previously published protocol.¹⁶ CID was performed on deuterated carbohydrates by isolating each mass-to-charge (m/z) peak in the deuterated distribution. The LM Res parameter was increased from a default of 4.9 to 15.0 to get narrower isolation windows and thus more compact distributions from each isolated m/z (Figure C.1). The collision energy was optimized for each carbohydrate-charge carrier pair to achieve high fragmentation efficiency. Specifically, CID was performed on sodium-adducted or deprotonated melezitose by increasing the collision energy in increments of 4 V, and on calcium-adducted melezitose in increments of 2 V. Ranges of collision voltages at which >80% fragmentation was achieved and the precursor, C₂/Y₂, and B₂/Z₂ fragments were detected at high intensity were selected for HDX experiments. The collision voltages selected were 24 – 36 V, 4 – 10 V, and 20 V for sodium-adducted, calcium-adducted, and deprotonated melezitose, respectively.

4.3.3 Calculations and Data Presentation

To obtain the deuteration levels of precursor and fragment ions generated from CID, the weighted average m/z of fragments from undeuterated and fully deuterated melezitose were first calculated from the equation:

$$m/z_{weighted} = \frac{\sum(m/z) \cdot I}{\sum I} \quad \text{Equation 4.4}$$

Where I is the intensity of each peak. By acquiring the weighted average of fully deuterated melezitose and its fragments, the number of labile hydrogens on each fragment was determined and confirmed with known structures reported by literature and predicted by GlycoWorkbench.³¹¹ Once m/z_{D0} and m/z_{Dmax} were established, the deuteration level of fragments from HDX experiments were obtained by calculating the weighted average of fragments and subtracting m/z_{HDX} from m/z_{Dmax} and converting to % deuteration (%D) (Equation 4.2).

$$\%D = \frac{m/z_{Dmax} - m/z_{HDX}}{m/z_{Dmax} - m/z_{D0}} \times 100 \quad \text{Equation 4.2}$$

Because each fragment had different numbers of labile hydrogens and the number of deuterium labels could not be compared against each other, all deuteration levels of fragments are reported as %D. The average %D of each fragment was plotted as a scatter plot against %D of the precursor ion with error bars as standard deviation ($n = 12$). Welch's t -test was performed to verify statistical differences in deuteration levels between fragments at the 95% and 99% confidence interval as outlined by Hageman and

Weis.³¹² The Hageman and Weis approach of statistical significance testing was adapted to avoid overinterpretation of false positives that could result from *t*-tests alone.

For comparison of samples from different conditions, for instance obtained from varying collision voltages, the equality of regression coefficients³¹³ test was performed to compare the slopes of percent deuterations.

4.3.4 Energy Calculations for HDX of Carbohydrate Hydroxyls

We used the Gaussian 16 platform to calculate ground state energies with the B3LYP method and 6-311G++ basis set. To reduce computational costs, systems were constructed using glucose surrounded by one solvation shell of ten water molecules with varying percentages of D₂O (10-100%) and one sodium ion. We then calculated the difference in total energy before and after deuterium exchange. From this data, we constructed energy diagrams for exchange and compared how the amount of D₂O, hydroxyl location, and location of the metal ion affected the energetics of HDX.

4.3.5 Molecular Dynamics and Electronic Structure Calculations of Sodium-Adducted Melezitose

The GROMACS package³¹⁴ was used for molecular dynamics (MD) simulations of ESI droplets following previously published protocols.⁹⁶ Briefly, molecular structures for melezitose were built and optimized using Glycam-Web³¹⁵. A 3 nm-radius methanol droplet (1673 ± 2 solvent molecules) containing a melezitose molecule and ten sodium ions was placed in vacuum and was energy-minimized. Following minimization, the equilibration step was initiated with random assignment of velocities to the system, generated from a Maxwell-Boltzmann distribution. During equilibration, a flat-bottomed spherical potential was used to prevent the solvent from evaporating from the droplet.

Following equilibration, the production phase, involving solvent evaporation and ion ejection, was performed with the exclusion of the flat-bottomed potential. Konermann's code^{316,317} was used to remove any methanol or ions that had evaporated from the droplets, and to automate equilibration of the droplets between runs. During the production run, methanol evaporated from the droplet and the charge density increased until the Rayleigh limit was reached, at which point, solvated sodium ions were ejected from the droplet. Successions of solvent evaporation and ion ejection events occurred, until a solvent-free adduct of melezitose bound to metal was obtained. Ten independent trials were performed, from building the initial droplets to adduct formation in the gas phase, to obtain multiple carbohydrate conformations. Output structures from the MD simulations were then used as input structures for structure optimizations and frequency calculations of gas-phase [melezitose + Na]⁺ ions using DFT calculations with B3LYP method and 6-311G++ (d) basis set.

4.4. Results and Discussion

4.4.1 Glycosidic Bond Cleavage Mechanisms Can be Used to Localize Deuterium Labels on Sodium-Adducted Melezitose Fragments

Sodium-adducted melezitose generated fragments at five different m/z (Figure 4.1A), four resulting from glycosidic bond cleavage and one from a combination of cross-ring and glycosidic bond cleavage (Figure 4.1B). Because of the isomeric nature of carbohydrates, each m/z may have more than one population of structures. Isotopic labeling such as ¹³C- or ¹⁸O-labeling was not viable since melezitose is a non-reducing sugar, and thus, was not performed. However, melezitose fragments are labeled as both A/B/C and X/Y/Z according to Domon and Costello nomenclature¹⁵⁵ to highlight

possible isomeric species. While B and Y or C and Z fragments are produced from the same glycosidic bond cleavage in pairs, B and Z fragments from melezitose share the same chemical composition and structure as do C and Y fragments because the glycosidic oxygen is retained for C and Y fragments and lost for B and Z fragments (Figure 4.1B).

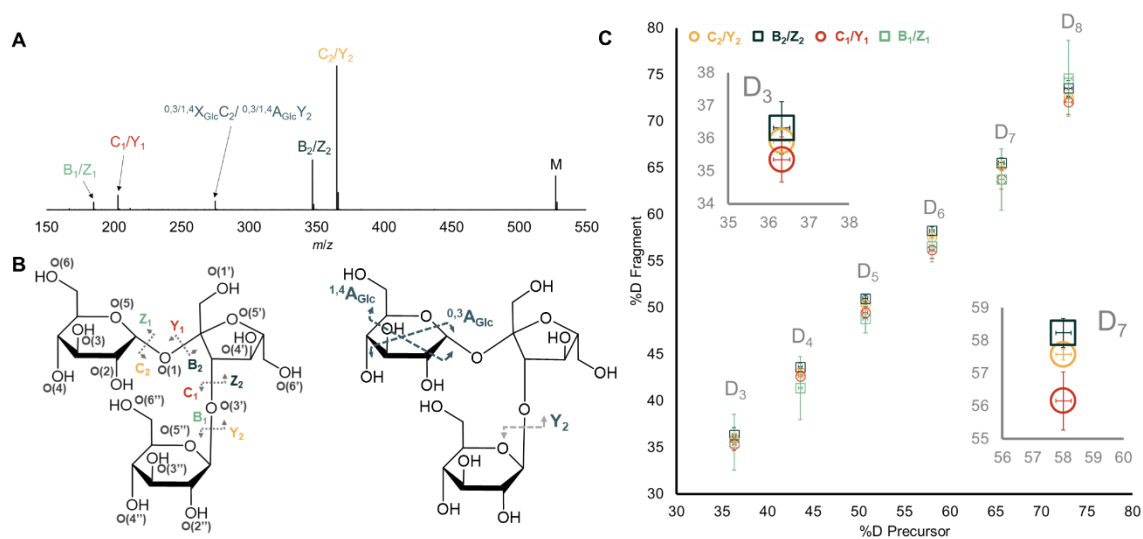
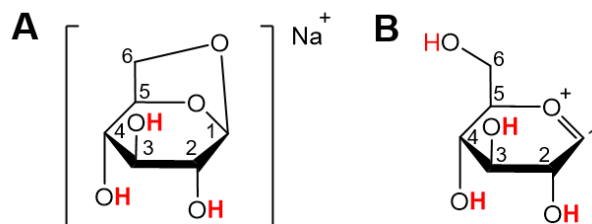


Figure 4.1. (A) Fragmentation spectrum of sodium-adducted melezitose and (B) structures of fragments with labeled hydroxyl positions. Isomeric species are annotated with the same color. (C) Deuteration plot of fragments from sodium-adducted melezitose in 50% D₂O. Each cluster of datapoints sharing the same %D precursor was generated from isolating each *m/z* peak in the distribution of deuterated analyte. Only fragments from glycosidic bond cleavages are shown. Insets show a comparison of B₂/Z₂, C₂/Y₂, and C₁/Y₁ at D₃ and D₇ to show the difference in deuteration level between the three fragments. The difference in deuteration levels between the three fragments increases at higher %D precursor.

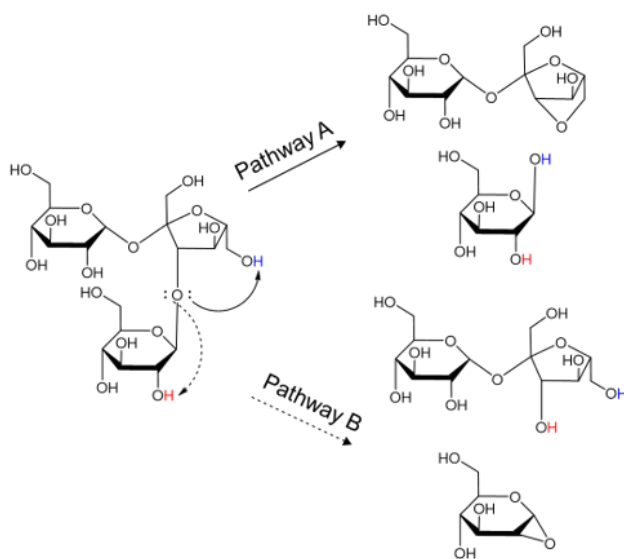
Upon comparing deuteration levels between fragments from sodium-adducted melezitose in 50% D₂O, a trend was observed where B₂/Z₂ fragments were detected with higher levels of deuteration (73.5 ± 0.8 %) compared to C₂/Y₂ fragments (72.6 ± 0.2 %). This trend was more pronounced when isolating higher %D precursor (Figure 4.1C). Fragmentation of sodium-adducted melezitose in 25% and 75% D₂O also revealed the

same pattern of deuteration between B₂/Z₂ and C₂/Y₂ fragments (Figure C.2). Therefore, we present representative data collected in 50% D₂O.

Bythell *et al.*³¹⁰ reported B and Z fragment structures that contained stacked-rings that formed by a bridge between the primary hydroxyl at the O(6) position and the bare carbon from C-O glycosidic bond cleavage (Scheme 4.1A). This structure has one less labile hydrogen than the B/Z fragments from protonated carbohydrates, which contain a carbonyl group (Scheme 4.1B).¹⁵⁵ Fragmentation of the fully deuterated [Melezitose + Na]⁺ complex supported the Bythell structure (Figure C.3), suggesting that there is a hydrogen-transfer reaction from B and Z type fragments to Y and C type fragments, respectively (Scheme 4.2). It is proposed that glycosidic bond cleavage is initiated from protonation of a glycosidic oxygen.^{155, 310} For CID of cation-adducted carbohydrates, the hydrogen is likely supplied from a hydroxyl within the carbohydrate-metal complex.³¹⁰ Because our carbohydrates are in a mixture of H₂O and D₂O, protonation of the glycosidic oxygen may be achieved by transfer of either hydrogen or deuterium.



Scheme 4.1. Structures of B-type fragments proposed by Bythell³¹⁰ (A) and Domon and Costello¹⁵⁵ (B). The labile hydrogens are highlighted in red. The sodium-adducted, stacked-ring structure (A) has one less labile hydrogen than the oxonium ion (B). The (A) structure shown above illustrates the B fragment from the non-reducing end, with the C-O cleavage occurring at the O(1) position, the same structure also predicts the isomeric Z fragment for melezitose because both terminal glucoses in melezitose have glycosidic bonds formed at the O(1) positions.



Scheme 4.2. Proposed scheme for movement of hydroxyl hydrogens during CID fragmentation of melezitose with structures of B_2/Z_2 (Pathway A, top), C_1/Y_1 (Pathway A, bottom), C_2/Y_2 (Pathway B, top), and B_1/Z_1 (Pathway B, bottom). Two of the hydrogens proposed to protonate the glycosidic oxygen are highlighted in red and blue. Initially, the two hydrogens are located on different monosaccharide subunits. After hydrogen is donated to the glycosidic oxygen and the glycosidic bond dissociates, the hydrogens migrate to C/Y fragments.

We hypothesize that the difference in deuteration level we observed between B_2/Z_2 fragments versus C_2/Y_2 fragments resulted from differences in the transfer of either a hydrogen or a deuterium for the glycosidic bond cleavage reactions. Bythell *et al.* proposed that in gas-phase sodium-adducted lactose, the primary hydroxyl at the O(6) position donates the hydrogen to the glycosidic oxygen.³¹⁰ Reports by Bekiroglu *et al.* show that the primary hydroxyls at O(6) positions of cyclodextrin and maltoheptaose have proton exchange rates that are five to six times faster than those of secondary hydroxyls at O(2) and O(3) positions.³¹⁸ We expect that melezitose, prepared in D_2O , undergoes back-exchange, or loss of deuterium labels back to hydrogen, during ESI due to the presence of atmospheric moisture. If a primary hydroxyl, with its faster exchange

rate and having back-exchanged to hydrogen during ESI, protonates the glycosidic bond and initiates fragmentation, transfer of a hydrogen would contribute to a relatively higher deuteration level for B/Z fragments that gave up a hydrogen instead of a deuterium. Conversely, the transfer of hydrogen would lead to a relatively lower deuteration level for C/Y fragments that received a hydrogen instead of a deuterium. On the other hand, a secondary hydroxyl, with its slower exchange rate compared to the primary hydroxyl, may have a higher likelihood of retaining deuterium labels than a primary hydroxyl. If a secondary hydroxyl donates to the glycosidic oxygen, the opposite trend for deuteration levels of B/Z and C/Y fragments is expected. Thus, we hypothesize that the difference in exchange rates between primary and secondary hydroxyls are reflected in the differential deuteration levels of B/Z and C/Y fragments.

We expect that the observation of faster exchange rates with primary hydroxyls compared to secondary hydroxyls³¹⁸ is applicable to our melezitose system as well. Thus, the exchange rates of the primary and secondary hydroxyls were not directly measured from HDX-MS of melezitose. Rather, the energy associated with H/D exchange of carbohydrate hydroxyls, both primary and secondary, was obtained via ground state energy calculations. Instead of melezitose, which is a trisaccharide, a glucose molecule was used as a model system to reduce computational cost. For both primary and secondary hydroxyls of neutral glucose, the forward HDX reaction was found to be slightly exothermic, with a primary hydroxyl releasing an average of -0.058 ± 0.002 kcal/mol and a secondary hydroxyl releasing an average of -0.074 ± 0.002 kcal/mol post-exchange ($n = 10$ at varying percentages of D₂O). While the difference in energy between the two functional groups is minimal for neutral glucose, the energetics associated with

HDX increases when charge is added to the system. When a sodium ion was introduced to interact with a secondary hydroxyl of glucose, the energy release associated with HDX of the interacting secondary hydroxyl was -1.94 ± 0.02 kcal/mol. On the other hand, the energy change of HDX for a primary hydroxyl neighboring the secondary hydroxyl became endothermic, with the energy post-exchange $+0.143 \pm 0.005$ kcal/mol higher than the energy before exchange. The difference in average release of energy between the primary and secondary hydroxyls was 2.09 kcal/mol, or 8.73 kJ/mol, favoring deuterium labels at the secondary hydroxyl, which was adducted to sodium.

There is evidence that interactions between metal ions and hydroxyl oxygens result in increased O-H bond lengths^{319, 320}, so the energy difference may be a result of the Na-O bond rather than the thermodynamics of the functional groups themselves. Therefore, we repeated the HDX calculations with the sodium ion adducted to the primary hydroxyl and compared the energies of HDX with the neighboring secondary hydroxyl. Again, the release of energy associated with the hydroxyl interacting with the sodium ion was greater, with -0.080 ± 0.003 kcal/mol for the primary hydroxyl interacting with sodium and -0.030 ± 0.002 kcal/mol for the neighboring secondary hydroxyl, both reactions being exothermic. However, the difference in the average energies between the two hydroxyls was only 0.05 kcal/mol, compared to 2.09 kcal/mol when the sodium ion was adducted to secondary hydroxyls. Therefore, we conclude that while metal adduction contributes to deuterium retention of carbohydrate hydroxyls in solution, the deuterium label is more stable at secondary hydroxyls compared to primary hydroxyls. Our data supports the experimental observations from differences observed between B₂/Z₂ and C₂/Y₂ fragments and the hypothesis that primary hydroxyls are more

likely to have a hydrogen rather than a deuterium. Because deuterium at secondary hydroxyls was energetically more favorable than at primary hydroxyls, the back-exchange in ESI likely occurred at primary hydroxyls first.

While B_2/Z_2 and C_2/Y_2 fragments differ by one hydroxyl and a labile hydrogen, the hydrogen that was transferred to C_2/Z_2 is not the same hydrogen that B_2/Z_2 fragments lost. For melezitose, glycosidic bond cleavage generates two fragments, one with one monosaccharide subunit, such as B_1/Z_1 or C_1/Y_1 , and one with two monosaccharide subunits, such as B_2/Z_2 or C_2/Y_2 . Therefore, the hydrogen from B_2/Z_2 fragments that protonated the glycosidic oxygen and initiated C-O bond dissociation is transferred to C_1/Y_1 fragments rather than C_2/Y_2 fragments. The details of statistical testing are presented in Appendix C. B_2/Z_2 fragments were detected at statistically higher levels of deuteration than C_1/Y_1 fragments, which were produced from the same glycosidic bond cleavage sites. This observation was true across the entire %D precursor distribution, ranging from 1.0 – 2.4 % higher deuteration levels for B_2/Z_2 . On the other hand, there was no statistical difference in the percent deuteration levels of B_1/Z_1 and C_2/Y_2 fragments (Figure 4.1C, Tables C.1-3), although this pair of fragments are generated from the same glycosidic bond cleavage. The high standard deviation observed for B_1/Z_1 fragments, ranging from 2 – 4 % in samples prepared in 50% D_2O , may be attributed to lower signal intensity and/or multiple isomeric species with different deuteration levels, representing more structures associated with a single fragment. Additionally, the hydrogen that is transferred during glycosidic bond cleavage reactions which results in production of B_1/Z_1 and C_2/Y_2 fragments may not be from a primary hydroxyl but rather a secondary hydroxyl. Whereas the fragmentation process generating B_2/Z_2 and C_1/Y_1 is

likely initiated by donation of hydrogen from the five-membered fructose, the glycosidic bond cleavage that produces B₁/Z₁ and C₂/Y₂ is likely initiated by donation of hydrogen from either of the two glucoses in the terminal positions.

To examine how close each hydroxyl is to each glycosidic oxygen in the gas phase, and thus how likely each is to protonate the glycosidic oxygen and cause C-O bond dissociation, ten structures of sodium-adducted melezitose were optimized by DFT calculations. For all ten structures, the sodium ion was found located in the middle with the trisaccharide wrapping around the metal. All ten structures revealed that the primary hydroxyls on the glucose units were pointing outward (Figure C.4), and the average distance between the hydrogen of the primary hydroxyls to the nearest glycosidic oxygen was $6.0 \pm 0.4 \text{ \AA}$, making it unlikely that the glycosidic oxygens were protonated by the primary hydroxyls of the terminal glucose units. Therefore, proton transfer from B₁/Z₁ to C₂/Y₂ fragments was more likely achieved from secondary hydroxyls rather than from primary hydroxyls. On the other hand, the primary hydroxyls on the middle fructose ring, particularly at the O(6')H position, were closer to the glycosidic oxygens ($4 \pm 1 \text{ \AA}$), compared to the secondary hydroxyl at the O(4')H position ($5.0 \pm 0.3 \text{ \AA}$) (Figure C.4). Such difference in primary compared to secondary hydroxyl contribution is significant because of the differences in exchange rates. We found that C₂/Y₂ fragments are detected at higher levels of deuteration compared to C₁/Y₁ fragments, ranging from 0.5 – 1.4 % higher percent deuteration for the C₂/Y₂ fragments. Therefore, we hypothesize that the primary hydroxyls more likely donated a hydrogen rather than a deuterium, contributing to lower deuteration levels for C₁/Y₁ fragments. Similarly, higher deuteration levels for C₂/Y₂ fragments, which were generated from proton transfer reactions from secondary

hydroxyls, suggests that the secondary hydroxyls donated deuterium at a higher percentage than primary hydroxyls. Conversely, C₂/Y₂ likely received a higher percentage deuterium from secondary hydroxyls than C₁/Y₁ fragments did from primary hydroxyls, contributing to higher percent deuteration. In turn, the observation of varying deuteration levels for sodium-adducted fragments that aligns with different exchange rates of primary and secondary hydroxyls suggests that deuterium labels are retained in place without scrambling.

4.4.2 HDX-CID MS of Calcium-Adducted Melezitose Reveals Minimal Differentiation Between Fragments

Carbohydrates have traditionally been analyzed by adducting to varying metal ions to achieve different fragmentation patterns and gas-phase structures.^{127, 156, 321-323} While obtaining different fragmentation patterns by adducting to other metals may offer new insights to carbohydrate structures, only sodium ions have been reported to reduce scrambling in peptides.³⁰⁸ To investigate the effect of different metal adducts on HDX and scrambling of carbohydrates, our experiment was repeated by fragmenting calcium-adducted melezitose. Doubly- and singly-charged species were observed, as [Fragment + Ca]²⁺ and [Fragment + Ca - H]⁺, respectively (Figure 4.2A). CID of calcium-adducted melezitose produced doubly-charged internal cleavage products at three different *m/z*, including one that was observed from sodium-adducted melezitose (Figure 4.1B) and two that were unique to calcium-adducted melezitose (Figure 4.2B).

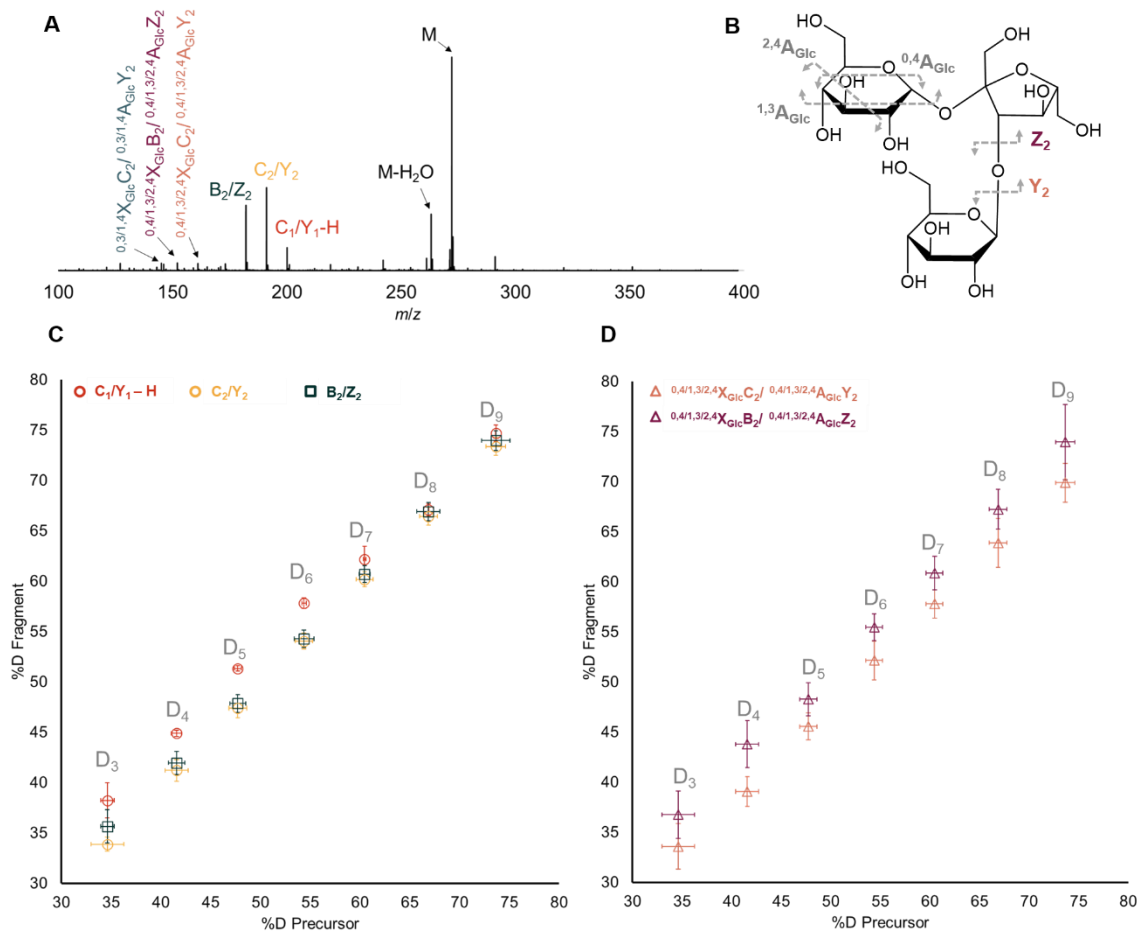


Figure 4.2. (A) Fragmentation spectrum of calcium-adducted melezitose and (B) structures of internal cleavage fragments. The two fragments have common cross-ring cleavage sites but different glycosidic bond cleavage sites. Structures of other fragments commonly generated from sodium-adducted species, including C_2/Y_2 , B_2/Z_2 , C_1/Y_1 , B_1/Z_1 , and $^{0,3/1,4}(X/A)_{Glc}(C/Y)_2$, are shown in Figure 4.1. Deuteration plots of fragments from calcium-adducted melezitose in 50% D_2O resulting from (C) glycosidic bond cleavage and (D) internal cleavage. For both fragment pairs shown in (C) and (D), the doubly-charged fragments with B_2/Z_2 glycosidic bond cleavage sites display higher levels of deuteration compared to the fragments with C_2/Z_2 glycosidic bond cleavage sites. The C_1/Y_1 fragment is singly-charged by deprotonation and is detected at higher deuteration levels compared to C_2/Y_2 and B_2/Z_2 in the lower m/z range of the precursor distribution.

Contrary to observations from sodium-adducted melezitose, $[B_2/Z_2 + Ca]^{2+}$ fragments were detected at lower deuteration levels compared to $[C_1/Y_1 + Ca - H]^+$ fragments when lower %D precursors were isolated (Figure 4.2C). One caveat to consider is that for the singly-charged C_1/Y_1 fragments from calcium-adducted

melezitose, the site of deprotonation is unclear. Fragmentation of fully deuterated $[\text{Melezitose} + \text{Ca}]^{2+}$ showed that the $[\text{C}_1/\text{Y}_1 + \text{Ca} - \text{H}]^+$ fragment is detected as a distribution with both three and four deuterium labels, compared to the five labile hydrogens with D_5 at the highest intensity for sodium-adducted C_1/Y_1 (Figure C.5). Detection of fully deuterated $[\text{C}_1/\text{Y}_1 + \text{Ca} - \text{H}]^+$ as a distribution, with multiple peaks with similar intensities, suggests the presence of more than one fragment structure, which have varying numbers of labile hydrogens. The loss of hydrogen for the deprotonated fragment presumably occurs on a hydroxyl group³²⁴, thus reducing the number of labile hydrogens by one. If hydrogen from a primary hydroxyl from B_2/Z_2 fragments is transferred to C_1/Y_1 , as we hypothesized for sodium-adducted melezitose, and an O-D hydrogen is lost, the number of labile hydrogens for deprotonated C_1/Y_1 fragments is expected to be four. Detection of deprotonated C_1/Y_1 fragments with three labile hydrogens could only be explained by transfer of a hydrogen, rather than a deuterium, followed by a loss of deuterium from O-D. Our precursor was fully deuterated, meaning all hydrogens on O-H bonds has been replaced by deuterium. Therefore, C_1/Y_1 fragments with three labile hydrogens must have received a hydrogen from a C-H bond rather than a primary hydroxyl (Scheme C.1).

This hypothesis that C-H hydrogen transfer results in glycosidic bond cleavage is supported by an alternative fragmentation mechanism that Bythell *et al.*³¹⁰ published together with a mechanism for glycosidic oxygen protonation by the O(6) hydroxyl. The number of labile hydrogens for the doubly-charged B_2/Z_2 fragment is seven, the same as the sodium-adducted B_2/Z_2 , indicating that B_2/Z_2 fragments still donate a proton when calcium-adducted. Detection of C_1/Y_1 with three and four labile hydrogens at similar

intensity, on the other hand, suggests that production of C_1/Y_1 occurs via two distinct fragmentation pathways that abstract a hydrogen from a C-H bond or a deuterium from an O-D bond, both accompanied by loss of a labile hydrogen, whether before or after glycosidic bond dissociation. The two distributions cannot be distinguished because they are isomeric. Whereas a C_1/Y_1 fragment that received a hydrogen from a primary hydroxyl of B_2/Z_2 fragment would be expected to have lower levels of deuteration compared to B_2/Z_2 fragments, as discussed above, a C_1/Y_1 fragment that received a hydrogen from a C-H bond should have no change in deuteration level because there is no movement of labile hydrogen in this pathway. Hypothesizing that the other deuterium labels remain in place, besides the one that is lost to produce the deprotonated fragment, the C_1/Y_1 fragment from the second fragmentation pathway should have higher levels of deuteration than the C_1/Y_1 fragment that received a hydrogen from a primary hydroxyl of the B_2/Z_2 fragments. Therefore, it is difficult to localize the deuterium labels to a specific hydroxyl for this fragment when two structures are not resolved.

The deuteration levels of doubly-charged $[C_2/Y_2 + Ca]^{2+}$ fragments were also within the measurement error of the deuteration levels of $[B_2/Y_2 + Ca]^{2+}$, with one exception where the B_2/Z_2 fragment was found to be more deuterated than the C_2/Y_2 fragment when the D_3 precursor was isolated from the 50% D_2O sample. One simple possibility is that the isolation width of the current instrument was set to be consistent for both sodium- and calcium-adducted samples, allowing a wider distribution of peaks to be fragmented for each precursor isolation when calcium-adducted melezitose was fragmented because it was doubly-charged. For instance, the same isolation width, which allowed fragmentation of three m/z peaks for singly-charged, sodium-adducted

melezitose, isolates five m/z peaks for doubly-charged, calcium-adducted melezitose. Therefore, the difference in %D between fragments of calcium-adducted melezitose may not be as distinguished compared to fragments from sodium-adducted precursors because there was greater variability in the calcium-adducted precursor population.

Another possibility for the difference in deuteration levels between sodium- and calcium-adducted melezitose comes from the difference in initial droplet sizes for the samples of carbohydrate with different salts present. Previous work from our lab revealed that carbohydrate-metal complexes in the gas phase do not undergo HDX reactions¹⁰⁰, meaning that the exchange time of carbohydrates in ESI droplets depends on the lifetime of the droplets.³⁰² It has also been reported that the conductivity of the spray solvent affects the initial ESI droplet sizes³²⁵, and thus the HDX reaction times for carbohydrate-metal complexes.²²⁵ While metal-adducted melezitose was prepared at equal concentrations and molar ratios of 1 salt to 1 carbohydrate, the conductivity of melezitose and calcium acetate was $3.149 \pm 0.004 \mu\text{S}/\text{cm}$ ($n = 5$) compared to $1.13 \pm 0.02 \mu\text{S}/\text{cm}$ ($n = 5$) for melezitose and sodium acetate. The higher conductivity of the melezitose and calcium sample is expected to generate smaller initial droplets, resulting in shorter exchange reaction times. Additionally, fragmentation of melezitose and sodium or calcium adducts sprayed in deuterated methanol, which is more volatile than water and thus generates smaller initial ESI droplets, also revealed smaller differences in deuteration levels between fragments (Figure C.6). Therefore, we hypothesize that the decrease in the sizes of initial ESI droplets for melezitose and calcium sample, compared to melezitose and sodium sample, results in deuteration patterns that is more

representative of random labeling in bulk solution, rather than more site-specific in-ESI HDX.

Finally, a common internal cleavage product was observed for sodium- and calcium-adducted melezitose (Figure 4.1B, right). Unlike C_2/Y_2 or B_2/Z_2 fragments which have two possible isomeric structures, the internal cleavage product has up to six possible isomeric structures. Therefore, the percent deuterations of the internal cleavage fragment and B_2/Z_2 and C_2/Y_2 from each metal adduct were analyzed to see if relative %D changed from sodium- to calcium-adducted melezitose. The internal cleavage fragment generated from the sodium-adducted precursor was found to have lower levels of deuteration compared to both B_2/Z_2 and C_2/Y_2 fragments when lower m/z precursor was isolated (Figure 4.3A) but within measurement error with C_2/Y_2 fragments at the higher %D precursor. On the other hand, the same fragment generated from calcium-adducted melezitose was found to be more deuterated than C_2/Y_2 fragments in the lower %D precursor distribution but less deuterated than both C_2/Y_2 and B_2/Z_2 at higher %D precursor (Figure 4.3B). Because multiple isomeric species can be predicted for this internal cleavage product, with no overlaps in labile hydrogens between the different structures (Figure 4.1B, right), the deuterium and hydrogen labels cannot be localized to a single labile site from current data alone. However, the changes in deuteration pattern with respect to other fragments, such as B_2/Y_2 and C_2/Z_2 suggest changes in the structure of the carbohydrate when adducted to different metals, which is supported by literature.^{156, 321, 323} The structural change may be either to the whole carbohydrate-metal complex, resulting in changes to the exchange rate at a given site, or to the type of fragment generated based on altered fragmentation pathways of different carbohydrate-

metal complexes. While different cations adducted to sugar may initiate different fragmentation pathways, fragmentation mechanisms have only been reported for sodium-adducted disaccharides³¹⁰ and future investigations of the fragmentation pathways of different carbohydrate-metal complexes could provide better insight into the structural differences between sodium- and calcium-adducted carbohydrates.

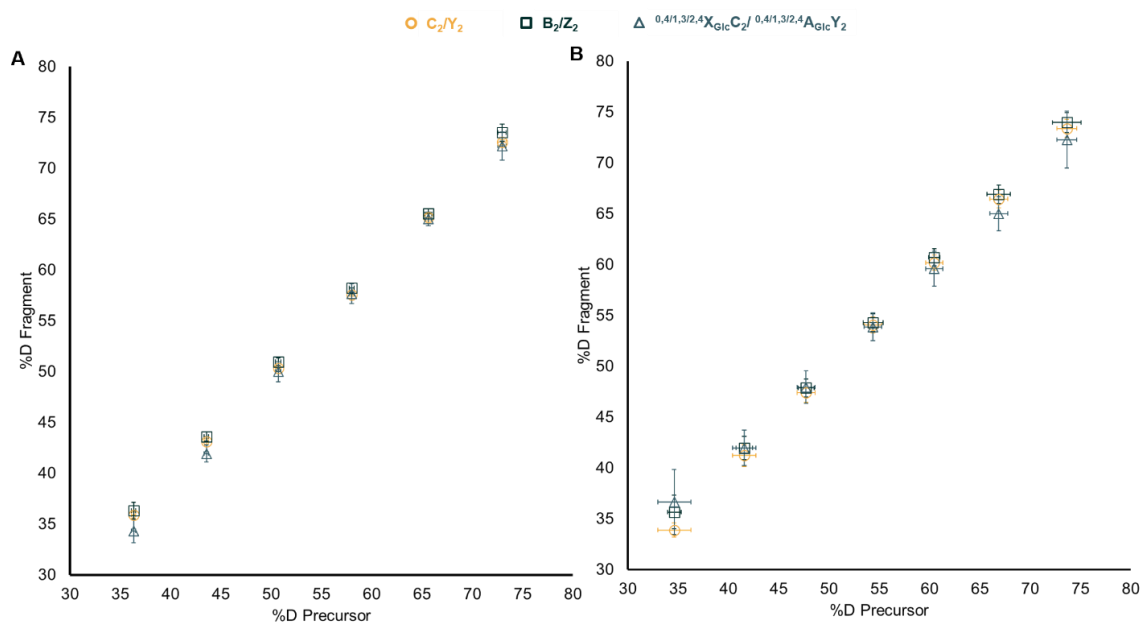


Figure 4.3. Deuteration plots of three common fragments from (A) sodium- and (B) calcium-adducted melezitose in 50% D₂O. The deuteration level of the internal cleavage product (teal triangle) relative to the deuteration levels of glycosidic bond cleavage fragments is altered when the precursor ion was adducted to different metals.

4.4.3 Sodium-Adduction Reduces Scrambling During CID

CID is traditionally associated with scrambling, posing challenges for interpretation of HDX data when assigning the correct site for labels. However, it has been observed that sodium-adducted peptides experience reduced scrambling from CID.³⁰⁸ On the other hand, zinc binding does not reduce scrambling in peptides.³⁰⁵ While the effect of metal-adduction on scrambling in carbohydrates has not been reported, we

hypothesized that scrambling would be reduced during CID of metal-adducted carbohydrates. Our results that the deuteration levels of different carbohydrate fragments vary suggests that (1) there is differential labeling of carbohydrate primary and secondary hydroxyls occurring in droplets despite limited diversity of functional groups and (2) the deuterium labels do not scramble during CID. However, nonuniform deuteration patterns have been observed for uniformly labeled peptides and protein fragments^{305, 326}, meaning that observed differences in deuteration levels between fragments may not confirm that scrambling did not occur. Ferguson *et al.*³²⁶ proposed that the contributing factors for such observations include (1) fragments undergoing additional forward or backward exchange in the gas phase and (2) deuterium enrichment or depletion at various sites of the polypeptide backbone based on differences in proton or deuterium affinities^{327, 328} while, as proposed by the mobile proton model³²⁹⁻³³¹, protons and deuterons migrate along the peptide backbone. However, we know that carbohydrate-metal complexes do not undergo HDX in the gas phase¹⁰⁰ so we can rule out the first explanation by Ferguson *et al.* for our melezitose system. As for the second hypothesis of proton scrambling, the mobile proton model has been thoroughly investigated to explain charge-directed fragmentation behaviors of protonated peptides.³²⁹ Charge-directed fragmentation occurs when a mobile proton, which can migrate from one protonation site to another, attaches to the amide nitrogen.³³² However, fragmentation of metal-adducted carbohydrates has been better supported by charge-remote mechanisms³³³, in which the charge is fixated at a specific location^{334, 335}, such as in the metal ion. Therefore, we hypothesize that the differences in deuteration levels between carbohydrate fragments are not affected by

mobile protons, and that the reduced HDX of gas-phase carbohydrate-metal complexes is correlated to restricted proton movement in gas phase.

Ferguson *et al.*³⁰⁵ warned against erroneously interpreting nonrandom deuteration patterns as not-scrambling without confirmation using controls. Therefore, we proceeded to investigate a model system that is known to scramble. While scrambling from CID is more commonly associated with protonated species, fragmentation of protonated melezitose only revealed B/Z type fragments, thus making the comparison between B/Z and C/Y fragments impossible. On the other hand, fragmentation of ammonium-adducted melezitose generated both B₂/Z₂ and C₂/Y₂ fragments that are protonated via loss of NH₃. However, there is no direct evidence that the two fragmentation processes proceed via the same pathway, or that fragmentation of ammonium-adducted carbohydrates initiates scrambling in the same mechanism as that for protonated carbohydrates.

Previous literature has reported both scrambling and charge migration within deprotonated carbohydrates analyzed in negative-ion mode.^{309, 336} Therefore, CID was performed on deprotonated melezitose in negative-ion mode. The C₂/Y₂ fragment intensity was low, thus only B₂/Z₂ and C₁/Y₁ fragments were analyzed. Deuteration levels of B₂/Z₂ and C₁/Y₁ fragments were not statistically different in any part of the precursor distribution (Figure 4.4), showing a distinctly different pattern compared to those observed for sodium-adducted melezitose, suggesting the occurrence of scrambling within the deprotonated carbohydrates. We should note that proton movement may occur in the precursor before vibrational activation by CID. If label randomizations take place before CID, the “scrambling” may not be directly associated with collisional activation, but rather with the ionization conditions. Our analysis of deprotonated carbohydrates in

negative-ion mode suffered from low signal intensity, which was again distributed over multiple peaks when deuterated. Poor ionization efficiency and low signal in negative-ion mode may have been contributing factors for high levels of variation in %D of deprotonated fragments as observed by the error bars shown in Figure 4.5. However, the statistically significant equivalence for %D of B₂/Z₂ and C₁/Y₁ fragments provides preliminary support for use of deprotonated carbohydrates as a control for scrambling in HDX-CID-MS experiments.

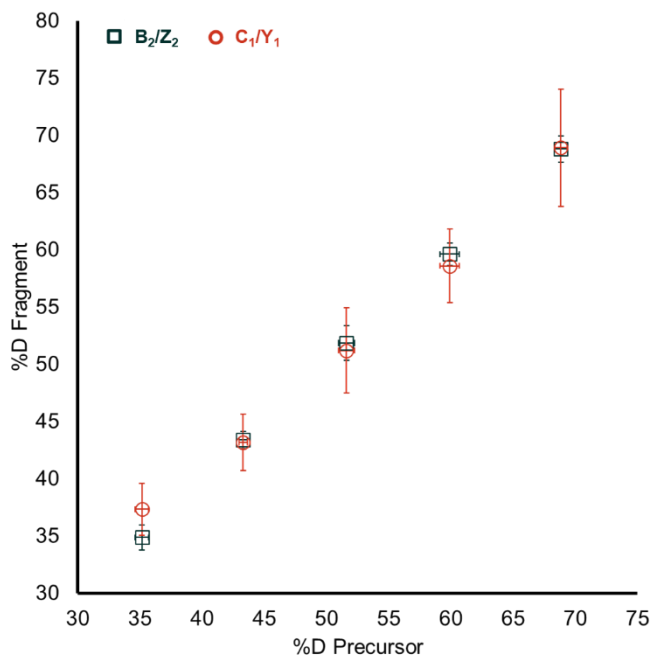


Figure 4.4. Deuteration plot of C₁/Y₁ and B₂/Z₂ fragments generated from deprotonated melezitose in 50% D₂O.

To further investigate the effect of vibrational activation on scrambling in the presence of metal adducts, CID of sodium-adducted melezitose in 75% MeOD was performed at varying collision voltages of 24 – 36 V at increments of 4 V. While D₂O was shown to reveal better distinction between present deuteration of fragments in earlier

data, MeOD provided better signal for fragments at varying collision energies where fragmentation efficiency was lower. C_1/Y_1 fragment signals overlapped with noise, especially when collision voltages of 24 – 28 V were applied. Therefore, only deuteration levels of B_2/Y_2 fragments and C_2/Z_2 fragments were compared. Hoerner *et al.* found that multiple low-energy collisions have been linked to higher levels of scrambling compared to high energy collisions.¹⁸⁶ Such observations are correlated to the time that it takes for the analytes to dissociate during collisions, similar to how the fast electron-based fragmentation techniques are associated with reduced scrambling. Therefore, we hypothesized that if scrambling occurred for sodium-adducted melezitose, scrambling would be observed when collision energy was reduced. Significantly different levels of deuteration were observed between B_2/Z_2 and C_2/Y_2 fragments when precursor ions with higher %D were isolated, at all collision energies tested, consistent with our earlier finding (Figures 4.1 and C.7). To verify that the %D of the fragments were not affected by collision energy, the equality of regression coefficients³¹³ was tested for %D of fragments at different collision voltages. The slopes of deuteration levels for C_2/Y_2 fragments at collision voltages of 24, 28, 32, and 36 V were compared against one another and were statistically equivalent at the 95% confidence interval. This was also observed for the B_2/Z_2 fragments across all collision voltages tested, indicating there was no effect on deuteration levels from varying the collision energy. Thus, this confirmed that the deuteration patterns were consistent regardless of the collision energy applied (Figure C.5). Therefore, we conclude that sodium adduction to carbohydrates reduces scrambling.

4.5 Conclusion

Although less common, application of HDX to non-peptide biomolecules can offer significant structural information for many analytes including carbohydrate. The potential of HDX methods to provide information on the three-dimensional structures, dynamics, and analyte interactions in bulk solution and droplets, offers new insights into carbohydrate chemistry and structures. Here, we reported deuterium label assignments on carbohydrates that have limited numbers of functional groups and a narrow range of exchange rates. Our results show that the different fragments of carbohydrates display varying deuteration levels despite the similarity between primary and secondary hydroxyls. The difference in HDX rates is increased in response to in-ESI HDX reactions while in droplets compared to deuteration in bulk solution. Moreover, our method overcomes the limitations of CID associated with scrambling by adducting to metal cations, particularly sodium. Thus, we have demonstrated a new method to utilize HDX-MS for structural analysis of metal-adducted carbohydrates via CID and deuterium localization based on carbohydrate fragmentation mechanisms. In our companion paper, we utilize this method to interpret varying deuteration patterns observed for carbohydrate isomers adducted to sodium, thus illustrating an application. Our achievement in differentiation of exchange rates between primary and secondary hydroxyls, which are the most common functional groups in carbohydrates, opens new prospects for HDX analysis of carbohydrates to obtain structural information at the local level.

4.6 Acknowledgments

This work was supported by the Welch Foundation, Grant AA-1899. The authors acknowledge the Baylor University Mass Spectrometry Center and Baylor University High Performance and Research Computing Services.

CHAPTER FIVE

Analysis of Conformational Differences in Carbohydrate Isomers via Hydrogen/Deuterium Exchange Coupled to Tandem Mass Spectrometry

This chapter is prepared for publication in *Analytical Chemistry* as: Kim, H. J., Calixte, E. I., Gallagher, E. S. Analysis of Conformational Differences in Carbohydrate Isomers via Hydrogen/Deuterium Exchange Coupled to Tandem Mass Spectrometry

5.1 Abstract

Carbohydrates are a complex and heterogeneous class of biomolecules that are crucial components of cellular function. Carbohydrate complexity comes from the diversity of isomeric monosaccharide subunits as well as linkage and stereochemistry, and structural analysis of such complex carbohydrates are often limited to sequencing. Hydrogen/deuterium exchange coupled to mass spectrometry (HDX-MS) is a powerful technique for structural elucidation that has previously been shown to reveal differences in carbohydrate isomers. However, applications of HDX-MS were confined to global observations with no local deuterium assignments. In this paper, we present a novel method to interpret observed differences in deuteration levels of fragments in isomeric trisaccharides. We observed differences in deuteration levels of carbohydrate fragments generated from collision induced dissociation (CID). The isomers also revealed varying deuteration patterns of fragments. We localized the deuterium labels for different sodium-adducted isomers by tracking likely sources of hydrogen or deuterium labels used in the initiation of glycosidic bond cleavage reactions using density functional theory (DFT) optimizations of carbohydrate conformations. Therefore, the structural differences

between the trisaccharide isomers and the likely fragmentation pathways for each respective system are reflected in the deuteration levels of fragments from each isomer, providing a new dimension for HDX analysis of carbohydrates.

5.2 Introduction

Carbohydrates are a complex class of biomolecules with significant biological implications in many cellular functions, including protein folding and localization²⁶⁵, cell-cell communication, and activation of immune responses.²⁹⁵ Such variety of involvement in biological activities is paralleled by the heterogeneous nature of carbohydrates. Carbohydrates are composed of isomeric monosaccharide subunits, in which five of the six carbons in each monosaccharide are chiral centers. Monosaccharides in solution exist as five- or six-membered rings or linear chains in equilibrium. Mutarotation, or the spontaneous interconversion of ring structures, also results in a unique set of isomers, called anomers, that interchange spontaneously. Additionally, all five hydroxyls in monosaccharides can form glycosidic linkages with other carbohydrates, sometimes with more than two hydroxyls serving as a branch point, resulting in a multitude of possible structures with various linkage and monosaccharide combinations. Such heterogeneity has led to challenges in analyzing carbohydrates and many analytical techniques have been developed to identify sequences of complex polysaccharides. However, the three-dimensional structures of carbohydrates are important as well because carbohydrates directly bind to proteins to trigger cellular responses.

Hydrogen/deuterium exchange coupled to mass spectrometry (HDX-MS) is a well-established technique that has traditionally been used to analyze protein

conformations and dynamics. Traditional bottom-up HDX-MS of proteins is performed by diluting protein samples in D₂O for varying lengths of time, ranging from seconds to days, and quenching the reaction at pH 2.5 and 0 °C. The traditional HDX method is optimized for backbone amide hydrogens of proteins, because the exchange rate of the backbone amide hydrogens is minimized at pH 2.5, minimizing the loss of deuterium labels on the amides during and after the quench step. However, the most abundant functional groups on carbohydrates are hydroxyls, which have exchange rates that are several orders of magnitude faster than amides.²¹⁶ Therefore, recent developments in HDX methodology for carbohydrate analysis have focused on labeling during ionization or in gas phase. Specifically, altering exchange times on the microsecond timescale has been achieved by varying the size of initial electrospray (ESI) droplets.^{225, 302} Carbohydrate isomers have also displayed varying deuteration behaviors via in-ESI²²⁵ and gas-phase HDX,²¹² offering an optimistic outlook for differentiating isomers by HDX. However, localization of the deuterium labels in these methods has not been achieved.

In a companion paper, we have established a method showing that fragments of a trisaccharide, melezitose, from collision induced dissociation (CID) display varying levels of deuteration, presenting an opportunity for assigning deuterium labels to specific sites despite the limited number of functional groups available. We have also shown that metal adduction, specifically to sodium ions, minimizes scrambling associated with collisional activation, which has been known to randomize deuterium labels on peptides. While fragmentation of deuterated carbohydrates revealed sub-local deuterium labels on melezitose, such sub-localization has not been compared between carbohydrate isomers.

Here we present an application of our method using HDX-CID-MS of sodium-adducted trisaccharides to show varying deuteration patterns of fragments from carbohydrate isomers. Three trisaccharide isomers are compared; melezitose, raffinose, and maltotriose. The relative deuteration levels between B/Z fragments, which are fragments that lose the glycosidic oxygen upon C-O bond cleavage, and C/Y fragments, which retain the glycosidic oxygen, across all carbohydrates tested show higher levels of deuteration for B/Z fragments, in agreement with our previous data. We attribute such differences in C/Y against B/Z fragments to the glycosidic bond cleavage mechanism of metal-adducted carbohydrates. In this paper, we illustrate a novel method of assigning deuterium labels on deuterated carbohydrates by tracking hydrogen or deuterium transfer during carbohydrate fragmentation. The deuterium localization on the carbohydrate hydroxyls were validated by density functional theory (DFT) calculations to deduce carbohydrate fragmentation mechanisms and the exchange rates of hydrogens involved. The differences in deuteration patterns observed for each isomer were closely related to the differences in conformations of the isomeric trisaccharides.

5.3 Methods

5.3.1 Materials

Melezitose (α -D-Glc-[1 \rightarrow 3]- β -D-Fru-[2 \rightarrow 1]- α -D-Glc), raffinose (α -D-Gal-[1 \rightarrow 6]- α -D-Glc-[1 \rightarrow 4]- β -D-Fru), and maltotriose (α -D-Glc-[1 \rightarrow 4]- α -D-Glc-[1 \rightarrow 4]-D-Glc) were purchased from Sigma Aldrich (St. Louis, MO). Chemical structures of the sugars are shown in Figure D.1. Sodium acetate was purchased from VWR International

(Randor, PA). Deuterium oxide (D₂O, 99.8%) was purchased from Cambridge Isotope Laboratories Inc. (Tewksbury, MA).

5.3.2 Collision Induced Dissociation of Deuterated Carbohydrate-Sodium Complexes

All CID experiments were performed on a Waters Synapt G2-S High Definition mass spectrometer equipped with a LockSpray Exact Mass Ionization Source (Waters Corporation, Milford, MA). Collision voltages were optimized for undeuterated carbohydrate-sodium adducts by increasing collision voltages in increments of 4 V and observing the fragmentation efficiency. Collision energies at which the disaccharide glycosidic bond cleavage products, such as C₂, B₂, Y₂, and Z₂ were produced at high intensities, were selected for experiments. Collision voltages in the ranges of 32 – 40 V were used for all sugars. Once collision energy was optimized, carbohydrate and sodium mixtures in 98% D₂O were fragmented to confirm the number of labile hydrogens for each fragment. All fragments were labeled following the Domon and Costello nomenclature.¹⁵⁵ While some carbohydrates are non-reducing sugars, both A/B/C and X/Y/Z fragments were assigned by following IUPAC nomenclature to show that isomeric species may exist for a given *m/z*.

All samples were prepared at a 1:1 molar ratio of carbohydrate and sodium acetate in 25%, 50%, or 75% D₂O and water and incubated and stored at 4 °C for at least 24 hours before experiments. Samples were directly infused into the ESI source at 5 μL/min. Data acquisition began after ~5 minutes of sample infusion to establish a D₂O:H₂O equilibrium in the ESI source to minimize variations over time due to changes in the residual solvent vapor composition in the source.¹⁶ A full mass spectrum was collected to obtain the deuteration level of the [M + Na]⁺ distribution. Then each *m/z*

peak in the distribution was isolated at LM Res 15.0 and fragmented. The number of replicates were $n = 12$.

5.3.3 Data Analysis and Presentation

Undeuterated samples were prepared in water. Fully deuterated samples were prepared in 98% D₂O. The weighted, experimentally determined average m/z for undeuterated and fully deuterated precursor and fragments were calculated (Equation 5.1), where m/z is the mass-to-charge ratio and I is the intensity of each isotopic peak.

$$(m/z) = \frac{\sum(m/z) \cdot I}{\sum I} \quad \text{Equation 5.1}$$

The difference between the two m/z values would give the number of labile hydrogens on the precursor and fragment ions, shown as the numerator of Equation 5.2. Because the fragments have different numbers of labile hydrogens, the number of deuterium labels from experimental data could not be compared directly for different fragments.

Therefore, all deuteration levels were reported as percent deuteration (%D) using the equation:

$$\%D = \frac{(m/z)_{\text{experimental}} - (m/z)_{0D}}{(m/z)_{98D} - (m/z)_{0D}} \times 100 \quad \text{Equation 5.2}$$

Fragment deuteration levels were represented as scatter plots with error bars as standard deviation. Welch's t -test was performed to confirm the statistical significance of differences in deuteration levels between fragments at 95% and 99% confidence interval, as outlined by Hageman and Weis.³¹² The Hageman and Weis approach of statistical significance testing was adapted to avoid overinterpretation of false positives that could

result from *t*-test alone. Briefly, two tests were utilized. First, Welch's *t*-test was performed. Then, confidence intervals were established by multiplying *t*-values to standard error of the mean (SEM) of each sample. We determined that the difference in deuteration levels of two fragments were significant when (1) the two %D values were statistically different from *t*-test, and (2) the difference in %D between fragments fell outside the range given by the confidence interval.

5.3.4 Computational Methods for Structural Analysis of Carbohydrate-Sodium Complexes

MD simulations of ESI droplets were performed to obtain various conformers of carbohydrate-sodium complexes.⁹⁶ The GROMACS package³¹⁴ was used for all molecular dynamics (MD) simulations. Molecular structures for carbohydrates were first built and optimized using Glycam-Web³¹⁵. The Paramchem/CGenFF-4.0^{337, 338} server was then used to generate topology files for each carbohydrate based on the CHARMM36 forcefield.³³⁹ In building the droplets, each carbohydrate molecule was surrounded by pre-equilibrated solvent in a cubic system, and a sphere containing the carbohydrate with a radius of 3 nm was carved out. This size of this droplet is typical for simulating droplets at the late stages of evaporation and has the added benefit of being less computationally expensive due to the smaller number of solvent molecules. The average number of methanol molecules for our 3 nm-radius systems were 1673 ± 2 solvent molecules. Ten sodium ions were added to each droplet, to serve as the charge carriers for ionization in positive-ion mode for each system. The number of ions was less than the Rayleigh limit²⁸², which is the maximum amount of charge which can be contained within a droplet of known radius, and is based on the surface tension of the solvent at the given temperature. Each droplet was placed in

vacuum and was energy-minimized using steepest descent and timesteps of 2 fs. All steps in the simulations employed the Verlet algorithm³⁴⁰. Following minimization, the equilibration step was initiated with random assignment of velocities to the system, generated from a Maxwell-Boltzmann distribution. The leapfrog integrator³⁴¹ was employed with a timestep of 1 fs. The droplets were then equilibrated to the reference temperature of 300 K, which was regulated using a Nosé-Hoover thermostat^{342, 343} with a time constant of 1 ps. During equilibration, a flat-bottomed spherical potential was used to prevent the solvent from evaporating from the droplet. A pseudo-PME³⁴⁴ treatment was employed, which is recommended for handling electrostatics in systems consisting mostly of vacuum with periodic boundary conditions in all directions.

Following equilibration, the production phase of the simulation, involving solvent evaporation and ion ejection, was performed with the exclusion of the flat-bottomed potential. Konermann's code^{316,317} was used to remove any water or ions that had evaporated from the droplets, and to automate equilibration of the droplets between runs or "trajectory stitches". This temperature equilibration is important to offset changes in temperature due to evaporative cooling.³⁴⁵ Each stitch was 50 ps long, with timesteps of 1 fs. Energies, coordinates, and velocities were saved every 0.5 ps. During the production run, methanol evaporated from the droplet and the charge density increased until the Rayleigh limit was reached. At this limit, solvated sodium ions were ejected from the droplet. Successions of solvent evaporation and ion ejection events occurred, until a solvent-free adduct of carbohydrate bound to metal was obtained. Ten independent trials were performed for each carbohydrate, from building the initial droplets to adduct

formation in the gas phase. Output structures from the MD simulations were then used as input structures for structure calculations using Gaussian16.

Density Functional Theory (DFT) calculations at the B3LYP 6-311++G(d) level of theory were used to optimize the above input structures of carbohydrate-metal complexes. The distance between hydroxyl hydrogens and the nearest glycosidic oxygens in the final optimized structures were measured using Avogadro software (v. 1.2.0).³⁴⁶

5.4 Results and Discussion

5.4.1 Exchange Rates of Primary and Secondary Hydroxyls on HDX of Melezitose

In our companion paper, we reported that B/Z type fragments were detected at higher levels of deuteration compared to C/Y type fragments when sodium-adducted melezitose was fragmented by CID. Our hypothesis is that the difference in deuteration levels resulted from the primary hydroxyls, which have a faster exchange rate, back-exchanging faster than secondary hydroxyls during ESI. This hypothesis is supported by reported exchange rates for cyclodextrin and maltoheptaose hydroxyls.³¹⁸ We reported that scrambling, or the random redistribution of hydrogen and deuterium labels upon multiple collisional activations, was minimized when carbohydrates were adducted to sodium ions. Therefore, in this paper, we focus on the application of HDX-CID-MS to compare HDX of sodium-adducted carbohydrate isomers.

Assuming that the fragmentation pathways of sodium-adducted carbohydrates proceed similarly, we compared the deuteration levels of B/Z and C/Y fragments from three isomers: melezitose, raffinose, and maltotriose. Although these three trisaccharides have different monosaccharide compositions and linkage patterns, they have been well

characterized and serve as good model systems for both structure and fragmentation analysis.

For each glycosidic bond cleavage event, we assume that two major fragments are produced, and fragments are detected depending on which fragment is adducted to the sodium ion. Our proposed fragmentation pathways are based on publications from Bythell *et al.*³¹⁰ in which a hydroxyl within the sodium-adducted carbohydrate donates a hydrogen to the glycosidic oxygen, initiating C-O bond cleavage. Upon bond dissociation, two types of fragments are formed: B/Z-type fragments and C/Y-type fragments. The hydrogen is donated to the glycosidic oxygen by a hydroxyl from the B/Z-type fragments. The same hydrogen and the glycosidic oxygen are transferred to the C/Y-type fragments (Figure D.2). A glycosidic bond cleavage in a trisaccharide leads to the production of four possible fragment pairs composed of equivalent structures to a disaccharide and a monosaccharide: B₂/Y₁, C₂/Z₁, Z₂/C₁, and Y₂/B₁. Melezitose, raffinose, and maltotriose are made up of three isomeric monosaccharide subunits, and isomeric fragments of B₂/Z₂, C₂/Y₂, B₁/Z₁, and C₁/Y₁ are produced. The isomeric fragments cannot be distinguished from one other without covalent labeling using isotopes such as ¹³C or ¹⁸O, so isomeric fragment pairs are compared as groups against other pairs of isomeric fragments in this paper.

Deuteration levels of B₂/Z₂ and C₁/Y₁ fragments were compared. The two fragment groups are produced from the same glycosidic bond cleavage sites, and the movement of hydrogens involved in fragmentation can be tracked by comparing the difference in deuteration levels, as shown in Figure D.2. B₂/Z₂ fragments from melezitose were detected at higher deuteration levels compared to C₁/Y₁ fragments for 18 out of 19

precursor m/z , which were generated by spraying from 25%, 50%, and 75% D₂O (Figure 5.1A, Table D.1-3). To produce B₂/Y₁ and Z₂/C₁ fragment pairs, a hydrogen from the middle fructose ring is donated to either glycosidic oxygen to initiate fragmentation. The middle fructose subunit of melezitose has two primary hydroxyls, at the O(1')H and O(6')H positions, and one secondary hydroxyl, at the O(4')H position.

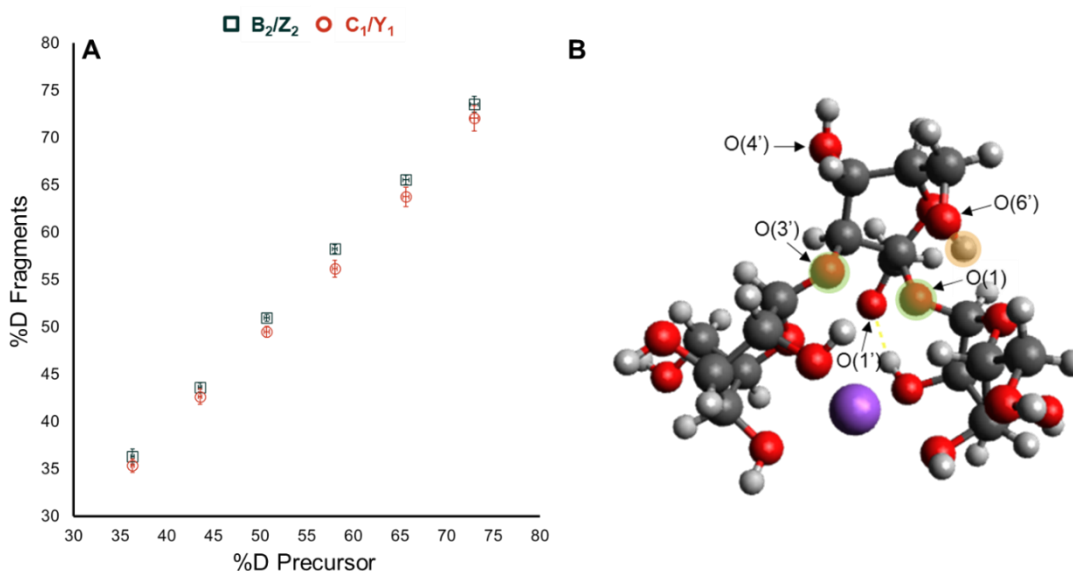


Figure 5.1. (A) Deuteration plots of B₂/Z₂ (navy square) and C₁/Y₁ (red circle) fragments generated from sodium-adducted melezitose and (B) representative structure of melezitose-sodium complex optimized by DFT calculations. Carbon atoms are shown in gray, oxygen atoms in red, hydrogen atoms in white, and sodium ion in purple. The glycosidic oxygens (O(3') and O(1)) are highlighted in green. The hydrogen that is closest to the glycosidic oxygen, thus likely to initiate the glycosidic bond cleavages is highlighted in orange (O(6')H). The O(1')H hydroxyl points away from the glycosidic oxygens, and is unlikely to donate hydrogen.

Intramolecular hydrogen bonding of carbohydrates are typically observed in a range of 1.8 to 2.6 Å³⁴⁷, but Jeffery categorized hydrogen bonds with donor-acceptor distances of 2.3 – 3.2 Å as “moderate, mostly electrostatic.”³⁴⁸ Therefore, OH—O distances less than or equal to 3.2 Å are considered meaningful interactions for our analysis. DFT optimizations of ten melezitose-sodium complexes showed that the

hydrogens of the primary hydroxyls, particularly O(6')H, is closer to the glycosidic oxygens compared to the hydrogen of the secondary hydroxyl, O(4')H (Figure 5.1B). The distance between the hydrogen of the O(6')H primary hydroxyl and the glycosidic oxygen, O(3'), was 4 ± 1 Å. The distance between the hydrogen of the O(4')H secondary hydroxyl and the same glycosidic oxygen, O(3'), was 4.0 ± 0.2 Å. While the distances between each of the hydroxyls and the glycosidic oxygen are similar, a closer look at the individual structures reveals that the distance and orientation for O(4')H—O(3') stay consistent across the ten examined conformations, which is reflected by the small standard deviation. However, the orientation for O(6')H—O(3') varies at different conformations, suggesting that there are conformations in which proton donation is more likely (Table D.4). Similarly, the average distance between the primary hydroxyl hydrogen at the O(6')H position and the glycosidic oxygen, O(1), is 4 ± 1 Å. While the distance between the secondary hydroxyl hydrogen at the O(4')H position and the glycosidic oxygen, O(1), is 5.0 ± 0.3 Å. However, five out of the ten examined conformations showed a conformation in which the O(6')H—O(1) distance was shorter than 3 Å, with the shortest distance being 2.5 Å. Therefore, DFT optimizations suggest that the primary hydroxyls, especially at the O(6')H position, likely donate a hydrogen to the glycosidic oxygens and initiate fragmentation to produce B₂/Z₂ fragments.

Bekiroglu *et al.* reported that the exchange rate of primary hydroxyls at the O(6)H position is five to six times higher than the exchange rates of secondary hydroxyls at the O(2)H and O(3)H positions of maltoheptaose and cyclodextrins.³¹⁸ We expect that the carbohydrates prepared in varying percentages of D₂O undergo back-exchange during ESI, which occurs under atmospheric conditions, thus in the presence of ambient

moisture. We hypothesize that the higher exchange rate of primary hydroxyls leads to faster back-exchange of O(6')H compared to the secondary hydroxyls. In turn, the O(6')H hydroxyl hydrogen, which is closer to the glycosidic oxygens of melezitose, compared to the other hydroxyls, and thus more likely to initiate glycosidic bond cleavage, is transferred from B₂/Z₂ fragments to C₁/Y₁ fragments upon fragmentation (Figure D.2). Our hypothesis explains the higher deuteration level of B₂/Z₂ fragments, that lost a hydrogen rather than a deuterium, compared to C₁/Y₁ fragments, that received a hydrogen rather than a deuterium.

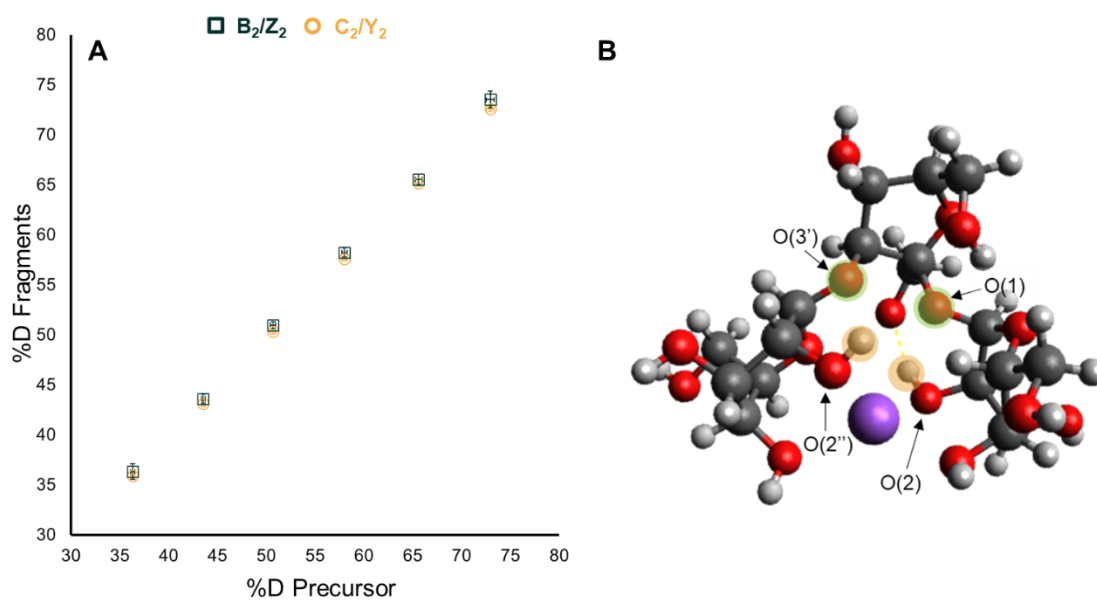


Figure 5.2. (A) Deuteration plots of B₂/Z₂ (navy square) and C₂/Y₂ (golden circle) fragments generated from sodium-adducted melezitose and (B) representative structure of melezitose-sodium complex optimized by DFT calculations. Carbon atoms are shown in gray, oxygen atoms in red, hydrogen atoms in white, and the sodium ion in purple. The glycosidic oxygens (O(3') and O(1)) are highlighted in green. The hydrogens that are closest to the glycosidic oxygen, and thus likely to initiate glycosidic bond cleavages, are highlighted in orange (O(2'')H and O(2)H).

Comparison of the C₂/Y₂ and B₂/Z₂ fragments of melezitose revealed that the %D of the B₂/Z₂ fragment was significantly higher than the %D of the C₂/Y₂ fragment when a

higher m/z precursor was isolated (Figure 5.2A, Table D.5-7). C_2/Y_2 and B_2/Z_2 fragment structures differ by one hydroxyl and a labile hydrogen. Unlike C_1/Y_1 and B_2/Z_2 fragments that are generated from the same glycosidic bond cleavage event, C_2/Y_2 and B_2/Z_2 fragments are produced from distinctive fragmentation sites. Therefore, the hydrogen that initiates the glycosidic bond cleavage for the two fragments should be tracked separately. As discussed earlier, fragmentation pathways leading to production of B_2/Z_2 are more likely initiated by the primary hydroxyl at the $O(6')H$ position. DFT optimized structures of melezitose-sodium complexes show that a secondary hydroxyl at the $O(2'')H$ position is in close proximity to the glycosidic oxygen $O(3')$, at $2.6 \pm 0.5 \text{ \AA}$, and thus it likely initiates fragmentation to generate the B_1/Y_2 fragment pair. On the other side of the molecule, one conformation shows the $O(2)H$ hydroxyl close to the $O(1)$ glycosidic oxygen, which may lead to production of the C_2/Z_1 fragment pair, again suggesting that contributions of the secondary hydroxyls are higher than primary hydroxyls for producing C_2/Y_2 fragments (Figure 5.2B). Following our earlier hypothesis that secondary hydroxyls would back-exchange more slowly compared to primary hydroxyls during ESI, we expect that the C_2/Y_2 fragments are more likely to receive a deuterium than a hydrogen, which would increase %D of C_2/Y_2 fragments. The increase in %D of the C_2/Y_2 fragments is also observed compared to C_1/Y_1 fragments, which likely received a hydrogen from the primary hydroxyl of the B_2/Z_2 fragments, as the difference in deuteration levels between C_2/Y_2 and B_2/Z_2 is reduced (Figure 5.2A). The structures for B_2/Z_2 fragments have two primary hydroxyls and four secondary hydroxyls, compared to three primary hydroxyls and five secondary hydroxyls of C_2/Y_2 fragments. The ratio of primary hydroxyls, which more likely back-exchanged to hydrogens, to

secondary hydroxyls, which more likely retained deuterium, also support the observation that B₂/Z₂ fragments are detected at higher deuteration levels compared to C₂/Y₂ fragments.

5.4.2 Hydrogen Bonds and Cooperativity Effects on HDX of Raffinose with Asymmetric Terminal Sugars

Unlike melezitose, raffinose does not have any primary hydroxyls available to donate a proton and initiate glycosidic cleavage, because the primary hydroxyl at the O(6')H position is covalently linked to galactose. Thus, all proton sources from B₂/Z₂ fragments come from secondary hydroxyls. While a C-H bond may also protonate the glycosidic oxygen³¹⁰, fragmentation of fully deuterated raffinose adducted to sodium reveals loss of a labile hydrogen for B₂/Z₂ and gain of a labile hydrogen for C₁/Y₁ fragments, meaning a hydrogen transfer occurred from an O-H rather than a C-H (Figure D.3). Although a deuterium likely retained by a slower exchanging secondary hydroxyl was transferred during raffinose fragmentation, B₂/Z₂ fragments of raffinose were detected at higher deuteration levels compared to C₁/Y₁ fragments (Figure 5.3A, Tables D.5-7). This observation is similar to that observed for melezitose, although a primary hydroxyl likely donated a hydrogen to initiate fragmentation of melezitose (Figure 5.1B). Moreover, the difference in deuteration level between B₂/Z₂ and C₁/Y₁ is larger for raffinose, with B₂/Z₂ being 2 ± 1 % more deuterated than C₁/Y₁ across all precursor *m/z* values in 25%, 50%, and 75% D₂O. For melezitose, B₂/Z₂ fragments were 0.5 ± 0.6 % more deuterated than C₁/Y₁ fragments. Such differences in deuteration pattern between the two isomers may be explained by the fragment structures of each isomer. While both melezitose and raffinose are composed of two pyranoses, or six-membered rings, and one

furanose, or a five-membered ring, the furanose is located in the middle for melezitose and on the end for raffinose. B₂ and Z₂ fragments of melezitose have similar structures, with a pyranose covalently linked to a stacked-furanose ring, while C₁ and Y₁ fragments are consequently a pyranose ring (Figure D.2). However, B₂ fragments of raffinose have two pyranose rings, producing a furanose Y₁ fragment, and Z₂ fragments of raffinose have one pyranose and one furanose ring linked together, producing a pyranose C₁ fragment (Figure D.4). Although B₂ and Z₂ fragments of raffinose are isomeric, as are C₁ and Y₁ fragments, the composition of labile hydrogens from primary and secondary hydroxyls differ.

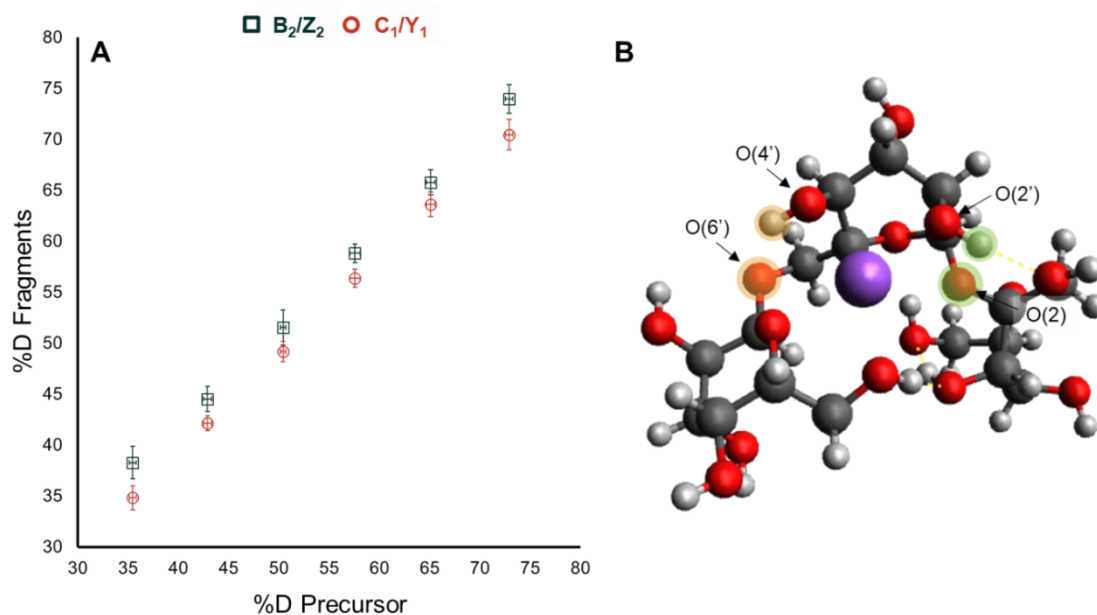


Figure 5.3. (A) Deuteration plots of B₂/Z₂ (navy square) and C₁/Y₁ (red circle) fragments generated from sodium-adducted raffinose and (B) representative structure of raffinose-sodium complex optimized by DFT calculations. Carbon atoms are shown in gray, oxygen atoms in red, hydrogen atoms in white, and the sodium ion in purple. The glycosidic oxygen (O(6')) and the most likely source of hydrogens to initiate the glycosidic bond cleavage (O(4')H) are highlighted in orange for production of the C₁/Z₂ fragment pair. The glycosidic oxygen (O(2)) and the most likely source of hydrogens to initiate the glycosidic bond cleavage (O(2')H) are highlighted in green for production of the B₂/Y₁ fragment pair.

The primary hydroxyl forming a 1→6 linkage, with a methyl between the hydroxyl and the sugar ring, results in a longer distance between the two monosaccharides compared to when a secondary hydroxyl forms the glycosidic bond, such as in the 2→1 linkage. Electronic structure calculations of sodium-adducted raffinose show that protonation of the glycosidic oxygen between the two pyranose rings bonded by a 1→6 linkage is less favorable than protonation of the glycosidic oxygen between the glucose and fructose. Thus, production of B₂ and Y₁ fragments is favored over production of Z₂ and C₁ fragments (Figure D.4), and fragmentation around O(6') oxygen for production of B₂/Y₁ is not considered. The average distance between the secondary hydroxyl hydrogen at the O(2')H position and the glycosidic oxygen linking glucose and fructose, O(2), is 2.6 ± 0.6 Å, whereas all other hydroxyl and glycosidic oxygen pairs are at least 4.5 Å apart (Table D.11). We hypothesize that a furanose Y₁ fragment with two primary hydroxyls, generated from fragmentation initiated by protonation of the glycosidic oxygen by the O(2')H hydroxyl, would have higher levels of back-exchange compared to the B₂ fragment with two pyranose rings and only one primary hydroxyl. Thus, the difference in deuteration levels between the two fragments is expected to be higher than if the Y₁ fragment was a pyranose ring with only one primary hydroxyl, such as in melezitose.

The deuteration levels of the B₂/Z₂ fragments from raffinose were significantly higher than the deuteration levels of the C₂/Y₂ fragments as well (Figure 5.4A, Table D.8-10). The hydroxyl hydrogen that was the closest to the glycosidic oxygen, O(2), was the secondary hydroxyl at the O(3)H position, at 2.6 ± 0.7 Å. All other hydroxyls were at least 3.8 Å away from O(2). Transfer of hydrogen from O(3)H to O(2) would produce the

C₂/Z₁ fragment pair. For the glycosidic bond cleavage site that would generate the B₁/Y₂ fragment pair, the O(2'')H hydroxyl was found in close proximity to the glycosidic oxygen O(6') in two of the conformations. Therefore, secondary hydroxyl contributions to the C₂/Y₂ fragments are expected to be greater than those of the primary hydroxyls.

Hypothesizing that the fragmentation pathway generating B₂ is more energetically favorable compared to the one leading to Z₂ production, due to the steric hindrance of the elongated 1→6 linkage, the structures that are compared are B₂ against C₂ and Y₂ fragments. The distinction of the C₂ and Y₂ fragment structures is important because the C₂ fragment would have two pyranose rings and the Y₂ fragment would consist of one pyranose and one furanose ring. From the conformations obtained from DFT calculations, both the C₂ and Y₂ products seem viable, although the O(3)H—O(2) interaction leading to C₂ production is observed more often. Therefore, we expect that the averaged %D of the C₂/Y₂ fragments have higher C₂ fragment population. The C₂ fragment would have the same structure as the B₂ fragment except for an extra hydroxyl and a labile hydrogen, and thus similar levels of deuteration are expected for the common structures shared by C₂ and B₂ fragments. Moreover, the C₂ fragment would more likely gain a deuterium rather than a hydrogen from the secondary hydroxyl O(2)H upon fragmentation and have only one fast-exchanging primary hydroxyl, O(6'')H. However, the %D of the C₂/Y₂ fragment was close to 2% lower than the %D of the B₂/Z₂ fragment, which more likely lost deuterium than hydrogen during fragmentation.

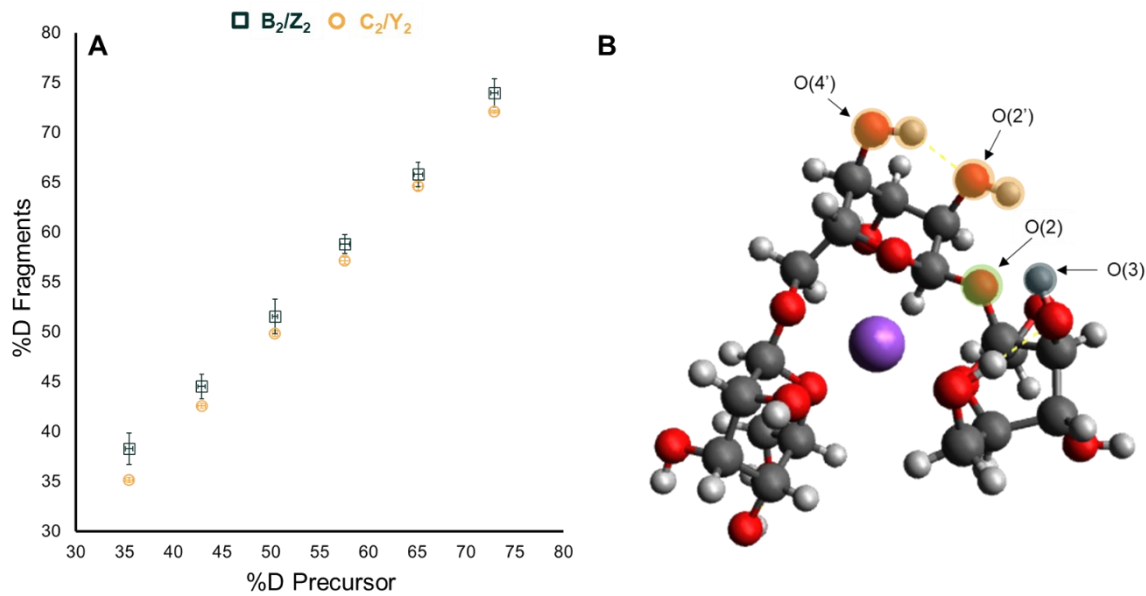


Figure 5.4. (A) Deuteration plots of B₂/Z₂ (navy square) and C₂/Y₂ (golden circle) fragments generated from sodium-adducted raffinose and (B) representative structure of raffinose-sodium complex optimized by DFT calculations. Carbon atoms are shown in gray, oxygen atoms in red, hydrogen atoms in white, and sodium ion in purple. The most likely source of hydrogen to initiate glycosidic bond cleavage for production of the B₂ fragment is (O(2')H). The hydrogen bonding network involving O(2')H is highlighted in orange. The glycosidic oxygen (O(2)) is highlighted in green. The most likely source of hydrogen to initiate glycosidic bond cleavage for the production of the C₂ fragment is (O(3)H), which is highlighted in blue.

One potential contributing factor to lower %D of C₂ is the hydrogen bonding network that is observed in raffinose molecules. The middle glucose subunit of raffinose has O(2')H and O(4')H hydroxyls in axial positions that form a O(4')H—O(2')H or a O(4')H—O(2')H—O(2) hydrogen bonding network (Figure 5.4B). Dashnau *et al.* reported that such interactions between O(2)H and O(4)H decrease the hydrogen bonding between the hydroxyls and solvent, leading to water structures characteristic of “hydrophobic solvation.”³⁴⁷ In this hydrophobic solvation structure, the interactions between water molecules are greater, similar to the interactions observed in bulk solution. If the hydroxyl bonding network is terminated by interacting with the ring oxygen, which

does not have a free hydroxyl hydrogen to continue the hydrogen bonding network, the hydrophobic solvation effect is increased. Moreover, the interactions between hydroxyl hydrogens and oxygens become stronger with additional hydroxyls involved in the network, known as cooperativity. In some conformations of raffinose, the O(4')H—O(2')H network is shown to interact with the glycosidic oxygen O(3), rather than the ring oxygen O(5). We hypothesize that similar hydrophobic solvation effects shield the secondary hydroxyls O(2')H and O(4')H from exchanging in solution. NMR studies of partially deuterated samples have shown that the hydroxyl that acts as the donor in a hydrogen bonding network reveals reduced exchange compared to unprotected groups.³⁴⁹ Moreover, stachyose, which has a strong intramolecular hydrogen bond, displayed lower deuteration level during MALDI-HDX.²⁴⁶ However, these interactions are transient, and we expect that the hydrophobic solvation effect would not completely inhibit HDX on the hydroxyls involved in the hydrogen bonding network during the 24-hour incubation time. Rather, these effects would more likely reduce back-exchange during ESI on the hydroxyls involved in hydrogen bonding network. Therefore, we hypothesize that B₂ and C₂ fragments have similar deuteration levels. on the other hand, the isomeric Y₂ fragment, containing the furanose ring with two fast-exchanging primary hydroxyls, is expected to have lower %D, consistent with the Y₁ fragment as discussed earlier. Thus, the detection of both C₂ and Y₂ fragments would collectively have lower %D compared to B₂ fragments having higher %D, supporting the observation that the deuteration levels of C₂/Y₂ compared to B₂/Z₂ fragments are lower.

5.4.3 HDX of Maltotriose with Fast-Exchanging Anomeric Hydroxyls on the Reducing End

Whereas melezitose and raffinose are non-reducing sugars with two pyranose and one furanose ring, maltotriose is a reducing sugar composed of three pyranose glucose subunits. While the reducing end is expected to interchange between α - and β -anomers in solution via mutarotation, glucose is rarely found in five-membered ring forms.³⁵⁰ Therefore, only pyranose forms for the reducing end of maltotriose are considered. Although protocols for ^{18}O -labeling of reducing sugars are available, isotope labeling of maltotriose was not performed here to avoid inaccurate interpretation of mass spectra where ^{18}O and deuterium peaks overlapped. Therefore, isomeric fragment pairs such as B_2/Z_2 and C_1/Y_1 are compared together in the same manner as for melezitose and raffinose.

Similar to patterns observed for melezitose and raffinose, deuteration levels of B_2/Z_2 fragments of sodium-adducted maltotriose were higher than deuteration levels of C_1/Y_1 fragments, although the differences are less pronounced (Figure 5.5A, Tables D.15-17). Overlaps between the two fragments were observed for maltotriose fragments, compared to melezitose and raffinose fragments. Electronic structure calculations of maltotriose show that fragmentation to generate B_2/Y_1 and Z_2/C_1 fragments are likely initiated by secondary hydroxyls of the middle glucose, particularly the one at the $\text{O}(2')\text{H}$ position, rather than the primary hydroxyl at the $\text{O}(6')\text{H}$ position (Figure 5.5B, Figure D.5). The average distance between the secondary $\text{O}(2')\text{H}$ hydroxyl hydrogen and the first glycosidic oxygen, $\text{O}(2')\text{H}-\text{O}(4')$, is $3 \pm 1 \text{ \AA}$, but only three of the ten examined conformations showed the $\text{O}(2')\text{H}$ hydroxyl hydrogen forming a hydrogen bond with the glycosidic oxygen $\text{O}(4')$ (Table D.18). The average distance between the secondary

O(2')H hydroxyl hydrogen and the second glycosidic oxygen, O(2')H—O(4), is 3.4 ± 0.3 Å. The average distances between the primary O(6')H hydroxyl hydrogen to the two glycosidic oxygens, O(4') and O(4), are 4.9 ± 0.2 Å and 6.0 ± 0.7 Å, respectively, suggesting that protonation of the glycosidic oxygens by the O(6')H primary hydroxyl hydrogen is less likely than by the O(4')H secondary hydroxyl. Therefore, our earlier hypothesis that the difference in deuteration levels between fragments reflect varying exchange rates of primary and secondary hydroxyls is not appropriate for maltotriose fragments.

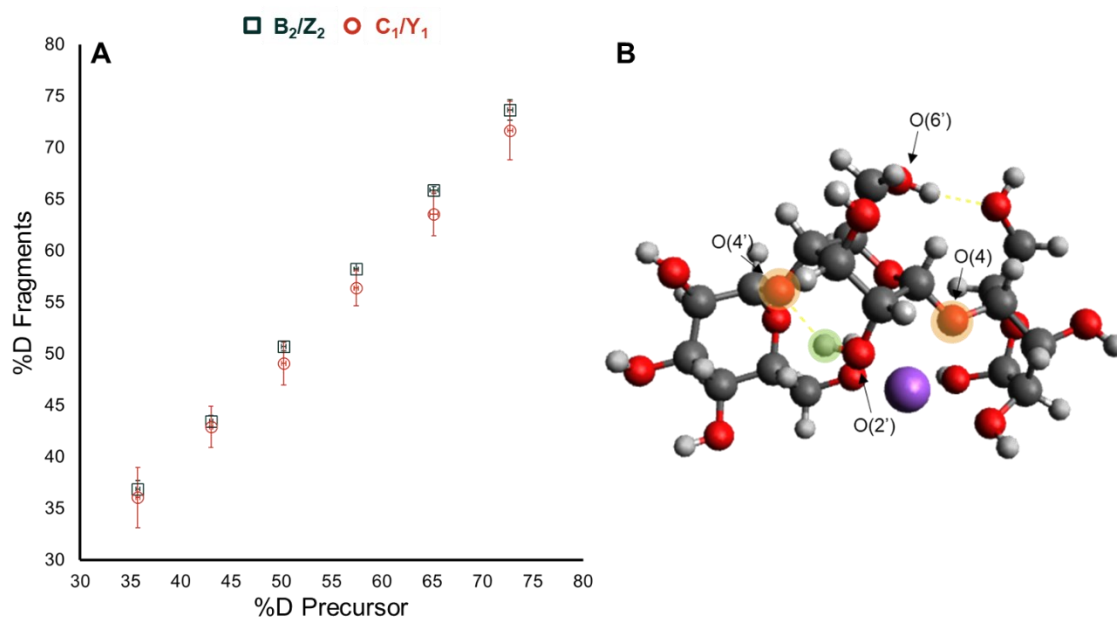


Figure 5.5. (A) Deuteration plots of B₂/Z₂ (navy square) and C₁/Y₁ (red circle) fragments generated from sodium-adducted maltotriose and (B) representative structure of a maltotriose-sodium complex optimized by DFT calculations. Carbon atoms are shown in gray, oxygen atoms in red, hydrogen atoms in white, and the sodium ion in purple. The glycosidic oxygens (O(4') and O(4)) are highlighted in orange. The most likely source of hydrogen to initiate the glycosidic bond cleavage (O(2')H) is highlighted in green.

Although ¹⁸O isotope-labeling of the anomeric hydroxyl was not performed in our experiment, Tsai *et al.* reported that both C₁ and Y₁ fragments were observed at similar

intensities from fragmentation of sodium- and lithium-adducted maltose, a disaccharide form of maltotriose.³⁵¹ Therefore, we hypothesize that both isomeric pairs of B₂/Y₁ and Z₂/C₁ are produced (Figure D.5). The identification of maltotriose fragments is particularly important when assigning deuterium labels because the hydroxyl at the anomeric carbon on the reducing end is the most acidic of the five hydroxyls of the monosaccharide¹¹⁹ and is expected to have a higher exchange rate than primary hydroxyls. The high standard deviation observed for the C₁/Y₁ fragments of sodium-adducted maltotriose also suggests the presence of multiple isomeric species at different deuteration levels, leading to more variability within the averaged percent deuteration values. However, electronic structure calculations of sodium-adducted maltotriose suggest that formation of Z₂/C₁ is more likely than B₂/Y₁, based on the distance between O(2')H—O(4') (Table D.19).

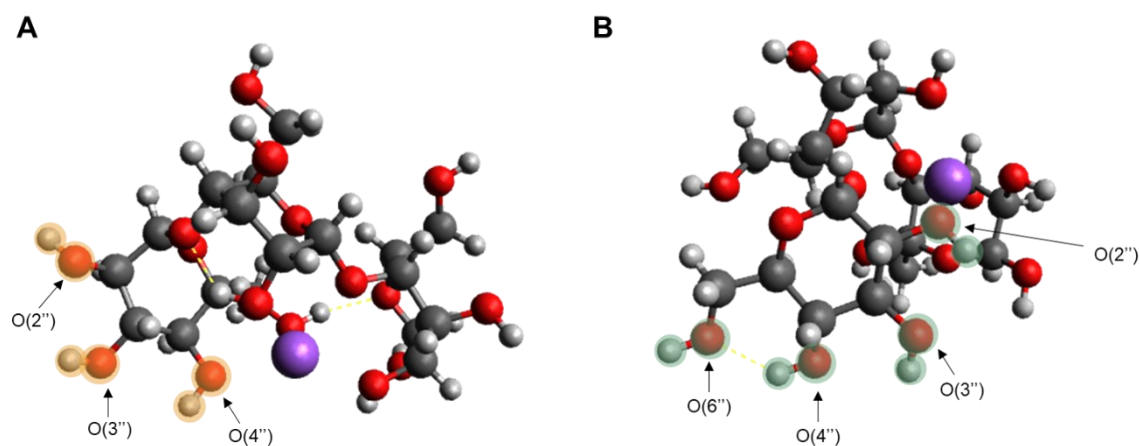


Figure 5.6. Representative structures of maltotriose-sodium complexes with extensive hydrogen bonding networks on the non-reducing end. Carbon atoms are shown in gray, oxygen atoms in red, hydrogen atoms in white, and the sodium ion in purple. The hydroxyls involved in the hydrogen bonding network are highlighted in (A) yellow for O(4'')H—O(3'')H—O(2'')H and (B) green for O(2'')H—O(3'')H—O(4'')H—O(6'')H. Notice that the directions of the two networks are opposite.

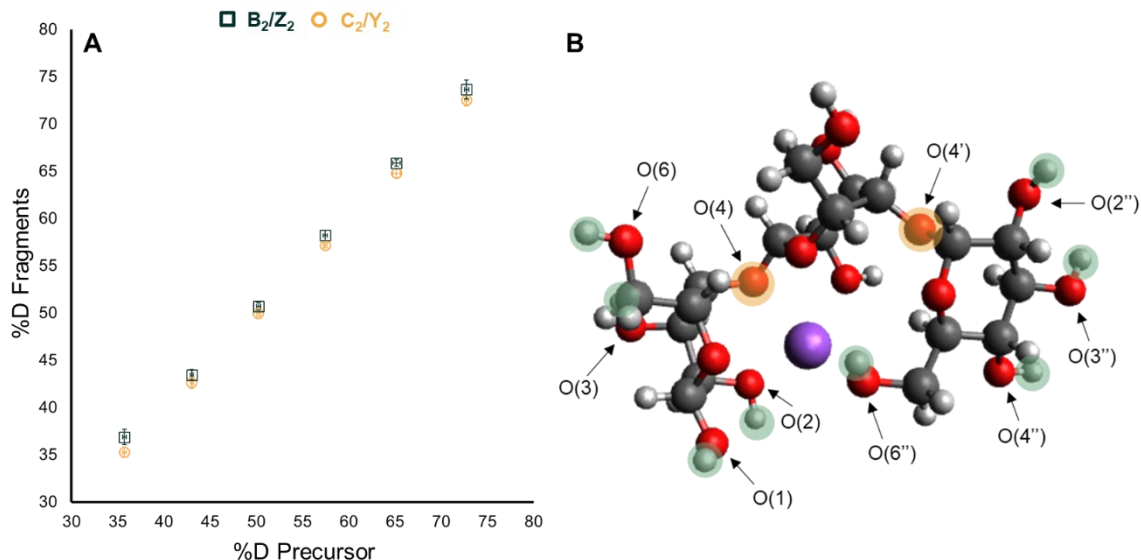


Figure 5.7. (A) Deuteration plots of B₂/Z₂ (navy square) and C₂/Y₂ (golden circle) fragments generated from sodium-adducted maltotriose and (B) representative structure of a maltotriose-sodium complex optimized by DFT calculations. Carbon atoms are shown in gray, oxygen atoms in red, hydrogen atoms in white, and the sodium ion in purple. The glycosidic oxygens, O(4) and O(4'), are highlighted in yellow. The hydroxyl hydrogens that would need to be donated to the glycosidic oxygens to produce the C₂ and Y₂ fragments are highlighted in green.

Optimized structures of maltotriose-sodium complexes revealed the presence of extended hydrogen-bonding network on the non-reducing end. Both O(4'')H—O(3'')H—O(2'')H and O(2'')H—O(3'')H—O(4'')H—O(6'')H interactions have been observed (Figure 5.6). Regardless of the direction of the hydrogen bonding, such an extensive network is expected to affect the solvent-hydroxyl interactions, as discussed earlier for raffinose, and induce hydrophobic solvation effects. Some intramolecular hydrogen bonding was observed on the reducing end as well, particularly for O(2)H—O(1)H, but the interactions involved smaller numbers of hydroxyls for the reducing end and were also less common. Therefore, we hypothesize that the hydrogen-bonding network on the non-reducing end likely increased the deuteration on the non-reducing end. C₁ and B₂ fragments contain the terminal glucose from the non-reducing end, whereas Y₁ and Z₂

fragments have the glucose on the reducing end with the anomeric hydroxyl. Regardless of which fragment pairs are detected at higher intensity, whether C₁/B₂ or Y₁/Z₂, we hypothesize that these structural difference between B₂/Z₂ and C₁/Y₁ fragments is minimal due to the terminal sugars equally affecting both fragment types.

Comparison of the %D between the C₂/Y₂ and B₂/Z₂ fragments of maltotriose revealed similar patterns to the one observed between C₁/Y₁ and B₂/Z₂ (Figure 5.7A, Table D.19-21). Previous literature examining maltotriose with an ¹⁸O-labeled anomeric hydroxyl in a deprotonated state favored formation of C₂ fragments over Y₂ fragments³⁵², retaining charge on the non-reducing end. Ion mobility of lithium-adducted trisaccharides revealed that two distinct arrival time distributions were observed for the C₂/Y₂ fragment of maltotriose, with one distribution detected at ten times the intensity of the other, as opposed to a single, compact feature for either melezitose or raffinose.³⁵³ However, DFT optimizations of maltotriose-sodium complexes showed very few conformations in which a clear hydroxyl contribution to the glycosidic oxygen would produce the C₂/Y₂ fragments (Figure 5.7B). One hypothesis that may explain our computational results is that the C₂/Y₂ fragments of maltotriose may be primarily products of secondary fragmentation, such as from the dehydrated precursors. It has been shown that dehydration occurs for reducing sugars with metal adducts, with high preference for the loss of H₂O occurring from the anomeric carbon on the reducing end^{324, 354, 355}, although dehydration may also occur on the non-reducing end.^{355, 356} Such dehydration products can also undergo additional fragmentation to produce glycosidic bond cleavage products such as B and C fragments, which are predominantly on the non-reducing side.³⁵⁶ Again, regardless of which fragment pairs are detected at higher intensity, we hypothesize that

both the reducing and non-reducing ends of maltotriose have similar levels of deuteration, leading to minimal difference in deuteration levels between B₂/Z₂ and C₂/Y₂ fragments.

5.5 Conclusion

Deuterium labels on fragments generated from sodium-adducted trisaccharides were assigned. The deuteration levels of fragments are closely linked to the fragmentation processes of each carbohydrate-metal complex. We hypothesize that the difference in exchange rates between primary and secondary hydroxyls and solution-phase intramolecular hydrogen bonding networks are reflected in the deuteration levels of fragments. Our hypothesis is supported from our comparison of isomeric carbohydrates that have contributions from different hydroxyl locations towards the glycosidic bond dissociation. We have provided groundwork for structural assignments of carbohydrate isomers via HDX-MS with our method combining experimental and computational approaches to correlate carbohydrate conformations and fragmentation pathways. Our method provides in-depth interpretations of carbohydrate structures and HDX patterns by computationally examining populations of carbohydrate conformations derived from simulations of evaporating ESI droplets, rather than a single theoretical conformation, thus better representing carbohydrate flexibility. Assigning deuterium labels based on conformations and therefore expected fragmentation pathways, instead of exchange rates alone, adds another dimension to the analysis that is crucial for molecules with rapidly exchanging functional groups that have a narrow range of exchange rates. Because we have validated deuterium assignment based on common motifs observed for carbohydrates, such as exchange rates of primary and secondary hydroxyls,

intramolecular hydrogen bonding, and linkage patterns, we expect that future HDX-CID-MS analysis of carbohydrates with similar structures may be achieved with experimental data alone. Therefore, our novel method lays out a significant step towards expanding the boundaries of HDX for the structural analysis of carbohydrates.

5.6 Acknowledgments

This work was supported by the Welch Foundation, Grant AA-1899. The authors acknowledge the Baylor University Mass Spectrometry Center and Baylor University High Performance and Research Computing Services.

CHAPTER SIX

Summary and Future Directions

6.1 Summary

Glycan analysis is significant for understanding cellular biology as well as scientifically intriguing due to the diverse and complex nature of carbohydrates and the analytical challenges they pose. While extensive research on carbohydrates is performed in numerous fields of science, three-dimensional structural analysis of carbohydrates is still limited. Multiple novel methods were presented here, especially regarding application of rapid hydrogen/deuterium exchange (HDX) for structural analysis of carbohydrates containing rapidly-exchanging hydroxyls. Carbohydrates were analyzed via mass spectrometry (MS) with some complementary studies using computational calculations.

Chapter One provided an overview for basic monosaccharides, analytical techniques currently employed in analysis of carbohydrates with emphasis on MS, and a brief introduction to HDX in the context of labeling rapidly exchanging functional groups.

In Chapter Two, we reported the in-source HDX effect of residual solvent vapors on carbohydrate hydroxyls. The build-up of residual water or methanol vapors from previous runs, as well as solvent from the current sample make up, resulted in accumulation of solvent vapors in electrospray sources and in-ESI HDX that overwrote solution-phase labeling. The residual solvent vapor HDX effect not only affected

carbohydrate hydroxyls but also other rapidly exchanging functional groups on peptides. Our report provides significant insight into analysis of other biomolecules, such as proteins, especially when deuterating reagent is present in the sample, because rapidly exchanging functional groups are affected by in-ESI HDX yet commonly disregarded. Our finding also laid groundwork for other investigations reported here because of our observation of carbohydrate hydroxyls undergo HDX during ESI.

Chapter Three explored utilization of double-barrel ESI tips, called theta-ESI emitters for rapid-labeling HDX of carbohydrates during ESI. Labeling in the microsecond timescale was achieved by spraying D₂O coaxially to carbohydrates. Deuteration time was manipulated by varying the spray tip diameter, affecting the initial ESI droplet sizes and thus changing the droplet desolvation time. Because carbohydrate-metal complexes in the gas phase do not undergo HDX, the exchange time was effectively limited by the droplet lifetime, which was measured by protein folding experiments. Our report illustrating the use of theta-ESI HDX is a significant step towards applying solution-phase HDX to carbohydrate analysis for biologically relevant structures, because the rapid exchange rate of hydroxyls has limited the ability to control the exchange time and thus obtain multiple deuteration stages for comparison. Controlling the exchange time is a crucial part of HDX for structural analysis because the difference in deuteration levels at two different timepoints give meaningful information based on exchange at various sites of the analyte as well as dynamics.

Chapter Four presented a novel application of collision induced dissociation (CID) for localization of deuterium labels on carbohydrate-metal complexes. We investigated the effect of vibrational activation on scrambling of sodium- and calcium-

adducted carbohydrates. We also observed that carbohydrate fragments were detected at varying levels of deuteration and linked the differences to carbohydrate fragmentation mechanisms to assign the labels. Specifically, the faster exchange rate of primary hydroxyls compared to secondary hydroxyls more likely led to more back-exchange during ESI, altering the percent deuteration (%D) for different fragments. Our findings provide a novel approach to carbohydrate analysis using HDX, because the rapid exchange rates of primary and secondary hydroxyls have traditionally been presented together. The ability to detect and interpret the close difference in exchange rates between primary and secondary hydroxyls is a significant contribution for HDX of carbohydrates, which typically have limited variety in functional groups.

In Chapter Five, we expanded our method in Chapter Four to investigate differences in isomeric trisaccharides that each have unique fragmentation pathways and illustrated the correlation between deuterium labels and carbohydrate conformations. Specifically, computational approaches were employed to obtain optimized gas-phase carbohydrate structures to determine the source of hydrogens used in each isomer for respective fragmentation pathways. Deuterium labels on carbohydrates were assigned by tracking the hydrogen that was used for initiating glycosidic bond cleavages. Therefore, we presented a novel application of HDX-MS/MS that is easily accessible by common mass spectrometers with CID, which provides multi-dimensional insight, including the carbohydrate conformation, fragmentation pathway, and local exchange rates that vary for carbohydrate isomers. Thus, our reports provide groundwork for in-depth interpretation of HDX patterns on carbohydrates, whose analysis has been limited by the heterogeneous and complex nature of isomeric sugars.

Overall, the work presented here has expanded the boundaries of traditional HDX for structural analysis of carbohydrates. We achieved rapid solution-phase labeling and assigned deuterium labels on functional groups that are closely related in exchange rates. While our work has focused on characterization of carbohydrates and hydroxyls, the implications of our findings extend to other biomolecules with rapidly exchanging functional groups, such as peptide side chains.

6.2 Future Directions

The work presented here have been performed with trisaccharide model systems that were adequate for proof-of-concept but smaller and less complex than glycans found in biological samples. Our work could be expanded to analyze larger oligosaccharides with more diverse functional groups and monosaccharide subunits.

The ability to vary HDX time in the microsecond timescale using theta-ESI emitters would enable comparative analysis of glycan isomers in the traditional time versus deuteration plot used for proteins. We expect that application of short time HDX for glycan analysis would be useful for obtaining not only structural and conformational details, but also dynamic properties of glycans which are highly flexible in solution. Furthermore, glycan-protein or glycoprotein-protein interactions may be explored by comparing free glycans against the interacting complexes. For interaction analysis, labeling can be achieved in both hydroxyls on glycans as well as side chains of proteins. The rapid labeling could be used to detect short-lived interactions, or more stable complexes that could be dissociated in the gas phase to observe local labeling.

Our HDX-CID-MS could be coupled to real-time online separations from LC to analyze mixtures of glycans. While every peak in the deuterated precursor distribution

was isolated and fragmented in Chapters Four and Five, the CID method could be modified to fragment the representative peak in the lower, middle, or higher %D part of the distribution. Coupling to separation techniques would enable HDX analysis of mixtures that would previously have required two different steps for separation and HDX. Similarly, glycans can be analyzed by using HDX-CID and ion mobility in tandem to achieve gas-phase separation of ions for additional structural information. For instance, carbohydrates that are observed in multiple conformations via IM-MS, due to changes in structure from metal adduction, may benefit from localization of deuterium labeling to obtain additional insight into structural shifts.

Finally, other types of fragmentation, such as electron transfer dissociation (ETD), which is commonly used for HDX-MS/MS experiments, can also improve our understanding of glycan conformations and fragmentation pathways as additional fragments could be obtained. Different fragmentation techniques have distinct fragmentation mechanisms, and deuterium labels on diverse locations may be tracked by changing fragmentation methods.

APPENDICES

APPENDIX A

Supplementary Information for Chapter Two: Mass Spectral Detection of Forward- and Reverse-Hydrogen/Deuterium Exchange Resulting from Residual Solvent Vapors in Electrospray Sources

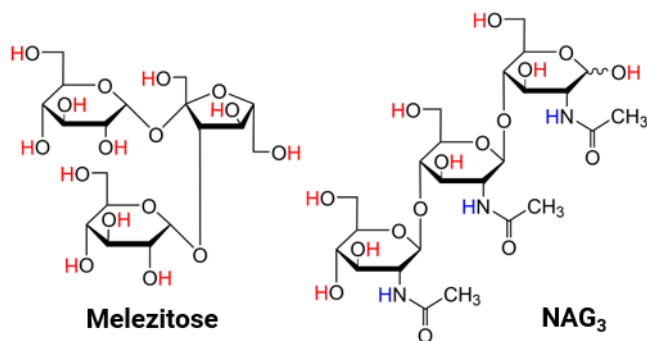


Figure A.1. Structures of melezitose and tri-*N*-acetylglucosamine (NAG₃). Both carbohydrates contain 11 labile hydrogens, including hydroxyls (red) and acetamido hydrogens (blue).

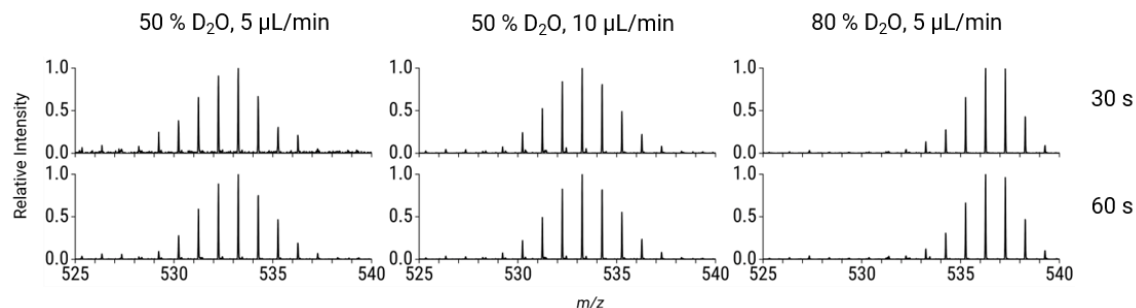


Figure A.2. HDX spectra of sodiated-melezitose in mixtures of D₂O and H₂O. Spectra were collected after pre-equilibrating the source with a solvent composition matching that of the sample: 50 % D₂O and 50 % H₂O or 80 % D₂O and 20 % H₂O. Representative mass spectra are shown following 30 s (top) and 60 s (bottom) of in-solution HDX labeling time.

The LockSpray Exact Mass Ionization Source of a Waters Synapt G2-S HDMS was pre-equilibrated with mixtures of D₂O and H₂O matching the solvent composition of the sample. Samples were infused at 5 μL/min or 10 μL/min. The source was not evacuated between runs.

Figure 2.2 of the paper showed that deuterium uptake increased with increasing sample infusion rate. However, pre-equilibration of the source with solvent matching the sample composition resulted in a constant deuterium uptake regardless of in-solution HDX time or sample flow rate. Sodiated-melezitose in 50 % D₂O was ~50 % deuterated at both infusion rates and after 30 s and 60 s of in-solution HDX. Sodiated-melezitose in 80 % D₂O remained ~80 % deuterated after in-solution HDX for 30 s or 60 s. Similar spectra were observed over approximately five minutes of data collection.

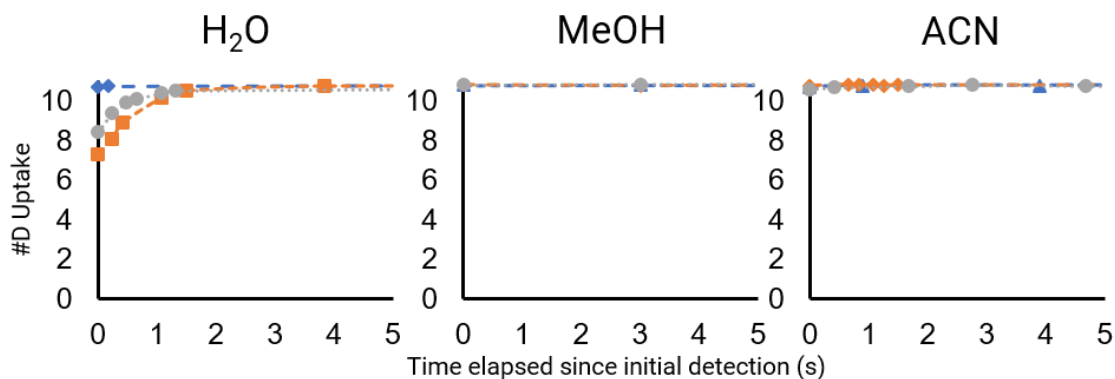


Figure A.3. Residual solvent vapors caused in-ESI HDX of sodiated-melezitose. Proton uptake of deuterated melezitose-sodium adducts is plotted for each replicate following pre-equilibration of the source with H₂O, methanol (MeOH), or acetonitrile (ACN). The number of deuterium exchanges is plotted versus time.

The experiments were performed in a Waters Synapt G2-S with LockSpray Exact Mass Ionization Source. The experimental procedure was described in the Experimental section of the paper, titled ‘HDX following pre-equilibration of the source.’

Acetonitrile, which does not have labile hydrogens, was used as a control and had a constant deuterium content of $97.2 \pm 0.5 \%$ (10.77 ± 0.05 D). Up to $\sim 15 \%$ back exchange was observed at the earliest time points following pre-equilibration with H₂O, whereas up to $\sim 9 \%$ back exchange was observed from pre-equilibration with methanol. Following pre-equilibration with H₂O, the deuteration level increased from 9 ± 1 D ($80 \pm 20 \%$) at $t = 0$ s to 10.754 ± 0.006 D ($97.16 \pm 0.06 \%$) after 20 s. Pre-equilibration with MeOH resulted in deuteration of 10.6 ± 0.4 D ($96.0 \pm 0.4 \%$) at $t = 0$ s and 10.79 ± 0.06 D ($97.4 \pm 0.4 \%$) after 20 s. The data for MeOH and H₂O are consistent with the data presented in Figure 2.3.

Examining the relationship between source temperature and residual solvent vapor HDX. The LockSpray Exact Mass Ionization Source of a Waters Synapt G2-S HDMS was pre-equilibrated with D₂O for 5 minutes at a flow rate of 20 µL/min. Then, melezitose and NaCl mixtures were infused for 2 minutes at a flow rate of 10 µL/min. To equilibrate the source back to atmospheric conditions, the source was then evacuated for 20 minutes with no solvent entering the source and with the capillary voltage set to 0 kV. Experiments were run in triplicate with the source at three temperatures, on two different days. The goal of these experiments was to determine if a higher source temperature, the temperature of the capillary from source cone into vacuum chamber, resulted in faster evacuation of residual D₂O vapor. The temperatures were selected around the boiling point of water to examine the correlation of residual solvent HDX and solvent volatility; however, the maximum temperature of the source was 150 °C. Initial detection of signal with ion count > 500 and S/N > 3 was set to t = 0 s. We calculated the time for the deuterium level of sodiated-melezitose to decrease to 95 % of the initial deuterium content.

Table A.1. Effect of source temperature on the time required for the initial deuterium uptake to decrease by 95 %

Source Temperature Variations						
	Day 1			Day 2		
Replicates	100 C	120 C	150 C	80 C	100 C	150 C
1	1.65 s	2.03 s	2.93 s	1.71 s	1.89 s	2.35 s
2	2.10 s	2.46 s	2.33 s	1.27 s	1.78 s	1.75 s
3	2.12 s	3.20 s	2.31 s	2.51 s	1.35 s	1.82 s
Average	1.96 s	2.56 s	2.52 s	1.83 s	1.67 s	1.97
Stdev	0.27	0.59	0.35	0.63	0.29	0.33
Range	1.7-2.3 s	2.0-3.2 s	2.1-2.9 s	1.2-2.4 s	1.4-2.0 s	1.5-2.1 s

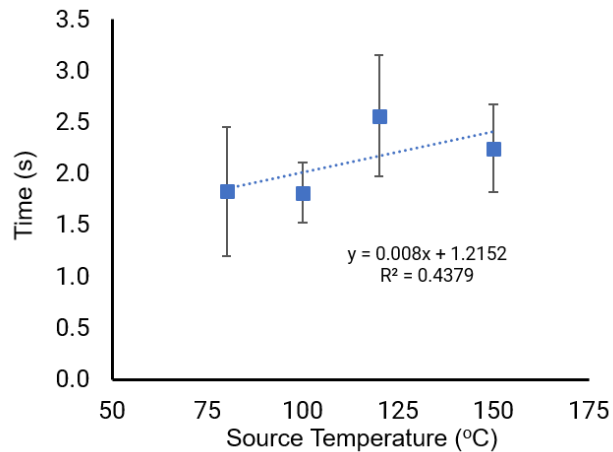


Figure A.4. Correlation plot illustrating no observable relationship between source temperature and time for deuterium uptake to decrease by 95 %. Data points are the average values with error bars illustrating the standard deviations of a minimum of three replicate measurements.

The desolvation temperature was also varied. The desolvation temperature is the temperature of the high-flow desolvating gas that aids in desolvation of the analytes from droplets. We calculated the length of time between observing the 10D peak and the 1D peak.

Table A.2. Effect of desolvation temperature on residual solvent vapor HDX. The rate of deuterium loss at the two desolvation temperatures were within the error of the measurements.

Desolvation Temperature		
Replicates	120 C	350 C
1	6.24 s	3.24 s
2	5.76 s	5.82 s
3	5.34 s	5.58 s
Average	5.78 s	4.88 s
Stdev	0.45	1.43
Range	5.3-6.2 s	3.5-6.3 s

Examining the relationship between source gas flow rates and residual solvent HDX. The LockSpray Exact Mass Ionization Source of a Waters Synapt G2-S HDMS was pre-equilibrated with D₂O for 5 minutes at a flow rate of 20 µL/min. Then, melezitose and NaCl were infused for 2 minutes at a flow rate of 10 µL/min. To equilibrate the source back to atmospheric conditions, the source was then evacuated for 20 minutes with no solvent entering the source and with the capillary voltage set to 0 kV. During evacuation, all pressures were set to control conditions, (cone gas = 60 L/h, desolvation = 500 L/h, and nebulizer = 6.0 bar) so that the evacuation occurred under the same conditions. Experiments were run in triplicate. The effects of cone gas, desolvation gas, and nebulizer gas flow were examined to determine if increasing the pressure in the closed source changed the rate of evacuation of residual D₂O vapor. Initial detection of signal with ion count > 500 and S/N > 3 was set as t = 0 s. We calculated the time for the deuterium level of sodiated-melezitose to decrease to 95 % of the initial deuterium level.

Table A.3. Effect of gas flow rates on residual solvent vapor HDX

Pressure Variations									
	Cone Gas (L/h)			Desolvation Gas (L/h)			Nebulizer Gas (Bar)		
Run	10	60	160	200	500	800	2.5	4.0	6.0
1	1.86 s	2.40 s	1.85 s	2.01 s	2.40 s	1.54 s	2.07 s	1.58 s	2.40 s
2	1.30 s	3.24 s	3.14 s	5.95 s	3.24 s	0.98 s	1.88 s	0.88 s	3.24 s
3	2.03 s	1.99 s	1.59 s	2.66 s	1.99 s	1.66 s	1.90 s	1.51 s	1.99 s
4	1.11 s					2.85 s			
Average (s)	1.58	2.54	2.19	3.54	2.54	1.76	1.95	1.32	2.54
Stdev (s)	0.44	0.64	0.83	2.11	0.64	0.79	0.1	0.39	0.64
Range (s)	1.2-2.0	1.9-3.1	1.4-3.0	2.0-6.0	1.9-3.1	1.0-2.6	1.9-2.1	0.9-1.7	1.9-3.1

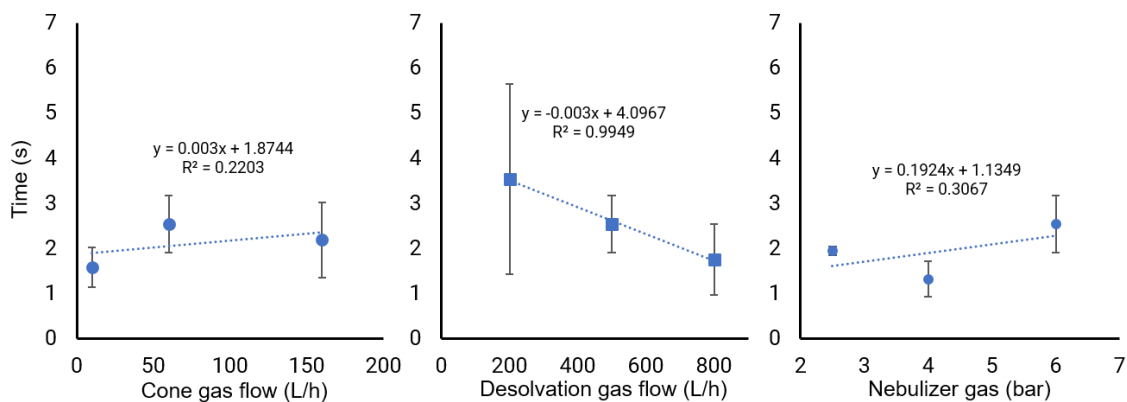


Figure A.5. Correlation plots of source gas flow rates and residual solvent vapor HDX. Data points are average values with error bars illustrating the standard deviations of three replicate measurements.

We hypothesized that increasing the gas flow rates could facilitate faster evacuation of the source and thus faster deuterium loss. However, no apparent correlation was found between the cone gas flow rate or nebulizer gas pressure and the rate of deuterium loss. Though an $R^2 > 0.99$ was observed for the correlation plot of desolvation gas flow rate versus time for deuterium loss, the large standard deviations for the data points made us question the validity of the relationship. Varying the gas flow rates also may have altered ionization efficiency as well as spray stability during these experiments. With such variabilities in ionization conditions, the time point at which the first signal was detected may not be representative of actual time that analytes were exposed to solvent vapors in the ionization source. Therefore, these measurements are likely limited by the experimental conditions.

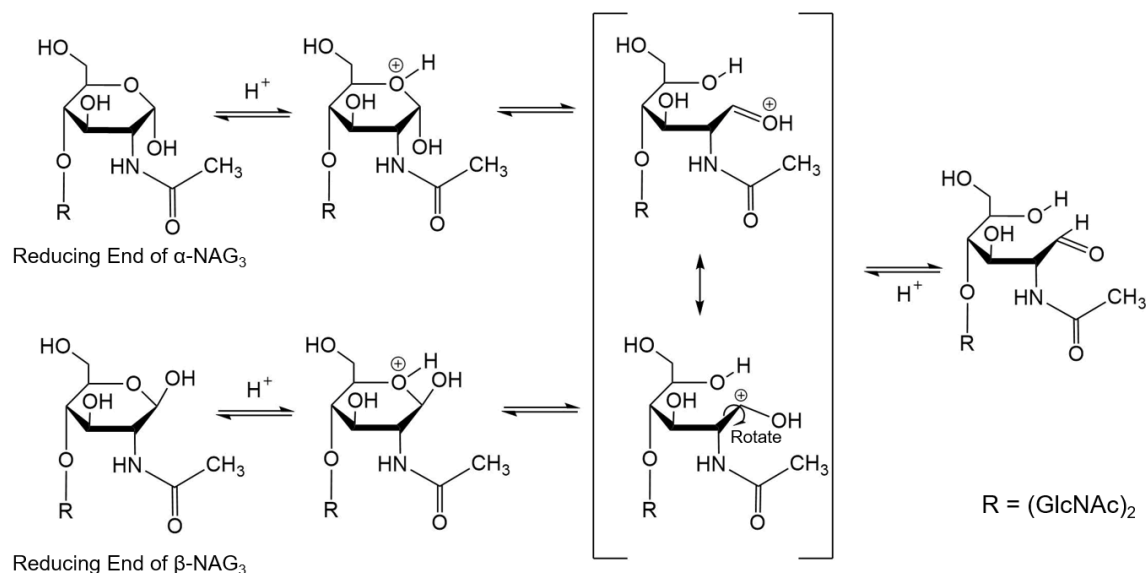


Figure A.6. Mechanism of mutarotation between α - and β -tri-*N*-acetylglucosamine (NAG₃).

In the ring-form of NAG₃, three hydroxyls are available for exchange in both the α and β isomers at the reducing end of the carbohydrate. Ring opening requires protonation (or deuteration) of the C5 oxygen, forming a hydroxyl. Additionally, ring opening results in the loss of the C1 hydroxyl as an aldehyde forms. Therefore, the total number of exchangeable hydroxyls remains the same in the chain and ring forms. In the intermediate structures, a fourth hydroxyl may become available for labeling. However, the extra proton (or deuteron) introduces mass and charge that will alter the m/z detected by the MS, forming either a protonated (or deuterated) species or a doubly charged ion that is both protonated (or deuterated) and sodiated. Neither ion was detected with sufficient S/N to observe the carbohydrate with this additional proton (or deuteron).

On the other hand, mutarotation of carbohydrates is mediated by H₂O, and in our experiments, D₂O as well, which is a separate process from deuterium labeling and on a different timescale. Solvent-mediated mutarotation likely facilitates deuterium labeling of

the α/β hydroxyl, which may contribute to higher deuterium uptake for the C1 hydroxyl compared to other hydroxyls in the same molecule.

APPENDIX B

Supplementary Information for Chapter Three: Achieving Multiple Hydrogen/Deuterium Exchange Timepoints of Carbohydrate Hydroxyls Using Theta-Electrospray Emitters

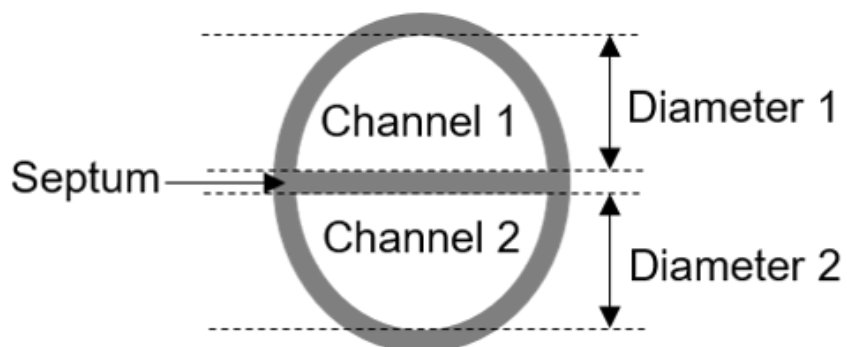


Figure B.1. Schematic drawing of a theta capillary cross-section. The two channels are divided by a glass septum. The height of each channel, measured perpendicular to the middle of the septum, is measured as the “outer diameter” because two separate droplets form from the two channels. The average of the diameters are calculated as the tip opening size.

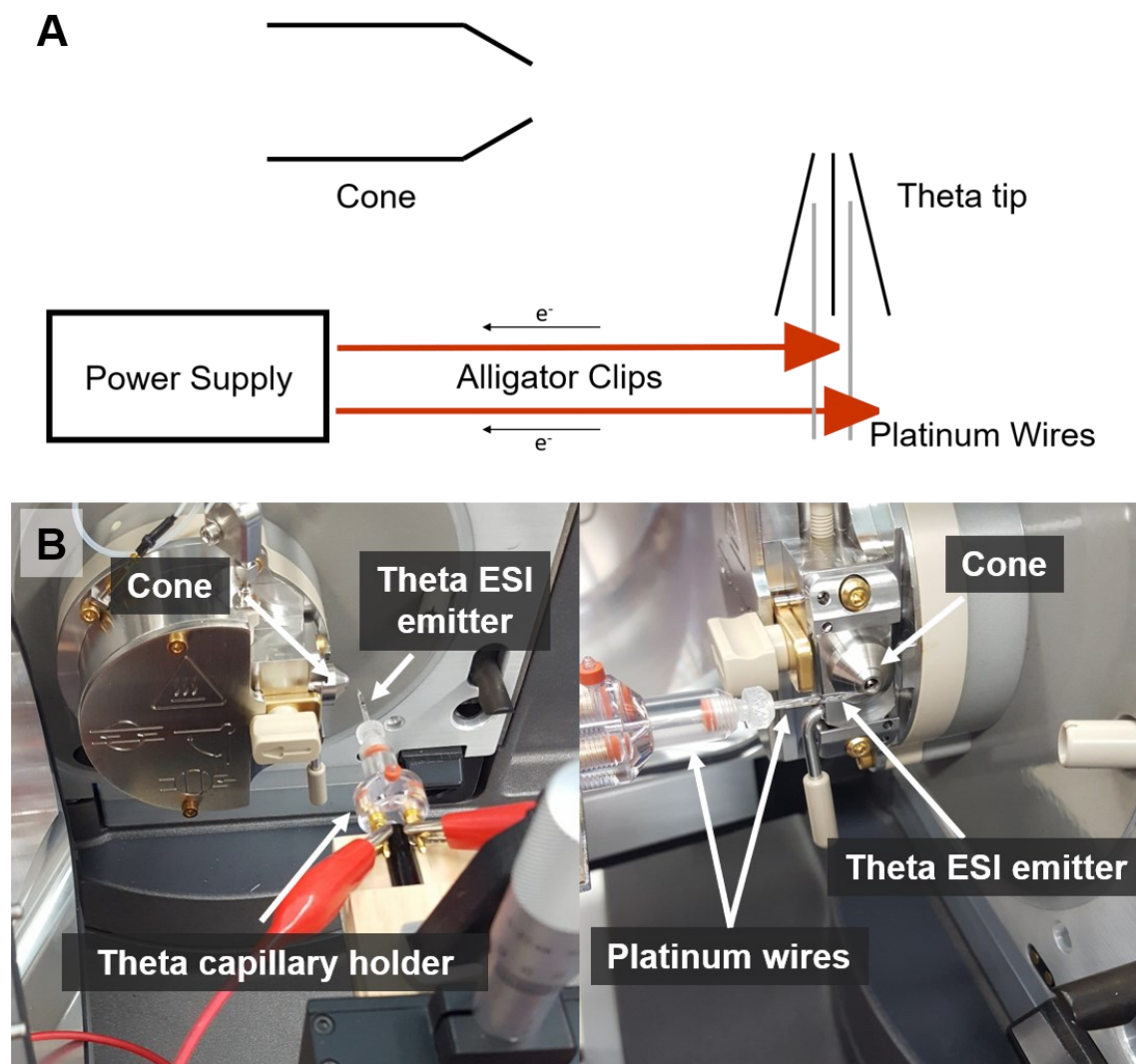


Figure B.2. (A) Diagram of the open-source setup used for theta-ESI experiments. Platinum wires are inserted into each barrel of the pulled theta tips and voltage is applied using alligator clips connecting the instrument power supply to the platinum wires. Due to the shape of the open instrument source and our XYZ setup, the theta tip was positioned so that the direction of the opening of the tip was perpendicular to the opening of the cone. (B) Pictures of the open-source setup used for theta-tip HDX experiments. A theta capillary holder (Warner Instruments, Hamden, CT) secures the pulled theta tips in place with the platinum wires inserted inside each barrel of the tip. The capillary holder system is mounted on an XYZ stage (Thorlabs, Newton, NJ) with a custom-built setup to secure the capillary holder.

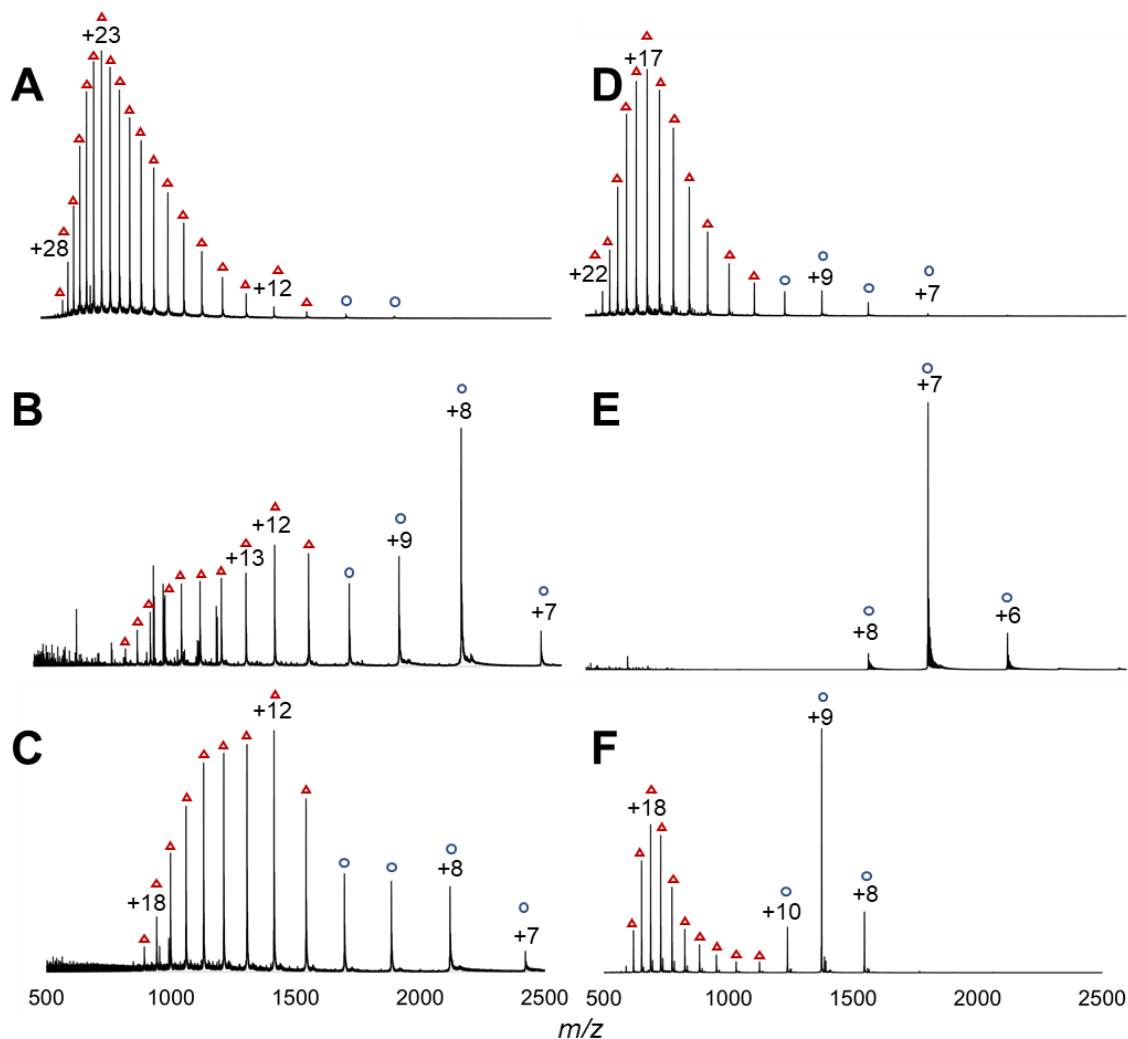


Figure B.3. Representative mass spectra of apomyoglobin (A-C, $4.5 \pm 0.3 \mu\text{m}$ channels) and cytochrome c (D-F, $20. \pm 9 \mu\text{m}$ channels) in protein folding experiments via theta tips. The top panels (A, D) represent denatured proteins in 0.1% formic acid, the middle panels (B, E) represent folded proteins at equilibrium in a premixed sample of denatured protein and 100 mM ammonium acetate at 1:1 (v/v), and the bottom panels (C, F) represent proteins folded during ESI after sprayed from theta tips. Protein folding via theta spray (C, F) show intermediate charge states between unfolded (A, D) and equilibrium (B, E) states. The peaks are labeled with blue circle and red triangle to show the charge states that have been used to calculate folded and unfolded populations, respectively, following the guidelines provided by Mortensen *et al.*^{273, 274}

Apomyoglobin has two folding states, one at a $7 \mu\text{s}$ time constant²⁷⁷ and one that occurs with a time constant greater than 1 ms,³⁵⁷ to which we attribute the multi-modal distribution observed for charge states of apomyoglobin in equilibrium. The presence of

both folded and unfolded charge states for apomyoglobin and primarily folded states for cytochrome *c* at equilibrium (B and E) are consistent with the previous reporting of Mortensen *et al.*^{273, 274}

APPENDIX C

Supplementary Information for Chapter Four: Deuterium Localization with Minimal Scrambling on Carbohydrate-Metal Complexes via Collision Induced Dissociation

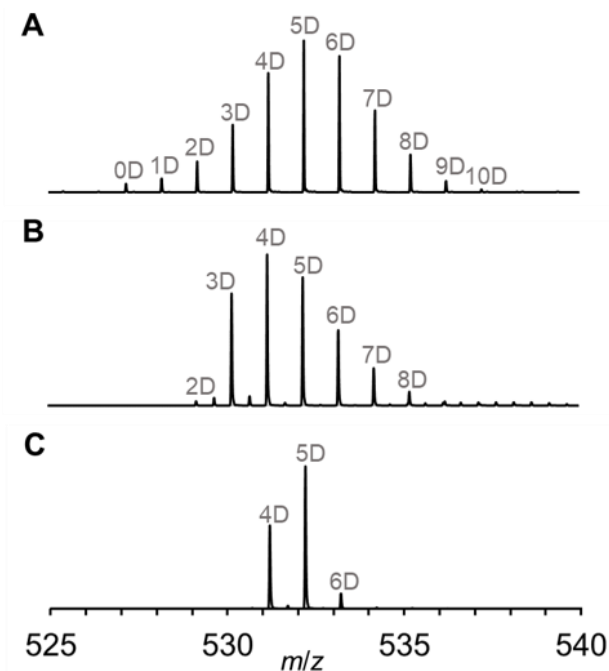


Figure C.1. Representative mass spectra of (A) [Melezitose+Na]⁺ at 50% deuteration and [M+Na+5D]⁺ (*m/z* 532) isolated with LM Res parameters of (B) 4.9 and (C) 15.0. A higher LM Res parameter resulted in narrower isolation windows. Increasing the LM Res parameter above 15.0 resulted in loss of signal. Unlabeled peaks are noise.

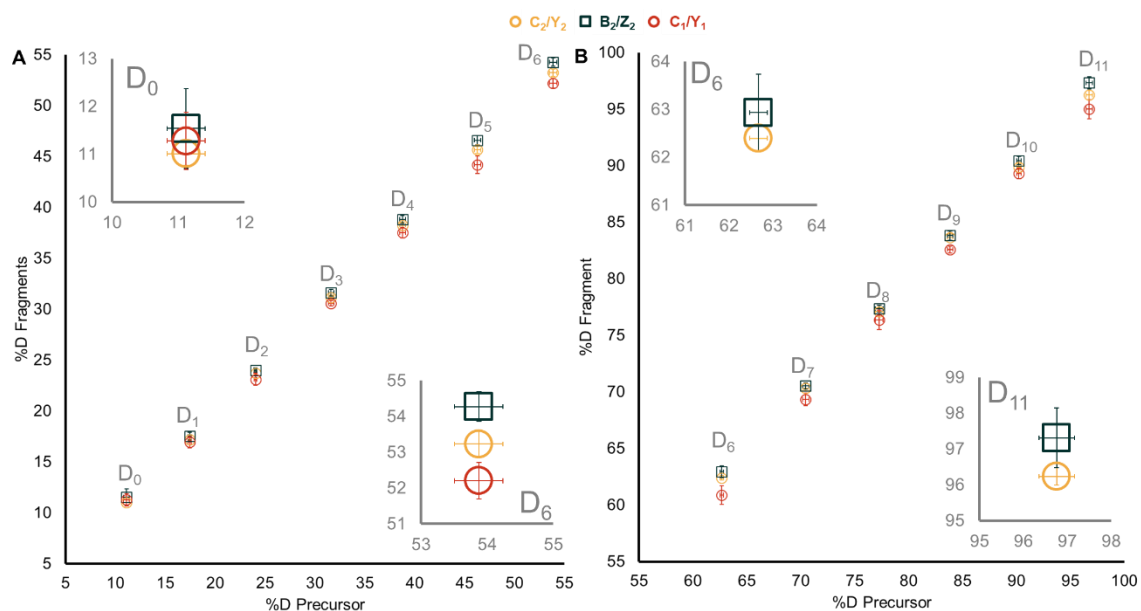


Figure C.2. Deuteration plots of B₂/Z₂ and C₂/Y₂ fragments generated from sodium-adducted melezitose in (A) 25% and (B) 75% D₂O. In all deuteration conditions, B₂/Z₂ fragments were detected at higher deuteration levels compared to C₂/Y₂ fragments when higher %D precursors were fragmented. In 25% D₂O, B₂/Z₂ was detected at higher deuteration level compared to its glycosidic bond cleavage pair, C₁/Y₁, when higher %D precursors were fragmented. In 50% and 75% D₂O, B₂/Z₂ was detected at higher deuteration levels compared to C₁/Y₁ across the whole precursor distribution. Insets in (B) only show C₂/Y₂ and B₂/Z₂ fragments because the difference in deuteration levels can be seen for C₁/Y₁ in the overall plot.

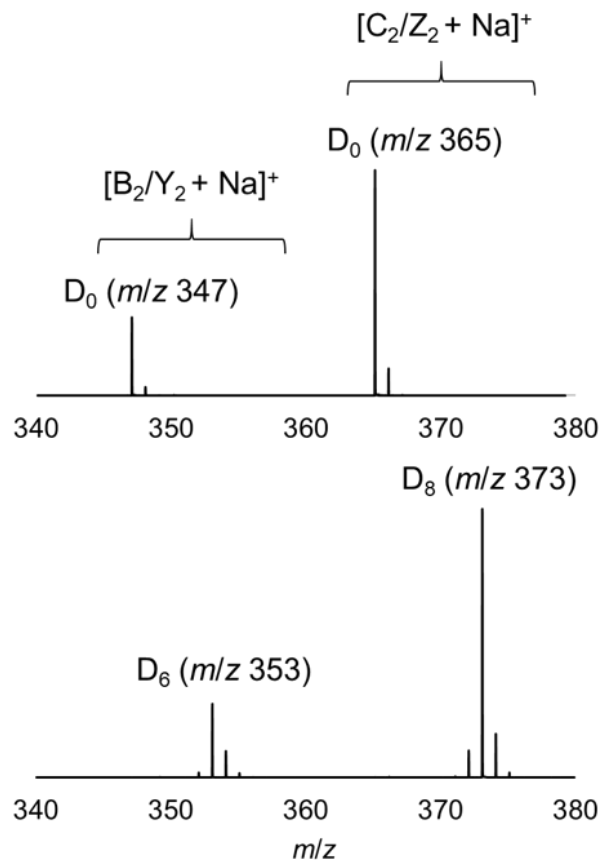


Figure C.3. Undeuterated (top) and fully deuterated fragment spectra (bottom) of sodium-adducted melezitose. The number of labile hydrogens for each fragment was calculated by obtaining the difference in the highest intensity m/z between undeuterated and fully deuterated fragments. The number of labile hydrogens on B/Y type fragments confirm a loss of hydrogen upon fragmentation (Scheme 4.1), as reported by Bythell *et al.*³¹⁰

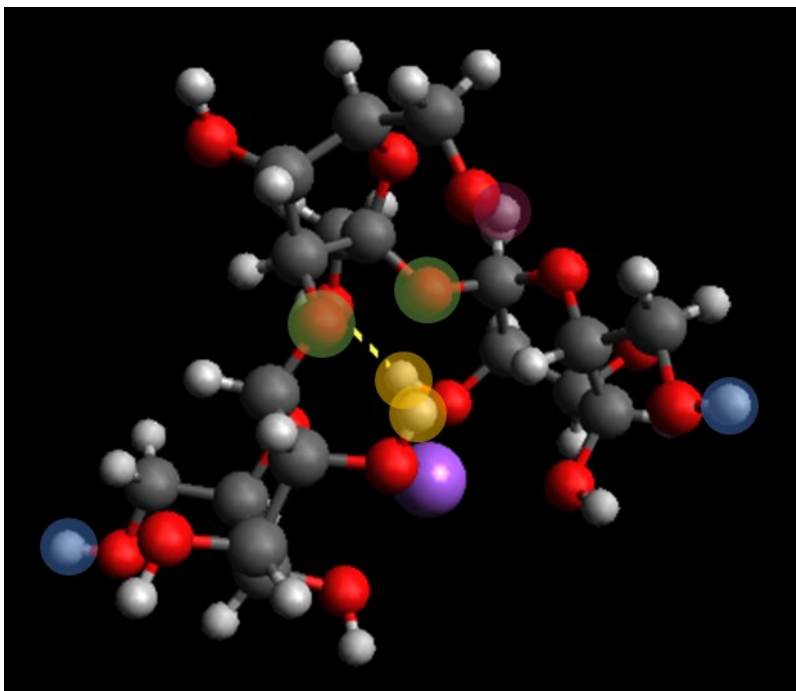


Figure C.4. Representative molecular structure of $[\text{Melezitose} + \text{Na}]^+$ complex. Structure optimization was achieved by DFT calculation. Sodium ion is located in the middle “pocket” of the melezitose trisaccharide. The two glycosidic oxygens of melezitose are highlighted in green. The two primary hydroxyls of the two terminal glucoses, both at the respective C-6 position, are highlighted in blue. The orientation of the primary hydroxyls (blue) and their distances to glycosidic oxygens (green) suggest that the protonation of glycosidic oxygens by primary hydroxyls of terminal glucoses is unlikely. On the other hand, the secondary hydroxyls at the O(2) and O(2'') positions of the terminal glucoses, highlighted in yellow, are in closer proximity to the glycosidic oxygens (green), the protonation of glycosidic oxygens by these secondary hydroxyls is likely more favorable. Therefore, fragmentation pathways generating B₁/Z₁ and C₂/Y₂ fragments likely involve secondary hydroxyl hydrogens. The primary hydroxyl of the middle fructose at the O(6') position is highlighted in purple, which is also located close to the glycosidic oxygens (green). Thus, protonation of glycosidic oxygen by a primary hydroxyl to generate B₂/Z₂ and C₁/Y₁ fragments is supported by the computational structure characterization.

Statistical significance testing of differences in deuteration levels between fragments

The difference in deuteration levels between two fragments was determined by a hybrid significance testing approach proposed by Hageman and Weis.³¹² Pooled standard deviations for the deuteration levels of either the precursor or fragment ions obtained for each experimental condition (% D₂O and charge carrier) were calculated by using the following equation:

$$s_{pooled} = \sqrt{\frac{(n_1 - 1)s_1^2 + (n_2 - 1)s_2^2 + \dots + (n_k - 1)s_k^2}{n_1 + n_2 + \dots + n_k - k}}$$

Standard error of the mean (SEM) was calculated by the following equation:

$$SEM = \sqrt{\frac{s_{pooled}^2}{n_1} + \frac{s_{pooled}^2}{n_2}}$$

The degrees of freedom (df) for each B₂/Z₂ and C₂/Y₂ pairs generated from the same precursor *m/z* (#D) was calculated by the following equation:

$$df = \frac{\left(\frac{s_1^2}{n_1} + \frac{s_2^2}{n_2}\right)^2}{\frac{\left(\frac{s_1^2}{n_1}\right)^2}{n_1 - 1} + \frac{\left(\frac{s_2^2}{n_2}\right)^2}{n_2 - 1}}$$

The *t* values were obtained from a two-tailed *t* distribution table at α 0.05 and 0.01. The confidence interval (CI) was calculated by multiplying the SEM by the *t* value and is reported as a range for values within measurement error.

Welch's *t*-test was performed using the equation:

$$t = \frac{\bar{x}_1 - \bar{x}_2}{\sqrt{\frac{s_1^2}{n_1} + \frac{s_2^2}{n_2}}}$$

For significance testing, two approaches were utilized. First, the difference in deuteration levels between the two fragments (%D diff) was obtained by subtracting the percent deuteration of C₂/Y₂ or C₁/Y₁ fragments from the percent deuteration of the B₂/Z₂ fragment. If %D diff was outside the range of the confidence interval, the difference in deuteration between the two fragments was marked as significance at the 95% or 99% confidence interval. The second approach to statistical significance testing utilized the Welch's *t*-test. Results were considered significantly different when $t_{\text{calc}} > t_{\text{table}}$. The deuteration levels of two fragments were marked significantly different when the difference in deuteration passed both criteria. If (1) %D diff was within the range for confidence intervals, (2) $t_{\text{calc}} < t_{\text{table}}$, or (3) both (1) and (2), then the difference in deuteration between the two fragments was marked not significant (N), meaning the values were within measurement error.

Table C.1. Test for statistical significance of differences in deuteration levels between B₂/Z₂ and C₂/Y₂ fragments from sodium-adducted melezitose in 25% D₂O. SEM is standard error of the mean, df is degrees of freedom, and CI is the confidence interval at each α value of 0.05 or 0.01. t calculated is compared against t values, and %D difference is compared against CI. If both t calculated and %D difference values exceed respective reference values at α value of 0.05 or 0.01, the difference in deuteration levels of two fragments are determined statistically significant at 95% or 99% confidence interval, respectively. If either or both values are within the ranges given for reference t or confidence interval, the difference in %D between the two fragments is not statistically significant (N).

Precursor	0D	1D	2D	3D	4D	5D	6D
SEM	0.245	0.245	0.245	0.245	0.245	0.245	0.245
%D B ₂ /Z ₂	11.54	17.51	24.00	31.64	38.84	46.60	54.28
%D C ₂ /Y ₂	11.01	17.21	23.69	31.16	38.26	45.66	53.23
df	13	15	20	20	20	21	22
t 0.05	2.160	2.131	2.086	2.086	2.086	2.080	2.074
t 0.01	3.012	2.947	2.845	2.845	2.845	2.831	2.819
CI 0.05	± 0.529	± 0.522	± 0.511	± 0.511	± 0.511	± 0.510	± 0.508
CI 0.01	± 0.738	± 0.722	± 0.697	± 0.697	± 0.697	± 0.694	± 0.691
%D diff	0.53	0.30	0.30	0.48	0.58	0.94	1.04
t calculated	2.11	2.46	3.32	4.11	4.24	5.67	6.51
	N	N	N	N	95%	99%	99%

Table C.2. Test for statistical significance of differences in deuteration levels between B₂/Z₂ and C₁/Y₁ fragments from sodium-adducted melezitose in 25% D₂O. SEM is standard error of the mean, df is degrees of freedom, and CI are confidence interval at each α value of 0.05 or 0.01. t calculated is compared against t values, and %D difference is compared against CI. If both t calculated and %D difference values exceed respective reference values at α value of 0.05 or 0.01, the difference in deuteration levels of two fragments are determined statistically significant at 95% or 99% confidence interval, respectively. If either or both values are within the ranges given for reference t or confidence interval, the difference in %D between the two fragments is not statistically significant (N).

Precursor	0D	1D	2D	3D	4D	5D	6D
SEM	0.245	0.245	0.245	0.245	0.245	0.245	0.245
%D B ₂ /Z ₂	11.54	17.51	24.00	31.64	38.84	46.60	54.28
%D C ₁ /Y ₁	11.28	16.93	23.11	30.59	37.51	44.21	52.21
df	20	19	15	21	20	16	21
t 0.05	2.086	2.093	2.131	2.080	2.086	2.120	2.080
t 0.01	2.845	2.861	2.947	2.831	2.845	2.921	2.831
CI 0.05	± 0.511	± 0.512	± 0.522	± 0.510	± 0.511	± 0.519	± 0.510
CI 0.01	± 0.697	± 0.701	± 0.722	± 0.694	± 0.697	± 0.716	± 0.694
%D diff	0.26	0.58	0.89	1.05	1.32	2.39	2.07
t calculated	0.87	2.92	4.83	8.58	7.03	8.53	10.94
	N	95%	99%	99%	99%	99%	99%

Table C.3. Test for statistical significance of differences in deuteration levels between B₂/Z₂ and C₂/Y₂ fragments from sodium-adducted melezitose in 50% D₂O. SEM is standard error of the mean, df is degrees of freedom, and CI are confidence interval at each α value of 0.05 or 0.01. *t* calculated is compared against *t* values, and %D difference is compared against CI. If both *t* calculated and %D difference values exceed respective reference values at α value of 0.05 or 0.01, the difference in deuteration levels of two fragments are determined statistically significant at 95% or 99% confidence interval, respectively. If either or both values are within the ranges given for reference *t* or confidence interval, the difference in %D between the two fragments is not statistically significant (N).

Precursor	3D	4D	5D	6D	7D	8D
SEM	0.284	0.284	0.284	0.284	0.284	0.284
%D B ₂ /Z ₂	36.31	43.60	50.96	58.23	65.53	73.51
%D C ₂ /Y ₂	35.91	43.10	50.32	57.57	65.18	72.57
df	14	18	20	14	19	13
<i>t</i> 0.05	2.145	2.101	2.086	2.145	2.093	2.160
<i>t</i> 0.01	2.977	2.878	2.845	2.977	2.861	3.012
CI 0.05	± 0.609	± 0.597	± 0.592	± 0.609	± 0.594	± 0.613
CI 0.01	± 0.845	± 0.817	± 0.808	± 0.845	± 0.813	± 0.855
%D diff	0.41	0.50	0.63	0.65	0.35	0.94
<i>t</i> calculated	1.66	3.25	4.96	4.81	2.00	3.74
	N	N	95%	95%	N	99%

Table C.4. Test for statistical significance of differences in deuteration levels between B₂/Z₂ and C₁/Y₁ fragments from sodium-adducted melezitose in 50% D₂O. SEM is standard error of the mean, df is degrees of freedom, and CI are confidence interval at each α value of 0.05 or 0.01. t calculated is compared against t values, and %D difference is compared against CI. If both t calculated and %D difference values exceed respective reference values at α value of 0.05 or 0.01, the difference in deuteration levels of two fragments are determined statistically significant at 95% or 99% confidence interval, respectively. If either or both values are within the ranges given for reference t or confidence interval, the difference in %D between the two fragments is not statistically significant (N).

Precursor	3D	4D	5D	6D	7D	8D
SEM	0.284	0.284	0.284	0.284	0.284	0.284
%D B ₂ /Z ₂	36.31	43.60	50.96	58.23	65.53	73.51
%D C ₁ /Y ₁	35.35	42.63	49.48	56.16	63.74	72.04
df	21	17	18	16	16	18
t 0.05	2.080	2.110	2.101	2.120	2.120	2.101
t 0.01	2.831	2.898	2.878	2.921	2.921	2.878
CI 0.05	± 0.591	± 0.599	± 0.597	± 0.602	± 0.602	± 0.597
CI 0.01	± 0.804	± 0.823	± 0.817	± 0.830	± 0.830	± 0.817
%D diff	0.97	0.97	1.48	2.07	1.79	1.48
t calculated	3.17	3.65	7.38	7.22	5.36	3.22
	99%	99%	99%	99%	99%	99%

Table C.5. Test for statistical significance of differences in deuteration levels between B₂/Z₂ and C₂/Y₂ fragments from sodium-adducted melezitose in 75% D₂O. SEM is standard error of the mean, df is degrees of freedom, and CI are confidence interval at each α value of 0.05 or 0.01. t calculated is compared against t values, and %D difference is compared against CI. If both t calculated and %D difference values exceed respective reference values at α value of 0.05 or 0.01, the difference in deuteration levels of two fragments are determined statistically significant at 95% or 99% confidence interval, respectively. If either or both values are within the ranges given for reference t or confidence interval, the difference in %D between the two fragments is not statistically significant (N).

Precursor	6D	7D	8D	9D	10D	11D
SEM	0.258	0.258	0.258	0.258	0.258	0.258
%D B ₂ /Z ₂	62.93	70.52	77.35	83.82	90.44	97.31
%D C ₂ /Y ₂	62.40	70.32	77.11	83.66	89.89	96.23
df	14	21	21	19	21	21
t 0.05	2.145	2.080	2.080	2.093	2.080	2.080
t 0.01	2.977	2.831	2.831	2.861	2.831	2.831
CI 0.05	± 0.553	± 0.537	± 0.537	± 0.540	± 0.537	± 0.537
CI 0.01	± 0.768	± 0.730	± 0.730	± 0.738	± 0.730	± 0.730
%D diff	0.54	0.20	0.24	0.16	0.55	1.08
t calculated	3.28	1.79	2.01	1.12	4.12	5.57
	N	N	N	N	95%	99%

Table C.6. Test for statistical significance of differences in deuteration levels between B₂/Z₂ and C₁/Y₁ fragments from sodium-adducted melezitose in 75% D₂O. SEM is standard error of the mean, df is degrees of freedom, and CI are confidence interval at each α value of 0.05 or 0.01. t calculated is compared against t values, and %D difference is compared against CI. If both t calculated and %D difference values exceed respective reference values at α value of 0.05 or 0.01, the difference in deuteration levels of two fragments are determined statistically significant at 95% or 99% confidence interval, respectively. If either or both values are within the ranges given for reference t or confidence interval, the difference in %D between the two fragments is not statistically significant (N).

Precursor	6D	7D	8D	9D	10D	11D
SEM	0.258	0.258	0.258	0.258	0.258	0.258
%D B ₂ /Z ₂	62.93	70.52	77.35	83.82	90.44	97.31
%D C ₁ /Y ₁	60.87	69.33	76.37	82.59	89.31	94.99
df	19	17	14	20	20	19
t 0.05	2.093	2.110	2.145	2.086	2.086	2.093
t 0.01	2.861	2.898	2.977	2.845	2.845	2.861
CI 0.05	± 0.540	± 0.544	± 0.553	± 0.538	± 0.538	± 0.540
CI 0.01	± 0.738	± 0.748	± 0.768	± 0.734	± 0.734	± 0.738
%D diff	2.06	1.18	0.98	1.23	1.13	2.32
t calculated	7.42	6.36	3.69	8.39	6.47	8.10
	99%	99%	99%	99%	99%	99%

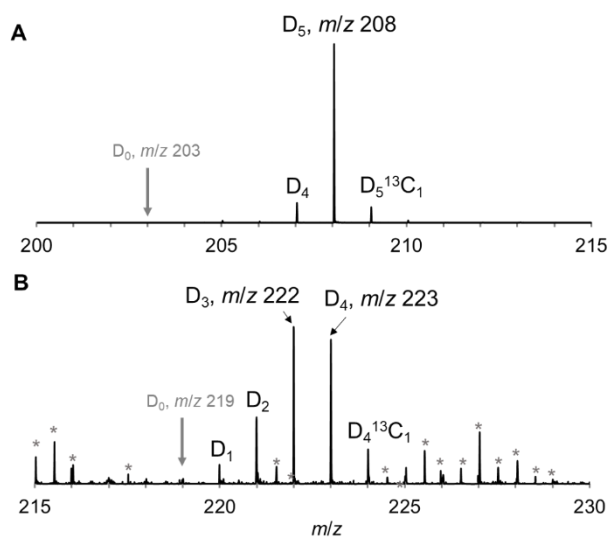
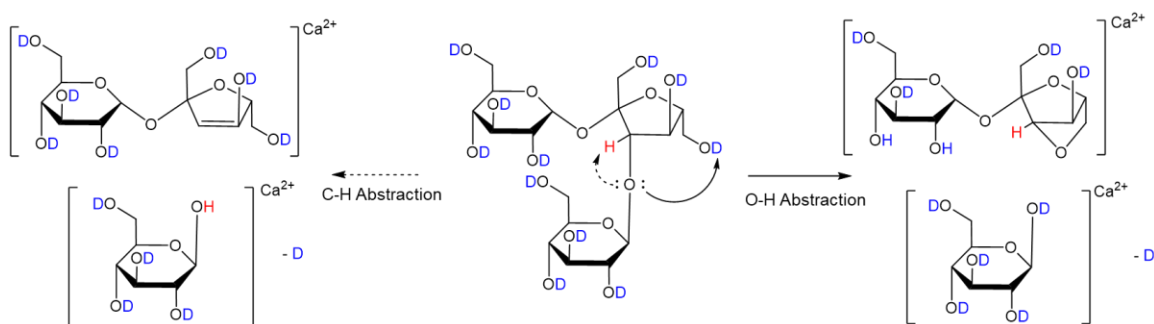


Figure C.5. Representative mass spectra of C₁/Z₁ fragments of melezitose adducted to (A) sodium or (B) calcium and singly-charged by deprotonation in 98% D₂O. Peaks labeled with asterisks are noise or other carbohydrate fragments. Whereas the sodium-adducted C₁/Z₁ fragment shows a clear max D at D₅ that matches the number of labile hydrogens with the structure shown in Figure 4.1B, [C₁/Z₁ + Ca - H]⁺ shows two peaks, D₃ and D₄, at similar intensity, suggesting the presence of multiple structures with varying numbers of labile hydrogens. The expected number of labile hydrogens for [C₁/Z₁ + Ca - H]⁺ is four if a labile hydrogen was transferred during C-O bond cleavage, and three if a non-labile hydrogen was transferred. Both mechanisms are proposed by Bythell *et al.*³¹⁰ Thus, the proposed fragmentation mechanisms are presented in Scheme C.1.



Scheme C.1. Proposed fragmentation mechanisms for $[C_1/Y_1 + Ca - H]^+$ fragments via C-H abstraction (left) and O-H abstraction (right). Labile hydrogens are highlighted blue. With C-H abstraction, where a non-labile hydrogen is acquired and a labile hydrogen is lost, the C_1/Y_1 fragment has three labile hydrogens (left, bottom). With O-H abstraction, the C_1/Y_1 fragment has four labile hydrogens (right, bottom). Fragmentation of fully deuterated $[Melezitose + Ca]^{2+}$ shows deprotonated C_1/Y_1 fragment with two structures with varying numbers of labile hydrogens, both three and four. B_2/Z_2 fragments are only detected with six labile hydrogens (right, top) rather than with seven labile hydrogens (left, top).

Table C.7. Test for statistical significance of differences in deuteration levels between B₂/Z₂ and C₂/Y₂ fragments from calcium-adducted melezitose in 25% D₂O. SEM is standard error of the mean, df is degrees of freedom, and CI are confidence interval at each α value of 0.05 or 0.01. *t* calculated is compared against *t* values, and %D difference is compared against CI. If both *t* calculated and %D difference values exceed respective reference values at α value of 0.05 or 0.01, the difference in deuteration levels of two fragments are determined statistically significant at 95% or 99% confidence interval, respectively. If either or both values are within the ranges given for reference *t* or confidence interval, the difference in %D between the two fragments is not statistically significant (N).

Precursor	0D	1D	2D	3D	4D	5D
SEM	0.511	0.511	0.511	0.511	0.511	0.511
%D B ₂ /Z ₂	11.69	16.29	20.91	25.81	32.14	39.14
%D C ₂ /Y ₂	10.98	15.70	20.44	25.49	31.61	38.27
df	22	21	19	22	22	21
<i>t</i> 0.05	2.074	2.080	2.093	2.074	2.074	2.080
<i>t</i> 0.01	2.819	2.831	2.861	2.819	2.819	2.831
CI 0.05	± 1.060	± 1.062	± 1.070	± 1.060	± 1.060	± 1.062
CI 0.01	± 1.441	± 1.447	± 1.462	± 1.441	± 1.441	± 1.447
%D diff	0.71	0.59	0.47	0.32	0.54	0.90
<i>t</i> calculated	3.26	2.82	1.78	0.81	4.99	3.33
	N	N	N	N	N	N

Table C.8. Test for statistical significance of differences in deuteration levels between B₂/Z₂ and C₂/Y₂ fragments from calcium-adducted melezitose in 50% D₂O. SEM is standard error of the mean, df is degrees of freedom, and CI are confidence interval at each α value of 0.05 or 0.01. t calculated is compared against t values, and %D difference is compared against CI. If both t calculated and %D difference values exceed respective reference values at α value of 0.05 or 0.01, the difference in deuteration levels of two fragments are determined statistically significant at 95% or 99% confidence interval, respectively. If either or both values are within the ranges given for reference t or confidence interval, the difference in %D between the two fragments is not statistically significant (N).

Precursor	3D	4D	5D	6D	7D	8D	9D
SEM	0.667	0.667	0.667	0.667	0.667	0.667	0.667
%D B ₂ /Z ₂	35.66	41.96	47.85	54.29	60.71	66.92	73.97
%D C ₂ /Y ₂	33.88	41.21	47.41	54.07	60.19	66.45	73.38
df	22	21	21	21	21	21	18
t 0.05	2.074	2.080	2.080	2.080	2.080	2.080	2.101
t 0.01	2.819	2.831	2.831	2.831	2.831	2.831	2.878
CI 0.05	± 1.383	± 1.387	± 1.387	± 1.387	± 1.387	± 1.387	± 1.401
CI 0.01	± 1.880	± 1.888	± 1.888	± 1.888	± 1.888	± 1.888	± 1.920
%D diff	1.77	0.75	0.45	0.22	0.53	0.47	0.59
t	6.45	1.93	1.25	0.61	1.98	1.11	1.19
	95%	N	N	N	N	N	N

Table C.9. Test for statistical significance of differences in deuteration levels between B₂/Z₂ and C₂/Y₂ fragments from calcium-adducted melezitose in 75% D₂O. SEM is standard error of the mean, df is degrees of freedom, and CI are confidence interval at each α value of 0.05 or 0.01. t calculated is compared against t values, and %D difference is compared against CI. If both t calculated and %D difference values exceed respective reference values at α value of 0.05 or 0.01, the difference in deuteration levels of two fragments are determined statistically significant at 95% or 99% confidence interval, respectively. If either or both values are within the ranges given for reference t or confidence interval, the difference in %D between the two fragments is not statistically significant (N).

Precursor	6D	7D	8D	9D	10D	11D
SEM	0.631	0.631	0.631	0.631	0.631	0.631
%D B ₂ /Z ₂	63.37	69.32	75.08	80.33	85.95	91.71
%D C ₂ /Y ₂	62.27	68.79	74.80	80.22	85.42	91.00
df	21	18	22	20	21	20
t 0.05	2.080	2.101	2.074	2.086	2.080	2.086
t 0.01	2.831	2.878	2.819	2.845	2.831	2.845
CI 0.05	± 1.312	± 1.326	± 1.309	± 1.316	± 1.312	± 1.316
CI 0.01	± 1.786	± 1.816	± 1.779	± 1.795	± 1.786	± 1.795
%D diff	1.10	0.53	0.28	0.11	0.56	0.72
t	3.10	1.71	0.96	0.32	1.45	1.80
	N	N	N	N	N	N

Table C.10. Test for statistical significance of differences in deuteration levels between $^{0,4/1,3/2,4}\text{X}_{\text{Glc}}\text{C}_2/\text{A}_{\text{Glc}}\text{Y}_2$ (A1) and $^{0,4/1,3/2,4}\text{X}_{\text{Glc}}\text{B}_2/\text{A}_{\text{Glc}}\text{Z}_2$ (A2) fragments from calcium-adducted melezitose in 25% D₂O. SEM is standard error of the mean, df is degrees of freedom, and CI are confidence interval at each α value of 0.05 or 0.01. t calculated is compared against t values, and %D difference is compared against CI. If both t calculated and %D difference values exceed respective reference values at α value of 0.05 or 0.01, the difference in deuteration levels of two fragments are determined statistically significant at 95% or 99% confidence interval, respectively. If either or both values are within the ranges given for reference t or confidence interval, the difference in %D between the two fragments is not statistically significant (N).

Precursor	0D	1D	2D	3D	4D	5D
SEM	0.511	0.511	0.511	0.511	0.511	0.511
%D A1	11.79	16.04	19.95	24.68	30.24	37.08
%D A2	12.67	17.10	21.81	26.97	32.57	39.52
df	21	19	20	19	19	22
t 0.05	2.080	2.093	2.086	2.093	2.093	2.074
t 0.01	2.831	2.861	2.845	2.861	2.861	2.819
CI 0.05	± 1.063	± 1.070	± 1.066	± 1.070	± 1.070	± 1.060
CI 0.01	± 1.447	± 1.462	± 1.454	± 1.462	± 1.462	± 1.441
%D diff	0.88	1.06	1.87	2.29	2.33	2.43
t	0.83	1.94	4.04	3.86	4.60	3.44
	N	N	99%	99%	99%	99%

Table C.11. Test for statistical significance of differences in deuteration levels between $^{0,4/1,3/2,4}\text{X}_{\text{Glc}}\text{C}_2/\text{A}_{\text{Glc}}\text{Y}_2$ (A1) and $^{0,4/1,3/2,4}\text{X}_{\text{Glc}}\text{B}_2/\text{A}_{\text{Glc}}\text{Z}_2$ (A2) fragments from calcium-adducted melezitose in 50% D₂O. SEM is standard error of the mean, df is degrees of freedom, and CI are confidence interval at each α value of 0.05 or 0.01. t calculated is compared against t values, and %D difference is compared against CI. If both t calculated and %D difference values exceed respective reference values at α value of 0.05 or 0.01, the difference in deuteration levels of two fragments are determined statistically significant at 95% or 99% confidence interval, respectively. If either or both values are within the ranges given for reference t or confidence interval, the difference in %D between the two fragments is not statistically significant (N).

Precursor	3D	4D	5D	6D	7D	8D	9D
SEM	0.667	0.667	0.667	0.667	0.667	0.667	0.667
%D A1	33.59	39.07	45.55	52.15	57.80	63.90	69.90
%D A2	36.76	43.79	48.28	55.49	60.88	67.25	73.96
df	22	19	21	20	21	21	16
t 0.05	2.074	2.093	2.080	2.086	2.080	2.080	2.120
t 0.01	2.819	2.861	2.831	2.845	2.831	2.831	2.921
CI 0.05	± 1.383	± 1.396	± 1.387	± 1.391	± 1.387	± 1.387	± 1.414
CI 0.01	± 1.880	± 1.908	± 1.888	± 1.898	± 1.888	± 1.888	± 1.948
%D diff	3.17	4.72	2.73	3.33	3.08	3.34	4.06
t	3.34	5.88	4.43	4.90	4.86	3.69	3.34
	99%	99%	95%	99%	99%	99%	99%

Table C.12. Test for statistical significance of differences in deuteration levels between $^{0,4/1,3/2,4}\text{X}_{\text{Glc}}\text{C}_2/\text{A}_{\text{Glc}}\text{Y}_2$ (A1) and $^{0,4/1,3/2,4}\text{X}_{\text{Glc}}\text{B}_2/\text{A}_{\text{Glc}}\text{Z}_2$ (A2) fragments from calcium-adducted melezitose in 75% D₂O. SEM is standard error of the mean, df is degrees of freedom, and CI are confidence interval at each α value of 0.05 or 0.01. t calculated is compared against t values, and %D difference is compared against CI. If both t calculated and %D difference values exceed respective reference values at α value of 0.05 or 0.01, the difference in deuteration levels of two fragments are determined statistically significant at 95% or 99% confidence interval, respectively. If either or both values are within the ranges given for reference t or confidence interval, the difference in %D between the two fragments is not statistically significant (N).

Precursor	6D	7D	8D	9D	10D	11D
SEM	0.631	0.631	0.631	0.631	0.631	0.631
%D A1	60.62	66.95	72.58	77.60	82.38	87.59
%D A2	64.26	71.50	77.00	81.41	87.55	90.73
df	19	18	21	22	22	18
t 0.05	2.093	2.101	2.080	2.074	2.074	2.101
t 0.01	2.861	2.878	2.831	2.819	2.819	2.878
CI 0.05	± 1.321	± 1.326	± 1.312	± 1.309	± 1.309	± 1.326
CI 0.01	± 1.805	± 1.816	± 1.786	± 1.779	± 1.779	± 1.816
%D diff	3.64	4.55	4.42	3.80	5.18	3.15
t	3.27	5.71	6.57	5.59	7.97	3.16
	99%	99%	99%	99%	99%	99%

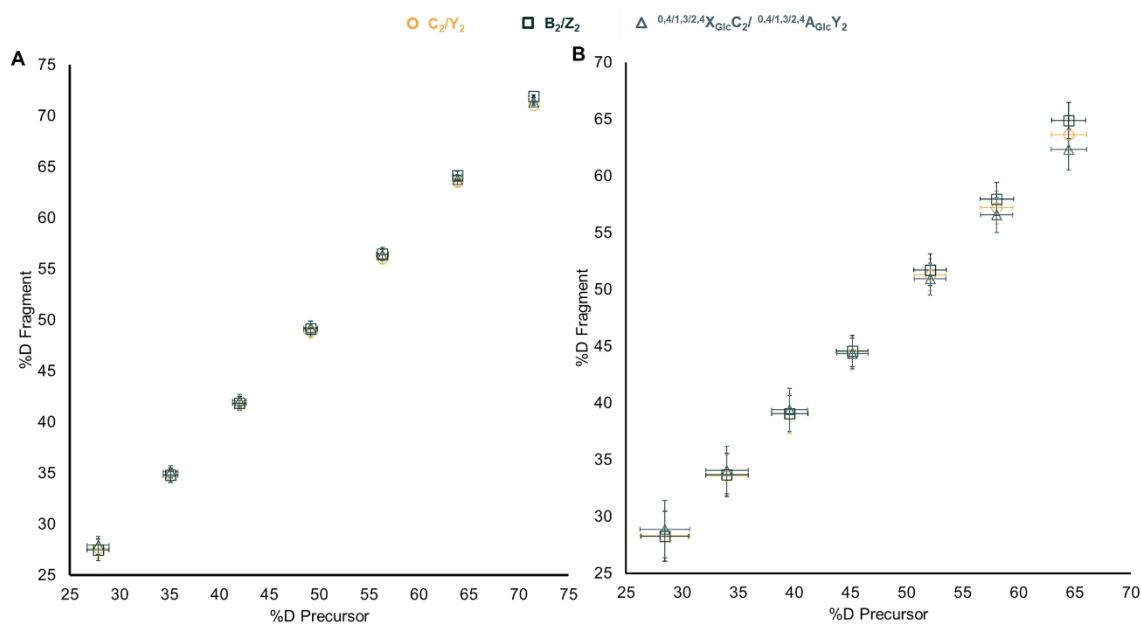


Figure C.6. Deuteration plots of three common fragments from (A) sodium- and (B) calcium-adducted melezitose in 50% MeOD. The deuteration level of internal cleavage product (teal triangle) is not statistically different from the deuteration levels of glycosidic bond cleavage fragments, contrary to the deuteration patterns collected when spraying from 50% D₂O.

Previous work from our lab reported changes in HDX of carbohydrates in varying solvent composition, namely water and methanol.^{16, 100} Sodium- and calcium-adducted melezitose prepared in 25%, 50%, and 75% deuterated methanol (MeOD) were fragmented and the deuteration levels of fragments were compared.

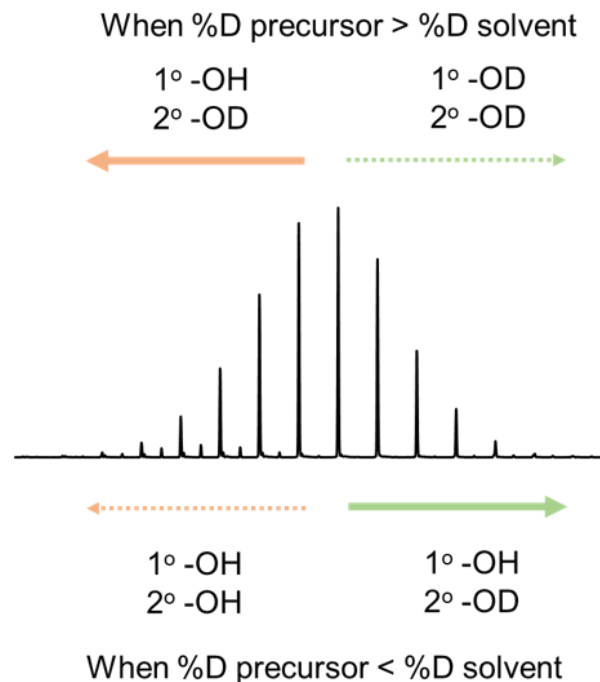
B₂/Z₂ fragments were observed at higher deuteration compared to C₂/Y₂ fragments in the higher *m/z* part of the distribution for sodium-adducted precursor, with C₂/Y₂ at 71.1 ± 0.1 % deuteration and B₂/Z₂ at 71.9 ± 0.1 % deuteration when the D₈ precursor was isolated. However, the difference in deuteration levels of doubly-charged C₂/Y₂ and B₂/Z₂ fragments from calcium-adducted melezitose was statistically insignificant. The internal cleavage product from sodium-adducted melezitose in D₂O was found at significantly lower deuteration levels compared to both B₂/Z₂ and C₂/Y₂

fragments when lower m/z precursors were isolated (Figure 4.3A). However, no statistical difference in deuteration levels were observed between the internal cleavage fragment and either B_2/Z_2 or C_2/Y_2 fragments in the lower m/z part of the distribution of sodium-adducted melezitose in MeOD (Figure C.6A). Similarly, the %D of the internal cleavage fragment generated from calcium-adducted melezitose in D_2O was statistically different from the %D of both C_2/Y_2 and B_2/Z_2 fragments. However, the %D of the same fragment generated from calcium-adducted melezitose in MeOD was within measurement error with either B_2/Z_2 or C_2/Y_2 fragments when the lower m/z precursor was isolated and only less deuterated than B_2/Z_2 fragments when the higher m/z precursor was fragmented (Figure C.6B). The changes for both sodium- and calcium-adducted fragments point towards less distinction between fragments when the solvent was changed from D_2O to MeOD. We hypothesize that the evaporation time of the two solvents contribute to such changes in observed deuteration patterns of different fragments. Underivatized carbohydrates ionize via the charged residue mechanism (CRM) in which the solvent evaporates until only the analyte and charge remain which then form gas-phase ions.⁹⁶ Gas-phase carbohydrate-metal complexes do not undergo HDX¹⁰⁰, meaning HDX only occurs in the bulk solution and inside the ESI droplets during our experiments. Methanol is more volatile than water and thus forms smaller initial ESI droplets and evaporates faster than water.³⁵⁸ Therefore, the deuteration pattern that was observed from metal-adducted melezitose prepared in MeOD represents the deuteration state of the carbohydrate in earlier stages of the ESI process, closer to HDX in bulk solution, in which we expect that the carbohydrate hydroxyls are labeled randomly. On the other hand, the statistically different deuteration levels fragments observed for metal-adducted

carbohydrates prepared in D₂O represent deuteration patterns that have undergone additional H/D and D/H reactions in the droplets during ESI while colliding with vapors present within the source.¹⁶ Therefore, we expect a less specific labeling of carbohydrates in solution and more site-specific labeling to occur in droplets that can distinguish between different functional groups, which may be attributed to increased interactions with metal ions during ESI.

It should be noted that while we expect the droplet lifetimes to be shorter for the samples prepared in MeOH and MeOD, the precursor distribution was detected at lower deuteration levels when sprayed from methanol-based solvents compared to deuteration levels when sprayed from water-based solvents. In the body of the paper, we discussed how sodium-adducted melezitose prepared in D₂O had higher back-exchange compared to calcium-adducted melezitose, likely due to the longer lifetime of the ESI droplets for samples with sodium due to the lower conductivity than samples with calcium, and resulting in larger initial droplets. Therefore, the lower deuteration levels of carbohydrate-metal complexes resulting from smaller initial droplets from methanol samples may seem unexpected. However, HDX is catalyzed by acid or base, and D₂O with its autoionization properties would serve as a better deuterating reagent than MeOD in solution. While all samples were prepared and incubated for at least 24 hours prior to MS analysis, it is possible that lower deuteration was achieved from MeOD in solution. Additionally, our previous work has described differences in deuterium uptake from ESI vapors of D₂O and MeOD, where ESI sources were saturated with D₂O or MeOD vapors and undeuterated carbohydrates were introduced.¹⁶ Disproportionately higher levels of deuteration were achieved from D₂O vapors compared to MeOD vapors. One reason for

such differences could be attributed to the difference in the condensation coefficient between water and methanol on the surface of the ESI source.³⁵⁹ Although back-exchange compared to forward-exchange was likely the more dominant reaction in the source due to atmospheric moisture, we expect some forward-exchange also occurring inside the source from the vaporized sample solvent. When samples prepared in MeOH and MeOD were sprayed, the methanol solvent molecules evaporated faster and were likely evacuated from the source earlier, leaving less deuterating reagent and more atmospheric moisture inside the source, compared to samples sprayed from water and D₂O, which likely interacted more with both water and D₂O vapors. Therefore, we hypothesize that the deuterium labels of melezitose sprayed from methanol represent deuteration in bulk solution with more random labeling, rather than back-exchange in the droplets during ESI.



Scheme C.2. When solvent conductivity is higher and carbohydrate-metal complexes undergo less back-exchange during ESI, such as in the sample of melezitose with calcium acetate, the detected %D precursor was higher than the %D of the solvent composition (top). We propose that both primary and secondary hydroxyls can retain their deuterium labels better when higher %D precursor is isolated, and the difference in deuteration levels between B_2/Z_2 and C_2/Y_2 is smaller. In the lower %D precursor distribution, however, primary hydroxyls have back-exchanged more compared to the secondary hydroxyls and the difference in deuteration levels between B_2/Z_2 and C_2/Y_2 fragments widens. When solvent conductivity is lower and carbohydrate-metal complexes undergo more back-exchange during ESI, such as in the case of melezitose and sodium acetate, the detected %D precursor was lower than the %D of the solvent composition (bottom). We propose that the primary hydroxyls, with their faster exchange rates, have back-exchanged in the higher %D precursor distribution, whereas secondary hydroxyls retain their deuterium. Therefore, the difference in deuteration levels between B_2/Z_2 and C_2/Y_2 fragments is observed. On the other hand, the secondary hydroxyls also undergo back-exchange when lower %D precursor is isolated, and the difference in deuteration levels between B_2/Z_2 and C_2/Y_2 fragments is reduced.

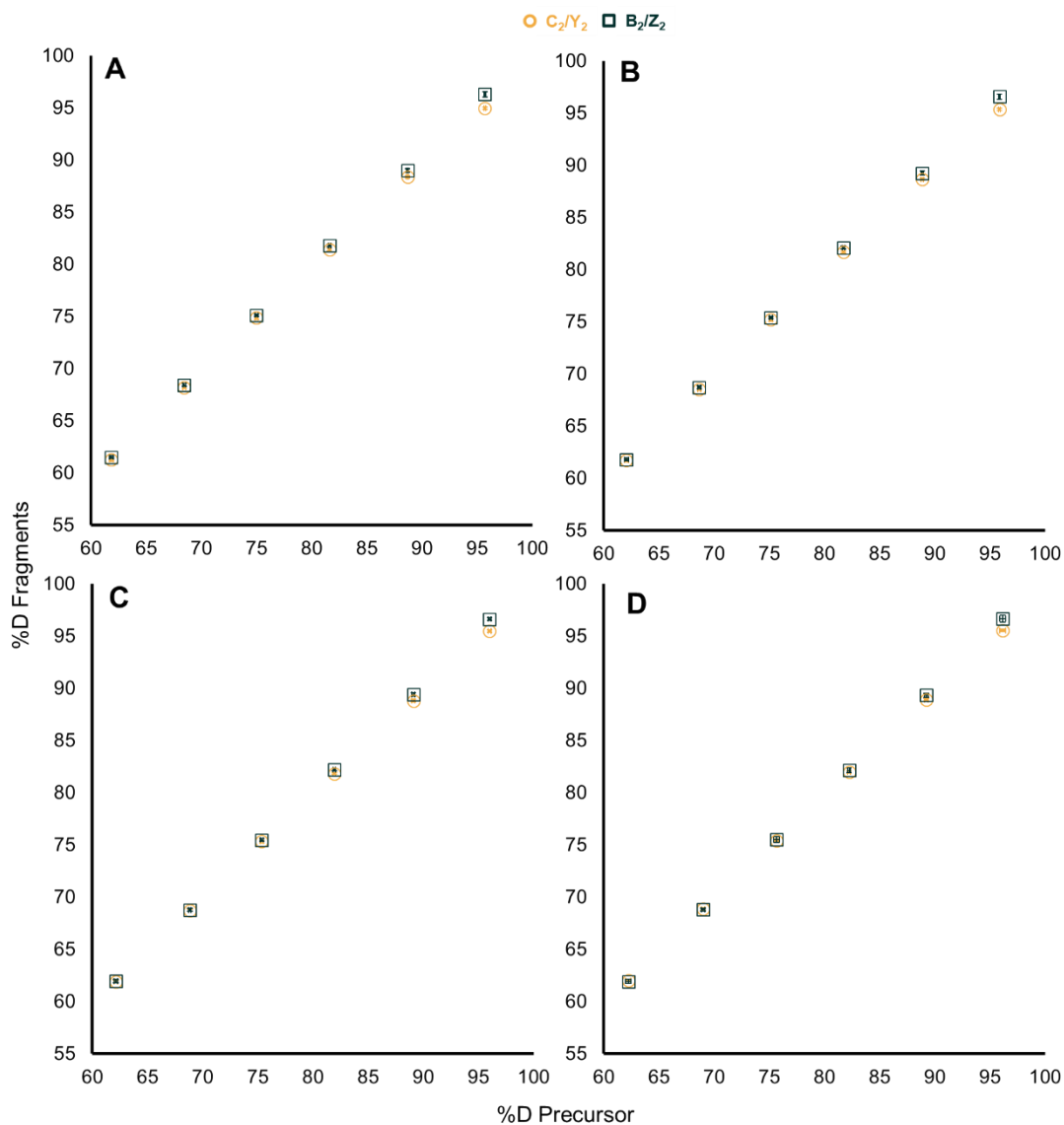


Figure C.7. Deuteration plots of sodium-adducted melezitose at collision voltage of (A) 24 V, (B) 28 V, (C) 32 V, and (D) 36 V. B_2/Z_2 fragments have higher levels of deuteration compared to both C_1/Y_1 and C_2/Y_2 fragments at all collision voltages tested for sodium-adducted melezitose.

APPENDIX D

Supplementary Information for Chapter Five

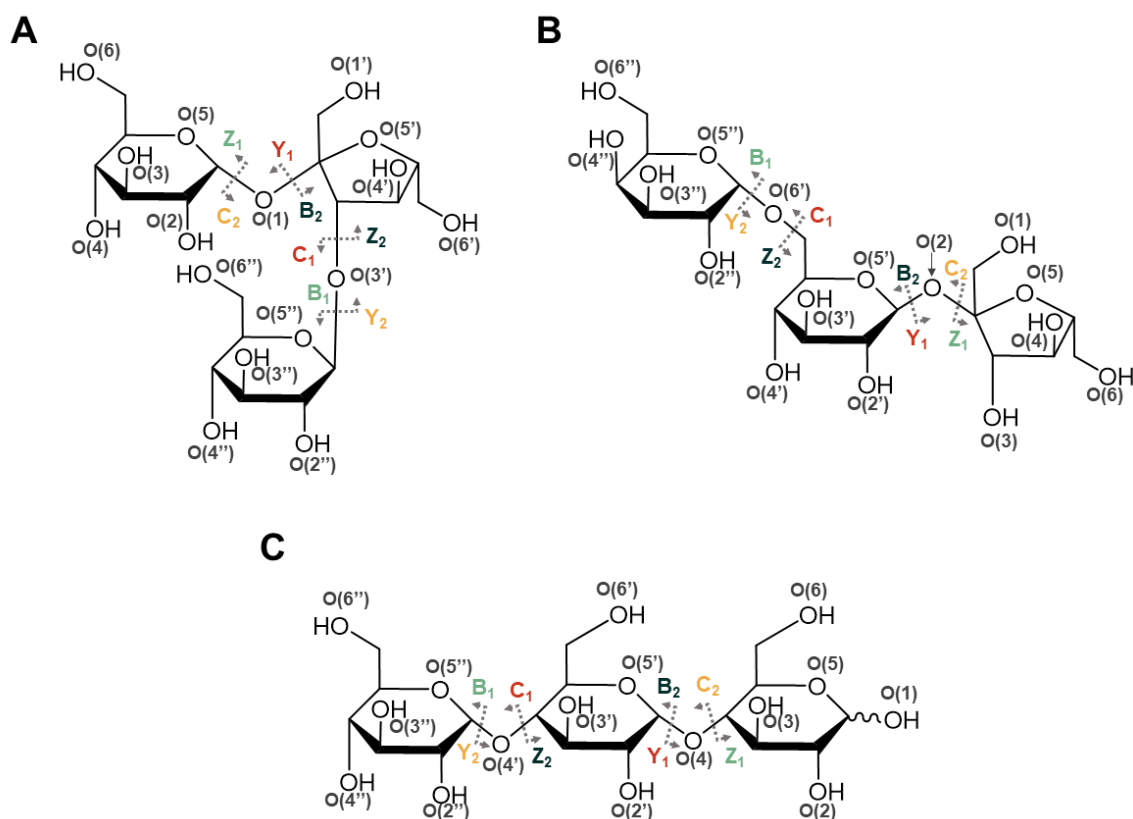


Figure D.1. Structures of (A) melezitose, (B) raffinose, and (C) maltotriose. The oxygens are labeled according to their positions starting from O(1) as the anomeric hydroxyl and O(2) through O(6) as hydroxyls on the terminal monosaccharide subunit on the reducing end, O(2') through O(6') as hydroxyls on the second (middle) monosaccharide subunit, and O(2'') through O(6'') as hydroxyls on the terminal monosaccharide subunit on the non-reducing end. Fragments from glycosidic bond cleavages are labeled according to Domon and Costello nomenclature.¹⁵⁵ While melezitose and raffinose are non-reducing sugars, Y- and Z- type fragments are still labeled to illustrate potential isomers from B- and C-type fragments. Isomeric fragments from different glycosidic bond cleavage sites can be generated and isomeric fragments are labeled in the same color.

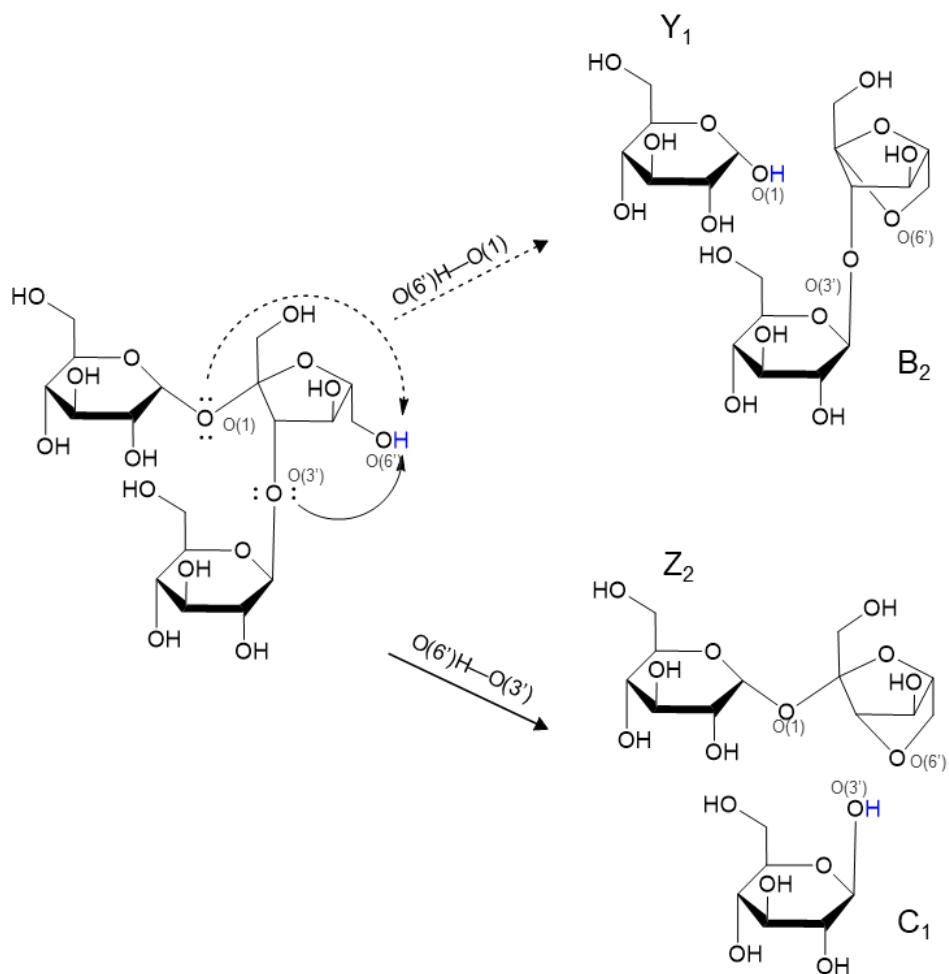


Figure D.2. Proposed fragmentation pathways of sodium-adducted melezitose via CID. C-O bond dissociation is initiated by protonation of glycosidic oxygens, at O(1) or O(3'). DFT optimizations of sodium-adducted melezitose show the O(6')H as the most likely proton source to initiate the fragmentation process. The O(6')H is highlighted in blue to show the movement of the hydrogen from the middle fructose ring to Y₁ and C₁ fragments. Y₁ and C₁ fragments are isomeric, as are B₂ and Z₂ fragments.

The following equations were used to calculate pooled standard deviations, standard error of the mean (SEM), degrees of freedom (df), and confidence interval (CI), where s is standard deviation and n is the number of samples:

$$S_{pooled} = \sqrt{\frac{(n_1 - 1)s_1^2 + (n_2 - 1)s_2^2 + \dots + (n_k - 1)s_k^2}{n_1 + n_2 + \dots + n_k - k}}$$

$$SEM = \sqrt{\frac{S_{pooled}^2}{n_1} + \frac{S_{pooled}^2}{n_2}}$$

$$df = \frac{\left(\frac{s_1^2}{n_1} + \frac{s_2^2}{n_2}\right)^2}{\frac{\left(\frac{s_1^2}{n_1}\right)^2}{n_1 - 1} + \frac{\left(\frac{s_2^2}{n_2}\right)^2}{n_2 - 1}}$$

$$CI_\alpha = \pm SEM \times t_\alpha$$

Welch's t -test was performed using the equation, where \bar{x} is the sample mean:

$$t = \frac{\bar{x}_1 - \bar{x}_2}{\sqrt{\frac{s_1^2}{n_1} + \frac{s_2^2}{n_2}}}$$

Percent deuteration (%D) differences between fragments were determined by following the guidelines of Hageman and Weis.³¹² First, the difference in %D of two fragments were compared against the CI. Secondly, Welch's t -test was performed. When the difference in %D was significant in both procedures, the difference was determined to be statistically significant. The reason for using two statistical methods, instead of one, was to avoid overinterpretation of differences in %D by minimizing false positives that may result from using t -tests alone.

Table D.1. Test for statistical significance of differences in deuteration levels between B₂/Z₂ and C₁/Y₁ fragments of sodium-adducted melezitose in 25% D₂O. SEM stands for standard error of the mean, df stands for degrees of freedom, and CI is the confidence interval at each α value, 0.05 or 0.01. t calculated is compared against t values, and %D difference is compared against CI. If both t calculated and %D difference values exceed respective reference values at α value of 0.05 or 0.01, the difference in deuteration levels of two fragments are determined to be statistically significant at 95% or 99% confidence interval, respectively. If either or both values are within the ranges given for reference t or confidence interval, the difference in %D between the two fragments is not statistically significant (N).

Precursor	0D	1D	2D	3D	4D	5D	6D
SEM	0.245	0.245	0.245	0.245	0.245	0.245	0.245
%D B ₂ /Z ₂	11.54	17.51	24.00	31.64	38.84	46.60	54.28
%D C ₁ /Y ₁	11.28	16.93	23.11	30.59	37.51	44.21	52.21
df	20	19	15	21	20	16	21
t 0.05	2.086	2.093	2.131	2.080	2.086	2.120	2.080
t 0.01	2.845	2.861	2.947	2.831	2.845	2.921	2.831
CI 0.05	± 0.511	± 0.512	± 0.522	± 0.510	± 0.511	± 0.519	± 0.510
CI 0.01	± 0.697	± 0.701	± 0.722	± 0.694	± 0.697	± 0.716	± 0.694
%D diff	0.26	0.58	0.89	1.05	1.32	2.39	2.07
t calculated	0.87	2.92	4.83	8.58	7.03	8.53	10.94
	N	95%	99%	99%	99%	99%	99%

Table D.2. Test for statistical significance of differences in deuteration levels between B₂/Z₂ and C₁/Y₁ fragments of sodium-adducted melezitose in 50% D₂O. SEM stands for standard error of the mean, df stands for degrees of freedom, and CI are confidence interval at each α value of 0.05 or 0.01. t calculated is compared against t values, and %D difference is compared against CI. If both t calculated and %D difference values exceed respective reference values at α value of 0.05 or 0.01, the difference in deuteration levels of two fragments are determined statistically significant at 95% or 99% confidence interval, respectively. If either or both values are within the ranges given for reference t or confidence interval, the difference in %D between the two fragments is not statistically significant (N).

Precursor	3D	4D	5D	6D	7D	8D
SEM	0.284	0.284	0.284	0.284	0.284	0.284
%D B ₂ /Z ₂	36.31	43.60	50.96	58.23	65.53	73.51
%D C ₁ /Y ₁	35.35	42.63	49.48	56.16	63.74	72.04
df	21	17	18	16	16	18
t 0.05	2.080	2.110	2.101	2.120	2.120	2.101
t 0.01	2.831	2.898	2.878	2.921	2.921	2.878
CI 0.05	± 0.591	± 0.599	± 0.597	± 0.602	± 0.602	± 0.597
CI 0.01	± 0.804	± 0.823	± 0.817	± 0.830	± 0.830	± 0.817
%D diff	0.97	0.97	1.48	2.07	1.79	1.48
t calculated	3.17	3.65	7.38	7.22	5.36	3.22
	99%	99%	99%	99%	99%	99%

Table D.3. Test for statistical significance of differences in deuteration levels between B₂/Z₂ and C₁/Y₁ fragments of sodium-adducted melezitose in 75% D₂O. SEM stands for standard error of the mean, df stands for degrees of freedom, and CI are confidence interval at each α value of 0.05 or 0.01. t calculated is compared against t values, and %D difference is compared against CI. If both t calculated and %D difference values exceed respective reference values at α value of 0.05 or 0.01, the difference in deuteration levels of two fragments are determined statistically significant at 95% or 99% confidence interval, respectively. If either or both values are within the ranges given for reference t or confidence interval, the difference in %D between the two fragments is not statistically significant (N).

Precursor	6D	7D	8D	9D	10D	11D
SEM	0.258	0.258	0.258	0.258	0.258	0.258
%D B ₂ /Z ₂	62.93	70.52	77.35	83.82	90.44	97.31
%D C ₁ /Y ₁	60.87	69.33	76.37	82.59	89.31	94.99
df	19	17	14	20	20	19
t 0.05	2.093	2.110	2.145	2.086	2.086	2.093
t 0.01	2.861	2.898	2.977	2.845	2.845	2.861
CI 0.05	± 0.540	± 0.544	± 0.553	± 0.538	± 0.538	± 0.540
CI 0.01	± 0.738	± 0.748	± 0.768	± 0.734	± 0.734	± 0.738
%D diff	2.06	1.18	0.98	1.23	1.13	2.32
t calculated	7.42	6.36	3.69	8.39	6.47	8.10
	99%	99%	99%	99%	99%	99%

Table D.4. Distances between hydroxyl hydrogens and glycosidic oxygens of sodium-adducted melezitose that can initiate fragmentation pathways for production of Z₂ and B₂ fragments. All lengths are reported in angstroms (Å).

Trial #	Z ₂ (O(3'))			B ₂ (O(1))		
	O(1')H	O(4')H	O(6')H	O(1')H	O(4')H	O(6')H
1	4.309	3.710	5.686	3.682	4.971	4.679
2	3.650	4.169	3.453	3.309	5.329	2.549
3	4.019	3.782	5.406	3.661	4.936	4.740
4	5.112	3.927	3.054	4.349	4.406	2.852
5	4.368	3.668	4.716	2.853	4.984	3.162
6	4.743	4.315	3.070	3.692	5.205	2.629
7	4.743	4.305	3.836	3.683	5.288	4.436
8	4.246	4.315	2.960	2.513	5.212	2.840
9	5.185	3.977	4.298	4.331	4.536	5.373
10	4.725	4.256	3.355	3.673	5.256	2.493
Average	4.510	4.042	3.983	3.575	5.012	3.575
Std Dev	0.481	0.261	1.000	0.572	0.319	1.101

Table D.5. Test for statistical significance of differences in deuteration levels between B₂/Z₂ and C₂/Y₂ fragments of sodium-adducted melezitose in 25% D₂O. SEM stands for standard error of the mean, df stands for degrees of freedom, and CI are confidence interval at each α value of 0.05 or 0.01. t calculated is compared against t values, and %D difference is compared against CI. If both t calculated and %D difference values exceed respective reference values at α value of 0.05 or 0.01, the difference in deuteration levels of two fragments are determined statistically significant at 95% or 99% confidence interval, respectively. If either or both values are within the ranges given for reference t or confidence interval, the difference in %D between the two fragments is not statistically significant (N).

Precursor	0D	1D	2D	3D	4D	5D	6D
SEM	0.245	0.245	0.245	0.245	0.245	0.245	0.245
%D B ₂ /Z ₂	11.54	17.51	24.00	31.64	38.84	46.60	54.28
%D C ₂ /Y ₂	11.01	17.21	23.69	31.16	38.26	45.66	53.23
df	13	15	20	20	20	21	22
t 0.05	2.160	2.131	2.086	2.086	2.086	2.080	2.074
t 0.01	3.012	2.947	2.845	2.845	2.845	2.831	2.819
CI 0.05	± 0.529	± 0.522	± 0.511	± 0.511	± 0.511	± 0.510	± 0.508
CI 0.01	± 0.738	± 0.722	± 0.697	± 0.697	± 0.697	± 0.694	± 0.691
%D diff	0.53	0.3	0.3	0.48	0.58	0.94	1.04
t calculated	2.11	2.46	3.32	4.11	4.24	5.67	6.51
	N	N	N	N	95%	99%	99%

Table D.6. Test for statistical significance of differences in deuteration levels between B₂/Z₂ and C₂/Y₂ fragments of sodium-adducted melezitose in 50% D₂O. SEM stands for standard error of the mean, df stands for degrees of freedom, and CI are confidence interval at each α value of 0.05 or 0.01. t calculated is compared against t values, and %D difference is compared against CI. If both t calculated and %D difference values exceed respective reference values at α value of 0.05 or 0.01, the difference in deuteration levels of two fragments are determined statistically significant at 95% or 99% confidence interval, respectively. If either or both values are within the ranges given for reference t or confidence interval, the difference in %D between the two fragments is not statistically significant (N).

Precursor	3D	4D	5D	6D	7D	8D
SEM	0.284	0.284	0.284	0.284	0.284	0.284
%D B ₂ /Z ₂	36.31	43.60	50.96	58.23	65.53	73.51
%D C ₂ /Y ₂	35.91	43.10	50.32	57.57	65.18	72.57
df	14	18	20	14	19	13
t 0.05	2.145	2.101	2.086	2.145	2.093	2.160
t 0.01	2.977	2.878	2.845	2.977	2.861	3.012
CI 0.05	± 0.609	± 0.597	± 0.592	± 0.609	± 0.594	± 0.613
CI 0.01	± 0.845	± 0.817	± 0.808	± 0.845	± 0.813	± 0.855
%D diff	0.41	0.50	0.63	0.65	0.35	0.94
t calculated	1.66	3.25	4.96	4.81	2.00	3.74
	N	N	95%	95%	N	99%

Table D.7. Test for statistical significance of differences in deuteration levels between B₂/Z₂ and C₂/Y₂ fragments of sodium-adducted melezitose in 75% D₂O. SEM stands for standard error of the mean, df stands for degrees of freedom, and CI are confidence interval at each α value of 0.05 or 0.01. *t* calculated is compared against *t* values, and %D difference is compared against CI. If both *t* calculated and %D difference values exceed respective reference values at α value of 0.05 or 0.01, the difference in deuteration levels of two fragments are determined statistically significant at 95% or 99% confidence interval, respectively. If either or both values are within the ranges given for reference *t* or confidence interval, the difference in %D between the two fragments is not statistically significant (N).

Precursor	6D	7D	8D	9D	10D	11D
SEM	0.258	0.258	0.258	0.258	0.258	0.258
%D B ₂ /Z ₂	62.93	70.52	77.35	83.82	90.44	97.31
%D C ₂ /Y ₂	62.40	70.32	77.11	83.66	89.89	96.23
df	14	21	21	19	21	21
<i>t</i> 0.05	2.145	2.080	2.080	2.093	2.080	2.080
<i>t</i> 0.01	2.977	2.831	2.831	2.861	2.831	2.831
CI 0.05	± 0.553	± 0.537	± 0.537	± 0.540	± 0.537	± 0.537
CI 0.01	± 0.768	± 0.730	± 0.730	± 0.738	± 0.730	± 0.730
%D diff	0.54	0.20	0.24	0.16	0.55	1.08
<i>t</i> calculated	3.28	1.79	2.01	1.12	4.12	5.57
	N	N	N	N	95%	99%

Table D.8. Distances between hydroxyl hydrogens and glycosidic oxygens of sodium-added melezitose that can initiate fragmentation pathways for production of B₁ and Z₁ fragments. All lengths are reported in angstroms (Å).

Trial #	B ₁ (O(3'))				Z ₁ (O(1))			
	O(2'')H	O(3'')H	O(4'')H	O(6'')H	O(2)H	O(3)H	O(4)H	O(6)H
1	2.391	5.043	4.790	6.281	3.597	4.810	5.003	6.066
2	2.390	4.847	5.096	5.102	3.410	3.410	5.131	5.215
3	3.365	5.108	5.212	6.312	3.610	4.853	4.968	4.889
4	2.398	4.209	4.888	6.030	3.595	4.389	4.922	5.904
5	2.399	5.209	5.051	6.311	3.686	4.904	5.130	6.129
6	2.261	5.036	4.743	6.285	3.390	5.108	5.221	6.306
7	2.261	5.023	5.980	5.682	3.608	4.797	4.982	6.041
8	2.296	5.186	5.491	6.278	3.547	4.336	4.771	5.770
9	3.529	4.862	5.108	6.110	3.694	4.658	5.258	5.336
10	2.393	5.190	5.335	6.242	2.352	5.000	4.685	5.872
Average	2.568	4.971	5.169	6.063	3.449	4.627	5.007	5.753
Std Dev	0.468	0.296	0.368	0.390	0.398	0.493	0.185	0.456

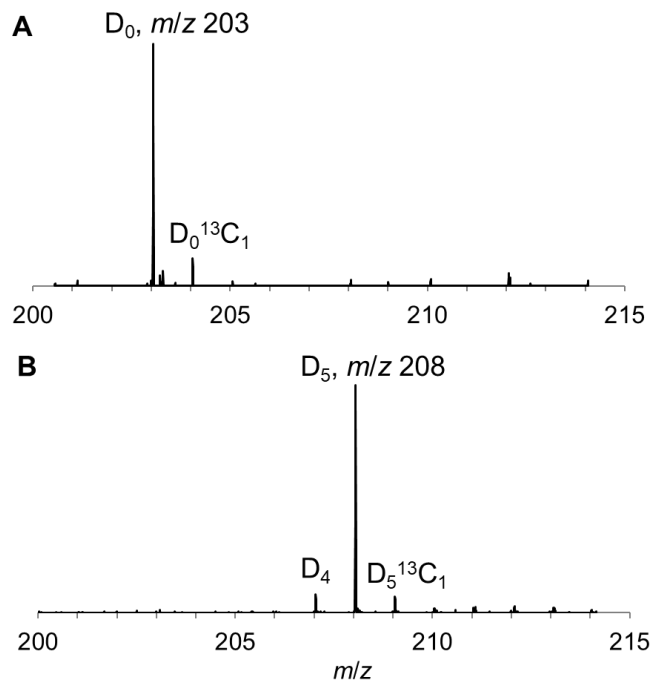


Figure D.3. Representative fragmentation spectra of C₁/Y₁ fragment generated from sodium-adducted raffinose in (A) water and (B) 98% D₂O. D_{max} is observed at D₅ for the C₁/Y₁ fragment, indicating that the C₁/Y₁ fragment received a labile hydrogen (therefore, a deuterium) during fragmentation. Unlabeled peaks are noise.

Table D.9. Test for statistical significance of differences in deuteration levels between B₂/Z₂ and C₁/Y₁ fragments of sodium-adducted raffinose in 25% D₂O. SEM stands for standard error of the mean, df stands for degrees of freedom, and CI are confidence interval at each α value of 0.05 or 0.01. t calculated is compared against t values, and %D difference is compared against CI. If both t calculated and %D difference values exceed respective reference values at α value of 0.05 or 0.01, the difference in deuteration levels of two fragments are determined statistically significant at 95% or 99% confidence interval, respectively. If either or both values are within the ranges given for reference t or confidence interval, the difference in %D between the two fragments is not statistically significant (N).

Precursor	0D	1D	2D	3D	4D	5D
SEM	0.437	0.437	0.437	0.437	0.437	0.437
%D B ₂ /Z ₂	14.04	19.07	25.40	32.68	39.40	46.22
%D C ₁ /Y ₁	11.91	16.86	22.60	29.71	36.48	43.24
df	17	22	20	20	22	22
t 0.05	2.110	2.074	2.086	2.086	2.074	2.074
t 0.01	2.898	2.819	2.845	2.845	2.819	2.819
CI 0.05	± 0.922	± 0.906	± 0.912	± 0.912	± 0.906	± 0.906
CI 0.01	± 1.266	± 1.232	± 1.243	± 1.243	± 1.232	± 1.232
%D diff	2.13	2.21	2.81	2.97	2.92	2.99
t calculated	3.29	4.09	6.45	7.00	6.33	4.95
	99%	99%	99%	99%	99%	99%

Table D.10. Test for statistical significance of differences in deuteration levels between B₂/Z₂ and C₁/Y₁ fragments of sodium-adducted raffinose in 50% D₂O. SEM stands for standard error of the mean, df stands for degrees of freedom, and CI are confidence interval at each α value of 0.05 or 0.01. t calculated is compared against t values, and %D difference is compared against CI. If both t calculated and %D difference values exceed respective reference values at α value of 0.05 or 0.01, the difference in deuteration levels of two fragments are determined statistically significant at 95% or 99% confidence interval, respectively. If either or both values are within the ranges given for reference t or confidence interval, the difference in %D between the two fragments is not statistically significant (N).

Precursor	3D	4D	5D	6D	7D	8D
SEM	0.458	0.458	0.458	0.458	0.458	0.458
%D B ₂ /Z ₂	38.27	44.52	51.54	58.81	65.78	73.96
%D C ₁ /Y ₁	34.83	42.13	49.17	56.37	63.60	70.45
df	20	18	18	22	22	22
t 0.05	2.086	2.101	2.101	2.074	2.074	2.074
t 0.01	2.845	2.878	2.878	2.819	2.819	2.819
CI 0.05	± 0.955	± 0.962	± 0.962	± 0.950	± 0.950	± 0.950
CI 0.01	± 1.303	± 1.318	± 1.318	± 1.291	± 1.291	± 1.291
%D diff	3.44	2.39	2.36	2.44	2.18	3.51
t calculated	6.00	5.76	4.07	6.59	4.37	5.92
	99%	99%	99%	99%	99%	99%

Table D.11. Test for statistical significance of differences in deuteration levels between B₂/Z₂ and C₁/Y₁ fragments of sodium-adducted raffinose in 75% D₂O. SEM stands for standard error of the mean, df stands for degrees of freedom, and CI are confidence interval at each α value of 0.05 or 0.01. t calculated is compared against t values, and %D difference is compared against CI. If both t calculated and %D difference values exceed respective reference values at α value of 0.05 or 0.01, the difference in deuteration levels of two fragments are determined statistically significant at 95% or 99% confidence interval, respectively. If either or both values are within the ranges given for reference t or confidence interval, the difference in %D between the two fragments is not statistically significant (N).

Precursor	6D	7D	8D	9D	10D	11D
SEM	0.380	0.380	0.380	0.380	0.380	0.380
%D B ₂ /Z ₂	63.20	70.63	77.13	83.97	90.35	98.07
%D C ₁ /Y ₁	60.39	68.44	75.65	82.59	87.74	95.59
df	20	21	22	21	22	19
t 0.05	2.086	2.080	2.074	2.080	2.074	2.093
t 0.01	2.845	2.831	2.819	2.831	2.819	2.861
CI 0.05	± 0.793	± 0.794	± 0.788	± 0.794	± 0.788	± 0.795
CI 0.01	± 1.081	± 1.076	± 1.071	± 1.076	± 1.071	± 1.087
%D diff	2.80	2.18	1.48	1.38	2.61	2.48
t calculated	5.34	5.14	4.20	5.19	5.27	5.11
	99%	99%	99%	99%	99%	99%

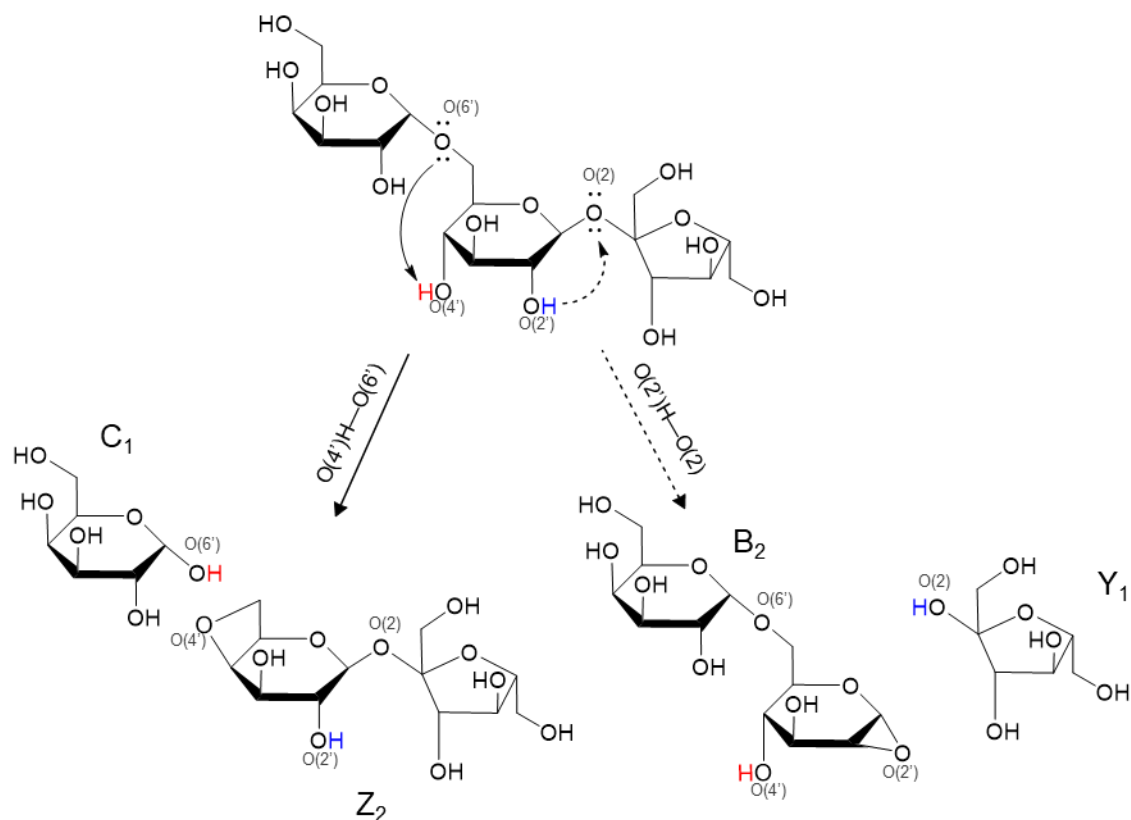


Figure D.4. Proposed fragmentation pathways of sodium-adducted raffinose via CID. C-O bond dissociation is initiated by protonation of glycosidic oxygens, at O(2) or O(6'). DFT optimizations of sodium-adducted raffinose shows O(2')H as the most likely proton source to initiate the fragmentation process to produce B₂ and Y₁ fragments. While O(4')H protonation of the O(6') glycosidic oxygen is also possible, this pathway which produces Z₂ and C₁ fragments seems less likely than the O(2')H-O(2) pathway that generate B₂ and Y₁ fragments based on the distance between O(4')H-O(2). The distances between hydroxyl hydrogens and glycosidic oxygens are presented in Table D.11.

Table D.12. List of distances between hydroxyl hydrogens and glycosidic oxygens of sodium-adducted raffinose that can initiate fragmentation for production of Z₂/C₁ and B₂/Y₁ fragments. All lengths are reported in angstroms (Å).

Trial #	Z ₂ (O(6'))			B ₂ (O(2))		
	O(2')H	O(3')H	O(4')H	O(2')H	O(3')H	O(4')H
1	5.308	5.904	4.637	2.318	5.158	4.391
2	6.253	5.263	5.681	2.317	4.791	4.961
3	5.985	5.052	5.170	2.365	5.151	3.995
4	6.997	6.786	5.102	3.720	4.525	5.108
5	6.055	5.095	5.111	2.433	5.163	3.999
6	6.371	4.973	5.252	2.360	5.186	3.908
7	5.308	5.904	4.637	2.318	5.158	4.391
8	5.861	5.501	2.398	2.323	5.227	4.952
9	7.017	6.793	5.073	3.663	4.524	5.147
10	6.082	5.315	5.099	2.472	4.889	4.060
Average	6.124	5.659	4.816	2.629	4.977	4.491
Std Dev	0.583	0.678	0.900	0.563	0.277	0.503

Table D.13. Test for statistical significance of differences in deuteration levels between B₂/Z₂ and C₂/Y₂ fragments of sodium-adducted raffinose in 25% D₂O. SEM stands for standard error of the mean, df stands for degrees of freedom, and CI are confidence interval at each α value of 0.05 or 0.01. *t* calculated is compared against *t* values, and %D difference is compared against CI. If both *t* calculated and %D difference values exceed respective reference values at α value of 0.05 or 0.01, the difference in deuteration levels of two fragments are determined statistically significant at 95% or 99% confidence interval, respectively. If either or both values are within the ranges given for reference *t* or confidence interval, the difference in %D between the two fragments is not statistically significant (N).

Precursor	0D	1D	2D	3D	4D	5D
SEM	0.437	0.437	0.437	0.437	0.437	0.437
%D B ₂ /Z ₂	14.04	19.07	25.40	32.68	39.40	46.22
%D C ₂ /Y ₂	10.64	16.69	23.20	30.41	37.77	45.18
df	11	11	12	12	12	11
<i>t</i> 0.05	2.201	2.201	2.179	2.179	2.179	2.201
<i>t</i> 0.01	3.106	3.106	3.055	3.055	3.055	3.106
CI 0.05	± 0.962	± 0.962	± 0.952	± 0.952	± 0.952	± 0.962
CI 0.01	± 1.357	± 1.357	± 1.335	± 1.335	± 1.335	± 1.357
%D diff	3.40	2.38	2.21	2.27	1.63	1.04
<i>t</i> calculated	5.97	5.76	8.25	9.13	5.31	2.52
	99%	99%	99%	99%	99%	95%

Table D.14. Test for statistical significance of differences in deuteration levels between B₂/Z₂ and C₂/Y₂ fragments of sodium-adducted raffinose in 50% D₂O. SEM stands for standard error of the mean, df stands for degrees of freedom, and CI are confidence interval at each α value of 0.05 or 0.01. t calculated is compared against t values, and %D difference is compared against CI. If both t calculated and %D difference values exceed respective reference values at α value of 0.05 or 0.01, the difference in deuteration levels of two fragments are determined statistically significant at 95% or 99% confidence interval, respectively. If either or both values are within the ranges given for reference t or confidence interval, the difference in %D between the two fragments is not statistically significant (N).

Precursor	3D	4D	5D	6D	7D	8D
SEM	0.458	0.458	0.458	0.458	0.458	0.458
%D B ₂ /Z ₂	38.27	44.52	51.54	58.81	65.78	73.96
%D C ₂ /Y ₂	35.14	42.58	49.85	57.14	64.60	72.09
df	12	12	12	14	13	11
t 0.05	2.179	2.179	2.179	2.145	2.160	2.201
t 0.01	3.055	3.055	3.055	2.998	3.012	3.106
CI 0.05	± 0.998	± 0.998	± 0.998	± 0.982	± 0.989	± 1.008
CI 0.01	± 1.399	± 1.399	± 1.399	± 1.373	± 1.379	± 1.423
%D diff	3.14	1.94	1.69	1.66	1.18	1.87
t calculated	6.72	5.31	3.31	5.82	3.13	4.58
	99%	99%	99%	99%	95%	99%

Table D.15. Test for statistical significance of differences in deuteration levels between B₂/Z₂ and C₂/Y₂ fragments of sodium-adducted raffinose in 75% D₂O. SEM stands for standard error of the mean, df stands for degrees of freedom, and CI are confidence interval at each α value of 0.05 or 0.01. *t* calculated is compared against *t* values, and %D difference is compared against CI. If both *t* calculated and %D difference values exceed respective reference values at α value of 0.05 or 0.01, the difference in deuteration levels of two fragments are determined statistically significant at 95% or 99% confidence interval, respectively. If either or both values are within the ranges given for reference *t* or confidence interval, the difference in %D between the two fragments is not statistically significant (N).

Precursor	6D	7D	8D	9D	10D	11D
SEM	0.380	0.380	0.380	0.380	0.380	0.380
%D B ₂ /Z ₂	63.20	70.63	77.13	83.97	90.35	98.07
%D C ₂ /Y ₂	61.70	69.54	76.59	83.21	89.62	96.15
df	12	11	13	15	12	12
<i>t</i> 0.05	2.179	2.201	2.160	2.131	2.179	2.179
<i>t</i> 0.01	3.055	3.106	3.012	2.947	3.055	3.055
CI 0.05	± 0.828	± 0.836	± 0.821	± 0.810	± 0.828	± 0.828
CI 0.01	± 1.161	± 1.180	± 1.145	± 1.120	± 1.161	± 1.161
%D diff	1.50	1.09	0.54	0.76	0.73	1.92
<i>t</i> calculated	3.43	3.33	1.99	4.18	2.20	7.18
	99%	95%	N	N	N	99%

Table D.16. List of distances between hydroxyl hydrogens and glycosidic oxygens of sodium-adducted raffinose that can initiate fragmentation for production of Y₂ and C₂ fragments. All lengths are reported in angstroms (Å).

Trial #	Y ₂ (O(6'))				C ₂ (O(2))			
	O(2'')H	O(3'')H	O(4'')H	O(6'')H	O(1)H	O(3)H	O(4)H	O(6)H
1	3.473	5.092	5.796	6.280	3.655	2.400	5.129	5.329
2	4.994	5.086	6.120	4.994	4.128	4.128	3.298	4.729
3	3.679	4.729	5.235	6.154	3.669	2.376	5.119	5.458
4	3.532	5.126	5.133	6.246	4.322	3.489	4.510	5.382
5	3.457	5.078	5.798	6.277	3.704	2.150	5.013	3.456
6	3.671	4.855	5.054	5.233	3.692	2.483	5.149	5.123
7	3.473	5.092	5.796	6.280	3.655	2.401	5.129	5.329
8	2.499	5.096	6.131	4.794	3.639	2.523	5.036	2.527
9	3.220	5.054	6.134	5.141	4.320	2.406	4.524	5.438
10	2.439	5.147	6.091	5.643	3.753	2.053	5.054	5.268
Average	3.444	5.036	5.729	5.704	3.854	2.641	4.796	4.804
Std Dev	0.705	0.134	0.432	0.611	0.285	0.650	0.579	1.002

Table D.17. Test for statistical significance of differences in deuteration levels between B₂/Z₂ and C₁/Y₁ fragments of sodium-adducted maltotriose in 25% D₂O. SEM stands for standard error of the mean, df stands for degrees of freedom, and CI are confidence interval at each α value of 0.05 or 0.01. t calculated is compared against t values, and %D difference is compared against CI. If both t calculated and %D difference values exceed respective reference values at α value of 0.05 or 0.01, the difference in deuteration levels of two fragments are determined statistically significant at 95% or 99% confidence interval, respectively. If either or both values are within the ranges given for reference t or confidence interval, the difference in %D between the two fragments is not statistically significant (N).

Precursor	0D	1D	2D	3D	4D	5D
SEM	0.455	0.455	0.455	0.455	0.455	0.455
%D B ₂ /Z ₂	11.28	17.38	23.92	31.30	39.03	47.11
%D C ₁ /Y ₁	13.12	18.85	24.01	30.56	36.83	45.04
df	13	14	13	17	13	12
t 0.05	2.160	2.145	2.160	2.110	2.160	2.179
t 0.01	3.012	2.977	3.012	2.898	3.012	3.055
CI 0.05	± 0.983	± 0.976	± 0.983	± 0.960	± 0.983	± 0.991
CI 0.01	± 1.370	± 1.355	± 1.370	± 1.319	± 1.370	± 1.390
%D diff	-1.84	-1.47	-0.09	0.74	2.20	2.06
t calculated	2.32	3.92	0.28	1.96	3.63	2.05
	95%	99%	N	N	99%	N

Table D.18. Test for statistical significance of differences in deuteration levels between B₂/Z₂ and C₁/Y₁ fragments of sodium-adducted maltotriose in 50% D₂O. SEM stands for standard error of the mean, df stands for degrees of freedom, and CI are confidence interval at each α value of 0.05 or 0.01. t calculated is compared against t values, and %D difference is compared against CI. If both t calculated and %D difference values exceed respective reference values at α value of 0.05 or 0.01, the difference in deuteration levels of two fragments are determined statistically significant at 95% or 99% confidence interval, respectively. If either or both values are within the ranges given for reference t or confidence interval, the difference in %D between the two fragments is not statistically significant (N).

Precursor	3D	4D	5D	6D	7D	8D
SEM	0.506	0.506	0.506	0.506	0.506	0.506
%D B ₂ /Z ₂	36.88	43.44	50.70	58.21	65.88	73.64
%D C ₁ /Y ₁	36.05	42.91	49.06	56.36	63.54	71.66
df	13	13	12	13	12	14
t 0.05	2.160	2.160	2.179	2.160	2.179	2.145
t 0.01	3.012	3.012	3.055	3.012	3.055	2.977
CI 0.05	± 1.093	± 1.093	± 1.102	± 1.093	± 1.102	± 1.085
CI 0.01	± 1.524	± 1.524	± 1.546	± 1.524	± 1.546	± 1.506
%D diff	0.83	0.53	1.65	1.84	2.34	1.99
t calculated	0.95	0.89	2.68	3.54	3.75	2.27
	N	N	95%	99%	99%	95%

Table D.19. Test for statistical significance of differences in deuteration levels between B₂/Z₂ and C₁/Y₁ fragments of sodium-adducted maltotriose in 75% D₂O. SEM stands for standard error of the mean, df stands for degrees of freedom, and CI are confidence interval at each α value of 0.05 or 0.01. t calculated is compared against t values, and %D difference is compared against CI. If both t calculated and %D difference values exceed respective reference values at α value of 0.05 or 0.01, the difference in deuteration levels of two fragments are determined statistically significant at 95% or 99% confidence interval, respectively. If either or both values are within the ranges given for reference t or confidence interval, the difference in %D between the two fragments is not statistically significant (N).

Precursor	6D	7D	8D	9D	10D	11D
SEM	0.441	0.441	0.441	0.441	0.441	0.441
%D B ₂ /Z ₂	62.33	70.21	77.06	83.58	90.33	97.41
%D C ₁ /Y ₁	61.98	68.67	76.34	81.99	89.16	96.33
df	13	13	12	20	14	15
t 0.05	2.160	2.160	2.179	2.086	2.145	2.131
t 0.01	3.012	3.012	3.055	2.845	2.977	2.947
CI 0.05	± 0.953	± 0.953	± 0.961	± 0.920	± 0.946	± 0.940
CI 0.01	± 1.328	± 1.328	± 1.348	± 1.255	± 1.313	± 1.300
%D diff	0.36	1.54	0.72	1.59	1.18	1.08
t calculated	0.41	2.70	1.36	5.15	2.29	1.52
	N	95%	N	99%	95%	N

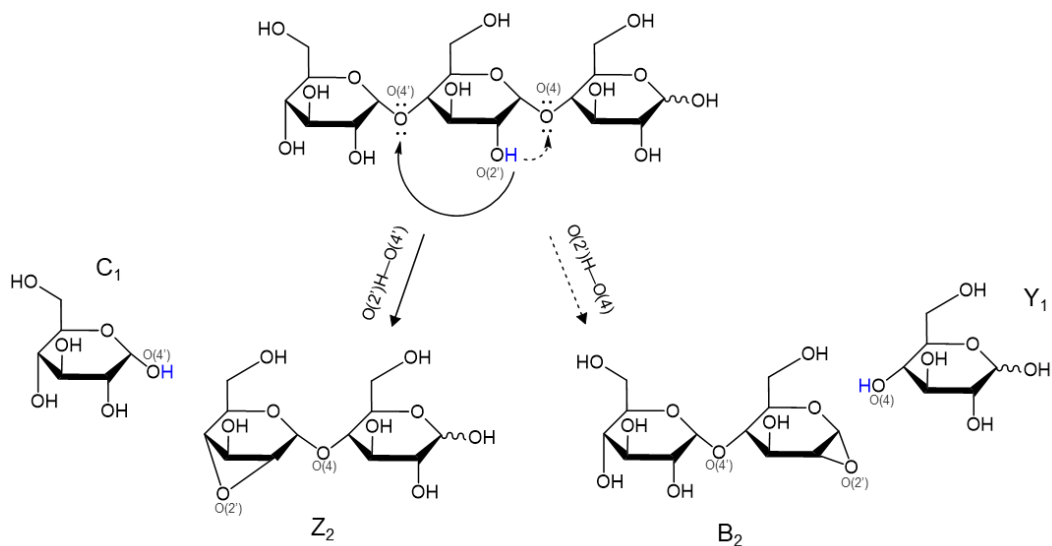


Figure D.5. Proposed fragmentation pathways of sodium-adducted maltotriose via CID. C-O bond dissociation is initiated by protonation of glycosidic oxygens, at the O(4) or O(4') positions. DFT optimizations of sodium-adducted maltotriose show the O(2')H as the closest to both glycosidic oxygens, and thus, the most likely source of a proton to initiate the fragmentation pathways for both B₂/Y₁ and Z₂/C₁ production. The distances between hydroxyl hydrogens and glycosidic oxygens are presented in Table D.18.

Table D.20. List of distances between hydroxyl hydrogens and glycosidic oxygens of sodium-adducted maltotriose that can initiate fragmentation pathways for production of Z₂ and B₂ fragments. All lengths are reported in angstroms (Å).

Trial #	Z ₂ (O(4'))			B ₂ (O(4))		
	O(2')H	O(3')H	O(6')H	O(2')H	O(3')H	O(6')H
1	1.947	3.958	5.289	3.465	5.093	4.058
2	4.881	3.446	4.883	3.657	4.687	6.293
3	4.044	3.941	4.744	3.519	5.154	6.034
4	4.046	3.941	4.744	3.520	5.154	6.035
5	2.952	3.858	4.919	3.555	5.106	6.297
6	4.044	3.942	4.744	3.519	5.154	6.035
7	3.850	4.224	5.048	2.468	4.993	6.342
8	3.525	3.986	4.677	3.535	4.178	5.919
9	1.931	3.946	4.971	3.498	5.095	6.329
10	1.974	3.909	5.061	3.423	5.189	6.337
Average	3.319	3.915	4.908	3.416	4.980	5.968
Std Dev	1.059	0.191	0.191	0.339	0.317	0.690

Table D.21. Test for statistical significance of differences in deuteration levels between B₂/Z₂ and C₂/Y₂ fragments of sodium-adducted maltotriose in 25% D₂O. SEM stands for standard error of the mean, df stands for degrees of freedom, and CI are confidence interval at each α value of 0.05 or 0.01. t calculated is compared against t values, and %D difference is compared against CI. If both t calculated and %D difference values exceed respective reference values at α value of 0.05 or 0.01, the difference in deuteration levels of two fragments are determined statistically significant at 95% or 99% confidence interval, respectively. If either or both values are within the ranges given for reference t or confidence interval, the difference in %D between the two fragments is not statistically significant (N).

Precursor	0D	1D	2D	3D	4D	5D
SEM	0.455	0.455	0.455	0.455	0.455	0.455
%D B ₂ /Z ₂	11.28	17.38	23.92	31.30	39.03	47.11
%D C ₂ /Y ₂	10.61	16.51	23.08	30.38	37.75	45.10
df	13	16	17	18	21	17
t 0.05	2.160	2.120	2.110	2.101	2.080	2.110
t 0.01	3.012	2.921	2.898	2.878	2.831	2.898
CI 0.05	± 0.983	± 0.965	± 0.960	± 0.956	± 0.946	± 0.960
CI 0.01	± 1.370	± 1.329	± 1.319	± 1.309	± 1.288	± 1.319
%D diff	0.67	0.87	0.84	0.92	1.27	2.01
t calculated	2.69	6.28	7.39	4.43	6.31	7.53
	N	N	N	N	95%	99%

Table D.22. Test for statistical significance of differences in deuteration levels between B₂/Z₂ and C₂/Y₂ fragments of sodium-adducted maltotriose in 50% D₂O. SEM stands for standard error of the mean, df stands for degrees of freedom, and CI are confidence interval at each α value of 0.05 or 0.01. t calculated is compared against t values, and %D difference is compared against CI. If both t calculated and %D difference values exceed respective reference values at α value of 0.05 or 0.01, the difference in deuteration levels of two fragments are determined statistically significant at 95% or 99% confidence interval, respectively. If either or both values are within the ranges given for reference t or confidence interval, the difference in %D between the two fragments is not statistically significant (N).

Precursor	3D	4D	5D	6D	7D	8D
SEM	0.506	0.506	0.506	0.506	0.506	0.506
%D B ₂ /Z ₂	36.88	43.44	50.70	58.21	65.88	73.64
%D C ₂ /Y ₂	35.25	42.60	49.94	57.16	64.75	72.51
df	19	22	20	17	20	18
t 0.05	2.093	2.074	2.086	2.110	2.086	2.101
t 0.01	2.861	2.819	2.845	2.898	2.845	2.878
CI 0.05	± 1.059	± 1.049	± 1.056	± 1.068	± 1.056	± 1.063
CI 0.01	± 1.448	± 1.426	± 1.440	± 1.466	± 1.440	± 1.456
%D diff	1.63	0.84	0.76	1.05	1.13	1.14
t calculated	5.70	3.70	4.94	5.83	6.57	3.39
	99%	N	N	N	95%	95%

Table D.23. Test for statistical significance of differences in deuteration levels between B₂/Z₂ and C₂/Y₂ fragments of sodium-adducted maltotriose in 75% D₂O. SEM stands for standard error of the mean, df stands for degrees of freedom, and CI are confidence interval at each α value of 0.05 or 0.01. *t* calculated is compared against *t* values, and %D difference is compared against CI. If both *t* calculated and %D difference values exceed respective reference values at α value of 0.05 or 0.01, the difference in deuteration levels of two fragments are determined statistically significant at 95% or 99% confidence interval, respectively. If either or both values are within the ranges given for reference *t* or confidence interval, the difference in %D between the two fragments is not statistically significant (N).

Precursor	6D	7D	8D	9D	10D	11D
SEM	0.441	0.441	0.441	0.441	0.441	0.441
%D B ₂ /Z ₂	62.33	70.21	77.06	83.58	90.33	97.41
%D C ₂ /Y ₂	62.03	69.67	76.64	83.00	89.79	96.28
df	15	20	22	21	16	17
<i>t</i> 0.05	2.131	2.086	2.074	2.080	2.120	2.110
<i>t</i> 0.01	2.947	2.845	2.819	2.831	2.921	2.898
CI 0.05	± 0.940	± 0.920	± 0.915	± 0.917	± 0.935	± 0.931
CI 0.01	± 1.300	± 1.255	± 1.243	± 1.248	± 1.288	± 1.278
%D diff	0.30	0.53	0.42	0.58	0.54	1.12
<i>t</i> calculated	1.04	2.74	2.78	2.43	2.56	3.62
	N	N	N	N	N	95%

Table D.24. List of distances between hydroxyl hydrogens and glycosidic oxygens of sodium-adducted maltotriose that can initiate fragmentation pathways for production of Y₂ and C₂ fragments. All lengths are reported in angstroms (Å).

Trial #	Y ₂ (O(4'))				C ₂ (O(4))			
	O(2'')H	O(3'')H	O(4'')H	O(6'')H	O(1)H	O(2)H	O(3)H	O(6)H
1	3.629	4.593	5.192	3.734	3.965	3.606	4.293	4.687
2	3.621	4.570	5.087	5.024	4.951	4.908	2.622	4.875
3	3.673	4.888	5.082	6.096	5.143	3.920	3.934	4.987
4	3.672	4.888	5.083	6.097	5.145	3.921	3.934	4.986
5	3.518	4.460	5.022	4.230	5.173	3.843	3.935	5.031
6	3.673	4.888	5.083	6.096	3.934	3.919	5.143	4.987
7	3.252	4.722	5.323	5.338	3.712	5.587	5.060	3.946
8	3.626	4.709	5.891	4.738	5.324	3.909	3.930	4.966
9	3.528	4.500	5.117	5.281	5.244	3.850	4.215	4.994
10	3.501	4.399	4.728	5.255	5.339	3.902	4.252	4.899
Average	3.569	4.662	5.161	5.189	4.793	4.137	4.132	4.836
Std Dev	0.130	0.185	0.297	0.801	0.649	0.614	0.697	0.328

APPENDIX E

Investigating Carbohydrate-Metal Complex Fragmentation Pathways via Collision Induced Dissociation and Transition State Calculations

E.1 Introduction

The significance of carbohydrates in cellular biology has been highlighted in recent years for their involvement in crucial biological processes such as protein folding and cell-cell communication.²²⁹ The diversity and complexity of carbohydrates, however, presents challenges for carbohydrate analysis. Mass spectrometry (MS) is a popular tool for carbohydrate and glycan analysis for its high sensitivity, which requires only small sample volumes. MS is also versatile and can be coupled to various solution- and gas-phase techniques that enable separation, sequencing, and online reactions. However, one main disadvantage of carbohydrate analysis by MS is that many carbohydrates are isomers. Because MS detects mass-to-charge ratios (m/z), isomers cannot be resolved. Therefore, sequencing of carbohydrates via MS typically requires tandem techniques such as gas-phase fragmentation to obtain MS/MS profiles that are characteristic of carbohydrate isomers.^{227, 297, 360}

Collision induced dissociation (CID) is a common fragmentation technique that has been used for analysis of numerous carbohydrate and glycan structures. CID is achieved by introducing gas-phase ions into a chamber filled with inert gas, and the collisions with gas molecules vibrationally activate the ions, inducing bond dissociation. Carbohydrates have been shown to generate varying fragmentation patterns depending on the composition and linkage of isomers. For instance, isomer fragmentation spectra show

preference for one fragment over another.^{361, 362} Fragmentation patterns also vary based on the type of charge carrier, such as sodium or lithium ions.¹⁵⁶ However, there is no straightforward answer as to why such differences are observed. A general mechanism of fragmentation cannot adequately describe the numerous carbohydrates of varying composition and linkages whose fragmentation pathways differ based on gas-phase conformations. Moreover, carbohydrates are flexible in solution and an averaged mass spectrum does not reflect the diverse carbohydrate conformations even within a single carbohydrate population. Connecting carbohydrate conformations to their fragmentation behavior could provide insight for understanding intra- and intermolecular carbohydrate interactions, such as coordinate bonds with metal ions, that are biologically relevant.

Here we present a combinatorial approach of carbohydrate fragmentation via collision induced dissociation (CID) and structure optimizations by density functional theory (DFT) calculations to correlate the experimental data and calculated structures and energetics. The intramolecular hydrogen bonding between carbohydrate hydroxyls and glycosidic oxygens was measured to predict isomeric fragment structures, and transition states were calculated. The energetics for each fragment product, the fragment-metal interactions, and the precursor carbohydrate-metal complex conformations were compared to interpret experimental MS/MS data. We argue that our method, which combines experimental observations and theoretical predictions, aptly describes many important aspects of carbohydrate fragmentation reactions such as the fragmentation pathway, fragment-metal interactions, and carbohydrate conformations. The work here describes sodium-adducted melezitose as the main system with focus on glycosidic bond cleavages, but other preliminary observations from isomeric trisaccharides and other

metal adducts are included as well. Although the work presented here is preliminary, we believe this work is sufficient groundwork to be expanded to other systems to examine cross-ring cleavages, secondary fragmentations, and other carbohydrate-metal complexes.

E.2 Materials and Methods

E.2.1 Sample Preparation

Melezitose, raffinose, and maltotriose were purchased from Sigma Aldrich (St. Louis, MO). The acetate salts were purchased from VWR (Randor, PA). Nanopure water was obtained from a Purelab Flex 3 purification system (Elga, Veolia Environment S. A., Paris, France). Carbohydrates were prepared in a 1:1 molar ratio with salts in water to generate carbohydrate-metal complexes. Permethylated melezitose, raffinose, and maltotriose were provided by Amanda Pearson. A 1:1 molar ratio of each permethylated carbohydrate and sodium acetate was prepared in methanol.

E.2.2 Collision Induced Dissociation

Mixtures of underivatized carbohydrates and salt was directly infused at 5 $\mu\text{L}/\text{min}$ into a LockSpray Exact Mass Ionization Source equipped on a Synapt G2-S High Definition MS (HDMS) (Waters Corporation, Millford, MA). Permethylated carbohydrates and sodium acetate mixtures were loaded on custom pulled electrospray tips, prepared from single-barrel borosilicate tubes using a P-1000 micropipette puller (Sutter Instrument, Novato, CA). Platinum wire (ADInstruments, Sydney, Australia) was inserted into the tip and voltage was applied from the open ESI source, similar to the one shown in Chapter Three and Appendix B (Figure B.2).³⁰²

A full mass spectrum was obtained for each carbohydrate-metal complex to see if in-source fragmentation occurred. Then, CID was achieved by a collision energy ramp for metal- or ammonium-adducted, protonated, and deprotonated carbohydrates. For permethylated carbohydrates, only sodium-adducts were fragmented because other metal adducts were not observed. CID in the Waters Synapt G2-S occurs in the trap cell, and the collision energy can be varied by changing the acceleration voltage into the trap region. The default acceleration voltage is set at 4 V, and significant signal loss was observed below the acceleration voltage of 4 V. Therefore, the minimum collision voltage used was 4 V, including when collecting a full mass spectrum during which precursor isolation was not performed. Following precursor isolation, the collision energy was increased in increments of 2 V if in-source fragmentation was observed, and in increments of 4 V if in-source fragmentation was not observed. Collision energy was only increased up to a point where the precursor intensity started disappearing, so that the effect of secondary fragmentation was reduced. Fragments of both underivatized and permethylated carbohydrates were assigned using fragment lists predicted by GlycoWorkbench³¹¹, following the Domon and Costello nomenclature.¹⁵⁵ Structures of underivatized melezitose, raffinose, and maltotriose with their fragments are shown in Figure E.1.

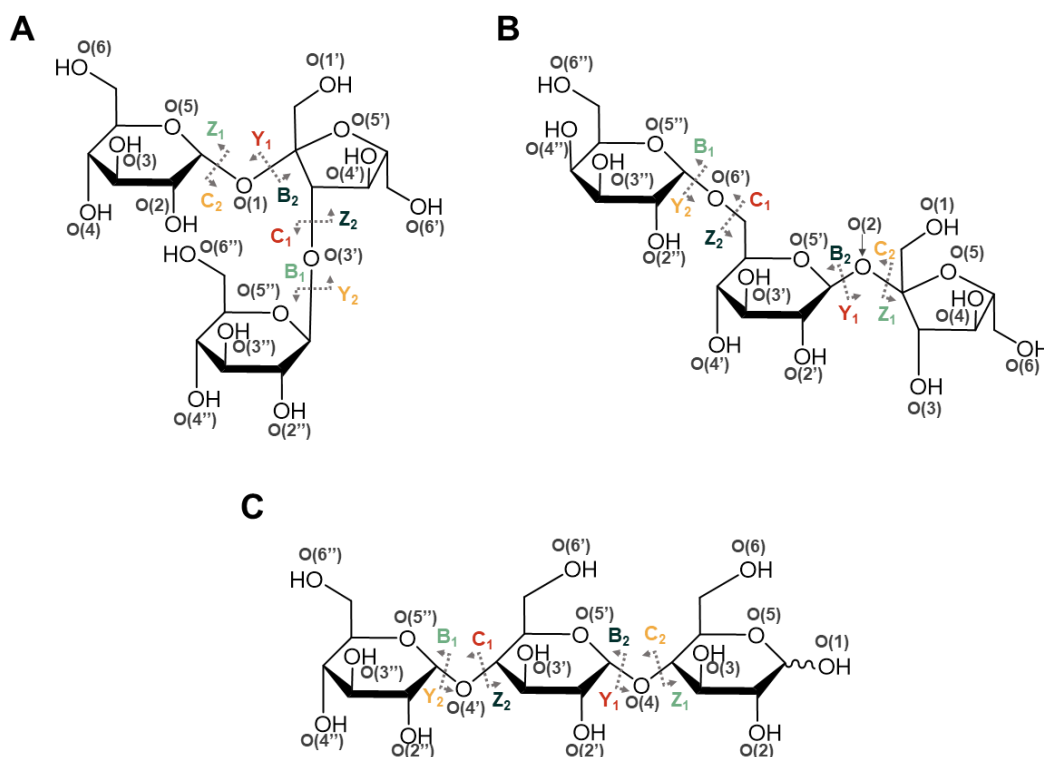


Figure E.1. Chemical structures of (A) melezitose, (B) raffinose, and (C) maltotriose with their glycosidic bond cleavage fragments. While melezitose and raffinose are non-reducing sugars, both B/C and Y/Z nomenclature are used to distinguish the two terminal ends. Assignment of “reducing” end is based on the IUPAC nomenclature of the carbohydrates. Isomeric fragments are indicated with the same color.

E.2.3 Transition State Calculations

The energetics for fragmenting each carbohydrate-metal complex were examined computationally. Initial carbohydrate structures were taken from the ZINC database³⁶³ or built using the GLYCAM Carbohydrate Builder Web Tool.³⁶⁴ MD simulation of ESI droplets containing carbohydrates and sodium ions⁹⁶ were performed by Dr. Emvia I Calixte. The details of the MD simulations can be found in Chapter Five. Briefly, the droplets containing one carbohydrate and ten sodium ions were subjected to solvent evaporation and ion ejection events in vacuum until carbohydrate-sodium complexes were released into the gas phase. Ten structures of sodium-adducted carbohydrates were

taken from the MD simulations to observe the various conformations, rather than one structure. The ten carbohydrate-metal complexes taken from MD simulations were optimized by density functional theory (DFT) calculations at the B3LYP 6-311++G(d) level of theory using Gaussian 16.

The optimized carbohydrate-metal structures were used to represent gas-phase precursor ions. Bythell *et al.*³¹⁰ proposed that glycosidic bond cleavage of metal-adducted carbohydrates is initiated by protonation of a glycosidic oxygen by a hydroxyl hydrogen within the carbohydrate-metal complex. Each glycosidic bond cleavage event following this fragmentation mechanism leads to production of two fragment structures. Therefore, conformations were selected in which a hydroxyl hydrogen was located near the glycosidic oxygen from the ten optimized structures. For instance, if one conformation of melezitose showed that the O(6')H hydroxyl was close to the O(3') glycosidic oxygen, that structure was selected as a precursor structure for fragment and transition state calculations for generating the C₁/Z₂ fragment pair (Figure E.1). If in another conformation of melezitose, the O(6')H hydroxyl was closer to the O(1) glycosidic oxygen, that structure was selected as precursor structure to examine the B₂/Y₁ fragment pair and associated transition states (Figure E.1). The goal of precursor structure selection was to find precursor conformations that would more likely lead to fragmentation, and thus minimize the energy difference between the precursor structure and the transition state or fragment structures. Once precursor ion structures were selected for a fragmentation pair, the bonds around the glycosidic oxygens and hydrogen-donating hydroxyls were modified to generate fragment structures. Only one of the fragments is detected in MS from each glycosidic bond cleavage event because there is only one

charge carrier (sodium ion) to which the fragments can adduct, leaving the other fragment to be lost as a neutral molecule. However, all computational calculations were performed with both fragments in the system. Once geometry optimizations and frequency calculations were performed on the fragments, transition state structures were predicted by QST2 calculations using the precursor and fragment structures. If QST2 calculations did not converge or the transition state structures reverted back to either the precursor ion or fragment structures, QST3 calculations were performed instead by predicting a transition state, typically by drawing a bond between the hydroxyl hydrogen and the glycosidic oxygen. Following successful transition state structure predictions, the energies of precursor ions, transition states, and fragments were compared to generate energy diagrams for each carbohydrate-metal complex.

Deprotonated carbohydrates were built directly on the structures obtained from the ZINC database, rather than performing MD simulations. Optimization of only precursor ions are discussed for deprotonated carbohydrates.

E.3 Results and Discussion

CID fragmentation of carbohydrates has been shown to be initiated by protonation of the glycosidic oxygen for both protonated¹⁵⁵ and sodium-adducted species.³¹⁰ In the case of sodium-adducted carbohydrates, it is proposed that protonation of the glycosidic oxygen occurs by donation of a hydrogen from a nearby hydroxyl within the carbohydrate.³¹⁰ Our data for fully deuterated fragments and the number of labile hydrogens for each fragment also show that B- and Z-type fragments have stacked-ring structures from donating a hydrogen (Chapter Four and Five). Fragmentation pathways of each carbohydrate, however, greatly depend on the gas-phase conformation of the sugars,

which are affected by the sequences of the carbohydrates and the carbohydrate-metal interactions. Melezitose, raffinose, and maltotriose are isomeric trisaccharides that have different monosaccharide compositions and linkage patterns. CID of each trisaccharide reveals vastly different fragmentation patterns both in terms of the types of fragments that are detected and the energy at which the fragments are produced.

Sodium-adducted melezitose produced fragments at five m/z values, but we hypothesize that each of these m/z peaks has multiple isomeric fragments (Figure E.1). Because no isotope labels are used to distinguish different parts of the carbohydrate, the isomeric species cannot be experimentally detected using MS in the current setup. Therefore, fragments are assigned with multiple labels to highlight that isomeric species may be present. C_2/Y_2 (m/z 365) is the fragment from sodium-adducted melezitose detected at the highest intensity, followed by B_2/Z_2 (m/z 347) (Figure E.2A). It is observed that while the intensities of C_1/Y_1 , B_1/Z_1 , and $^{0,3/1,4}X_{\text{Glc}}C_2/^{0,3/1,4}A_{\text{Glc}}Y_2$ fragments continually increase with increasing collision voltage, the intensities of C_2/Y_2 and B_2/Z_2 fragments increase between 28 – 32 V and then decrease beyond 32 V (Figure E.2B). We hypothesize that such a decrease in intensity for bigger fragments is indicative of secondary fragmentation that occurs with C_2/Y_2 and B_2/Z_2 fragments, while the smaller fragments are products of these secondary fragmentation events.

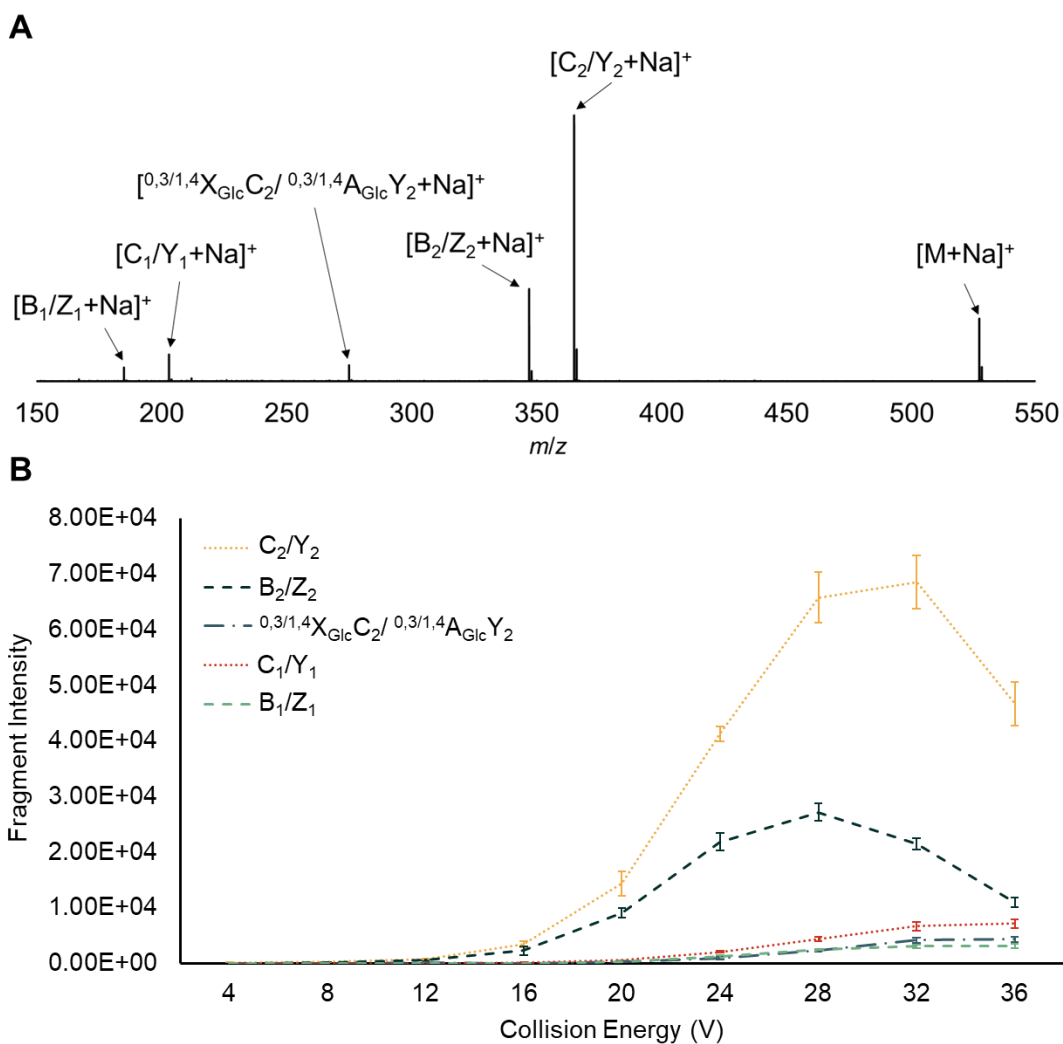


Figure E.2. (A) Representative fragmentation spectrum of sodium-adducted melezitose at collision voltage of 32 V. (B) Intensities of sodium-adducted melezitose fragments at collision voltage ranging 4 – 36 V. Error bars represent standard deviation ($n = 3$).

Based on the fragmentation pathway proposed for sodium-adducted carbohydrates, in which a hydroxyl protonates a glycosidic oxygen and the C-O bond dissociates, glycosidic bond cleavage at one site likely leads to formation of two fragments: the C_2/Y_2 and B_1/Z_1 pair, or the B_2/Z_2 and C_1/Y_1 pair (Figure E.1). However, C_2/Y_2 and B_2/Z_2 fragments are detected at much higher intensities than their fragment pairs. We hypothesize that such differences can be explained by the affinity of each

fragment to the metal charge carrier, leading to sodium adduction of one fragment. The other fragment would dissociate from the complex and be lost as a neutral molecule. On the other hand, higher intensities of the C_2/Y_2 fragment compared to the B_2/Z_2 fragment would suggest a more energetically favorable fragmentation pathway for glycosidic bond cleavages that generate C_2/Y_2 compared to the one that leads to production of the B_2/Z_2 fragment. To determine which of the four glycosidic bond cleavage sites are energetically favorable and thus coincide with observed intensities of fragments, transition state structure optimization calculations were performed for melezitose-sodium complexes. The energetics of six fragment pairs were compared: (1) B_1 and Y_2 , where the $O(2'')$ H hydroxyl of the B_1 fragment donates a proton to the glycosidic oxygen $O(3')$; (2) Z_1 and C_2 , where the $O(2)$ H hydroxyl of the Z_1 fragment donates a proton to the glycosidic oxygen $O(1)$; (3) C_1 and Z_2 fragments, where the protonation of the glycosidic oxygen $O(3')$ may occur by donation from either the $O(4')$ H hydroxyl or (4) the $O(6')$ H hydroxyl of the middle fructose ring; and (5) Y_1 and B_2 fragments, where the glycosidic oxygen $O(1)$ may receive a hydrogen from either the $O(1')$ hydroxyl or (6) the $O(6')$ H hydroxyl of the middle fructose (Figure E.3).

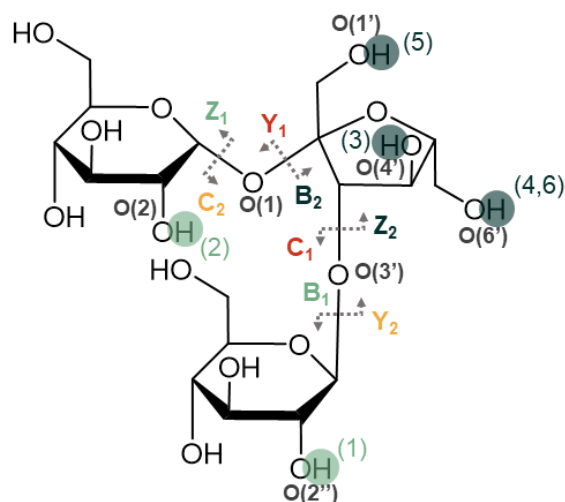


Figure E.3. Melezitose fragmentation nomenclature. Only glycosidic bond cleavage sites are shown. Hydroxyl hydrogens that were used in generating transition state structures are indicated with green or navy circles, for production of B₁/Z₁ and B₂/Z₂ fragments, respectively.

Most reaction pathways were endothermic, consistent with experimental data that fragments began to form after input of high collisional activation associated with acceleration at > 20 V) (Figure E.1). The full list of transition state and product energies relative to the precursor is shown in Table E.1.

Table E.1. Glycosidic bond cleavage energetics of sodium-adducted melezitose. B₁ and Z₁, C₁ and Y₁, B₂ and Z₂, and C₂ and Y₂ are isomeric. Transition state (TS) energy and product (P) energy are reported relative to the precursor.

Fragments	Cleavage Site	-OH used	TS E (kJ/mol)	P E (kJ/mol)
B ₁ /Y ₂	O(3')	O(2'')H	163	65
Z ₁ /C ₂	O(1)	O(2)H	143	74
C ₁ /Z ₂	O(3')	O(4')H	414	349
C ₁ /Z ₂	O(3')	O(6')H	319	19
Y ₁ /B ₂	O(1)	O(1')H	153	52
Y ₁ /B ₂	O(1)	O(6')H	179	-29

For the isomeric fragments, the transition state energy for production of Z_1/C_2 fragments (143 kJ/mol) and the transition state energy for production of B_1/Y_2 fragments (163 kJ/mol) were similar. The energy for the product structures of the Z_1/C_2 fragment pair was also only 9 kJ/mol higher than the B_1/Y_2 fragment pair after C-O bond dissociation. These energy differences are considered small. Therefore, it can be inferred that for the m/z values associated with the C_2/Y_2 (m/z 365) and B_1/Z_1 (m/z 185) fragments, there is equal likelihood that Y_2 and B_1 fragments are detected as their respective, isomeric C_2 and Z_1 fragments. Melezitose has two terminal glucose residues with both in the α anomeric configuration that can donate a hydroxyl hydrogen to glycosidic oxygen to produce B_1/Y_2 or C_2/Z_1 fragments. Therefore, it is reasonable to hypothesize that the interaction between each glycosidic oxygen and the O(2)H or O(2'')H hydroxyls of each terminal glucose would be similar. The O(2)H hydroxyl was found to be 3.4 ± 0.4 Å away from the glycosidic oxygen O(1) ($n = 10$), and the O(2'')H hydroxyl was 2.6 ± 0.5 Å from the glycosidic oxygen O(3') (Figure E.4). Therefore, the orientation of the hydroxyls with respect to the glycosidic oxygens is consistent with the fragmentation energetics obtained from transition state calculations (Table E.1).

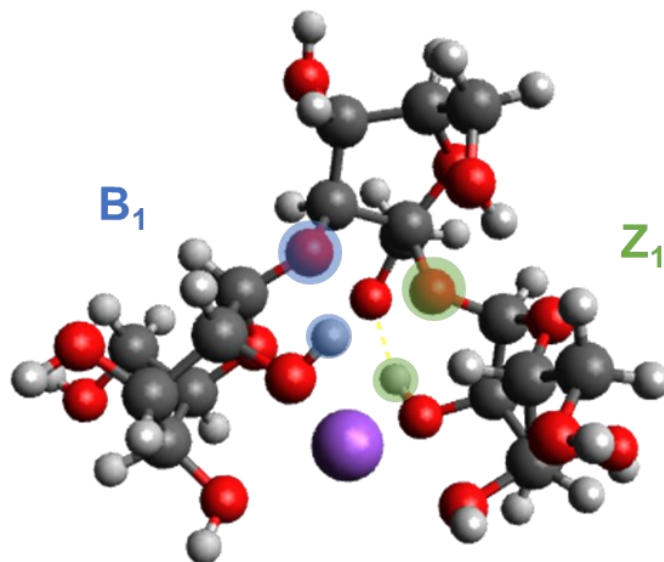


Figure E.4. Representative structure of the sodium-adducted melezitose precursor optimized by DFT calculations. Carbon atoms are shown in gray, oxygen atoms in red, hydrogen atoms in white, and the sodium ion in purple. The two glycosidic oxygens and the carbohydrate hydroxyls that are donated to the glycosidic oxygens are highlighted in blue and green for the two glycosidic bond cleavage sites that produce B₁/Y₂ and Z₁/C₂ fragments, respectively.

For the C₁/Y₁ and B₂/Z₂ isomeric fragment pairs, the pathways for production of C₁/Z₂ fragments have transition state energies that are 150 - 260 kJ/mol higher than the transition states for Y₁/B₂ fragments (Table E.1). Therefore, the fragmentation pathways involving protonation of the glycosidic bond O(3') by the O(4')H or O(6')H hydroxyl towards production of C₁/Z₂ are much less favorable than those in which the O(1) glycosidic oxygen receives a hydrogen from either the O(1')H or O(6')H hydroxyl for generation of the Y₁/B₂ fragments.

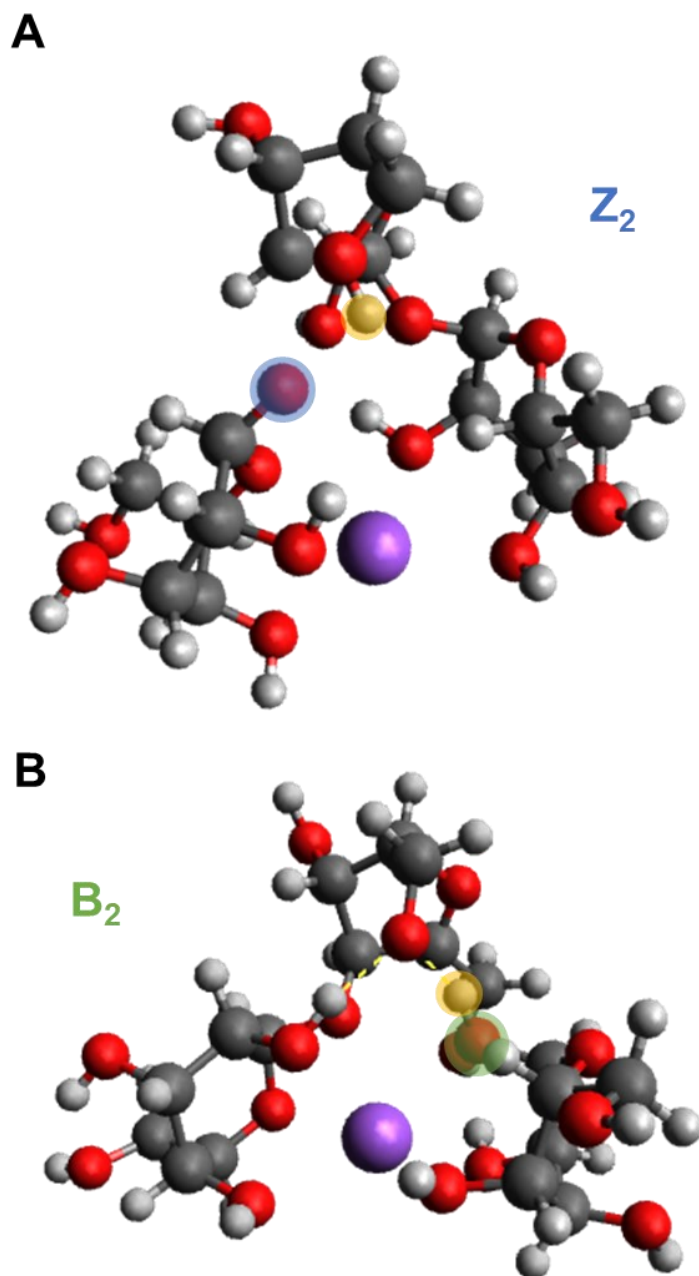


Figure E.5. Transition state structures for (A) C_1/Z_2 and (B) Y_1/B_2 fragments. Carbon atoms are shown in gray, oxygen atoms in red, hydrogen atoms in white, and the sodium ion in purple. The O(6')H hydroxyl hydrogen that was donated to either glycosidic oxygens is highlighted in yellow. The glycosidic oxygens, O(3') and O(1), are highlighted in blue and green, respectively. (B) structure is 140 kJ/mol lower in energy compared to the structure in (A).

Experimentally, it was observed that the C_2/Y_2 fragments were detected at higher intensity compared to the B_2/Z_2 fragments (Figure E.1). However, the transition state calculations show that the reaction coordinate energetics for forming B_1/Y_2 , Z_1/C_2 , and Y_1/B_2 are similarly competitive (Table E.1). Additionally, reaction of the of $O(6')H$ hydroxyl to produce Y_1/B_2 was exothermic. Therefore, the energies obtained from the transition state calculations may not adequately support experimental data by themselves. It is advantageous to have multiple initial structures that more realistically represent the flexible carbohydrate conformation in solution, such as the ones we obtained from MD simulations of ESI droplets. Out of the ten optimized structures, it was found that the orientation of the $O(2'')H$ hydroxyl near the $O(3')$ glycosidic oxygen was more rigid, whereas the $O(6')H$ hydroxyl of the fructose ring was more flexible (Figure E.6). The average distance between the $O(2'')H—O(3')$, which produced the B_1/Y_2 fragment pair, was $2.6 \pm 0.5 \text{ \AA}$, and between $O(6')H—O(1)$ producing B_2/Y_1 fragment pair was $4 \pm 1 \text{ \AA}$. Although energetically competitive with the production of B_1/Y_2 , protonation of the $O(1)$ glycosidic oxygen by the $O(6')H$ hydroxyl of fructose to generate the Y_1/B_2 fragments required a more specific orientation of the fructose ring with respect to the glycosidic oxygen (Figure E.6A). This precise orientation was observed less frequently than alignment of the $O(2'')H$ hydroxyl with the $O(3)$ glycosidic oxygen (Figure E.6A and B). Therefore, we hypothesize that of the multiple gas-phase conformations of metal-adducted carbohydrates, the conformations that enable fragmentation pathways for B_1/Y_2 are more commonly found than the conformations that initiate fragmentation for Y_1/B_2 .

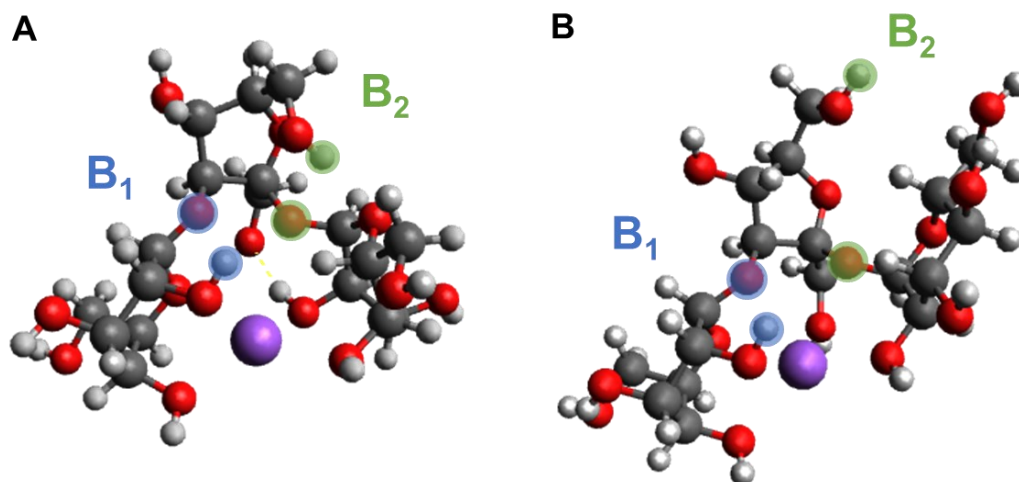


Figure E.6. Representative conformations of melezitose-sodium complexes in which hydroxyl contributions to glycosidic oxygens lead to different fragmentation pathways favoring production of (A) B_1/Y_2 and B_2/Y_1 or (B) only B_1/Y_2 . Carbon atoms are shown in gray, oxygen atoms in red, hydrogen atoms in white, and the sodium ion in purple. The $O(2'')$ H hydroxyl and $O(3')$ glycosidic oxygen are highlighted in blue. The $O(6')$ H hydroxyl and $O(1)$ glycosidic oxygen are highlighted in green.

Finally, a single glycosidic bond cleavage is expected to produce two fragments but one of the fragments is detected at much higher intensity than the other. For instance, the intensity of the B_2/Z_2 fragments at a collision voltage of 20 V was ten-fold higher than the intensity of the C_1/Y_1 fragments (Figure E.2B). The two fragment molecules generated from a glycosidic bond cleavage are neutral and there is only one sodium ion that can adduct to the fragments to give charge, thus enabling MS detection. To examine the affinity of the metal to each of the fragments, the distance between the hydroxyl oxygens and the metal ion were compared for each of the fragment pairs in the optimized fragment structures. For the B_2/Y_1 pair, the sodium ion was coordinated with seven oxygens, four from the B_2 fragment and three from the Y_1 fragment (Figure E.7A). More oxygens interacting with the sodium ion would suggest stronger interactions between the fragment and the charge carrier in the gas phase, and it can be expected that B_2 is

detected at a higher intensity compared to Y_1 . This hypothesis is supported by the experimental data (Figure E.2). On the other hand, optimization of the isomeric fragment pair, Z_2/C_1 , reveal that the C_1 fragment has more oxygens in coordination with the sodium ion compared to the Z_2 fragment (Figure E.7B). While the Z_2 fragment has stronger interactions with the charge carrier in this structure, this fragmentation pathway for production of Z_2/C_1 is much less energetically favorable than the B_2/Y_1 fragmentation pathway (Table E.1). Therefore, the relative intensities of the fragments observed in the experimental data could be correlated to theoretical calculations by combining the energetics of the fragmentation pathways with the conformations of the carbohydrate-metal adducts.

Fragmentation of sodium-adducted raffinose, an isomer of melezitose, reveals a different fragmentation pattern, which strongly favors C/Y-type fragments over B/Z-type fragments, and C_2/Y_2 fragments over C_1/Y_1 fragments (Figure E.8). Whereas melezitose has a fructose residue in the middle of the carbohydrate with two primary hydroxyls, raffinose has a fructose ring as a terminal sugar. Therefore, donation of a hydrogen from a primary hydroxyl on the five-membered fructose ring would produce C_2 and Z_1 fragments (Figure E.1). Raffinose also has a [1→6] linkage between the two pyranose rings, meaning that there is no primary hydroxyl available on the middle glucose residue. Therefore, we hypothesize that the fructose on the terminal position, as well as the [1→6] linkage, favor conformations that generate C_2/Y_2 fragments over B_2/Z_2 fragments.

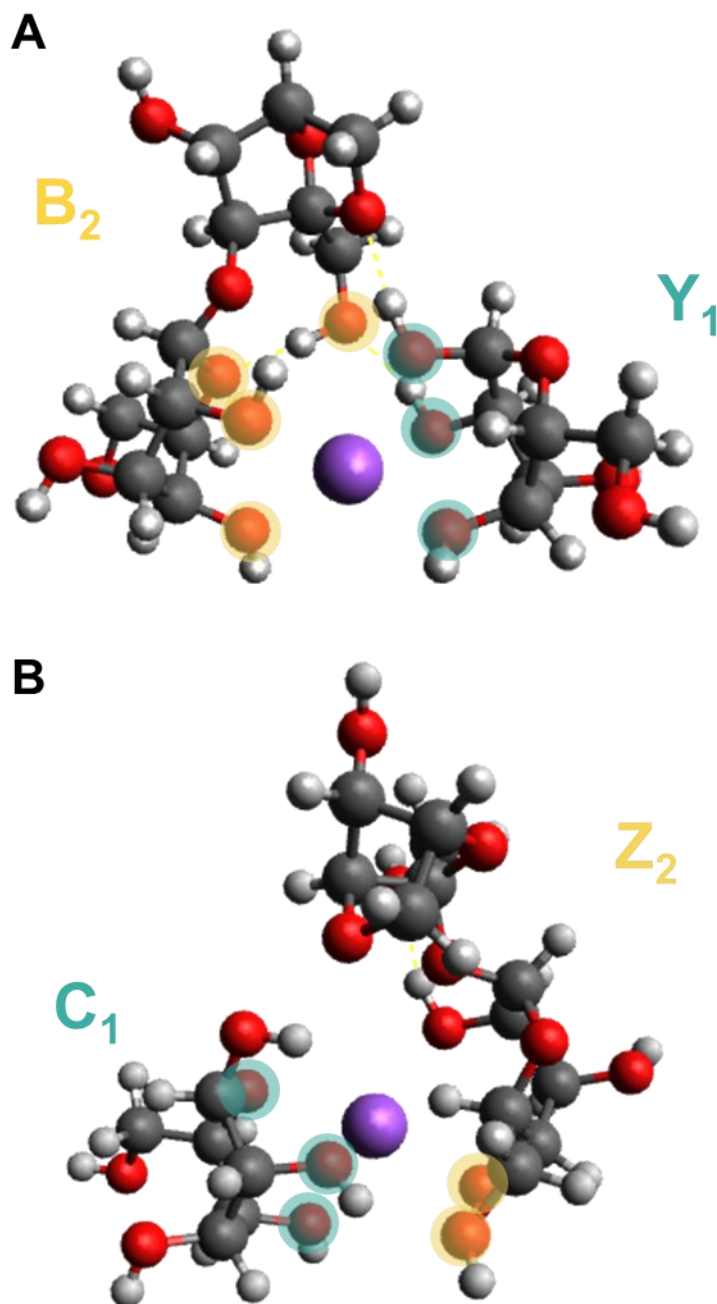


Figure E.7. Optimized structures of (A) B₂/Y₁ and (B) C₁/Z₂ fragment pairs adducted to sodium after glycosidic bond dissociation of melezitose. Carbon atoms are shown in gray, oxygen atoms in red, hydrogen atoms in white, and the sodium ion in purple. The oxygens interacting with the sodium ion (< 2.5 Å distance) are highlighted in yellow and teal for B₂/Z₂ and C₁/Y₁ fragments, respectively.

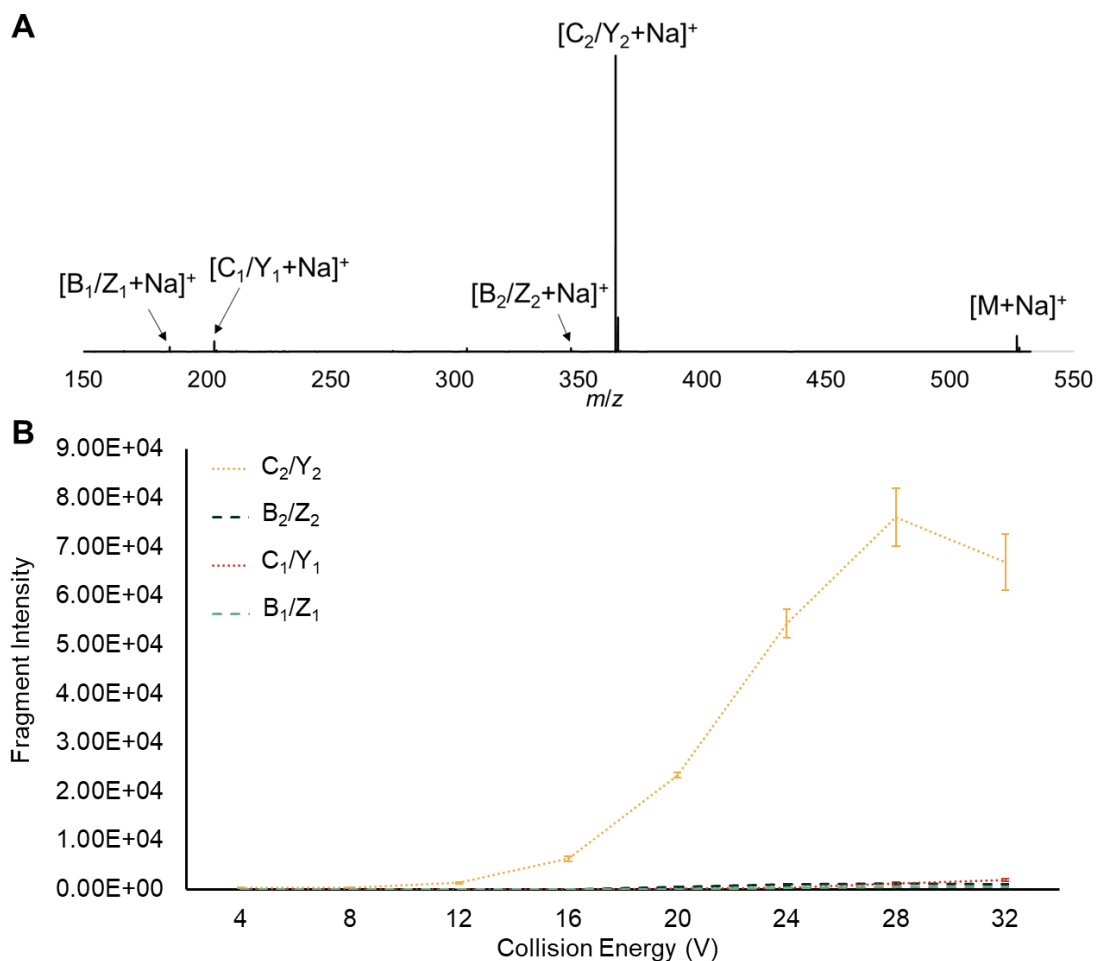


Figure E.8. (A) Representative fragmentation spectrum of sodium-adducted raffinose at collision voltage of 32 V. Unlabeled peaks are cross-ring cleavage products. (B) Intensities of sodium-adducted raffinose fragments at collision voltages ranging from 4 – 32 V. Error bars represent standard deviations ($n = 3$).

While transition state structure calculations of sodium-adducted raffinose have not been completed for energetics of possible fragmentation pathways, the optimized structures of the precursor ions and fragment pairs of raffinose-sodium complexes offer insight on the conformations. On average, the most viable fragmentation pathways for sodium-adducted raffinose seem to be the O(2')H—O(2) transfer for production of B₂/Y₁ fragments (2.6 ± 0.6 Å) and the O(3)H—O(2) transfer for production of C₂/Z₁ fragments (2.8 ± 0.7 Å) (Figure E.8A). However, other conformations are observed in which

O(2'')H—O(6') contribution for Y₂/B₁ fragment production is likely as well (Figure E.8B). Therefore, assuming that the energetics of the three glycosidic bond cleavage events are similar to one another, the detected peak at *m/z* 365 (Figure E.7A) would likely include both C₂ and Y₂ populations, generated from the same glycosidic bond cleavages as Z₁ and B₁ fragments, respectively. On the other hand, the peak at *m/z* 347 (Figure E.7A) would be mostly B₂ fragments, rather than Z₂.

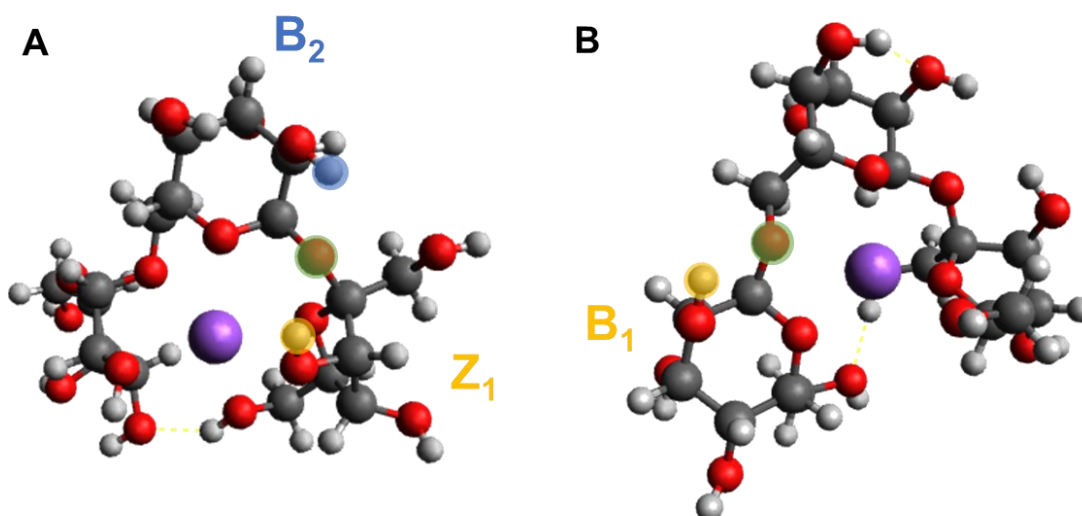


Figure E.9. Representative structures of sodium-adducted raffinose. Carbon atoms are shown in gray, oxygen atoms in red, hydrogen atoms in white, and the sodium ion in purple. The O(2')H hydroxyl hydrogen producing the B₂ fragment is highlighted in blue (A). The O(3)H and O(2'')H hydroxyl hydrogens, leading to isomeric Z₁ (A) and B₁ fragments (B), are highlighted in yellow. The glycosidic oxygens O(2) (A) and O(6') (B) are highlighted in green.

A closer look at the optimized structures of the raffinose fragments reveal fragment-metal interactions that favor detection of C₂/Y₂ fragments as well. The B₂ fragment was found with three oxygens coordinating with the sodium ion, compared to two for the Y₁ fragment (Figure E.10A). The intensities of the B₂/Z₂ and C₁/Y₁ fragments were similar at a collision voltage of 32 V (Figure E.7A), and the theoretical calculations

are in accordance with experimental observations. On the other hand, both C_2 and Y_2 fragments were found to have stronger interactions with the sodium ion compared to their Z_1 and B_1 glycosidic bond cleavage pairs (Figure E.10B and C). We expect that the greater number of oxygen-sodium coordination bonds observed for the C_2/Y_2 fragments led to a higher intensity in the fragmentation spectrum, compared to the B_1/Z_1 fragments (Figure E.7A). The number of fragmentation pathways available for the C_2/Y_2 fragments and the fragment-metal interactions both support the high intensity of the C_2/Y_2 fragments observed in the CID experiments. The transition state calculations for the energetics of the C_2/Y_2 and B_2/Z_2 fragments are underway to obtain the energetics perspective of the fragmentation pathways.

Maltotriose is another isomer of melezitose that has three glucose residues and no furanose ring. CID of sodium-adducted maltotriose shows that the C_2/Y_2 and B_2/Z_2 fragments are detected at similar intensities up to collision voltages of 24 V. However, C_2/Y_2 fragment is detected at higher intensity compared to B_2/Z_2 at collision voltage higher than 28 V, when the intensity of both fragments decreases (Figure E.11B). Based on the observation that detection of the smaller C_1/Y_1 and B_1/Z_1 fragments increase in the higher collision energy, we hypothesize that C_2/Y_2 and B_2/Z_2 fragments may undergo secondary fragmentation to produce the smaller fragments. The change in relative intensity of the C_2/Y_2 and B_2/Z_2 fragments suggests that secondary fragmentation of the B_2/Z_2 fragments may be more favorable compared to C_2/Y_2 , although transition state calculations are needed to confirm our hypothesis.

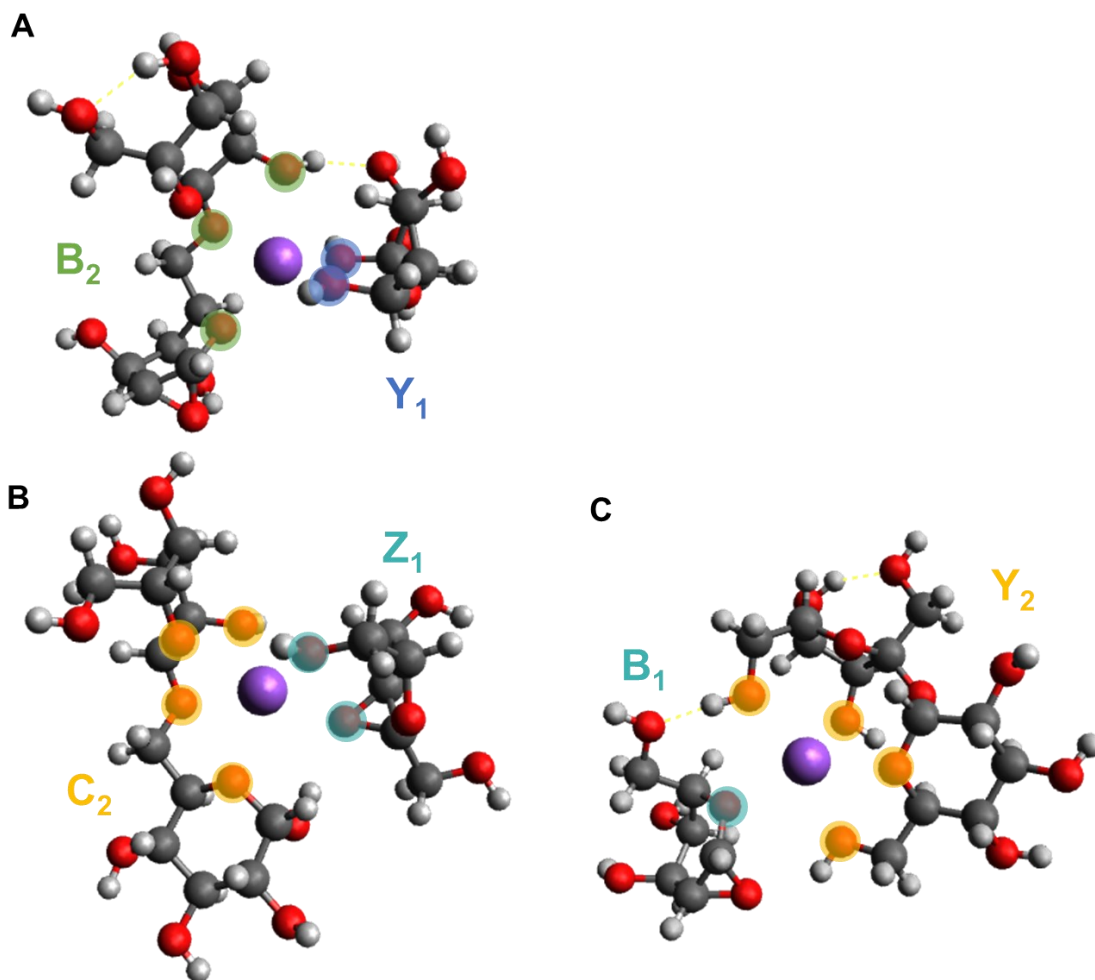


Figure E.10. Optimized structures of (A) B₂/Y₁, (B) C₂/Z₁, and (C) B₁/Y₂ fragment pairs adducted to sodium after glycosidic bond dissociation of raffinose. Carbon atoms are shown in gray, oxygen atoms in red, hydrogen atoms in white, and the sodium ion in purple. The oxygens interacting with the sodium ion (< 2.5 Å distance) are highlighted in green, blue, yellow, and teal for B₂, Y₁, C₂/Y₂, and B₁/Z₁ fragments, respectively.

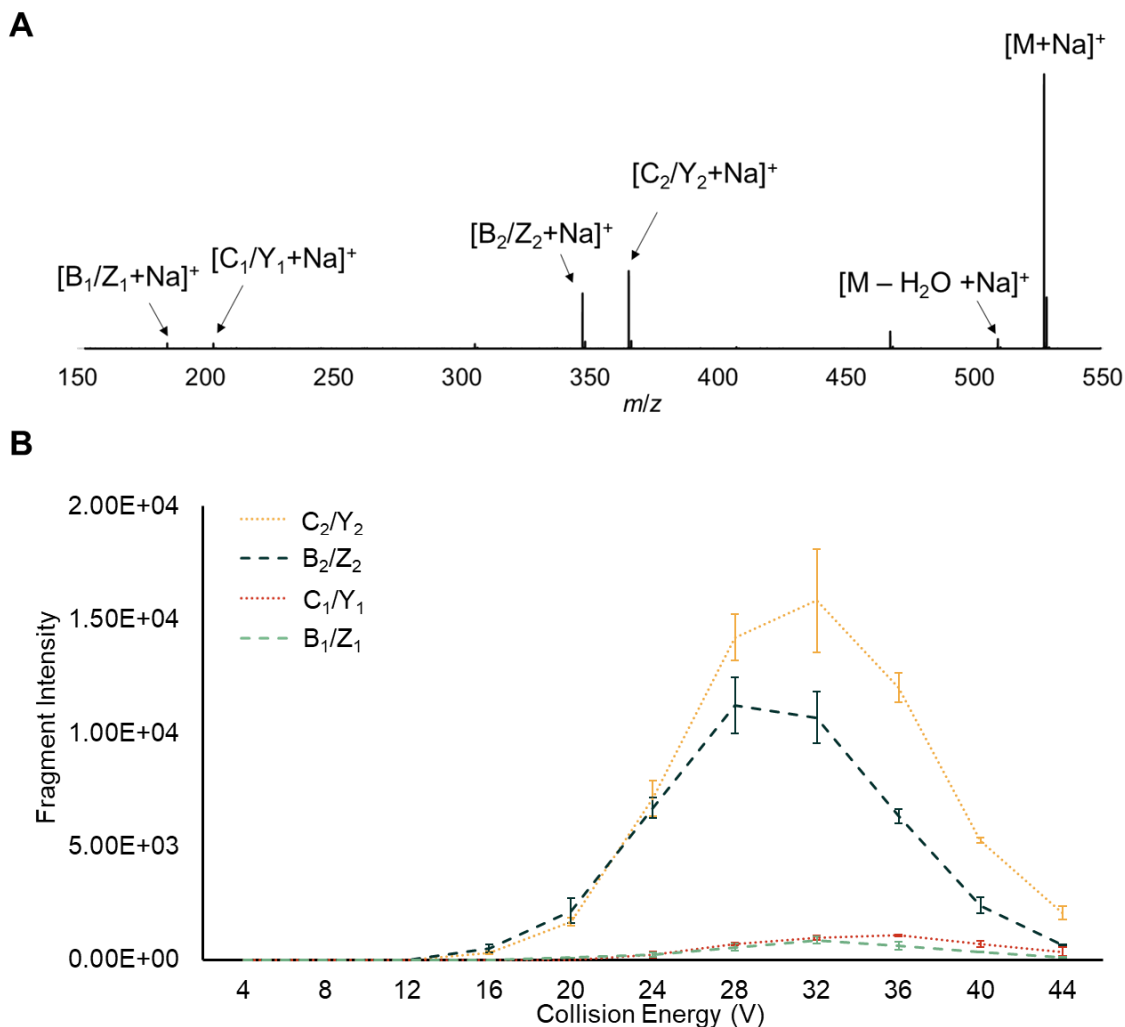


Figure E.11. (A) Representative fragmentation spectrum of sodium-adducted maltotriose at collision voltage of 32 V. Unlabeled peaks are cross-ring cleavage products. (B) Intensities of sodium-adducted maltotriose fragments at collision voltages ranging from 4 – 44 V. Error bars represent standard deviations ($n = 3$). Only fragments from glycosidic bond cleavages are shown.

While the fragmentation patterns vary for each isomer, the energy profile from experimental data is consistent across the three carbohydrates when they are adducted to the same metal. All three isomers adducted to sodium show that the bigger fragments, C_2/Y_2 and B_2/Z_2 , are detected at the highest intensity, around 28 – 32 V, and the intensities decrease after 32 V. Similarly, the energetics of lithium-adducted isomers

reveal energy profiles in which the fragments with the highest intensity are produced around 28 – 32 V (Figure E.12). All three isomers fragmented at lower collision energies, around 4 – 10 V (Figure E.13), when adducted to calcium compared to either sodium- or lithium-adducted trisaccharides. On the other hand, the three isomers fragmented at different energies when they were deprotonated in negative-ion mode (Figure E.14). Deprotonated melezitose and raffinose similarly produced the highest intensity fragments around collision voltages of 16 – 20 V (Figure E.14A and B). However, deprotonated maltotriose produced extensive fragments starting at a collision voltage of 4 V and precursor ions disappeared above a collision energy of 10 V (Figure E.14C).

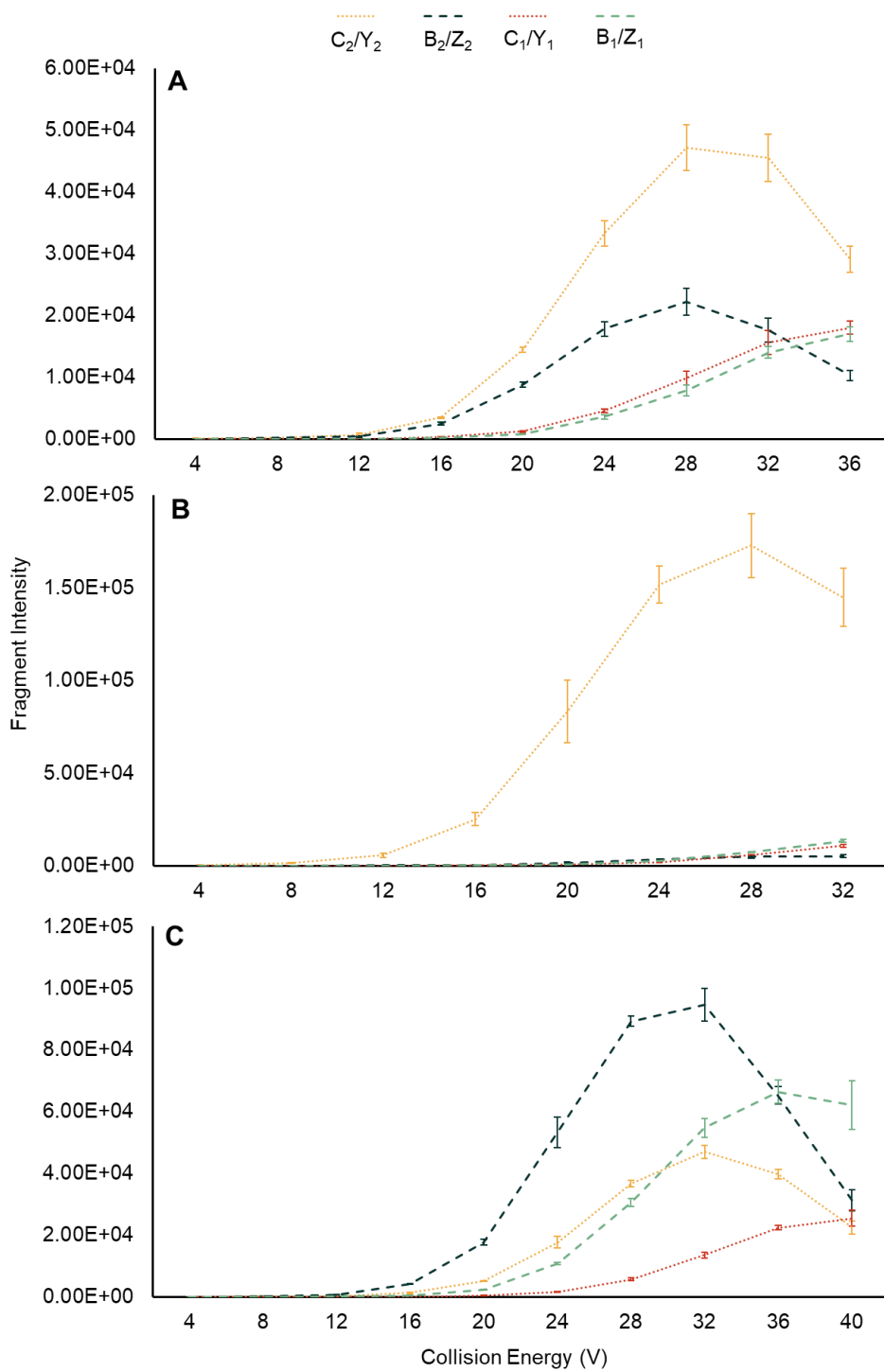


Figure E.12. Intensities of lithium-adducted (A) melezitose, (B) raffinose, and (C) maltotriose fragments at varying collision voltages. Error bars represent standard deviations ($n = 3$). Only fragments from glycosidic bond cleavages are shown.

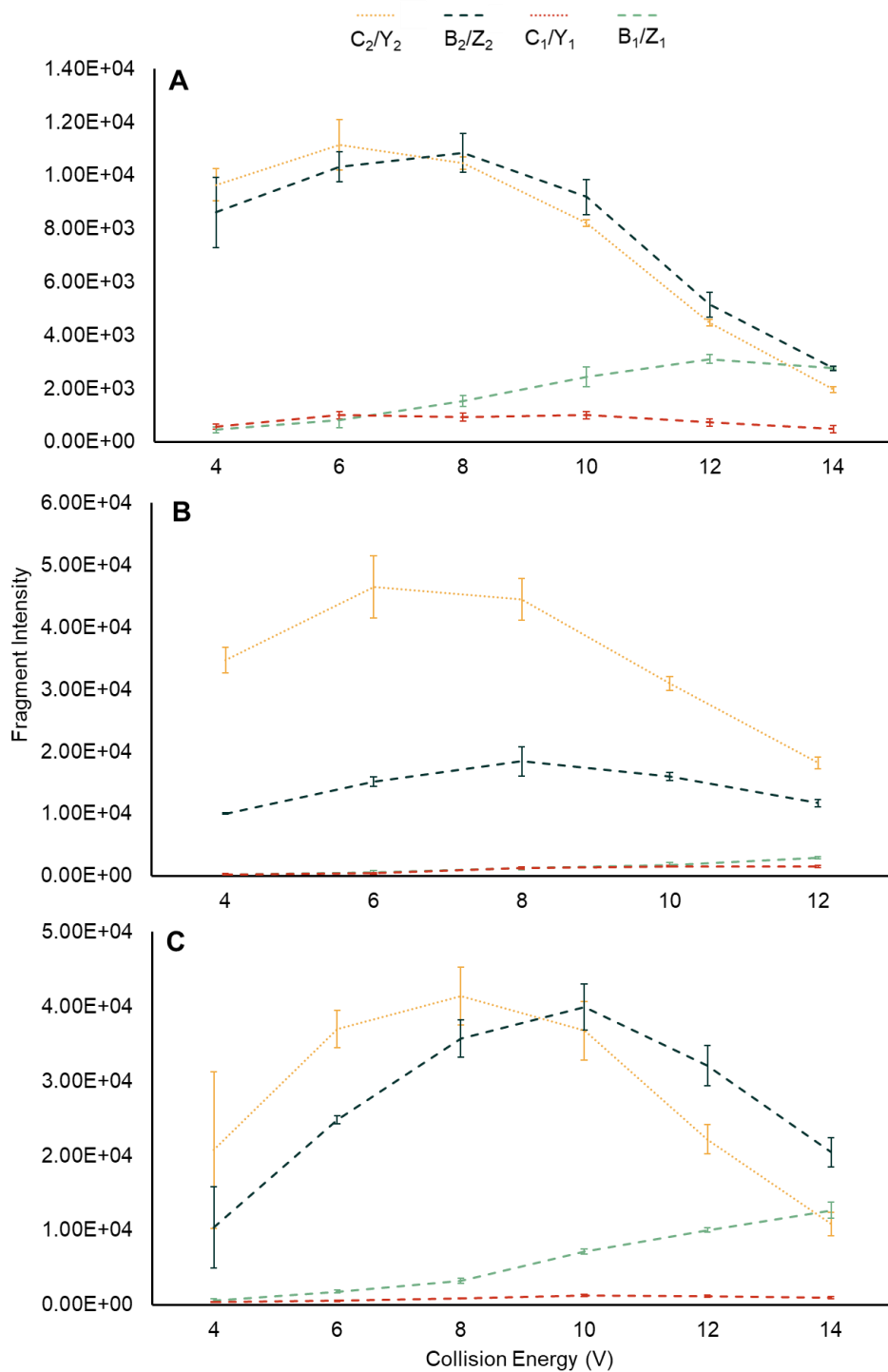


Figure E.13. Intensities of calcium-adducted (A) melezitose, (B) raffinose, and (C) maltotriose fragments at varying collision voltages. Error bars represent standard deviations ($n = 3$). Only fragments from glycosidic bond cleavages are shown.

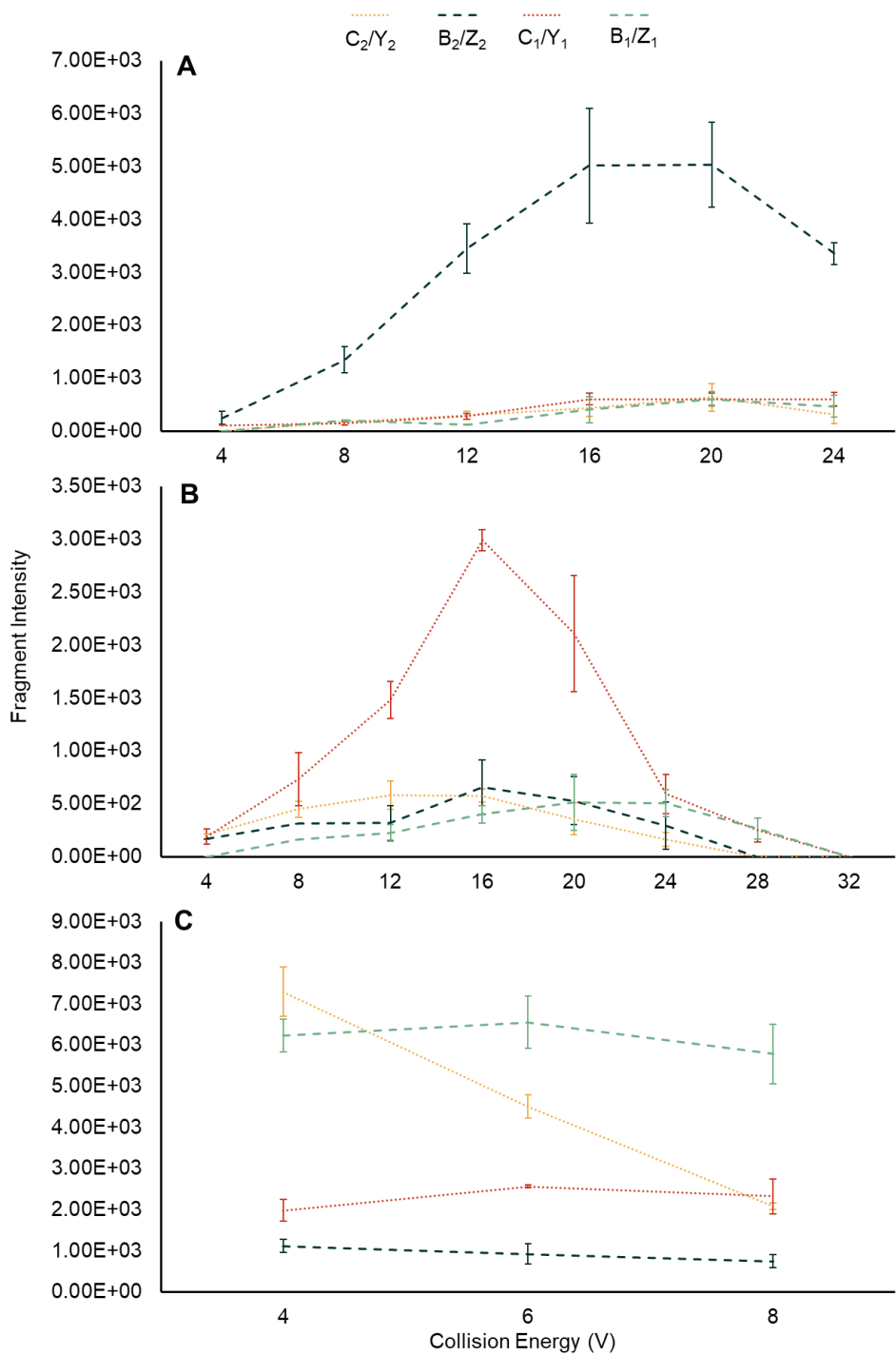


Figure E.14. Intensities of deprotonated (A) melezitose, (B) raffinose, and (C) maltotriose fragments at varying collision voltages. Error bars represent standard deviation ($n = 3$). Only fragments from glycosidic bond cleavages are shown.

We hypothesize that the changes in fragmentation patterns and energetics, based on the different types of charges and charge carriers, result from alterations in the carbohydrate conformations that lead to different fragmentation sites. For instance, sodium-adducted isomers in the gas phase have compact conformations in which the trisaccharides wrap around the sodium ion (Figure E.15A, B, C). Isomers adducted to other metals, such as lithium and calcium ions, are expected to have similar conformations in which the carbohydrate hydroxyls and metal interactions are maximized as well.³⁶⁵ While our experimental data show that the carbohydrate-metal interactions change for the varying metal ions and produce different fragmentation patterns, such as between sodium and lithium adducts, and different energy profiles, such as between sodium and calcium adducts, the overall energy profiles across the isomers are similar when their globular conformations are similar. However, deprotonated maltotriose has a linearized structure that may not solvate the negative charge as well as deprotonated melezitose and raffinose structures, which both have extensive intramolecular hydrogen bonding (Figure E.15D, E, F). Struwe *et al.* showed that human milk oligosaccharide (HMO) isomers adducted either a cation or anion in positive- or negative-ion mode, respectively, have similar collisional cross sections (CCSs), but the same isomers displayed significantly different values of CCS when deprotonated,³⁰⁹ suggesting higher variability in deprotonated carbohydrate conformations in the gas phase. Such differences in conformations between the different isomers are expected to result in changes in fragmentation pathways.

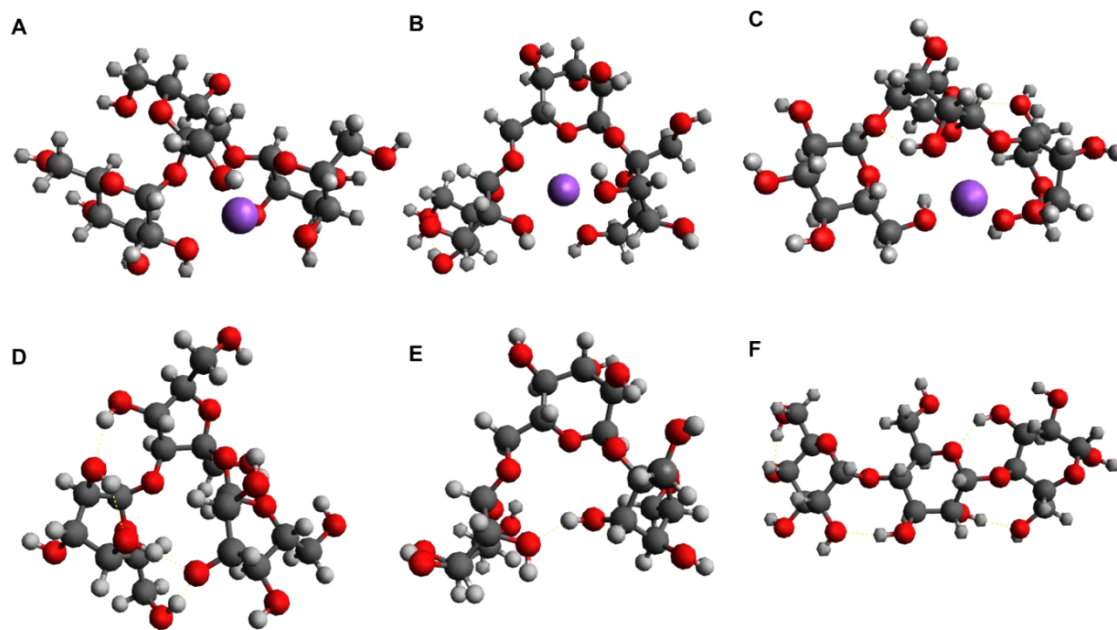


Figure E.15. Representative structures of sodium-adducted (A) melezitose, (B) raffinose, and (C) maltotriose, and deprotonated (D) melezitose, (E) raffinose, and (F) maltotriose.

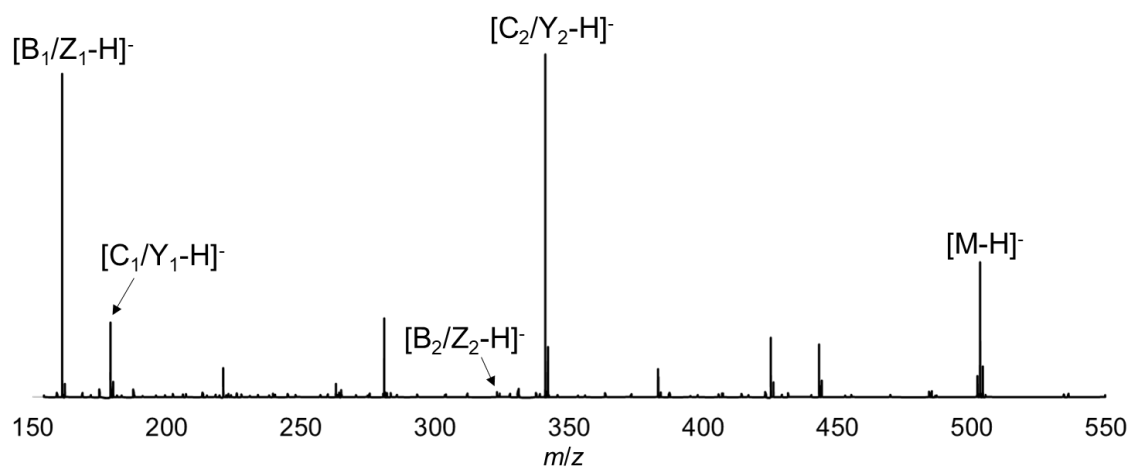


Figure E.16. Representative fragmentation spectrum of deprotonated maltotriose in negative-ion mode at collision voltage of 4 V. Unlabeled peaks are cross-ring cleavage products.

Permethylated melezitose produces fragments that have varying locations of C=C and C=O double bonds, suggesting more diverse fragmentation pathways compared to metal-adducted underivatized carbohydrates (Figure E.17). Due to the complexity of the

data with the variety of fragments, an energy profile is not shown, but fragmentation of permethylated melezitose was achieved in the collision voltage range of 20 – 44 V, compared to 16 – 36 V for the underivatized melezitose-sodium adduct. Unlike underivatized melezitose, containing hydroxyls that can donate hydrogens to glycosidic oxygens, all hydroxyl hydrogens have been replaced by methyl groups in permethylated melezitose and only -CH hydrogens are available to initiate glycosidic bond cleavages. The size of methyl groups as well as the chemical properties of C-H bonds compared to O-H bonds likely alter the fragmentation process in permethylated carbohydrates from the one observed for underivatized sugars. However, multiple fragments are observed from a single glycosidic bond cleavage site (Figure E.17 c and d, and h and i), suggesting that the source of protons that initiates the fragmentation may vary. Similarly, more cross-ring cleavage products are observed for permethylated melezitose compared to underivatized melezitose adducted to sodium (Figure E.1 and E.17). While we hypothesize that the greater number of fragments from permethylated melezitose compared to underivatized melezitose results from more diverse fragmentation pathways from C-H contributions, transition state calculations would need to confirm our hypothesis.

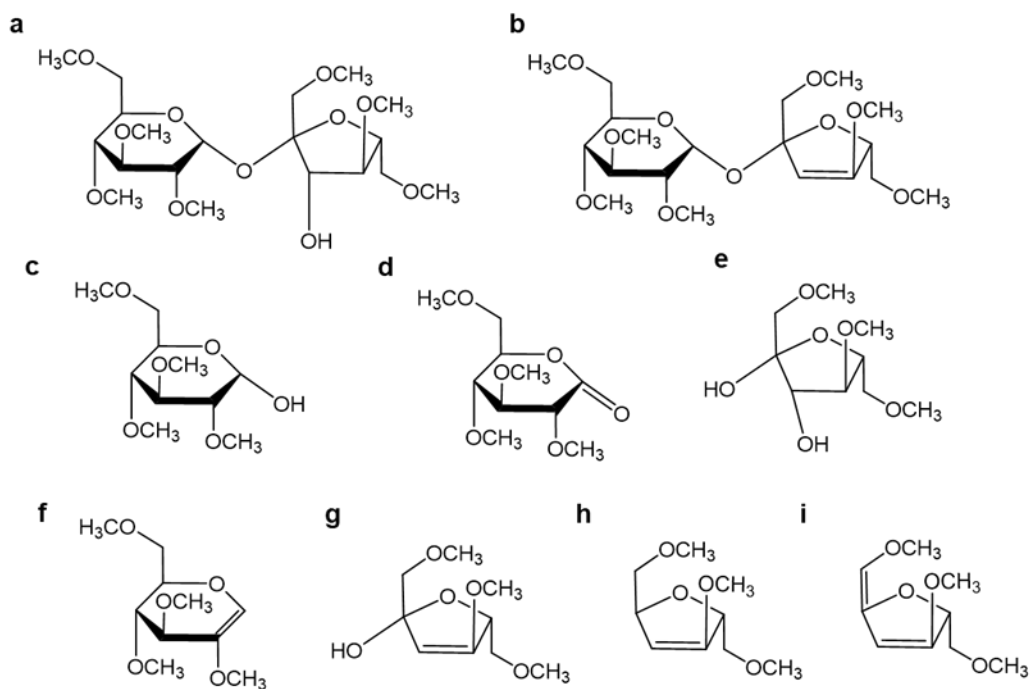
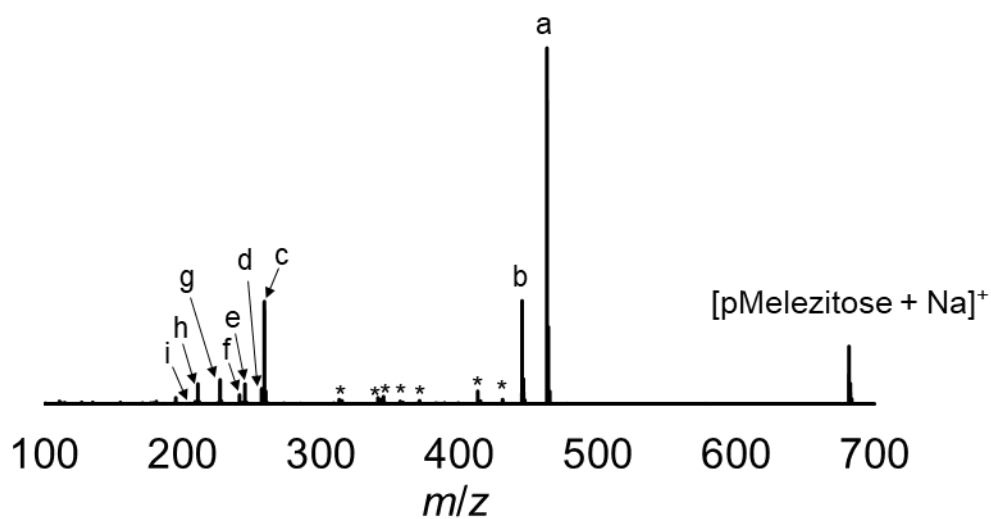


Figure E.17. Representative fragmentation spectrum of permethylated melezitose adducted to sodium (top) and the proposed structures of the fragments resulting from glycosidic bond cleavages. Peaks labeled with asterisks (*) are cross-ring cleavage products. Although only fragments from one terminal are shown for simplicity of representation, equivalent structures from the other terminal may also be produced.

E.4 Conclusions and Future Directions

This Appendix has provided the groundwork for connecting CID experimental data examining collision energy profiles of carbohydrates with computational methods to observe transition state structures and energetics as well as fragment-metal interactions. Using sodium-adducted melezitose as an example, the energies of transition states were acquired for various glycosidic bond cleavage sites for the source of hydrogen to protonate the glycosidic oxygen. Optimization of the resulting fragments and the sodium ion revealed the fragment-metal interactions and provided another explanation for fragment detection in MS. Finally, the globular conformations of the carbohydrate-metal complexes generated from MD simulations of ESI droplets, rather than a single conformation obtained from initial gas-phase structures, were compared to observe the likelihood of different fragmentation sites based on the flexibility of the carbohydrate conformations. While our computational method of obtaining transition state calculations and fragment-metal coordination has been demonstrated for one carbohydrate-metal complex, melezitose adducted to sodium, it can be extended to examine other carbohydrate-metal pairs such as lithium-adducted melezitose or sodium-adducted maltotriose. Our method may add valuable insights to HDX analysis of carbohydrate and the localization of deuterium labels, as the limited number of functional groups and their close exchange rates may not be resolved with current experimental work alone. Further investigation of fragmentation pathways for cross-ring cleavages and secondary fragmentations could also help understand structural differences in carbohydrate isomers that are crucial for biological activities.

References

1. Dell, A.; Galadari, A.; Sastre, F.; Hitchen, P., Similarities and Differences in the Glycosylation Mechanisms in Prokaryotes and Eukaryotes. *Int. J. Microbiol.* **2010**, *2010*, Article ID 148178.
2. Weerapana, E.; Imperiali, B., Asparagine-linked Protein Glycosylation: from Eukaryotic to Prokaryotic Systems. *Glycobiology* **2006**, *16* (6), 91R-101R.
3. Abu-Qarn, M.; Eichler, J.; Sharon, N., Not Just for Eukarya Anymore: Protein Glycosylation in Bacteria and Archaea. *Curr. Opin. Struc. Biol.* **2008**, *18* (5), 544-550.
4. Calo, D.; Kaminski, L.; Eichler, J., Protein Glycosylation in Archaea: Sweet and Extreme. *Glycobiology* **2010**, *20* (9), 1065-76.
5. Eichler, J., Extreme Sweetness: Protein Glycosylation in Archaea. *Nat. Rev. Microbiol.* **2013**, *11* (3), 151-156.
6. Vigerust, D. J.; Shepherd, V. L., Virus Glycosylation: Role in Virulence and Immune Interactions. *Trends Microbiol.* **2007**, *15* (5), 211-218.
7. Bagdonaite, I.; Wandall, H. H., Global Aspects of Viral Glycosylation. *Glycobiology* **2018**, *28* (7), 443-467.
8. Apweiler, R.; Hermjakob, H.; Sharon, N., On the Frequency of Protein Glycosylation, as Deduced from Analysis of the SWISS-PROT Database. *Biochim. Biophys. Acta (BBA) - Gen. Subjects* **1999**, *1473* (1), 4-8.
9. Nilsson, J.; Halim, A.; Grahn, A.; Larson, G., Targeting the Glycoproteome. *Glycoconjugate J.* **2013**, *30* (2), 119-136.
10. Dodd, R. B.; Drickamer, K., Lectin-like Proteins in Model Organisms: Implications for Evolution of Carbohydrate-binding Activity. *Glycobiology* **2001**, *11* (5), 71R-79R.

11. Seeberger, P. H., Monosaccharide Diversity. **2017**. In Varki, A.; Cummings R. D.; Esko, J. D.; Stanley P.; Hart, G. W.; Aebi, M.; Darvill, A. G.; Kinoshita, T.; Packer, N. H.; Prestegard, J. H.; Schnaar, R. L.; Seeberger, P. H., Eds. *Essentials of Glycobiology*. 3rd ed. Cold Spring harbor (NY): Cold Spring Harbor Laboratory Press; 2015-2017. Chapter 2. PMID: 28876863.
12. Angyal, S., Conformational Analysis in Carbohydrate Chemistry. I. Conformational Free Energies. The Conformations and α : β Ratios of Aldopyranoses in Aqueous Solution. *Aust. J. Chem.* **1968**, *21* (11), 2737-2746.
13. Edward, J. T., Stability of Glycosides to Acid Hydrolysis. *Chem. Ind.* **1955**, 1102-1104.
14. Lemieux, R.; Chu, N. J. *Abstracts of Papers, Amer. Chem. Soc.* **133**, 31N.
15. Corchado, J. C.; Sánchez, M. L.; Aguilar, M. A., Theoretical Study of the Relative Stability of Rotational Conformers of α and β -d-Glucopyranose in Gas Phase and Aqueous Solution. *J. Am. Chem. Soc.* **2004**, *126* (23), 7311-7319.
16. Kim, H. J.; Liyanage, O. T.; Mulenos, M. R.; Gallagher, E. S., Mass Spectral Detection of Forward- and Reverse-Hydrogen/Deuterium Exchange Resulting from Residual Solvent Vapors in Electrospray Sources. *J. Am. Soc. Mass Spectrom.* **2018**, *29* (10), 2030-2040.
17. Lauc, G.; Huffman, J. E.; Pučić, M.; Zgaga, L.; Adamczyk, B.; Mužinić, A.; Novokmet, M.; Polašek, O.; Gornik, O.; Krištić, J.; Keser, T.; Vitart, V.; Scheijen, B.; Uh, H.-W.; Molokhia, M.; Patrick, A. L.; McKeigue, P.; Kolčić, I.; Lukić, I. K.; Swann, O.; van Leeuwen, F. N.; Ruhaak, L. R.; Houwing-Duistermaat, J. J.; Slagboom, P. E.; Beekman, M.; de Craen, A. J. M.; Deelder, A. M.; Zeng, Q.; Wang, W.; Hastie, N. D.; Gyllensten, U.; Wilson, J. F.; Wuhrer, M.; Wright, A. F.; Rudd, P. M.; Hayward, C.; Aulchenko, Y.; Campbell, H.; Rudan, I., Loci Associated with N-Glycosylation of Human Immunoglobulin G Show Pleiotropy with Autoimmune Diseases and Haematological Cancers. *PLOS Genet.* **2013**, *9* (1), e1003225.
18. Hossler, P.; Khattak, S. F.; Li, Z. J., Optimal and Consistent Protein Glycosylation in Mammalian Cell Culture. *Glycobiology* **2009**, *19* (9), 936-949.
19. Maverakis, E.; Kim, K.; Shimoda, M.; Gershwin, M. E.; Patel, F.; Wilken, R.; Raychaudhuri, S.; Ruhaak, L. R.; Lebrilla, C. B., Glycans in the Immune System and the Altered Glycan Theory of Autoimmunity: A Critical Review. *J. Autoimmun.* **2015**, *57*, 1-13.

20. Thompson, S.; Dargan, E.; Griffiths, I.; Kelly, C.; Turner, G., The Glycosylation of Haptoglobin in Rheumatoid Arthritis. *Clin. Chim. Acta* **1993**, *220* (1), 107-114.
21. Goodarzi, M. T.; Turner, G. A., Reproducible and Sensitive Determination of Charged Oligosaccharides from Haptoglobin by PNGase F Digestion and HPAEC/PAD Analysis: Glycan Composition Varies with Disease. *Glycoconjugate J.* **1998**, *15* (5), 469-475.
22. Mkhikian, H.; Grigorian, A.; Li, C. F.; Chen, H.-L.; Newton, B.; Zhou, R. W.; Beeton, C.; Torossian, S.; Tatarian, G. G.; Lee, S.-U.; Lau, K.; Walker, E.; Siminovitch, K. A.; Chandy, K. G.; Yu, Z.; Dennis, J. W.; Demetriou, M., Genetics and the Environment Converge to Dysregulate N-glycosylation in Multiple Sclerosis. *Nat. Commun.* **2011**, *2* (1), 334.
23. Miller, H. R., Gastrointestinal Mucus, a Medium for Survival and for Elimination of Parasitic Nematodes and Protozoa. *Parasitology* **1987**, *94 Suppl*, S77-100.
24. Yamauchi, J.; Kawai, Y.; Yamada, M.; Uchikawa, R.; Tegoshi, T.; Arizono, N., Altered Expression of Goblet Cell- and Mucin Glycosylation-related Genes in the intestinal epithelium during infection with the nematode *Nippostrongylus Brasiliensis* in Rat. *Apmis* **2006**, *114* (4), 270-8.
25. Marco, M. L.; Pavan, S.; Kleerebezem, M., Towards Understanding Molecular Modes of Probiotic Action. *Curr. Opin. Biotechnol.* **2006**, *17* (2), 204-10.
26. St Geme, J. W., 3rd; Falkow, S.; Barenkamp, S. J., High-molecular-weight Proteins of Nontypable *Haemophilus Influenzae* Mediate Attachment to Human Epithelial Cells. *Proc. Natl. Acad. Sci. USA* **1993**, *90* (7), 2875-9.
27. Chen, S.; Sun, C.; Wang, H.; Wang, J., The Role of Rho GTPases in Toxicity of *Clostridium difficile* Toxins. *Toxins (Basel)* **2015**, *7* (12), 5254-67.
28. Lin, B.; Qing, X.; Liao, J.; Zhuo, K., Role of Protein Glycosylation in Host-Pathogen Interaction. *Cells* **2020**, *9* (4).
29. Bock, K.; Thøgersen, H., Nuclear Magnetic Resonance Spectroscopy in the Study of Mono- and Oligosaccharides. In *Annual Reports on NMR Spectroscopy*, Webb, G. A., Ed. Academic Press: 1983, 13, 1-57.
30. De Bruyn, A.; Anteunis, M.; van Beeumen, J., Chemical Shifts of Aldohexopyranoses Revisited and Application to Gulosylglucose. *Bulletin des Sociétés Chimiques Belges* **1977**, *86* (4), 259-265.

31. Hobley, P.; Howarth, O.; Ibbett, R. N., ^1H and ^{13}C NMR Shifts for Aldopyranose and Aldofuranose Monosaccharides: Conformational Analysis and Solvent Dependence. *Magn. Reson. Chem.* **1996**, *34* (10), 755-760.
32. Bubb, W. A., NMR Spectroscopy in the Study of Carbohydrates: Characterizing the Structural Complexity. *Concepts Magn. Reson. A* **2003**, *19A* (1), 1-19.
33. Vliegthart, J. F. G.; Dorland, L.; Halbeek, H. v., High-Resolution, ^1H -Nuclear Magnetic Resonance Spectroscopy as a Tool in the Structural Analysis of Carbohydrates Related to Glycoproteins. In *Advances in Carbohydrate Chemistry and Biochemistry*, Tipson, R. S.; Horton, D., Eds. Academic Press: 1983, 41, 209-374.
34. Jonsson, K. H. M.; Pendrill, R.; Widmalm, G., NMR Analysis of Conformationally Dependent $n\text{J}_\text{C}$, H and $n\text{J}_\text{C}$, C in the Trisaccharide $\alpha\text{-L-Rhap-(1} \rightarrow 2)[\alpha\text{-L-Rhap-(1} \rightarrow 3)]\text{-}\alpha\text{-L-Rhap-OMe}$ and a Site-specifically Labeled Isotopologue Thereof. *Magn. Reson. Chem.* **2011**, *49* (3), 117-124.
35. Kamiya, Y.; Yamamoto, S.; Chiba, Y.; Jigami, Y.; Kato, K., Overexpression of a Homogeneous Oligosaccharide with ^{13}C Labeling by Genetically Engineered Yeast Strain. *J. Biomol. NMR* **2011**, *50* (4), 397-401.
36. Williams, C.; Allerhand, A., Detection of $\beta\text{-d-glucofuranose}$ in Aqueous Solutions of D-glucose. Application of Carbon-13 Fourier-transform NMR Spectroscopy. *Carbohydr. Res.* **1977**, *56* (1), 173-179.
37. Maple, S. R.; Allerhand, A., Detailed Tautomeric Equilibrium of Aqueous D-glucose. Observation of Six Tautomers by Ultrahigh Resolution Carbon-13 NMR. *J. Am. Chem. Soc.* **1987**, *109* (10), 3168-3169.
38. King-Morris, M. J.; Serianni, A. S., Carbon-13 NMR studies of $[1\text{-}^{13}\text{C}]\text{aldoses}$: Empirical Rules Correlating Pyranose Ring Configuration and Conformation with Carbon-13 Chemical Shifts and Carbon-13/carbon-13 Spin Couplings. *J. Am. Chem. Soc.* **1987**, *109* (12), 3501-3508.
39. Goux, W. J., Complex Isomerization of Ketoses: a Carbon-13 NMR Study of the Base-catalyzed Ring-opening and Ring-closing Rates of D-fructose Isomers in Aqueous Solution. *J. Am. Chem. Soc.* **1985**, *107* (14), 4320-4327.
40. Roldós, V.; Cañada, F. J.; Jiménez-Barbero, J., Carbohydrate-Protein Interactions: A 3D View by NMR. *Chembiochem* **2011**, *12* (7), 990-1005.

41. Bewley, C. A.; Shahzad-ul-Hussan, S., Characterizing Carbohydrate–Protein Interactions by Nuclear Magnetic Resonance Spectroscopy. *Biopolymers* **2013**, *99* (10), 796-806.
42. del Carmen Fernandez-Alonso, M.; Diaz, D.; Alvaro Berbis, M.; Marcelo, F.; Canada, J.; Jimenez-Barbero, J., Protein-Carbohydrate Interactions Studied by NMR: From Molecular Recognition to Drug Design. *Curr. Protein Pept. Sci.* **2012**, *13* (8), 816-830.
43. Martin, A.; Arda, A.; Désiré, J.; Martin-Mingot, A.; Probst, N.; SinaÿP .; Jiménez-Barbero, J.; Thibaudeau, S.; Blériot, Y., Catching Elusive Glycosyl Cations in a Condensed Phase with HF/SbF₅ Superacid. *Nat. Chem.* **2016**, *8* (2), 186-191.
44. Baek, J. Y.; Kwon, H.-W.; Myung, S. J.; Park, J. J.; Kim, M. Y.; Rathwell, D. C. K.; Jeon, H. B.; Seeberger, P. H.; Kim, K. S., Directing Effect by Remote Electron-withdrawing Protecting Groups at O-3 or O-4 Position of Donors in Glucosylations and Galactosylations. *Tetrahedron* **2015**, *71* (33), 5315-5320.
45. Cox, D. J.; Singh, G. P.; Watson, A. J. A.; Fairbanks, A. J., Neighbouring Group Participation During Glycosylation: Do 2-Substituted Ethyl Ethers Participate? *Eur. J. Org. Chem.* **2014**, *2014* (21), 4624-4642.
46. Singh, G. P.; Watson, A. J. A.; Fairbanks, A. J., Achiral 2-Hydroxy Protecting Group for the Stereocontrolled Synthesis of 1,2-cis- α -Glycosides by Six-Ring Neighboring Group Participation. *Org. Lett.* **2015**, *17* (17), 4376-4379.
47. Buda, S.; Nawój, M.; Mlynarski, J., Chapter Four - Recent Advances in NMR Studies of Carbohydrates. In *Annual Reports on NMR Spectroscopy*, Webb, G. A., Ed. Academic Press: 2016, 89, 185-223.
48. Emwas, A.-H. M.; Salek, R. M.; Griffin, J. L.; Merzaban, J., NMR-based Metabolomics in Human Disease Diagnosis: Applications, Limitations, and Recommendations. *Metabolomics* **2013**, *9* (5), 1048-1072.
49. Cai, S.-S.; Short, L. C.; Syage, J. A.; Potvin, M.; Curtis, J. M., Liquid Chromatography–Atmospheric Pressure Photoionization–Mass Spectrometry Analysis of Triacylglycerol Lipids—Effects of Mobile Phases on Sensitivity. *J. Chromatogr. A* **2007**, *1173* (1), 88-97.
50. Cai, S.-S.; Syage, J. A., Atmospheric Pressure Photoionization Mass Spectrometry for Analysis of Fatty Acid and Acylglycerol Lipids. *J. Chromatogr. A* **2006**, *1110* (1), 15-26.

51. Forseth, R. R.; Schroeder, F. C., NMR-spectroscopic Analysis of Mixtures: from Structure to Function. *Curr. Opin. Chem. Biol.* **2011**, *15* (1), 38-47.
52. Hakomori, S.-I., A Rapid Permethylation of Glycolipid, and Polysaccharide Catalyzed by Methylsulfinyl Carbanion in Dimethyl Sulfoxide. *J. Biochem.* **1964**, *55* (2), 205-208.
53. Ciucanu, I.; Kerek, F., A Simple and Rapid Method for the Permethylation of Carbohydrates. *Carbohydr. Res.* **1984**, *131* (2), 209-217.
54. Ciucanu, I.; Costello, C. E., Elimination of Oxidative Degradation during the per-O-Methylation of Carbohydrates. *J. Am. Chem. Soc.* **2003**, *125* (52), 16213-16219.
55. Nicholas, S. D.; Smith, F., Acetylation of Sugars. *Nature* **1948**, *161* (4088), 349-349.
56. Klepach, T.; Zhao, H.; Hu, X.; Zhang, W.; Stenutz, R.; Hadad, M. J.; Carmichael, I.; Serianni, A. S., Informing Saccharide Structural NMR Studies with Density Functional Theory Calculations. In *Glycoinformatics*, Lütke, T.; Frank, M., Eds. Springer New York: New York, NY, 2015, 289-331.
57. Woods, R. J., Three-dimensional Structures of Oligosaccharides. *Curr. Opin. Struc. Biol.* **1995**, *5* (5), 591-598.
58. Woods, R. J., Computational Carbohydrate Chemistry: What Theoretical Methods Can Tell Us. *Glycoconjugate J.* **1998**, *15* (3), 209-216.
59. Bock, K., The Preferred Conformation of Oligosaccharides in Solution Inferred from High Resolution NMR Data and Hard Sphere Exo-anomeric Calculations. *Pure App. Chem.* **1983**, *55* (4), 605-622.
60. Thøgersen, H.; Lemieux, R. U.; Bock, K.; Meyer, B., Further Justification for the Exo-anomeric Effect. Conformational Analysis Based on Nuclear Magnetic Resonance Spectroscopy of Oligosaccharides. *Can. J. Chem.* **1982**, *60* (1), 44-57.
61. Lemieux, R. U.; Bock, K., The Conformational Analysis of Oligosaccharides by ¹H-NMR and HSEA Calculation. *Arch. Biochem. Biophys.* **1983**, *221* (1), 125-134.
62. Woods, R. J.; Dwek, R. A.; Edge, C. J.; Fraser-Reid, B., Molecular Mechanical and Molecular Dynamic Simulations of Glycoproteins and Oligosaccharides. 1. GLYCAM_93 Parameter Development. *J. Phys. Chem.* **1995**, *99* (11), 3832-3846.

63. Glennon, T. M.; Zheng, Y.-J.; Le Grand, S. M.; Shutzberg, B. A.; Merz Jr., K. M., A Force Field for Monosaccharides and (1 → 4) Linked Polysaccharides. *J. Comput. Chem.* **1994**, *15* (9), 1019-1040.
64. Homans, S. W., A Molecular Mechanical Force Field for the Conformational Analysis of Oligosaccharides: Comparison of Theoretical and Crystal Structures of Man α 1-3Man β 1-4GlcNAc. *Biochemistry* **1990**, *29* (39), 9110-9118.
65. Ha, S. N.; Giammona, A.; Field, M.; Brady, J. W., A Revised Potential-energy Surface for Molecular Mechanics Studies of Carbohydrates. *Carbohyd. Res.* **1988**, *180* (2), 207-221.
66. Rasmussen, K., Conformation and Anomer Ratio of D-glucopyranose in Different Potential Energy Functions. *Acta Chem. Scand. A* **1982**, *36* (0), 4.
67. Woods, R. J.; Pathiaseril, A.; Wormald, M. R.; Edge, C. J.; Dwek, R. A., The High Degree of Internal Flexibility Observed for an Oligomannose Oligosaccharide Does Not Alter the Overall Topology of the Molecule. *Eur. J. Biochem.* **1998**, *258* (2), 372-386.
68. Allinger, N. L., Conformational analysis. 130. MM2. A Hydrocarbon Force Field Utilizing V1 and V2 Torsional Terms. *J. Am. Chem. Soc.* **1977**, *99* (25), 8127-8134.
69. Allinger, N. L.; Yuh, Y. H.; Lii, J. H., Molecular Mechanics. The MM3 Force Field for Hydrocarbons. 1. *J. Am. Chem. Soc.* **1989**, *111* (23), 8551-8566.
70. Parr, R. G. In *Density Functional Theory of Atoms and Molecules*, Horizons of Quantum Chemistry, Fukui, K.; Pullman, B., Eds. Springer Netherlands: Dordrecht, 1980, 5-15.
71. Levy, M., Universal Variational Functionals of Electron Densities, First-order Density Matrices, and Natural Spin-orbitals and Solution of the v-representability Problem. *Proc. Nat. Acad. Sci.* **1979**, *76* (12), 6062-6065.
72. Ziegler, T., Approximate Density Functional Theory as a Practical Tool in Molecular Energetics and Dynamics. *Chem. Rev.* **1991**, *91* (5), 651-667.
73. Jones, R. O.; Gunnarsson, O., The Density Functional Formalism, Its Applications and Prospects. *Rev. Mod. Phys.* **1989**, *61* (3), 689-746.

74. Novoa, J. J.; Sosa, C., Evaluation of the Density Functional Approximation on the Computation of Hydrogen Bond Interactions. *J. Phys. Chem.* **1995**, *99* (43), 15837-15845.
75. Baseden, K. A.; Tye, J. W., Introduction to Density Functional Theory: Calculations by Hand on the Helium Atom. *J. Chem. Educ.* **2014**, *91* (12), 2116-2123.
76. Becke, A. D., Density-functional Thermochemistry. III. The Role of Exact Exchange. *J. Chem. Phys.* **1993**, *98* (7), 5648-5652.
77. Perdew, J. P.; Ernzerhof, M.; Burke, K., Rationale for Mixing Exact Exchange with Density Functional Approximations. *J. Chem. Phys.* **1996**, *105* (22), 9982-9985.
78. Zhao, Y.; Truhlar, D. G., A New Local Density Functional for Main-group Thermochemistry, Transition Metal Bonding, Thermochemical Kinetics, and Noncovalent interactions. *J. Chem. Phys.* **2006**, *125* (19), 194101.
79. Mucha, E.; Stuckmann, A.; Marianski, M.; Struwe, W. B.; Meijer, G.; Pagel, K., In-depth Structural Analysis of Glycans in the Gas Phase. *Chem. Sci.* **2019**, *10* (5), 1272-1284.
80. Hillenkamp, F.; Karas, M.; Beavis, R. C.; Chait, B. T., Matrix-Assisted Laser Desorption/Ionization Mass Spectrometry of Biopolymers. *Anal. Chem.* **1991**, *63* (24), 1193A-1203A.
81. Dole, M.; Mack, L. L.; Hines, R. L.; Mobley, R. C.; Ferguson, L. D.; Alice, M. B., Molecular Beams of Macroions. *J. Chem. Phys.* **1968**, *49* (5), 2240-2249.
82. Yamashita, M.; Fenn, J. B., Electrospray Ion Source. Another Variation on the Free-jet Theme. *J. Phys. Chem.* **1984**, *88* (20), 4451-4459.
83. Taylor, G. I., Disintegration of Water Drops in an Electric Field. *P. R. Soc. Lond. A Mat.* **1964**, *280* (1382), 383-397.
84. Mora, J. F. d. l., The Fluid Dynamics of Taylor Cones. *Annu. Rev. Fluid Mech.* **2007**, *39* (1), 217-243.
85. Rayleigh, L., XX. On the Equilibrium of Liquid Conducting Masses Charged with Electricity. *Lond. Edinb. Dubl. Phil. Mag.* **1882**, *14* (87), 184-186.

86. Banerjee, S.; Mazumdar, S., Electrospray Ionization Mass Spectrometry: A Technique to Access the Information beyond the Molecular Weight of the Analyte. *Int. J. Anal. Chem.* **2012**, *2012*, Article ID 282574.
87. Konermann, L.; Ahadi, E.; Rodriguez, A. D.; Vahidi, S., Unraveling the Mechanism of Electrospray Ionization. *Anal. Chem.* **2013**, *85* (1), 2-9.
88. Iribarne, J.; Thomson, B., On the Evaporation of Small Ions From Charged Droplets. *J. Chem. Phys.* **1976**, *64* (6), 2287-2294.
89. Ahadi, E.; Konermann, L., Ejection of Solvated Ions from Electrosprayed Methanol/Water Nanodroplets Studied by Molecular Dynamics Simulations. *J. Am. Chem. Soc.* **2011**, *133* (24), 9354-9363.
90. Fernandez de la Mora, J., Electrospray Ionization of Large Multiply Charged Species Proceeds via Dole's Charged Residue Mechanism. *Anal. Chim. Acta* **2000**, *406* (1), 93-104.
91. Iavarone, A. T.; Williams, E. R., Mechanism of Charging and Supercharging Molecules in Electrospray Ionization. *J. Am. Chem. Soc.* **2003**, *125* (8), 2319-2327.
92. Hogan, C. J.; Carroll, J. A.; Rohrs, H. W.; Biswas, P.; Gross, M. L., Combined Charged Residue-Field Emission Model of Macromolecular Electrospray Ionization. *Anal. Chem.* **2009**, *81* (1), 369-377.
93. Konermann, L.; Rodriguez, A. D.; Liu, J., On the Formation of Highly Charged Gaseous Ions from Unfolded Proteins by Electrospray Ionization. *Anal. Chem.* **2012**, *84* (15), 6798-6804.
94. Ahadi, E.; Konermann, L., Modeling the Behavior of Coarse-Grained Polymer Chains in Charged Water Droplets: Implications for the Mechanism of Electrospray Ionization. *J. Phys. Chem. B* **2012**, *116* (1), 104-112.
95. Fersht, A., *Structure and Mechanism in Protein Science: a Guide to Enzyme Catalysis and Protein Folding*, W. H. Freeman and Company: 1999.
96. Calixte, E. I.; Liyanage, O. T.; Kim, H. J.; Ziperman, E. D.; Pearson, A. J.; Gallagher, E. S., Release of Carbohydrate-Metal Adducts from Electrospray Droplets: Insight into Glycan Ionization by Electrospray. *J. Phys. Chem. B* **2020**, *124* (3), 479-486.

97. Çarçabal, P.; Jockusch, R. A.; Hünig, I.; Snoek, L. C.; Kroemer, R. T.; Davis, B. G.; Gamblin, D. P.; Compagnon, I.; Oomens, J.; Simons, J. P., Hydrogen Bonding and Cooperativity in Isolated and Hydrated Sugars: Mannose, Galactose, Glucose, and Lactose. *J. Am. Chem. Soc.* **2005**, *127* (32), 11414-11425.
98. Battistel, M. D.; Pendrill, R.; Widmalm, G.; Freedberg, D. I., Direct Evidence for Hydrogen Bonding in Glycans: A Combined NMR and Molecular Dynamics Study. *J. Phys. Chem. B* **2013**, *117* (17), 4860-4869.
99. Battistel, M. D.; Azurmendi, H. F.; Freedberg, D. I., Glycan OH Exchange Rate Determination in Aqueous Solution: Seeking Evidence for Transient Hydrogen Bonds. *J. Phys. Chem. B* **2017**, *121* (4), 683-695.
100. Liyanage, O. T.; Brantley, M. R.; Calixte, E. I.; Solouki, T.; Shuford, K. L.; Gallagher, E. S., Characterization of Electrospray Ionization (ESI) Parameters on In-ESI Hydrogen/Deuterium Exchange of Carbohydrate-Metal Ion Adducts. *J. Am. Soc. Mass Spectrom.* **2019**, *30* (2), 235-247.
101. Loo, J. A., Studying Noncovalent Protein Complexes by Electrospray Ionization Mass Spectrometry. *Mass Spectrom. Rev.* **1997**, *16* (1), 1-23.
102. Chowdhury, S. K.; Katta, V.; Chait, B. T., Probing Conformational Changes in Proteins by Mass Spectrometry. *J. Am. Chem. Soc.* **1990**, *112* (24), 9012-9013.
103. Blanc, J. C. Y. L.; Beuchemin, D.; Siu, K. W. M.; Guevremont, R.; Berman, S. S., Thermal Denaturation of Some Proteins and Its Effect on Their Electrospray Mass Spectrat. *Org. Mass Spectrom.* **1991**, *26* (10), 831-839.
104. Loo, J. A.; Loo, R. R. O.; Udseth, H. R.; Edmonds, C. G.; Smith, R. D., Solvent-induced Conformational Changes of Polypeptides Probed by Electrospray-ionization Mass Spectrometry. *Rapid Commun. Mass Spectrom.* **1991**, *5* (3), 101-105.
105. Smith, R. D.; Light-Wahl, K. J.; Winger, B. E.; Loo, J. A., Preservation of Non-covalent Associations in Electrospray Ionization Mass Spectrometry: Multiply Charged Polypeptide and Protein Dimers. *Org. Mass Spectrom.* **1992**, *27* (7), 811-821.
106. Light-Wahl, K. J.; Schwartz, B. L.; Smith, R. D., Observation of the Noncovalent Quaternary Associations of Proteins by Electrospray Ionization Mass Spectrometry. *J. Am. Chem. Soc.* **1994**, *116* (12), 5271-5278.

107. Lifshitz, C.; Laskin, J., *Principles of Mass Spectrometry Applied to Biomolecules*. John Wiley & Sons: 2006.
108. Breuker, K.; McLafferty, F. W., Stepwise Evolution of Protein Native Structure with Electrospray into the Gas Phase, 10^{-12} to 10^2 s. *Proc. Natl. Acad. Sci.* **2008**, *105* (47), 18145-18152.
109. Naidoo, K. J.; Chen, J. Y.-J., The Role of Water in the Design of Glycosidic Linkage Flexibility. *Mol. Phys.* **2003**, *101* (17), 2687-2694.
110. Jockusch, R. A.; Kroemer, R. T.; Talbot, F. O.; Snoek, L. C.; Çarçabal, P.; Simons, J. P.; Havenith, M.; Bakker, J. M.; Compagnon, I.; Meijer, G.; von Helden, G., Probing the Glycosidic Linkage: UV and IR Ion-Dip Spectroscopy of a Lactoside. *J. Am. Chem. Soc.* **2004**, *126* (18), 5709-5714.
111. Veillon, L.; Huang, Y.; Peng, W.; Dong, X.; Cho, B. G.; Mechref, Y., Characterization of Isomeric Glycan Structures by LC-MS/MS. *Electrophoresis* **2017**, *38* (17), 2100-2114.
112. Alpert, A. J., Hydrophilic-interaction Chromatography for the Separation of Peptides, Nucleic Acids and Other Polar Compounds. *J. Chromatogr. A* **1990**, *499*, 177-196.
113. Wuhrer, M.; de Boer, A. R.; Deelder, A. M., Structural Glycomics Using Hydrophilic Interaction Chromatography (HILIC) with Mass Spectrometry. *Mass Spectrom. Rev.* **2009**, *28* (2), 192-206.
114. Ahn, J.; Bones, J.; Yu, Y. Q.; Rudd, P. M.; Gilar, M., Separation of 2-Aminobenzamide Labeled Glycans Using Hydrophilic Interaction Chromatography Columns Packed with $1.7\mu\text{m}$ Sorbent. *J. Chromatogr. B* **2010**, *878* (3), 403-408.
115. Williams, D. K.; Meadows, C. W.; Bori, I. D.; Hawkrige, A. M.; Comins, D. L.; Muddiman, D. C., Synthesis, Characterization, and Application of Iodoacetamide Derivatives Utilized for the ALiPHAT Strategy. *J. Am. Chem. Soc.* **2008**, *130* (7), 2122-2123.
116. Zhou, S.; Wooding, K. M.; Mechref, Y., Analysis of Permethylated Glycan by Liquid Chromatography (LC) and Mass Spectrometry (MS). In *High-Throughput Glycomics and Glycoproteomics*, Springer, 2017, 83-96.

117. West, C.; Elfakir, C.; Lafosse, M., Porous Graphitic Carbon: A Versatile Stationary Phase for Liquid Chromatography. *J. Chromatogr. A* **2010**, *1217* (19), 3201-3216.
118. Behan, J. L.; Smith, K. D., The Analysis of Glycosylation: a Continued Need for High pH Anion Exchange Chromatography. *Biomed. Chromatogr.* **2011**, *25* (1-2), 39-46.
119. Rendleman, J. A., Ionization of Carbohydrates in the Presence of Metal Hydroxides and Oxides. In *Carbohydrates in Solution*, American Chemical Society, 1973, Vol. 117, 51-69.
120. Hardy, M. R.; Townsend, R. R.; Lee, Y. C., Monosaccharide Analysis of Glycoconjugates by Anion Exchange Chromatography with Pulsed Amperometric Detection. *Anal. Biochem.* **1988**, *170* (1), 54-62.
121. Stadheim, T. A.; Li, H.; Kett, W.; Burnina, I. N.; Gerngross, T. U., Use of High-performance Anion Exchange Chromatography with Pulsed Amperometric Detection for O-glycan Determination in Yeast. *Nat. Protoc.* **2008**, *3* (6), 1026-1031.
122. Giles, K.; Pringle, S. D.; Worthington, K. R.; Little, D.; Wildgoose, J. L.; Bateman, R. H., Applications of a Travelling Wave-based Radio-frequency-only Stacked Ring Ion Guide. *Rapid Commun. Mass Spectrom.* **2004**, *18* (20), 2401-2414.
123. Clowers, B. H.; Dwivedi, P.; Steiner, W. E.; Hill, H. H.; Bendiak, B., Separation of Sodiated Isobaric Disaccharides and Trisaccharides Using Electrospray Ionization-Atmospheric Pressure Ion Mobility-Time of Flight Mass Spectrometry. *J. Am. Soc. Mass Spectrom.* **2005**, *16* (5), 660-669.
124. Dwivedi, P.; Bendiak, B.; Clowers, B. H.; Hill, H. H., Rapid Resolution of Carbohydrate Isomers by Electrospray Ionization Ambient Pressure Ion Mobility Spectrometry-Time-of-Flight Mass Spectrometry (ESI-APIMS-TOFMS). *J. Am. Soc. Mass Spectrom.* **2007**, *18* (7), 1163-1175.
125. Ujma, J.; Ropartz, D.; Giles, K.; Richardson, K.; Langridge, D.; Wildgoose, J.; Green, M.; Pringle, S., Cyclic Ion Mobility Mass Spectrometry Distinguishes Anomers and Open-Ring Forms of Pentasaccharides. *J. Am. Soc. Mass Spectrom.* **2019**, *30* (6), 1028-1037.
126. Fenn, L. S.; McLean, J. A., Structural Resolution of Carbohydrate Positional and Structural Isomers Based on Gas-phase Ion Mobility-Mass Spectrometry. *Phys. Chem. Chem. Phys.* **2011**, *13* (6), 2196-2205.

127. Huang, Y.; Dodds, E. D., Ion Mobility Studies of Carbohydrates as Group I Adducts: Isomer Specific Collisional Cross Section Dependence on Metal Ion Radius. *Anal. Chem.* **2013**, *85* (20), 9728-9735.
128. Fenn, L. S.; McLean, J. A., Enhanced Carbohydrate Structural Selectivity in Ion Mobility-Mass Spectrometry Analyses by Boronic Acid Derivatization. *Chem. Commun.* **2008**, (43), 5505-5507.
129. Pagel, K.; Harvey, D. J., Ion Mobility–Mass Spectrometry of Complex Carbohydrates: Collision Cross Sections of Sodiated N-linked Glycans. *Anal. Chem.* **2013**, *85* (10), 5138-5145.
130. Hofmann, J.; Struwe, W. B.; Scarff, C. A.; Scrivens, J. H.; Harvey, D. J.; Pagel, K., Estimating Collision Cross Sections of Negatively Charged N-Glycans using Traveling Wave Ion Mobility-Mass Spectrometry. *Anal. Chem.* **2014**, *86* (21), 10789-10795.
131. Li, H.; Bendiak, B.; Siems, W. F.; Gang, D. R.; Hill Jr, H. H., Ion Mobility Mass Spectrometry Analysis of Isomeric Disaccharide Precursor, Product and Cluster Ions. *Rapid Commun. Mass Spectrom.* **2013**, *27* (23), 2699-2709.
132. Li, H.; Bendiak, B.; Kaplan, K.; Davis, E.; Siems, W. F.; Hill, H. H., Evaluation of Ion Mobility-Mass Spectrometry for Determining the Isomeric Heterogeneity of Oligosaccharide-Alditols Derived from Bovine Submaxillary Mucin. *Int. J. Mass Spectrom.* **2013**, *352*, 9-18.
133. Yamaguchi, Y.; Nishima, W.; Re, S.; Sugita, Y., Confident Identification of Isomeric N-glycan Structures by Combined Ion Mobility Mass Spectrometry and Hydrophilic Interaction Liquid Chromatography. *Rapid Commun. Mass Spectrom.* **2012**, *26* (24), 2877-2884.
134. Lee, S.; Valentine, S. J.; Reilly, J. P.; Clemmer, D. E., Analyzing a Mixture of Disaccharides by IMS-VUVPD-MS. *Int. J. Mass Spectrom.* **2012**, *309*, 161-167.
135. Hoffmann, W.; Hofmann, J.; Pagel, K., Energy-Resolved Ion Mobility-Mass Spectrometry—A Concept to Improve the Separation of Isomeric Carbohydrates. *J. Am. Soc. Mass Spectrom.* **2014**, *25* (3), 471-479.
136. Ibrahim, Y. M.; Hamid, A. M.; Deng, L.; Garimella, S. V. B.; Webb, I. K.; Baker, E. S.; Smith, R. D., New Frontiers for Mass Spectrometry Based upon Structures for Lossless Ion Manipulations. *Analyst* **2017**, *142* (7), 1010-1021.

137. Giles, K.; Ujma, J.; Wildgoose, J.; Pringle, S.; Richardson, K.; Langridge, D.; Green, M., A Cyclic Ion Mobility-Mass Spectrometry System. *Anal. Chem.* **2019**, *91* (13), 8564-8573.
138. McLafferty, F., Tandem Mass Spectrometry. *Science* **1981**, *214* (4518), 280-287.
139. R, W., Rays of Positive Electricity and their Application to Chemical Analysis. *Nature* **1914**, *92* (2307), 549-550.
140. Aston, F. W., *The Distribution of Intensity Along the Positive Ray Parabolas of Atoms and Molecules of Hydrogen and Its Possible Explanation*. Cambridge University Press: 1920.
141. Jennings, K. R., Collision-induced Decompositions of Aromatic Molecular Ions. *Int. J. Mass Spectrom. Ion Phys.* **1968**, *1* (3), 227-235.
142. Haddon, W. F.; McLafferty, F. W., Metastable Ion Characteristics. VII. Collision-induced Metastables. *J. Am. Chem. Soc.* **1968**, *90* (17), 4745-4746.
143. Wysocki, V. H.; Kenttämaa, H. I.; Cooks, R. G., Internal Energy Distributions of Isolated Ions after Activation by Various Methods. *Int. J. Mass Spectrom. Ion Processes* **1987**, *75* (2), 181-208.
144. Vékey, K., Internal Energy Effects in Mass Spectrometry. *J. Mass Spectrom.* **1996**, *31* (5), 445-463.
145. Roepstorff, P.; Fohlman, J., Proposal for a Common Nomenclature for Sequence Ions in Mass Spectra of Peptides. *Biomed. Mass Spectrom.* **1984**, *11* (11), 601.
146. Wysocki, V. H.; Resing, K. A.; Zhang, Q.; Cheng, G., Mass Spectrometry of Peptides and Proteins. *Methods* **2005**, *35* (3), 211-222.
147. Zubarev, R. A.; Kelleher, N. L.; McLafferty, F. W., Electron Capture Dissociation of Multiply Charged Protein Cations. A Nonergodic Process. *J. Am. Chem. Soc.* **1998**, *120* (13), 3265-3266.
148. Zubarev, R. A.; Kruger, N. A.; Fridriksson, E. K.; Lewis, M. A.; Horn, D. M.; Carpenter, B. K.; McLafferty, F. W., Electron Capture Dissociation of Gaseous Multiply-Charged Proteins Is Favored at Disulfide Bonds and Other Sites of High Hydrogen Atom Affinity. *J. Am. Chem. Soc.* **1999**, *121* (12), 2857-2862.

149. Zubarev, R. A.; Haselmann, K. F.; Budnik, B.; Kjeldsen, F.; Jensen, F., Towards An Understanding of the Mechanism of Electron-Capture Dissociation: A Historical Perspective and Modern Ideas. *Eur. J. Mass Spectrom.* **2002**, *8* (5), 337-349.
150. Kjeldsen, F.; Haselmann, K. F.; Budnik, B. A.; Jensen, F.; Zubarev, R. A., Dissociative Capture of Hot (3–13 eV) Electrons by Polypeptide Polycations: an Efficient Process Accompanied by Secondary Fragmentation. *Chem. Phys. Lett.* **2002**, *356* (3), 201-206.
151. Zubarev, R. A.; Horn, D. M.; Fridriksson, E. K.; Kelleher, N. L.; Kruger, N. A.; Lewis, M. A.; Carpenter, B. K.; McLafferty, F. W., Electron Capture Dissociation for Structural Characterization of Multiply Charged Protein Cations. *Anal. Chem.* **2000**, *72* (3), 563-573.
152. Tsybin, Y. O.; Håkansson, P.; Budnik, B. A.; Haselmann, K. F.; Kjeldsen, F.; Gorshkov, M.; Zubarev, R. A., Improved Low-energy Electron Injection Systems for High Rate Electron Capture Dissociation in Fourier Transform Ion Cyclotron Resonance Mass Spectrometry. *Rapid Commun. Mass Spectrom.* **2001**, *15* (19), 1849-1854.
153. Syka, J. E. P.; Coon, J. J.; Schroeder, M. J.; Shabanowitz, J.; Hunt, D. F., Peptide and Protein Sequence Analysis by Electron Transfer Dissociation Mass Spectrometry. *Proc. Natl. Acad. Sci. USA* **2004**, *101* (26), 9528-9533.
154. Gunawardena, H. P.; He, M.; Chrisman, P. A.; Pitteri, S. J.; Hogan, J. M.; Hodges, B. D. M.; McLuckey, S. A., Electron Transfer versus Proton Transfer in Gas-Phase Ion/Ion Reactions of Polyprotonated Peptides. *J. Am. Chem. Soc.* **2005**, *127* (36), 12627-12639.
155. Domon, B.; Costello, C. E., A Systematic Nomenclature for Carbohydrate Fragmentations in FAB-MS/MS Spectra of Glycoconjugates. *Glycoconjugate J.* **1988**, *5* (4), 397-409.
156. Harvey, D. J., Collision-induced Fragmentation of Underivatized N-linked Carbohydrates Ionized by Electrospray. *J. Mass Spectrom.* **2000**, *35* (10), 1178-1190.
157. Pearson, W. L.; Contreras, C.; Powell, D.; Berden, G.; Oomens, J.; Bendiak, B.; Eyler, J. R., Differentiation of Rubidiated Methyl-d-Glycoside Stereoisomers by Infrared Multiple-Photon Dissociation Spectroscopy in the O–H and C–H Stretching Regions. *J. Phys. Chem. B* **2015**, *119* (41), 12970-12981.

158. Hernandez, O.; Isenberg, S.; Steinmetz, V.; Glish, G. L.; Maitre, P., Probing Mobility-Selected Saccharide Isomers: Selective Ion–Molecule Reactions and Wavelength-Specific IR Activation. *J. Phys. Chem. A* **2015**, *119* (23), 6057-6064.
159. Barnes, L.; Schindler, B.; Chambert, S.; Allouche, A.-R.; Compagnon, I., Conformational Preferences of Protonated N-acetylated Hexosamines Probed by InfraRed Multiple Photon Dissociation (IRMPD) Spectroscopy and Ab Initio Calculations. *Int. J. Mass Spectrom.* **2017**, *421*, 116-123.
160. Tan, Y.; Zhao, N.; Liu, J.; Li, P.; Stedwell, C. N.; Yu, L.; Polfer, N. C., Vibrational Signatures of Isomeric Lithiated N-acetyl-D-hexosamines by Gas-Phase Infrared Multiple-Photon Dissociation (IRMPD) Spectroscopy. *J. Am. Soc. Mass Spectrom.* **2017**, *28* (3), 539-550.
161. Schindler, B.; Renois-Predelus, G.; Bagdadi, N.; Melizi, S.; Barnes, L.; Chambert, S.; Allouche, A.-R.; Compagnon, I., MS/IR, a New MS-based Hyphenated Method for Analysis of Hexuronic Acid Epimers in Glycosaminoglycans. *Glycoconjugate J.* **2017**, *34* (3), 421-425.
162. Cagmat, E. B.; Szczepanski, J.; Pearson, W. L.; Powell, D. H.; Eyler, J. R.; Polfer, N. C., Vibrational Signatures of Metal-chelated Monosaccharide Epimers: Gas-phase Infrared Spectroscopy of Rb⁺-tagged Glucuronic and Iduronic Acid. *Phys. Chem. Chem. Phys.* **2010**, *12* (14), 3474-3479.
163. Wattjes, J.; Schindler, B.; Trombotto, S.; David, L.; Moerschbacher, B. M.; Compagnon, I., Discrimination of Patterns of N-acetylation in Chitooligosaccharides by Gas Phase IR Spectroscopy Integrated to Mass Spectrometry. *Pure Appl. Chem.* **2017**, *89* (9), 1349-1357.
164. Little, D. P.; Speir, J. P.; Senko, M. W.; O'Connor, P. B.; McLafferty, F. W., Infrared Multiphoton Dissociation of Large Multiply Charged Ions for Biomolecule Sequencing. *Anal. Chem.* **1994**, *66* (18), 2809-2815.
165. Zhu, Y.; Roy, H. A.; Cunningham, N. A.; Strobehn, S. F.; Gao, J.; Munshi, M. U.; Berden, G.; Oomens, J.; Rodgers, M. T., Effects of Sodium Cationization versus Protonation on the Conformations and N-glycosidic Bond Stabilities of Sodium Cationized Urd and dUrd: Solution Conformation of [Urd+Na]⁺ is Preserved upon ESI. *Phys. Chem. Chem. Phys.* **2017**, *19* (27), 17637-17652.
166. Zhu, Y.; Hamlow, L. A.; He, C. C.; Lee, J. K.; Gao, J.; Berden, G.; Oomens, J.; Rodgers, M. T., Gas-Phase Conformations and N-Glycosidic Bond Stabilities of Sodium Cationized 2'-Deoxyguanosine and Guanosine: Sodium Cations Preferentially Bind to the Guanine Residue. *J. Phys. Chem. B* **2017**, *121* (16), 4048-4060.

167. Zhu, Y.; Yang, Z.; Rodgers, M. T., Influence of Linkage Stereochemistry and Protecting Groups on Glycosidic Bond Stability of Sodium Cationized Glycosyl Phosphates. *J. Am. Soc. Mass Spectrom.* **2017**, *28* (12), 2602-2613.
168. Gray, C. J.; Schindler, B.; Migas, L. G.; Pičmanová, M.; Allouche, A. R.; Green, A. P.; Mandal, S.; Motawia, M. S.; Sánchez-Pérez, R.; Bjarnholt, N.; Møller, B. L.; Rijs, A. M.; Barran, P. E.; Compagnon, I.; Evers, C. E.; Flitsch, S. L., Bottom-Up Elucidation of Glycosidic Bond Stereochemistry. *Anal. Chem.* **2017**, *89* (8), 4540-4549.
169. Stefan, S. E.; Eyler, J. R., Differentiation of Methyl-glucopyranoside Anomers by Infrared Multiple Photon Dissociation with a Tunable CO₂ Laser. *Anal. Chem.* **2009**, *81* (3), 1224-1227.
170. Cocinero, E. J.; Carcabal, P.; Vaden, T. D.; Simons, J. P.; Davis, B. G., Sensing the Anomeric Effect in a Solvent-free Environment. *Nature* **2011**, *469* (7328), 76-79.
171. Schindler, B.; Barnes, L.; Renois, G.; Gray, C.; Chambert, S.; Fort, S.; Flitsch, S.; Loison, C.; Allouche, A.-R.; Compagnon, I., Anomeric Memory of the Glycosidic Bond upon Fragmentation and its Consequences for Carbohydrate Sequencing. *Nat. Commun.* **2017**, *8* (1), 973.
172. Masson, G. R.; Burke, J. E.; Ahn, N. G.; Anand, G. S.; Borchers, C.; Brier, S.; Bou-Assaf, G. M.; Engen, J. R.; Englander, S. W.; Faber, J.; Garlish, R.; Griffin, P. R.; Gross, M. L.; Guttman, M.; Hamuro, Y.; Heck, A. J. R.; Houde, D.; Iacob, R. E.; Jørgensen, T. J. D.; Kaltashov, I. A.; Klinman, J. P.; Konermann, L.; Man, P.; Mayne, L.; Pascal, B. D.; Reichmann, D.; Skehel, M.; Snijder, J.; Strutzenberg, T. S.; Underbakke, E. S.; Wagner, C.; Wales, T. E.; Walters, B. T.; Weis, D. D.; Wilson, D. J.; Wintrode, P. L.; Zhang, Z.; Zheng, J.; Schriemer, D. C.; Rand, K. D., Recommendations for Performing, Interpreting and Reporting Hydrogen Deuterium Exchange Mass Spectrometry (HDX-MS) Experiments. *Nat. Methods* **2019**, *16* (7), 595-602.
173. Englander, S. W.; Kallenbach, N. R., Hydrogen Exchange and Structural Dynamics of Proteins and Nucleic Acids. *Q. Rev. Biophys.* **1983**, *16* (4), 521-655.
174. Hamuro, Y.; Coales, S. J.; Southern, M. R.; Nemeth-Cawley, J. F.; Stranz, D. D.; Griffin, P. R., Rapid Analysis of Protein Structure and Dynamics by Hydrogen/deuterium Exchange Mass Spectrometry. *J. Biomol. Tech.* **2003**, *14* (3), 171-82.

175. Konermann, L.; Pan, J.; Liu, Y.-H., Hydrogen Exchange Mass Spectrometry for Studying Protein Structure and Dynamics. *Chem. Soc. Rev.* **2011**, *40* (3), 1224-1234.
176. Englander, S. W.; Mayne, L.; Bai, Y.; Sosnick, T. R., Hydrogen Exchange: The Modern Legacy of Linderstrøm-Lang. *Protein Sci.* **1997**, *6* (5), 1101-1109.
177. Sowole, M. A.; Konermann, L., Effects of Protein–Ligand Interactions on Hydrogen/Deuterium Exchange Kinetics: Canonical and Noncanonical Scenarios. *Anal. Chem.* **2014**, *86* (13), 6715-6722.
178. Huang, R. Y. C.; Hudgens, J. W., Effects of Desialylation on Human α 1-Acid Glycoprotein–Ligand Interactions. *Biochemistry* **2013**, *52* (40), 7127-7136.
179. Liu, Y.-H.; Belcheva, A.; Konermann, L.; Golemi-Kotra, D., Phosphorylation-Induced Activation of the Response Regulator VraR from *Staphylococcus aureus*: Insights from Hydrogen Exchange Mass Spectrometry. *J. Mol. Biol.* **2009**, *391* (1), 149-163.
180. Katta, V.; Chait, B. T.; Carr, S., Conformational Changes in Proteins Probed by Hydrogen-exchange Electrospray-ionization Mass Spectrometry. *Rapid Commun. Mass Spectrom.* **1991**, *5* (4), 214-217.
181. Siuti, N.; Kelleher, N. L., Decoding Protein Modifications Using Top-down Mass Spectrometry. *Nat. Methods* **2007**, *4* (10), 817-821.
182. Kaltashov, I. A.; Bobst, C. E.; Abzalimov, R. R., H/D Exchange and Mass Spectrometry in the Studies of Protein Conformation and Dynamics: Is There a Need for a Top-Down Approach? *Anal. Chem.* **2009**, *81* (19), 7892-7899.
183. Abzalimov, R. R.; Kaltashov, I. A., Extraction of Local Hydrogen Exchange Data from HDX CAD MS Measurements by Deconvolution of Isotopic Distributions of Fragment Ions. *J. Am. Soc. Mass Spectrom.* **2006**, *17* (11), 1543-1551.
184. Jørgensen, T. J. D.; Gårdsvoll, H.; Ploug, M.; Roepstorff, P., Intramolecular Migration of Amide Hydrogens in Protonated Peptides upon Collisional Activation. *J. Am. Chem. Soc.* **2005**, *127* (8), 2785-2793.
185. Boyd, R.; Somogyi, Á., The Mobile Proton Hypothesis in Fragmentation of Protonated Peptides: A Perspective. *J. Am. Soc. Mass Spectrom.* **2010**, *21* (8), 1275-1278.

186. Hoerner, J. K.; Xiao, H.; Dobo, A.; Kaltashov, I. A., Is There Hydrogen Scrambling in the Gas Phase? Energetic and Structural Determinants of Proton Mobility within Protein Ions. *J. Am. Chem. Soc.* **2004**, *126* (24), 7709-7717.
187. Rand, K. D.; Adams, C. M.; Zubarev, R. A.; Jørgensen, T. J. D., Electron Capture Dissociation Proceeds with a Low Degree of Intramolecular Migration of Peptide Amide Hydrogens. *J. Am. Chem. Soc.* **2008**, *130* (4), 1341-1349.
188. Pan, J.; Han, J.; Borchers, C. H.; Konermann, L., Electron Capture Dissociation of Electrosprayed Protein Ions for Spatially Resolved Hydrogen Exchange Measurements. *J. Am. Chem. Soc.* **2008**, *130* (35), 11574-11575.
189. Pan, J.; Han, J.; Borchers, C. H.; Konermann, L., Hydrogen/Deuterium Exchange Mass Spectrometry with Top-Down Electron Capture Dissociation for Characterizing Structural Transitions of a 17 kDa Protein. *J. Am. Chem. Soc.* **2009**, *131* (35), 12801-12808.
190. Karch, K. R.; Coradin, M.; Zandarashvili, L.; Kan, Z.-Y.; Gerace, M.; Englander, S. W.; Black, B. E.; Garcia, B. A., Hydrogen-Deuterium Exchange Coupled to Top- and Middle-Down Mass Spectrometry Reveals Histone Tail Dynamics before and after Nucleosome Assembly. *Structure* **2018**, *26* (12), 1651-1663.e3.
191. Felix, T.; Reyzer, M.; Brodbelt, J., Hydrogen/deuterium Exchange of Nucleoside Analogs in a Quadrupole Ion Trap Mass Spectrometer. *Int. J. Mass Spectrom.* **1999**, *190-191*, 161-170.
192. Robinson, J. M.; Greig, M. J.; Griffey, R. H.; Mohan, V.; Laude, D. A., Hydrogen/Deuterium Exchange of Nucleotides in the Gas Phase. *Anal. Chem.* **1998**, *70* (17), 3566-3571.
193. Deng, Y.; Zhang, Z.; Smith, D. L., Comparison of Continuous and Pulsed Labeling Amide Hydrogen Exchange/mass Spectrometry for Studies of Protein Dynamics. *J. Am. Soc. Mass Spectrom.* **1999**, *10* (8), 675-684.
194. Pan, J.; Han, J.; Borchers, C. H.; Konermann, L., Characterizing Short-Lived Protein Folding Intermediates by Top-Down Hydrogen Exchange Mass Spectrometry. *Anal. Chem.* **2010**, *82* (20), 8591-8597.
195. Keppel, T. R.; Weis, D. D., Analysis of Disordered Proteins Using a Simple Apparatus for Millisecond Quench-Flow H/D Exchange. *Anal. Chem.* **2013**, *85* (10), 5161-5168.

196. Zinck, N.; Stark, A.-K.; Wilson, D. J.; Sharon, M., An Improved Rapid Mixing Device for Time-Resolved Electrospray Mass Spectrometry Measurements. *ChemistryOpen* **2014**, *3* (3), 109-114.
197. Brown, K. A.; Lento, C.; Rajendran, S.; Dowd, J.; Wilson, D. J., Epitope Mapping for a Preclinical Bevacizumab (Avastin) Biosimilar on an Extended Construct of Vascular Endothelial Growth Factor A Using Millisecond Hydrogen–Deuterium Exchange Mass Spectrometry. *Biochemistry* **2020**, *59* (30), 2776-2781.
198. Amon, S.; Trelle, M. B.; Jensen, O. N.; Jørgensen, T. J. D., Spatially Resolved Protein Hydrogen Exchange Measured by Subzero-Cooled Chip-Based Nanoelectrospray Ionization Tandem Mass Spectrometry. *Anal. Chem.* **2012**, *84* (10), 4467-4473.
199. Rob, T.; Liuni, P.; Gill, P. K.; Zhu, S.; Balachandran, N.; Berti, P. J.; Wilson, D. J., Measuring Dynamics in Weakly Structured Regions of Proteins Using Microfluidics-Enabled Subsecond H/D Exchange Mass Spectrometry. *Anal. Chem.* **2012**, *84* (8), 3771-3779.
200. Svejidal, R. R.; Dickinson, E. R.; Sticker, D.; Kutter, J. P.; Rand, K. D., Thiolene Microfluidic Chip for Performing Hydrogen/Deuterium Exchange of Proteins at Subsecond Time Scales. *Anal. Chem.* **2019**, *91* (2), 1309-1317.
201. Kostyukevich, Y.; Kononikhin, A.; Popov, I.; Nikolaev, E., Simple Atmospheric Hydrogen/Deuterium Exchange Method for Enumeration of Labile Hydrogens by Electrospray Ionization Mass Spectrometry. *Anal. Chem.* **2013**, *85* (11), 5330-5334.
202. Hemling, M. E.; Conboy, J. J.; Bean, M. F.; Mentzer, M.; Carr, S. A., Gas Phase Hydrogen/deuterium Exchange in Electrospray Ionization Mass Spectrometry as a Practical Tool for Structure Elucidation. *J. Am. Soc. Mass Spectrom.* **1994**, *5* (5), 434-442.
203. Takáts, Z.; Schlosser, G.; Vékey, K., Hydrogen/deuterium Exchange of Electrosprayed Ions in the Atmospheric Interface of a Commercial Triple–Quadrupole Mass Spectrometer. *Int. J. Mass Spectrom.* **2003**, *228* (2), 729-741.
204. Chanthamontri, C. K.; Stopford, A. P.; Snowdon, R. W.; Oldenburg, T. B. P.; Larter, S. R., On-Line Desalting of Crude Oil in the Source Region of a Fourier Transform Ion Cyclotron Resonance Mass Spectrometer. *J. Am. Soc. Mass Spectrom.* **2014**, *25* (8), 1506-1510.

205. Wolff, J. C.; Laures, A. M., 'On-the-fly' Hydrogen/deuterium Exchange Liquid Chromatography/Mass Spectrometry Using a Dual-sprayer Atmospheric Pressure Ionisation Source. *Rapid Commun. Mass Spectrom.* **2006**, *20* (24), 3769-79.
206. Rashid, S.; Overton, S.; Mazigh, B.; Mayer, P. M., Dual-spray Hydrogen/deuterium Exchange (HDX) Reactions: A New Method of Probing Protein Structure. *Rapid Commun. Mass Spectrom.* **2016**, *30* (13), 1505-1512.
207. Mark, L. P.; Gill, M. C.; Mahut, M.; Derrick, P. J., Dual Nano-Electrospray for Probing Solution Interactions and Fast Reactions of Complex Biomolecules. *Eur. J. Mass Spectrom.* **2012**, *18* (5), 439-446.
208. Jansson, E. T.; Lai, Y.-H.; Santiago, J. G.; Zare, R. N., Rapid Hydrogen–Deuterium Exchange in Liquid Droplets. *J. Am. Chem. Soc.* **2017**, *139* (20), 6851-6854.
209. Geller, O.; Lifshitz, C., A Fast Flow Tube Study of Gas Phase H/D Exchange of Multiply Protonated Ubiquitin. *J. Phys. Chem. A* **2005**, *109* (10), 2217-2222.
210. Rand, K. D.; Pringle, S. D.; Murphy, J. P.; Fadgen, K. E.; Brown, J.; Engen, J. R., Gas-Phase Hydrogen/Deuterium Exchange in a Traveling Wave Ion Guide for the Examination of Protein Conformations. *Anal. Chem.* **2009**, *81* (24), 10019-10028.
211. Pan, J.; Heath, B. L.; Jockusch, R. A.; Konermann, L., Structural Interrogation of Electrosprayed Peptide Ions by Gas-Phase H/D Exchange and Electron Capture Dissociation Mass Spectrometry. *Anal. Chem.* **2012**, *84* (1), 373-378.
212. Uppal, S. S.; Beasley, S. E.; Scian, M.; Guttman, M., Gas-Phase Hydrogen/Deuterium Exchange for Distinguishing Isomeric Carbohydrate Ions. *Anal. Chem.* **2017**, *89* (8), 4737-4742.
213. Dempsey, C. E., Hydrogen exchange in peptides and proteins using NMR spectroscopy. *Prog. NMR Spec.* **2001**, *39* (2), 135-170.
214. Eigen, M., Proton Transfer, Acid-Base Catalysis, and Enzymatic Hydrolysis. Part I: Elementary Processes. *Angew. Chem. Int. Ed.* **1964**, *3* (1), 1-19.
215. Gregory, R. B.; Crabo, L.; Percy, A. J.; Rosenberg, A., Water Catalysis of Peptide Hydrogen Isotope Exchange. *Biochemistry* **1983**, *22* (4), 910-917.

216. Brier, S.; Engen, J. R., Hydrogen Exchange Mass Spectrometry: Principles and Capabilities. In *Mass Spectrometry Analysis for Protein-protein Interactions and Dynamics*, Chance, M., Ed.; Wiley-Blackwell: New York, **2008**, 11-43.
217. Bai, Y.; Milne, J. S.; Mayne, L.; Englander, S. W., Primary Structure Effects on Peptide Group Hydrogen Exchange. *Proteins* **1993**, *17* (1), 75-86.
218. Oganessian, I.; Lento, C.; Wilson, D. J., Contemporary Hydrogen Deuterium Exchange Mass Spectrometry. *Methods* **2018**, *144*, 27-42.
219. Narang, D.; Lento, C.; J. Wilson, D., HDX-MS: An Analytical Tool to Capture Protein Motion in Action. *Biomedicines* **2020**, *8* (7), 224.
220. Campbell, S.; Rodgers, M. T.; Marzluff, E. M.; Beauchamp, J. L., Deuterium Exchange Reactions as a Probe of Biomolecule Structure. Fundamental Studies of Gas Phase H/D Exchange Reactions of Protonated Glycine Oligomers with D₂O, CD₃OD, CD₃CO₂D, and ND₃. *J. Am. Chem. Soc.* **1995**, *117* (51), 12840-12854.
221. Wyttenbach, T.; Bowers, M. T., Gas Phase Conformations of Biological Molecules: the Hydrogen/deuterium Exchange Mechanism. *J. Am. Soc. Mass Spectrom.* **1999**, *10* (1), 9-14.
222. Rožman, M., The Gas-phase H/D Exchange Mechanism of Protonated Amino Acids. *J. Am. Soc. Mass Spectrom.* **2005**, *16* (11), 1846-1852.
223. Guttman, M.; Scian, M.; Lee, K. K., Tracking Hydrogen/Deuterium Exchange at Glycan Sites in Glycoproteins by Mass Spectrometry. *Anal. Chem.* **2011**, *83* (19), 7492-7499.
224. Kostyukevich, Y.; Kononikhin, A.; Popov, I.; Nikolaev, E., In-ESI Source Hydrogen/Deuterium Exchange of Carbohydrate Ions. *Anal. Chem.* **2014**, *86* (5), 2595-2600.
225. Liyanage, O. T.; Quintero, A. V.; Hatvany, J. B.; Gallagher, E. S., Distinguishing Carbohydrate Isomers with Rapid Hydrogen/Deuterium Exchange-Mass Spectrometry. *J. Am. Soc. Mass Spectrom.* **2020**.
226. Mistarz, Ulrik H.; Brown, Jeffery M.; Haselmann, Kim F.; Rand, Kasper D., Probing the Binding Interfaces of Protein Complexes Using Gas-Phase H/D Exchange Mass Spectrometry. *Structure* **2016**, *24* (2), 310-318.

227. Mookherjee, A.; Uppal, S. S.; Guttman, M., Dissection of Fragmentation Pathways in Protonated N-Acetylhexosamines. *Anal. Chem.* **2018**, *90* (20), 11883-11891.
228. Apweiler, R.; Hermjakob, H.; Sharon, N., On the Frequency of Protein Glycosylation, as Deduced from Analysis of the SWISS-PROT Database. *Biochim. et Biophys. Acta (BBA) - Gen. Subjects* **1999**, *1473* (1), 4-8.
229. Varki A, C. R., Esko J. D., et al., editors. , *Essentials of Glycobiology [Internet]. 3rd edition. Cold Spring Harbor (NY): Cold Spring Harbor Laboratory Press; 2015-2017. Available from: <https://www.ncbi.nlm.nih.gov/books/NBK310274/>.*
230. Brockhausen, I., Glycodynamics of Mucin Biosynthesis in Gastrointestinal Tumor Cells. In *Glycobiology and Medicine*, Axford, J. S., Ed. Springer US: Boston, MA, 2003, 163-188.
231. Dube, D. H.; Bertozzi, C. R., Glycans in Cancer and Inflammation — Potential for Therapeutics and Diagnostics. *Nat. Rev. Drug Discov.* **2005**, *4*, 477.
232. Saso, L.; Silvestrini, B.; Guglielmotti, A.; Lahita, R.; Cheng, C. Y., Abnormal Glycosylation of α 2-Macroglobulin, a Non-acute-phase Protein, in Patients with Autoimmune Diseases. *Inflammation* **1993**, *17* (4), 465-479.
233. Tramontano, A.; Makker, S. P., Conformation and Glycosylation of a Megalin Fragment Correlate with Nephritogenicity in Heymann Nephritis. *J. Immunol.* **2004**, *172* (4), 2367-2373.
234. Gallagher, E. S.; Hudgens, J. W., Chapter Fourteen - Mapping Protein–Ligand Interactions with Proteolytic Fragmentation, Hydrogen/Deuterium Exchange-Mass Spectrometry. In *Methods in Enzymology*, Kelman, Z., Ed. Academic Press: 2016; Vol. 566, pp 357-404.
235. Shaw, B. F.; Arthanari, H.; Narovlyansky, M.; Durazo, A.; Frueh, D. P.; Pollastri, M. P.; Lee, A.; Bilgicer, B.; Gygi, S. P.; Wagner, G.; Whitesides, G. M., Neutralizing Positive Charges at the Surface of a Protein Lowers Its Rate of Amide Hydrogen Exchange without Altering Its Structure or Increasing Its Thermostability. *J. Am. Chem. Soc.* **2010**, *132* (49), 17411-17425.
236. Bai, Y.; Milne, J. S.; Mayne, L.; Englander, S. W., Primary Structure Effects on Peptide Group Hydrogen Exchange. *Proteins* **1993**, *17* (1), 75-86.
237. Englander, S. W., Hydrogen Exchange and Mass Spectrometry: A Historical Perspective. *J. Am. Soc. Mass Spectrom.* **2006**, *17* (11), 1481-1489.

238. Chait, B. T., Mass Spectrometry: Bottom-Up or Top-Down? *Science* **2006**, *314* (5796), 65-66.
239. Compton, P. D.; Zamdborg, L.; Thomas, P. M.; Kelleher, N. L., On the Scalability and Requirements of Whole Protein Mass Spectrometry. *Anal. Chem.* **2011**, *83* (17), 6868-6874.
240. Shen, L. L.; Hermans, J., Kinetics of Conformation Change of Sperm-whale Myoglobin. I. Folding and Unfolding of Metmyoglobin Following pH Jump. *Biochemistry* **1972**, *11* (10), 1836-1841.
241. Konermann, L.; Rosell, F. I.; Mauk, A. G.; Douglas, D. J., Acid-Induced Denaturation of Myoglobin Studied by Time-Resolved Electrospray Ionization Mass Spectrometry. *Biochemistry* **1997**, *36* (21), 6448-6454.
242. Winger, B. E.; Light-Wahl, K. J.; Rockwood, A. L.; Smith, R. D., Probing Qualitative Conformation Differences of Multiply Protonated Gas-phase Proteins via Hydrogen/deuterium Isotopic Exchange with Water-D₂. *J. Am. Chem. Soc.* **1992**, *114* (14), 5897-5898.
243. Wolff, J.-C.; Laures, A. M. F., 'On-the-fly' Hydrogen/deuterium Exchange Liquid Chromatography/Mass Spectrometry Using a Dual-sprayer Atmospheric Pressure Ionisation Source. *Rapid Commun. Mass Spectrom.* **2006**, *20* (24), 3769-3779.
244. Jeong, E. S.; Cha, E.; Cha, S.; Kim, S.; Oh, H. B.; Kwon, O.-S.; Lee, J., Online Simultaneous Hydrogen/Deuterium Exchange of Multitarget Gas-Phase Molecules by Electrospray Ionization Mass Spectrometry Coupled with Gas Chromatography. *Anal. Chem.* **2017**, *89* (22), 12284-12292.
245. Brenner, N.; Haapala, M.; Vuorensola, K.; Kostianen, R., Simple Coupling of Gas Chromatography to Electrospray Ionization Mass Spectrometry. *Anal. Chem.* **2008**, *80* (21), 8334-8339.
246. Price, N. P. J., Oligosaccharide Structures Studied by Hydrogen-Deuterium Exchange and MALDI-TOF Mass Spectrometry. *Anal. Chem.* **2006**, *78* (15), 5302-5308.
247. Kostyukevich, Y.; Kononikhin, A.; Popov, I.; Nikolaev, E., Conformations of Cationized Linear Oligosaccharides Revealed by FTMS Combined with in-ESI H/D Exchange. *J. Mass Spectrom.* **2015**, *50* (10), 1150-1156.

248. McCloskey, J. A., [16] Introduction of Deuterium by Exchange for Measurement by Mass Spectrometry. In *Methods in Enzymology*, Academic Press: 1990, Vol. 193, 329-338.
249. Katta, V.; Chait, B. T., Hydrogen/deuterium Exchange Electrospray Ionization Mass Spectrometry: a Method for Probing Protein Conformational Changes in Solution. *J. Am. Chem. Soc.* **1993**, *115* (14), 6317-6321.
250. S W Englander; N W Downer, a.; Teitelbaum, H., Hydrogen Exchange. *Annu. Rev. Biochem.* **1972**, *41* (1), 903-924.
251. Liepinsh, E.; Otting, G., Proton Exchange Rates from Amino Acid Side Chains—Implications for Image Contrast. *Magn. Reson. Med.* **1996**, *35* (1), 30-42.
252. Mortensen, D. N.; Williams, E. R., Theta-Glass Capillaries in Electrospray Ionization: Rapid Mixing and Short Droplet Lifetimes. *Anal. Chem.* **2014**, *86* (18), 9315-9321.
253. Smith, J. N.; Flagan, R. C.; Beauchamp, J. L., Droplet Evaporation and Discharge Dynamics in Electrospray Ionization. *J. Phys. Chem. A* **2002**, *106* (42), 9957-9967.
254. Bawa Singh; Johh H. Thomas, I., Chapter 1.8 - Surface Physics and Its Relation to Vacuum Science. In *Handbook of Vacuum Science and Technology*, Dorothy M. Hoffman; Bawa Singh; III, J. H. T., Eds. Academic Press: San Diego, 1998; pp 40-55.
255. Bureiko, S. F.; Denisov, G. S.; Lange, I. Y., Kinetics of the Fast Proton Exchange between Ethanol and Water in an Inert Solvent. *Kinet. Catal.(Engl. Transl.)* 1976, *17*(6), 1232-1235; *Kinet. Katal.* 1976, *17*(6), 1431-1434.
256. Klotz, I. M.; Frank, B. H., Activation Energy of Deuterium-Hydrogen Exchange in Amides. *J. Am. Chem. Soc.* **1964**, *86* (18), 3889-3889.
257. Offenbacher, A. R.; Iavarone, A. T.; Klinman, J. P., Hydrogen–deuterium Exchange Reveals Long-range Dynamical Allostery in Soybean Lipoxygenase. *J. Biol. Chem.* **2018**, *293* (4), 1138-1148.
258. Guttman, M.; Wales, T. E.; Whittington, D.; Engen, J. R.; Brown, J. M.; Lee, K. K., Tuning a High Transmission Ion Guide to Prevent Gas-Phase Proton Exchange During H/D Exchange MS Analysis. *J. Am. Soc. Mass Spectrom.* **2016**, *27* (4), 662-668.

259. Waters: Dramatically Enhanced Analytical Sensitivity with the Use of Novel StepWave Ion Transfer Technology in the SYNAPT G2-S System. Waters Application Note Literature No. 720003964EN. 2011.
260. Kaltashov, I. A.; Doroshenko, V. M.; Cotter, R. J., Gas Phase Hydrogen/deuterium Exchange Reactions of Peptide Ions in a Quadrupole Ion Trap Mass Spectrometer. *Proteins* **1997**, *28* (1), 53-58.
261. Reyzer, M. L.; Brodbelt, J. S., Gas-phase H/D Exchange Reactions of Polyamine Complexes: (M + H)⁺, (M + alkali metal)⁺, and (M + 2H)²⁺. *J. Am. Soc. Mass Spectrom.* **2000**, *11* (8), 711-721.
262. Jurchen, J. C.; Cooper, R. E.; Williams, E. R., The Role of Acidic Residues and of Sodium Ion Adduction on the Gas-phase H/D Exchange of Peptides and Peptide Dimers. *J. Am. Soc. Mass Spectrom.* **2003**, *14* (12), 1477-1487.
263. Chen, Y.; Yue, L.; Li, Z.; Ding, X.; Wang, L.; Dai, X.; Fang, X.; Pan, Y.; Ding, C.-F., Investigation of Protonated and Sodiated Leucine-enkephalin by Hydrogen-deuterium Exchange and Theoretical Calculations. *Anal. Methods* **2015**, *7* (13), 5551-5556.
264. Skelley, A. M.; Mathies, R. A., Rapid On-column Analysis of Glucosamine and Its Mutarotation by Microchip Capillary Electrophoresis. *J. Chromatogr. A* **2006**, *1132* (1), 304-309.
265. Helenius, A., How N-linked Oligosaccharides Affect Glycoprotein Folding in the Endoplasmic Reticulum. *Mol. Biol. Cell* **1994**, *5* (3), 253-265.
266. Lis, H.; Sharon, N., Protein Glycosylation: Structural and Functional Aspects. *Eur. J. Biochem.* **1993**, *218* (1), 1-27.
267. Hemling, M. E.; Conboy, J. J.; Bean, M. F.; Mentzer, M.; Carr, S. A., Gas Phase Hydrogen/Deuterium Exchange in Electrospray Ionization Mass Spectrometry as a Practical Tool for Structure Elucidation. *J. Am. Soc. Mass Spectrom.* **1994**, *5* (5), 434-442.
268. Zhrebker, A.; Kostyukevich, Y.; Kononikhin, A.; Roznyatovsky, V. A.; Popov, I.; Grishin, Y. K.; Perminova, I. V.; Nikolaev, E., High Desolvation Temperature Facilitates the ESI-Source H/D Exchange at Non-Labile Sites of Hydroxybenzoic Acids and Aromatic Amino Acids. *Analyst* **2016**, *141* (8), 2426-2434.

269. Liyanage, O. T.; Seneviratne, C. A.; Gallagher, E. S., Applying an Internal Standard to Improve the Repeatability of In-electrospray H/D Exchange of Carbohydrate-Metal Adducts. *J. Am. Soc. Mass Spectrom.* **2019**, *30* (8), 1368-1372.
270. Hamuro, Y., Determination of Equine Cytochrome c Backbone Amide Hydrogen/Deuterium Exchange Rates by Mass Spectrometry Using a Wider Time Window and Isotope Envelope. *J. Am. Soc. Mass Spectrom.* **2017**, *28* (3), 486-497.
271. Wilson, D. J.; Konermann, L., A Capillary Mixer with Adjustable Reaction Chamber Volume for Millisecond Time-Resolved Studies by Electrospray Mass Spectrometry. *Anal. Chem.* **2003**, *75* (23), 6408-6414.
272. Resetca, D.; Wilson, D. J., Mapping Ligand Binding Using Microfluidics-Enabled Millisecond Timescale Hydrogen-Deuterium Exchange. *Int. J. Mass Spectrom.* **2017**, *420*, 67-73.
273. Mortensen, D. N.; Williams, E. R., Ultrafast (1 μ s) Mixing and Fast Protein Folding in Nanodrops Monitored by Mass Spectrometry. *J. Am. Chem. Soc.* **2016**, *138* (10), 3453-3460.
274. Mortensen, D. N.; Williams, E. R., Investigating Protein Folding and Unfolding in Electrospray Nanodrops Upon Rapid Mixing Using Theta-Glass Emitters. *Anal. Chem.* **2015**, *87* (2), 1281-1287.
275. Fisher, C. M.; Kharlamova, A.; McLuckey, S. A., Affecting Protein Charge State Distributions in Nano-Electrospray Ionization via In-Spray Solution Mixing Using Theta Capillaries. *Anal. Chem.* **2014**, *86* (9), 4581-4588.
276. Xia, Z.; Williams, E. R., Effect of Droplet Lifetime on Where Ions are Formed in Electrospray Ionization. *Analyst* **2019**, *144* (1), 237-248.
277. Ballew, R. M.; Sabelko, J.; Gruebele, M., Direct Observation of Fast Protein Folding: The Initial Collapse of Apomyoglobin. *Proc. Natl. Acad. Sci.* **1996**, *93* (12), 5759-5764.
278. Shastry, M. C. R.; Luck, S. D.; Roder, H., A Continuous-Flow Capillary Mixing Method to Monitor Reactions on the Microsecond Time Scale. *Biophys. J.* **1998**, *74* (5), 2714-2721.

279. Susa, A. C.; Xia, Z.; Williams, E. R., Small Emitter Tips for Native Mass Spectrometry of Proteins and Protein Complexes from Nonvolatile Buffers That Mimic the Intracellular Environment. *Anal. Chem.* **2017**, *89* (5), 3116-3122.
280. Pfeifer, R. J.; Hendricks Jr., C. D., Parametric Studies of Electrohydrodynamic Spraying. *AIAA J.* **1968**, *6* (3), 496-502.
281. Jones, A. R.; Thong, K. C., The Production of Charged Monodisperse Fuel Droplets by Electrical Dispersion. *J. Phys. D Appl. Phys.* **1971**, *4* (8), 1159-1166.
282. De La Mora, J. F.; Loscertales, I. G., The Current Emitted by Highly Conducting Taylor Cones. *J. Fluid Mech.* **1994**, *260*, 155-184.
283. Horn, D. M.; Breuker, K.; Frank, A. J.; McLafferty, F. W., Kinetic Intermediates in the Folding of Gaseous Protein Ions Characterized by Electron Capture Dissociation Mass Spectrometry. *J. Am. Chem. Soc.* **2001**, *123* (40), 9792-9799.
284. Breuker, K.; Oh, H.; Lin, C.; Carpenter, B. K.; McLafferty, F. W., Nonergodic and Conformational Control of the Electron Capture Dissociation of Protein Cations. *Proc. Natl. Acad. Sci. USA* **2004**, *101* (39), 14011-14016.
285. Badman, E. R.; Myung, S.; Clemmer, D. E., Evidence for Unfolding and Refolding of Gas-phase Cytochrome c Ions in a Paul Trap. *J. Am. Soc. Mass Spectrom.* **2005**, *16* (9), 1493-1497.
286. Schennach, M.; Breuker, K., Proteins with Highly Similar Native Folds Can Show Vastly Dissimilar Folding Behavior When Desolvated. *Angew. Chem. Int. Ed.* **2014**, *53* (1), 164-168.
287. Schennach, M.; Breuker, K., Probing Protein Structure and Folding in the Gas Phase by Electron Capture Dissociation. *J. Am. Soc. Mass Spectrom.* **2015**, *26* (7), 1059-1067.
288. Kebarle, P.; Verkerk, U. H., Electrospray: From Ions in Solution to Ions in the Gas Phase, What We Know Now. *Mass Spectrom. Rev.* **2009**, *28* (6), 898-917.
289. Wilm, M.; Mann, M., Analytical Properties of the Nanoelectrospray Ion Source. *Anal. Chem.* **1996**, *68* (1), 1-8.
290. Wilm, M. S.; Mann, M., Electrospray and Taylor-Cone Theory, Dole's Beam of Macromolecules at Last? *Int. J. Mass Spectrom. Ion Processes* **1994**, *136* (2), 167-180.

291. Smith, D. P. H., The Electrohydrodynamic Atomization of Liquids. *IEEE Trans. Ind. Appl.* **1986**, IA-22 (3), 527-535.
292. Rohner, T. C.; Lion, N.; Girault, H. H., Electrochemical and Theoretical Aspects of Electrospray Ionisation. *Phys. Chem. Chem. Phys.* **2004**, 6 (12), 3056-3068.
293. Sze, A.; Erickson, D.; Ren, L.; Li, D., Zeta-potential Measurement Using the Smoluchowski Equation and the Slope of the Current–time Relationship in Electroosmotic Flow. *J. Colloid Interf. Sci.* **2003**, 261 (2), 402-410.
294. Valaskovic, G. A.; Murphy, J. P.; Lee, M. S., Automated Orthogonal Control System for Electrospray Ionization. *J. Am. Soc. Mass Spectrom.* **2004**, 15 (8), 1201-1215.
295. Lis, H.; Sharon, N., Protein Glycosylation. Structural and Functional Aspects. *Eur. J. Biochem.* **1993**, 218 (1), 1-27.
296. Ashline, D. J.; Lapadula, A. J.; Liu, Y.-H.; Lin, M.; Grace, M.; Pramanik, B.; Reinhold, V. N., Carbohydrate Structural Isomers Analyzed by Sequential Mass Spectrometry. *Anal. Chem.* **2007**, 79 (10), 3830-3842.
297. Nagy, G.; Pohl, N. L. B., Complete Hexose Isomer Identification with Mass Spectrometry. *J. Am. Soc. Mass Spectrom.* **2015**, 26 (4), 677-685.
298. Yang, H.; Shi, L.; Zhuang, X.; Su, R.; Wan, D.; Song, F.; Li, J.; Liu, S., Identification of Structurally Closely Related Monosaccharide and Disaccharide Isomers by PMP Labeling in Conjunction with IM-MS/MS. *Sci. Reports* **2016**, 6 (1), 28079.
299. Hofmann, J.; Hahm, H. S.; Seeberger, P. H.; Pagel, K., Identification of Carbohydrate Anomers Using Ion Mobility–Mass Spectrometry. *Nature* **2015**, 526 (7572), 241-244.
300. Cheng, H. L.; Her, G. R., Determination of Linkages of Linear and Branched Oligosaccharides Using Closed-ring Chromophore Labeling and Negative Ion Trap Mass Spectrometry. *J. Am. Soc. Mass Spectrom.* **2002**, 13 (11), 1322-1330.
301. Galermo, A. G.; Nandita, E.; Barboza, M.; Amicucci, M. J.; Vo, T.-T. T.; Lebrilla, C. B., Liquid Chromatography–Tandem Mass Spectrometry Approach for Determining Glycosidic Linkages. *Anal. Chem.* **2018**, 90 (21), 13073-13080.

302. Kim, H. J.; Gallagher, E. S., Achieving Multiple Hydrogen/deuterium Exchange Timepoints of Carbohydrate Hydroxyls Using Theta-electrospray Emitters. *Analyst* **2020**, *145* (8), 3056-3063.
303. Mueller, D.; Eckersley, M.; Richter, W., Hydrogen Transfer Reactions in the Formation of “Y+ 2” Sequence Ions from Protonated Peptides. *Org. Mass Spectrometry* **1988**, *23* (3), 217-222.
304. Johnson, R.; Krylov, D.; Walsh, K., Proton Mobility within Electrosprayed Peptide Ions. *J. Mass Spectrom.* **1995**, *30* (2), 386-387.
305. Ferguson, P. L.; Pan, J.; Wilson, D. J.; Dempsey, B.; Lajoie, G.; Shilton, B.; Konermann, L., Hydrogen/Deuterium Scrambling during Quadrupole Time-of-Flight MS/MS Analysis of a Zinc-Binding Protein Domain. *Anal. Chem.* **2007**, *79* (1), 153-160.
306. Abzalimov, R. R.; Kaltashov, I. A., Controlling Hydrogen Scrambling in Multiply Charged Protein Ions during Collisional Activation: Implications for Top-Down Hydrogen/Deuterium Exchange MS Utilizing Collisional Activation in the Gas Phase. *Anal. Chem.* **2010**, *82* (3), 942-950.
307. Abzalimov, R. R.; Kaplan, D. A.; Easterling, M. L.; Kaltashov, I. A., Protein Conformations Can be Probed in Top-down HDX MS Experiments Utilizing Electron Transfer Dissociation of Protein Ions without Hydrogen Scrambling. *J. Am. Soc. Mass Spectrom.* **2009**, *20* (8), 1514-1517.
308. Demmers, J. A. A.; Rijkers, D. T. S.; Haverkamp, J.; Killian, J. A.; Heck, A. J. R., Factors Affecting Gas-Phase Deuterium Scrambling in Peptide Ions and Their Implications for Protein Structure Determination. *J. Am. Chem. Soc.* **2002**, *124* (37), 11191-11198.
309. Struwe, W. B.; Baldauf, C.; Hofmann, J.; Rudd, P. M.; Pagel, K., Ion Mobility Separation of Deprotonated Oligosaccharide Isomers – Evidence for Gas-phase Charge Migration. *Chem. Commun.* **2016**, *52* (83), 12353-12356.
310. Bythell, B. J.; Abutokaikah, M. T.; Wagoner, A. R.; Guan, S.; Rabus, J. M., Cationized Carbohydrate Gas-Phase Fragmentation Chemistry. *J. Am. Soc. Mass Spectrom.* **2017**, *28* (4), 688-703.
311. Ceroni, A.; Maass, K.; Geyer, H.; Geyer, R.; Dell, A.; Haslam, S. M., GlycoWorkbench: A Tool for the Computer-Assisted Annotation of Mass Spectra of Glycans. *J. Proteome Res.* **2008**, *7* (4), 1650-1659.

312. Hageman, T. S.; Weis, D. D., Reliable Identification of Significant Differences in Differential Hydrogen Exchange-Mass Spectrometry Measurements Using a Hybrid Significance Testing Approach. *Anal. Chem.* **2019**, *91* (13), 8008-8016.
313. Paternoster, R.; Brame, R.; Mazerolle, P.; Piquero, A., Using the Correct Statistical Test for the Equality of Regression Coefficients. *Criminology* **1998**, *36*, 859-866.
314. Hess, B.; Kutzner, C.; van der Spoel, D.; Lindahl, E., GROMACS 4: Algorithms for Highly Efficient, Load-Balanced, and Scalable Molecular Simulation. *J. Chem. Theory Comput.* **2008**, *4* (3), 435-447.
315. Group, W., GLYCAM Web. Complex Carbohydrate Research Center, University of Georgia, Athens, GA. **2005-2020**
316. Konermann, L.; Metwally, H.; McAllister, R. G.; Popa, V., How to run molecular dynamics simulations on electrospray droplets and gas phase proteins: Basic guidelines and selected applications. *Methods* **2018**, *144*, 104-112.
317. McAllister, R. G.; Metwally, H.; Sun, Y.; Konermann, L., Release of Native-like Gaseous Proteins from Electrospray Droplets via the Charged Residue Mechanism: Insights from Molecular Dynamics Simulations. *J. Am. Chem. Soc.* **2015**, *137* (39), 12667-12676.
318. Bekiroglu, S.; Kenne, L.; Sandström, C., ¹H NMR Studies of Maltose, Maltoheptaose, α -, β -, and γ -Cyclodextrins, and Complexes in Aqueous Solutions with Hydroxy Protons as Structural Probes. *J. Org. Chem.* **2003**, *68* (5), 1671-1678.
319. Kodad, H.; Mokhlisse, R.; Davin, E.; Mille, G., Etude des interactions sucrées en solution aqueuse par spectroscopie IRTF. *Can. J. Anal. Sci. Spect.* **1998**, *43* (5), 129-136.
320. Rondeau, P.; Sers, S.; Jhurry, D.; Cadet, F., Sugar Interaction with Metals in Aqueous Solution: Indirect Determination from Infrared and Direct Determination from Nuclear Magnetic Resonance Spectroscopy. *Appl. Spectrosc.* **2003**, *57* (4), 466-472.
321. Harvey, D. J., Ionization and Collision-induced Fragmentation of N-linked and Related Carbohydrates Using Divalent Cations. *J. Am. Soc. Mass Spectrom.* **2001**, *12* (8), 926-937.

322. Huang, Y.; Dodds, E. D., Discrimination of Isomeric Carbohydrates as the Electron Transfer Products of Group II Cation Adducts by Ion Mobility Spectrometry and Tandem Mass Spectrometry. *Anal. Chem.* **2015**, *87* (11), 5664-5668.
323. Schaller-Duke, R. M.; Bogala, M. R.; Cassady, C. J., Electron Transfer Dissociation and Collision-Induced Dissociation of Underivatized Metallated Oligosaccharides. *J. Am. Soc. Mass Spectrom.* **2018**, *29* (5), 1021-1035.
324. Hofmeister, G. E.; Zhou, Z.; Leary, J. A., Linkage Position Determination in Lithium-cationized Disaccharides: Tandem Mass Spectrometry and Semiempirical Calculations. *J. Am. Chem. Soc.* **1991**, *113* (16), 5964-5970.
325. de Juan, L.; de la Mora, J. F., Charge and Size Distributions of Electrospray Drops. *J. Colloid Interf. Sci.* **1997**, *186* (2), 280-293.
326. Ferguson, P. L.; Konermann, L., Nonuniform Isotope Patterns Produced by Collision-Induced Dissociation of Homogeneously Labeled Ubiquitin: Implications for Spatially Resolved Hydrogen/Deuterium Exchange ESI-MS Studies. *Anal. Chem.* **2008**, *80* (11), 4078-4086.
327. Harrison, A. G., The Gas-phase Basicities and Proton Affinities of Amino Acids and Peptides. *Mass Spectrom. Rev.* **1997**, *16* (4), 201-217.
328. Deakyne, C. A., Proton Affinities and Gas-phase Basicities: Theoretical Methods and Structural Effects. *Int. J. Mass Spectrom.* **2003**, *227* (3), 601-616.
329. Dongré, A. R.; Jones, J. L.; Somogyi, Á.; Wysocki, V. H., Influence of Peptide Composition, Gas-Phase Basicity, and Chemical Modification on Fragmentation Efficiency: Evidence for the Mobile Proton Model. *J. Am. Chem. Soc.* **1996**, *118* (35), 8365-8374.
330. Tang, X. J.; Thibault, P.; Boyd, R. K., Fragmentation Reactions of Multiply-protonated Peptides and Implications for Sequencing by Tandem Mass Spectrometry with Low-energy Collision-induced Dissociation. *Anal. Chem.* **1993**, *65* (20), 2824-2834.
331. Harrison, A. G.; Yalcin, T., Proton Mobility in Protonated Amino Acids and Peptides. *Int. J. Mass Spectrom. Ion Processes* **1997**, *165-166*, 339-347.

332. Tsapraïlis, G.; Nair, H.; Somogyi, Á.; Wysocki, V. H.; Zhong, W.; Futrell, J. H.; Summerfield, S. G.; Gaskell, S. J., Influence of Secondary Structure on the Fragmentation of Protonated Peptides. *J. Am. Chem. Soc.* **1999**, *121* (22), 5142-5154.
333. Röllgen, F. W.; Giessmann, U.; Borchers, F.; Levsen, K., Collisional Activation Spectra of [M + Li]⁺, [M + Na]⁺ and [M + K]⁺ Ions Formed by Field Desorption of Some Monosaccharides. *Org. Mass Spectrom.* **1978**, *13* (8), 459-461.
334. Cheng, C.; Gross, M. L., Applications and Mechanisms of Charge-remote Fragmentation. *Mass Spectrom. Rev.* **2000**, *19* (6), 398-420.
335. Adams, J., Charge-remote Fragmentations: Analytical Applications and Fundamental Studies. *Mass Spectrom. Rev.* **1990**, *9* (2), 141-186.
336. Wang, Q.; Borotto, N. B.; Håkansson, K., Gas-Phase Hydrogen/Deuterium Scrambling in Negative-Ion Mode Tandem Mass Spectrometry. *J. Am. Soc. Mass Spectrom.* **2019**, *30* (5), 855-863.
337. Vanommeslaeghe, K.; Hatcher, E.; Acharya, C.; Kundu, S.; Zhong, S.; Shim, J.; Darian, E.; Guvench, O.; Lopes, P.; Vorobyov, I.; Mackerell Jr, A. D., CHARMM General Force Field: A Force Field for Drug-like Molecules Compatible with the CHARMM All-atom Additive Biological Force Fields. *J. Comput. Chem.* **2010**, *31* (4), 671-690.
338. Vanommeslaeghe, K.; Raman, E. P.; MacKerell, A. D., Jr., Automation of the CHARMM General Force Field (CGenFF) II: Assignment of Bonded Parameters and Partial Atomic Charges. *J. Chem. Inf. Model* **2012**, *52* (12), 3155-3168.
339. Guvench, O.; Mallajosyula, S. S.; Raman, E. P.; Hatcher, E.; Vanommeslaeghe, K.; Foster, T. J.; Jamison, F. W.; MacKerell, A. D., CHARMM Additive All-Atom Force Field for Carbohydrate Derivatives and Its Utility in Polysaccharide and Carbohydrate-Protein Modeling. *J. Chem. Theory Comput.* **2011**, *7* (10), 3162-3180.
340. Verlet, L., Computer "Experiments" on Classical Fluids. I. Thermodynamical Properties of Lennard-Jones Molecules. *Phys. Rev.* **1967**, *159* (1), 98-103.
341. Hockney, R. W.; Goel, S. P.; Eastwood, J. W., Quiet High-resolution Computer Models of a Plasma. *J. Comput. Phys.* **1974**, *14* (2), 148-158.
342. Nosé, S., A Molecular Dynamics Method for Simulations in the Canonical Ensemble. *Mol. Phys.* **1984**, *52* (2), 255-268.

343. Hoover, W. G., Canonical Dynamics: Equilibrium Phase-space Distributions. *Phys. Rev. A* **1985**, *31* (3), 1695-1697.
344. Konermann, L.; Omar, H.; G. McAllister, R.; Popa, V., *How to Run Molecular Dynamics Simulations on Electrospray Droplets and Gas Phase Proteins: Basic Guidelines and Selected Applications*. 2018; Vol. 144.
345. Schlesinger, D.; Sellberg, J. A.; Nilsson, A.; Pettersson, L. G. M., Evaporative Cooling of Microscopic Water Droplets in Vacuo: Molecular Dynamics Simulations and Kinetic Gas Theory. *J. Chem. Phys.* **2016**, *144* (12), 124502.
346. Hanwell, M. D.; Curtis, D. E.; Lonie, D. C.; Vandermeersch, T.; Zurek, E.; Hutchison, G. R., Avogadro: an Advanced Semantic Chemical Editor, Visualization, and Analysis Platform. *J. Cheminformatics* **2012**, *4* (1), 17.
347. Dashnau, J. L.; Sharp, K. A.; Vanderkooi, J. M., Carbohydrate Intramolecular Hydrogen Bonding Cooperativity and Its Effect on Water Structure. *J. Phys. Chem. B* **2005**, *109* (50), 24152-24159.
348. Jeffrey, G. A.; Jeffrey, G. A., *An Introduction to Hydrogen Bonding*. Oxford University Press New York: 1997; Vol. 12.
349. Craig, B. N.; Janssen, M. U.; Wickersham, B. M.; Rabb, D. M.; Chang, P. S.; O'Leary, D. J., Isotopic Perturbation of Intramolecular Hydrogen Bonds in Rigid 1,3-Diols: NMR Studies Reveal Unusually Large Equilibrium Isotope Effects. *J. Org. Chem.* **1996**, *61* (26), 9610-9613.
350. Zhu, J.; Cole, R. B., Ranking of Gas-phase Acidities and Chloride Affinities of Monosaccharides and Linkage Specificity in Collision-induced Decompositions of Negative Ion Electrospray-generated Chloride Adducts of Oligosaccharides. *J. Am. Soc. Mass Spectrom.* **2001**, *12* (11), 1193-1204.
351. Tsai, S.-T.; Chen, J.-L.; Ni, C.-K., Does Low-energy Collision-induced Dissociation of Lithiated and Sodiated Carbohydrates Always Occur at Anomeric Carbon of the Reducing End? *Rapid Commun. Mass Spectrom.* **2017**, *31* (21), 1835-1844.
352. Tan, Y.; Polfer, N. C., Linkage and Anomeric Differentiation in Trisaccharides by Sequential Fragmentation and Variable-Wavelength Infrared Photodissociation. *J. Am. Soc. Mass Spectrom.* **2015**, *26* (2), 359-368.

353. Gaye, M. M.; Kurulugama, R.; Clemmer, D. E., Investigating Carbohydrate Isomers by IMS-CID-IMS-MS: Precursor and Fragment Ion Cross-sections. *Analyst* **2015**, *140* (20), 6922-6932.
354. Asam, M. R.; Glish, G. L., Tandem Mass Spectrometry of Alkali Cationized Polysaccharides in a Quadrupole Ion Trap. *J. Am. Soc. Mass Spectrom.* **1997**, *8* (9), 987-995.
355. da Costa, E. V.; Moreira, A. S. P.; Nunes, F. M.; Coimbra, M. A.; Evtuguin, D. V.; Domingues, M. R. M., Differentiation of Isomeric Pentose Disaccharides by Electrospray Ionization Tandem Mass Spectrometry and Discriminant Analysis. *Rapid Commun. Mass Spectrom.* **2012**, *26* (24), 2897-2904.
356. Hsu, H. C.; Liew, C. Y.; Huang, S.-P.; Tsai, S.-T.; Ni, C.-K., Simple Method for De Novo Structural Determination of Underivatized Glucose Oligosaccharides. *Sci. Reports* **2018**, *8* (1), 5562.
357. Robert H. Callender; R. Brian Dyer; Rudolf Gilmanshin; Woodruff, W. H., Fast Events in Protein Folding: The Time Evolution of Primary Processes. *Annu. Rev. Phys. Chem.* **1998**, *49* (1), 173-202.
358. Chickos, J. S.; Jr., W. E. A., Enthalpies of Vaporization of Organic and Organometallic Compounds, 1880–2002. *J. Phys. Chem. Ref. Data* **2003**, *32* (2), 519-878.
359. Singh, B.; Thomas, J. H. I., Chapter 1.8 - Surface Physics and Its Relation to Vacuum Science. In *Handbook of Vacuum Science and Technology*, Hoffman, D. M.; Singh, B.; Thomas, J. H. I., Eds. Academic Press: San Diego, 1998; pp 40-55.
360. Abutokaikah, M. T.; Frye, J. W.; Tschampel, J.; Rabus, J. M.; Bythell, B. J., Fragmentation Pathways of Lithiated Hexose Monosaccharides. *J. Am. Soc. Mass Spectrom.* **2018**, *29* (8), 1627-1637.
361. Zhu, X.; Sato, T., The Distinction of Underivatized Monosaccharides Using Electrospray Ionization Ion Trap Mass Spectrometry. *Rapid Commun. Mass Spectrom.* **2007**, *21* (2), 191-8.
362. Chen, J.-L.; Nguan, H. S.; Hsu, P.-J.; Tsai, S.-T.; Liew, C. Y.; Kuo, J.-L.; Hu, W.-P.; Ni, C.-K., Collision-induced Dissociation of Sodiated Glucose and Identification of Anomeric Configuration. *Phys. Chem. Chem. Phys.* **2017**, *19* (23), 15454-15462.

363. Sterling, T.; Irwin, J. J., ZINC 15 – Ligand Discovery for Everyone. *J. Chem. Inf. Model.* **2015**, *55* (11), 2324-2337.
364. Woods, R., GLYCAM Web (<http://www.glycam.com>). Complex Carbohydrate Research Center, University of Georgia. Athens: 2014.
365. Zheng, Y.-J.; Ornstein, R. L.; Leary, J. A., A Density Functional Theory Investigation of Metal Ion Binding Sites in Monosaccharides. *J. Mol. Structure THEOCHEM* **1997**, *389* (3), 233-240.